

Analysis and Design of a Planar Radiating Element for Automotive Satellite Broadcasting Reception Systems

THÈSE N° 5123 (2011)

PRÉSENTÉE LE 28 OCTOBRE 2011

À LA FACULTÉ SCIENCES ET TECHNIQUES DE L'INGÉNIEUR
LABORATOIRE D'ÉLECTROMAGNÉTISME ET ACOUSTIQUE
PROGRAMME DOCTORAL EN GÉNIE ÉLECTRIQUE

ÉCOLE POLYTECHNIQUE FÉDÉRALE DE LAUSANNE

POUR L'OBTENTION DU GRADE DE DOCTEUR ÈS SCIENCES

PAR

Roberto TORRES SÁNCHEZ

acceptée sur proposition du jury:

Prof. M. A. Ionescu, président du jury
Prof. J. R. Mosig, directeur de thèse
Dr C. Mangenot, rapporteur
Prof. P. Otero, rapporteur
Prof. J. Perruisseau-Carrier, rapporteur



ÉCOLE POLYTECHNIQUE
FÉDÉRALE DE LAUSANNE

Suisse
2011

This thesis has been typeset using the MiKTeX2.5 distribution of L^AT_EX 2_ε.
An electronic version is available at <http://library.epfl.ch/theses/?nr=5123>

(...) En effet, je crois que ce monde global où nous habitons, global notamment en ce qui concerne l'information, est nettement différent de tout autre monde de toute autre époque. Ceci distingue notre génération, ceux qui vivent à cette époque-ci, par rapport à ceux qui ont vécu dans tout autre lieu et à toute autre période de l'histoire. Nous avons le privilège de vivre à une époque où nous ne savons pas ce qui va se passer, parce que nous n'avons pas d'expérience en ce sens. La globalisation pose des problèmes très sérieux et très graves, mais il y a aussi des avantages.

Tout au long de l'histoire, les grandes puissances hégémoniques n'ont globalisé qu'une partie de ce qui est globalisable, spécialement ce qui a à voir avec la production, les matières premières et les ressources de la planète.

Globaliser signifierait, de mon point de vue, le fait d'essayer de faire parvenir à tous, de rendre globales, des idées qui je crois doivent être universelles. Des idées comme la démocratie, comme la liberté, comme l'égalité, comme la justice.

Une chose qui a attiré mon attention, très récemment, lors de mon voyage dans le désert de la Syrie, a été de voir la tente d'un Bédouin avec une antenne parabolique à ses côtés. Ce qui veut dire que ce Bédouin-ci, indépendamment du fait qu'il habite sous une tente dans un désert, est parfaitement informé de ce qui se passe dans n'importe quelle partie du monde. La globalisation fera que tout devienne global et que cette opulence dont jouissent certains dans le monde soit un fait connu de tous et, par conséquent, que l'inégalité existante entre ce qu'on appelle le Premier-Monde et Tiers-Monde soit une inégalité insoutenable à moyen terme.

Je crois que maintenant nous avons un certain espoir que les idées humanistes deviennent enfin universelles. Si elles ne le deviennent pas maintenant, il sera très difficile qu'elles le deviennent, car c'est maintenant qu'il y a le plus de chances que cela arrive (...)

Prof. BERNARDO SOUVIRÓN (circa 2008).

Abstract

The present thesis deals with the electromagnetic modeling, design and practical implementation of a planar antenna for the reception of satellite broadcasting services from user terminals on board automotive platforms. This antenna is intended to address the market of low cost consumer applications. As a consequence, stringent structural and performance-to-price ratio requirements have to be imposed.

The antenna has been conceived as a low profile phased array, on a multilayer planar technology, with fully electronic beam steering and polarization tracking capabilities. The success of this approach strongly relies on the ability of designing highly sophisticated planar multilayered radiators that will act as array elements providing both adequate performance and enough geometrical flexibility to match the constraints dictated by the imposed array topology and structure.

The main subject of this thesis is the basic building block of such an antenna, the so-called Elementary Radiating Cell. This cell not only comprises the bare radiators but also the passive circuits (hybrids, power combiners, long via-holes through the multilayered substrates) able to connect the radiating elements to the array beamforming feeding network.

The implementation of this Elementary Radiating Cell must be compatible with the available multilayer technologies and with the selected array lattice. This severely limits the available volume and poses some trade-off problems, whose solution has been one of the most challenging efforts in this thesis.

This thesis has been carried out in the framework of a joint project between the European Space Agency, several key industrial partners in the sector of satellite R&D and consumer applications, led by IMST-Germany, and the EPFL Laboratoire d'Électromagnétisme et d'Acoustique (EPFL-LEMA). The project has demonstrated the feasibility of the electronically steered phased array antenna concept in the development of a new generation of compact satellite terminals for the automotive market.

Keywords

Direct Broadcasting Satellite, Consumer Applications, Microwave Antenna, Ku-Band, Phased Array, Circular Polarisation, Radiating Element, Multilayer Printed Circuits, Electromagnetic Modeling and Design.

Résumé

Cette thèse traite de la modélisation électromagnétique, de la conception et de la réalisation pratique d'une antenne planaire pour la réception de services de radiodiffusion par satellite à bord d'automobiles et autres plateformes mobiles semblables. Cette antenne est destinée au marché de consommation d'applications à bas coût. Cela demande alors l'imposition de contraintes structurelles strictes ainsi qu'un compromis entre performances et prix.

L'antenne a été conçue comme un réseau phasé à bas profil et faible encombrement, ayant la possibilité de pointer électroniquement son faisceau et de suivre la polarisation de l'onde incidente. La réussite de cette stratégie dépend fortement de la capacité de concevoir des radiateurs planaires multicouche très sophistiqués, qui agiront comme éléments du réseau, en assurant à la fois des performances suffisantes et assez de flexibilité géométrique pour s'adapter aux restrictions imposées par la topologie et par la structure du réseau.

Le sujet principal de cette thèse est la cellule de base de cette antenne, appelée "Elementary Radiating Cell." Cette cellule comprend non seulement les radiateurs de base mais aussi les circuits passifs (hybrides, diviseurs de puissance, interconnexions verticales entre les couches du substrat) servant à connecter les radiateurs au circuit d'alimentation du réseau.

L'implémentation de cette cellule élémentaire doit être compatible avec la technologie multicouche sélectionnée et avec la maille choisie pour le réseau. Ceci limite drastiquement le volume disponible et pose le problème des compromis, dont la solution a été un des principaux défis relevés par cette thèse.

Ce travail a été réalisé dans le cadre d'un projet commun octroyé par l'Agence Spatiale Européenne à une équipe internationale de partenaires industriels dans le domaine des applications automobiles des satellites, conduit par IMST-Allemagne et incluant le Laboratoire d'Electromagnétisme et d'Acoustique (LEMA) de l'EPFL. Le projet a montré la faisabilité du concept d'antenne réseau planaire à pointage électronique pour développer une nouvelle génération de terminaux compact assurant la réception satellite au bord d'automobiles et autres plateformes mobiles.

Mots-clés

Radiodiffusion Directe par Satellite, Applications Domestiques, Antennes Microondes, Bande-Ku, Réseau Phasé, Polarisation Circulaire, Eléments Rayonnants, Circuits Imprimés Multicouche, Modélisation Electromagnétique et Conception d'Antennes

Acknowledgements

First and foremost, to my thesis advisor, Prof. Juan R. Mosig. This work has been possible thanks to his invaluable support and advise. I am very grateful to him and to Dr. Michael Mattes for being confident on my chances of doing a good work and giving me the opportunity to join the *Laboratoire d'Electromagnétisme et d'Acoustique* (LEMA) during my PhD. At LEMA I have enjoyed an excellent working environment and witnessed the great human capital treasured by its members. My gratitude also to Prof. Pablo Otero from the Escuela Técnica Superior de Ingeniería de Telecomunicación de la Universidad de Málaga (ETSIT-UMA) for all of his guidance and his assistance during my first steps in the field of planar antennas.

My appreciation goes to my other committee members as well: Dr. Cyril Mangenot, from the European Space Agency Space Research and Technology Centre (ESA-ESTEC) at Noordwijk and Prof. Julien Perruisseau-Carrier from EPFL, for having accepted to examine this work, providing valuable insights and for their contribution to improve the quality of this thesis. Thanks are also due to Prof. Adrian M. Ionescu for chairing my thesis committee.

Thank you specially to Prof. Anja Skrivervik for her valuable advise and plenty of timely hints. Thanks again to Dr. M. Mattes, Prof. Benjamin Fuchs and Dr. Sergio López for their support in the preparation and proofreading of this memoir. I would also like to acknowledge all the industrial partners of the NATALIA project, in particular the *Ku* teams from JAST Antenna Systems and IMST GmbH, for so many fruitful collaborations and friendly exchanges.

Un grand merci to Jean-François Zürcher and *l'équipe de l'Atelier de Circuits Imprimés* (EPFL-STI-ACI) *au complet* for their wise recommendations and their decisive support in the conception, manufacturing, photographing and measurement of the prototypes presented in this document and many others not shown here.

I am indebted to Mrs. Eulalia Durussel. From her key position in the secretary, she helps the lab to run smoothly and assists all of us in many important matters. Thank you also to Mr. David Desscan for all his technical support and for keeping our computational resources in optimal conditions.

Thanks go to all the colleagues and friends I could meet during my time at LEMA and in Lausanne. For the pleasure of learning together, for the opportunity of learning from each one of you, for your support in so many peripeteia and for all the good moments we shared during these years.

Y, con el permiso de todos ustedes, quisiera dedicar esta memoria a las personas que, a lo largo de todos estos años tesis, me han enseñado que con un poquito de amor, todo tiene arreglo.

Contents

Contents	vii
List of Acronyms	xi
1 Introduction	1
1.1 Scope. The NATALIA project	3
1.1.1 Project Goal	3
1.1.2 Project Overview	6
1.2 Objectives	21
1.3 Methodology	21
1.4 Outline	22
1.5 Original Contributions	22
References	24
2 Elementary Radiating Cell. Design Guidelines	29
2.1 Introduction	29
2.2 Design Approach	31
2.3 Design Guidelines	32
2.4 Radiating Element with Single Linear Polarization	33
2.4.1 Buildup	33
2.4.2 Metalization Planes	44
2.4.3 Parametric Study	48
2.5 Radiating Element with Dual Linear Polarization	69
2.5.1 Buildup	69
2.5.2 Metalization Planes	75
2.6 Radiating Element with Dual Circular Polarization	75
References	80
3 Elementary Radiating Cell. Design Process	85

3.1	Introduction	85
3.2	Integration within the Antenna PCB Buildup	86
3.2.1	First Design Iteration	88
3.2.2	Proof of Concept	98
3.3	Integration within the Array Lattice	122
3.3.1	Radiating Element Description	124
3.3.2	Layout Comparison	126
3.3.3	Justification of Layout Differences	127
3.3.4	Justification of Buildup Differences	133
3.4	Conclusion	137
	References	138

4 Elementary Radiating Cell Evaluation 141

4.1	Introduction	141
4.2	Fabrication of the prototypes	143
4.3	Linearly Polarized Radiating Element	144
4.3.1	Fabrication Tolerances	144
4.3.2	Measured Performance	154
4.3.3	Conclusion	162
4.4	The Long Via	165
4.4.1	Nominal Performance	166
4.4.2	Fabrication Tolerances	167
4.4.3	Measured Performance	168
4.4.4	Conclusion	171
4.5	The Power Combiner	171
4.5.1	Nominal Performance	171
4.5.2	Perturbed Performance	176
4.5.3	Measured Performance	178
4.5.4	Conclusion	180
4.6	Circularly Polarized Radiating Element. The Cell	183
4.6.1	Fabrication Tolerances	184
4.6.2	Measured Performance	193
4.6.3	Conclusion	203
4.7	Conclusion	203
	References	205

5 Conclusion and Perspectives	207
References	210
A Infinite Array Modeling	211
A.1 Introduction	211
A.2 The Unit Cell	211
A.3 Active reflection coefficients	212
A.3.1 Active coupling coefficients	219
References	222
B Definition of the Axial Ratio	223
B.1 Introduction	223
B.2 Definition	223
B.2.1 Discussion	226
References	228
List of Tables	217
List of Figures	219
Curriculum Vitae	237
List of Publications	239
Refereed Journal Papers	239
Refereed Conference Papers	239
Patents	240
Technical Reports	240

List of Acronyms

ACMPA	Aperture Coupled Microstrip Patch Antenna
ALD	Array Lattice Directivity
AR	Axial Ratio
ARTES	Advanced Research in Telecommunication Systems
BSS	Broadcasting Satellite Service
CPS	Combined Phase Shifter
DBS	Direct Broadcasting Satellite
DC	Direct Current
DCPRE	Dual Circularly Polarized Radiating Element
DLPRE	Dual Linearly Polarized Radiating Element
EPFL	Ecole Polytechnique Fédérale de Lausanne
EM	Electromagnetic
ERC	Elementary Radiating Cell
ESA	European Space Agency
FAC	Fragmented Aperture Concept
FBR	Front-to-Back Ratio
FSS	Fixed Satellite Service
GEO	Geostationary Earth Orbit
GPS	Global Positioning System
G/T	Gain over noise Temperature
HPBW	Half-Power Beam-Width
EMC	Electromagnetic Compatibility
LEMA	Laboratoire d'Electromagnétisme et d'Acoustique
LHCP	Left Hand Circular Polarization

LNA	Low Noise Amplifier
MMIC	Monolithic Microwave Integrated Circuit
NATALIA	New Automotive Tracking Antenna for Low-cost Innovative Applications
PCB	Printed Circuit Board
PD	Photodetector
PIFA	Planar Inverted-F shaped Antenna
PPWM	Parallel Plate Waveguide Mode
RD	Research & Development
RE	Radiating Element
RF	Radio Frequency
RHCP	Right Hand Circular Polarization
S3FIP	Shielded Strip Slot Foam Inverted Patch
SLPRE	Single Linearly Polarized Radiating Element
SSFIP	Strip Slot Foam Inverted Patch
TCDA	Tightly Coupled Dipole Array
TRL	Thru-Reflect-Line
TU	Tracking Unit
VIA	Vertical Interconnect Access
VNA	Vector Network Analyzer
XPD	Cross-Polarization Discrimination

1. Introduction

*If you wish to make an apple pie from scratch,
you must first invent the Universe.*

CARL SAGAN

In general, systems conceived for space, aviation, defense and basic research applications are subject to particularly stringent performance requirements. The goals envisaged by these applications are very ambitious and often imply high levels of risk, cost and urgency. The fulfillment of these demanding performance requirements usually ends up by fostering innovation in many of the domains of technology involved in the conception and implementation of such systems.

A good example of this trend may be found in the domain of communications at radio and microwave frequencies, where a great deal of the developments which are nowadays available in civil-consumer applications were originally conceived to make possible missions that once constituted a challenge by themselves (e.g. GPS or Global Positioning System) [1,2].

Notably, the conciliation between the antenna subsystem electromagnetic (EM) performance and the structural requirements imposed by the host platform plays a preponderant role in the conception of any communications system. Such structural requirements may ask for a miniaturization of the antenna subsystem, enhanced robustness, light weight, low profile and conformability to unobtrusive, aerodynamic or easily deployable surfaces.

Though there have been many contributions towards this conciliation, there is still a long way ahead, since the number of applications keeps growing and in many cases their requirements are more and more demanding. Just for the sake of illustration, these contributions may be categorized into three groups:

- the fundamental theoretical developments, as the formulation of the physical limits for the relation between the EM performance of an antenna and the volume occupied by it [3–5] as well as the antenna array theory [6, 7],

- the emergence of new technological concepts, such as the *printed antenna concept* [8–13], and
- the setting up of specific mathematical tools, which provide antenna engineers with accurate and efficient tools to predict and optimize the EM performance of these new concepts [14–19].

In particular, the field of printed antennas remains, after more than sixty years of intense activity, among the most fertile areas in the domain of antenna engineering¹ and it is already some time ago that its fruits have been successfully integrated in plenty of consumer applications: mobile telephony, wireless networks, satellite television reception, global positioning, radio frequency identification, collision avoidance systems, etc. These applications do not only take advantage of the inherently appealing properties (both structural and EM) of the printed antenna concept, but keep calling for further improvements of these properties. In fact, this continuous demand for higher performance standards is an important source of new challenges for the antenna engineer.

One of such challenges, which will help to focus the framework of the present thesis, can be outlined as follows. Nowadays the parabolic reflector antennas used for the domestic reception of Direct Broadcasting Satellite (DBS) services are being successfully substituted by flat fixed beam antennas, which are more robust, compact and suitable for outdoor environments [20–24]. This process of substitution may:

- be extended to several paraboloidal reflector antennas, with a further reduction of their aesthetic impact, by applying multibeam concepts to the planar antenna. In this way, an entirely planar antenna system would become able to receive the signal from various satellites simultaneously [25–28].
- Allow the integration, thanks to the streamlined profile of this antenna concept, of complete DBS receivers in the bodywork of mobile platforms (cars, boats, aircrafts). This would address the increasing demand of mobile communication services by both the vehicle manufacturers and the end-users.

This demand is so important that DBS satellite operators, on their side, are currently enabling the access to a wide range of low-cost broadband mobile communication services. These services benefit from both the large capacity and the homogeneous continental coverage of satellite communication systems and are mainly related to safety, telemetry & control, tolling, real-time driver information and entertainment.

On the other hand, the expansion of these mobile communication services is currently limited by the shortage of compact and cost-effective user interfaces to access them. And this shortage is, in fact, related with the demanding engineering challenge that underlies the integration of the terminal antenna system into the targeted mobile platform (touring cars, mainly).

¹Between 2001 and 2011, more than 9.000 publications on the subject are reported by the Institute of Electrical and Electronics Engineers (IEEE).

Basically, the integration of DBS antennas in mobile platforms requires the capability of synthesizing and dynamically steering a beam that should be kept oriented towards the desired satellite along all the route of the vehicle. In the case of cars, the complexity of an antenna system providing such tracking capability, which is already paramount, must be made compatible with the particular structural and economical requirements imposed by the automotive industry. These latter requirements, that concern mainly aesthetics, comfort, dynamics, size and cost issues, are decisive for a successful penetration of the user interface into the automotive market [29–35].

Within this framework, the European Space Agency (ESA) has launched a project aiming to investigate the feasibility of such a satellite terminal for automotive consumer applications. The NATALIA (New Automotive Tracking Antenna for Low-cost Innovative Applications) project is funded by ESA under contract number 18612/04/NL/US (ARTES 5) and involves a consortium of several key industrial partners in the sectors of satellite R&D and consumer applications from Germany, Switzerland and Luxembourg, led by IMST Germany [36].

1.1 Scope. The NATALIA project

As member of the European consortium engaged in the development of the NATALIA project, the EPFL *Laboratoire d'Electromagnétisme et d'Acoustique* (EPFL-LEMA) has contributed along all its phases, from the conception up to the implementation and experimental verification of the first prototypes. Most of the work presented in this memoir has been developed as part of the contribution of the EPFL-LEMA to the NATALIA project.

This section is an overview of some of the main topics addressed during the development of the NATALIA project and is based on a series of parent documents, where these topics as well as many others are discussed more in depth [37–43].

1.1.1 Project Goal

The NATALIA project is devoted to the development of a new generation of high-performance low-profile antenna terminals for mobile satellite communication services. Such terminals are addressed to mass consumer markets and are intended to be embedded on the vehicle profile, enabling the access to broadband satellite communication services from vehicles while in-motion.

In particular, the design and prototyping of a receive only antenna terminal for the European automotive market is envisaged by the NATALIA project. This design should constitute a first step to identify and tackle the main challenges involved in the development of bidirectional (Transmit & Receive) user terminals. A typical application scenario is depicted in *Fig. 1.1*.

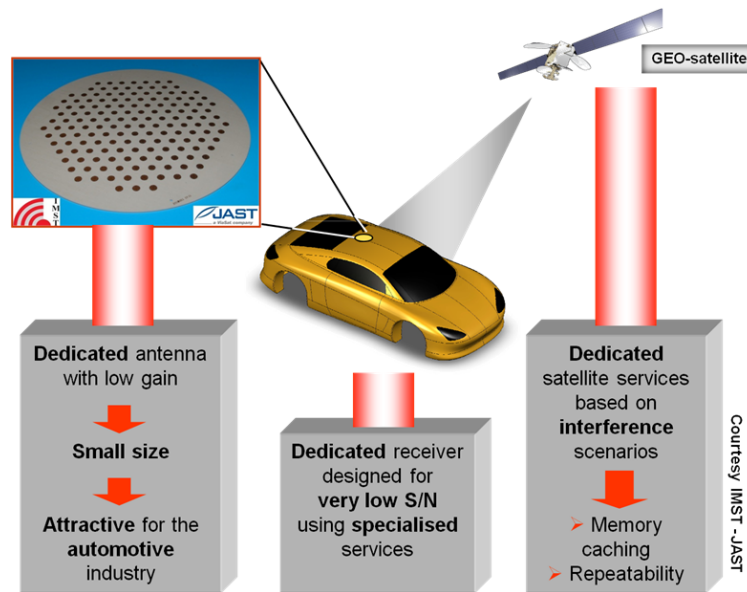


Figure 1.1. NATALIA typical application scenario.

Technical Requirements

Basically, for a proper reception of the DBS signal broadcast from the Geostationary Earth Orbit (GEO) satellites operating in the European continent, the antenna terminal should provide a certain gain (around 20 dB), to guarantee that the level and quality of the signal delivered to the radio-frequency (RF) front-end are high enough for a proper signal reception. The receiving antenna polarization (linear) should match that of the emitted fields within a given accuracy (typically over 15 dB of cross-polar discrimination) [37].

Keeping such a communication link in an scenario where the receiver terminal is traveling on a mobile platform (i.e. a car) requires some re-configuration capabilities for the receiving antenna. Namely, these capabilities are:

- beam steering, to maintain the directive pattern of the antenna pointed towards the broadcasting satellite, and
- polarization tracking, to retain a proper alignment between the polarizations of the emitting and the receiving antennas.

The aforementioned performance requirements must be made compatible with those derived from the market the antenna terminal is targeting. Consumer automotive market in Europe is strongly driven by high performance-to-cost ratios as well as demanding (aero)dynamics and aesthetics criteria. This implies that the terminal should be, on the one hand, compatible with standard mass production techniques, to enable a convenient scaling of cost with production volume, and, on the other hand, as streamlined, robust and compact as possible.

The main performance and environmental requirements of the antenna terminal, as originally requested by ESA, are summarized in *Table 1.1* and *Table 1.2*.

Parameter	Requirement
Frequency Band	10.7 – 12.75 GHz
Half-Power Beam-Width (HPBW)	< 9° in azimuth, < 18° in elevation
G/T	> –6 dB/K
Polarization	Linear
Cross-polarization discrimination (XPD)	> 15 dB
Polarization tilt	0° – 180°
Scanning Range	360° in az., 20° – 70° in el. (from broadside)
Aperture Size	≈ 20 cm (diameter)
Thickness	2 – 3 cm
Height above vehicle surface	1 cm
Weight	< 5 kg

Table 1.1. Performance & Structural Requirements. The G/T is an important figure of merit for antennas. It stands for the relation between the antenna *Gain* and the antenna Equivalent Noise *Temperature*. From [37].

Parameter	Requirement
Velocity	≤ 200 km/h
Roll rate of change	≤ 10.6°/s
Pitch rate of change	≤ 31.7°/s
Heading rate of change	≤ 42.7°/s
Environmental conditions	In accordance with IEC 6072-3-5 standard and the appropriate class designations with the exception of Rain, Snow, Hail and Wind conditions.
EMC conditions	In accordance with EN 300339 and EN 300673 stds.

Table 1.2. Vehicle Dynamics & Environmental Requirements. From [37].

1.1.2 Project Overview

The NATALIA project is dealing with the strong compromise between cost, performance and size posed by both the service and the market for which the antenna terminal is intended. The factors driving the design strategy are illustrated in *Fig. 1.2*. The constraints derived from this compromise are going to deeply condition every stage of the development of the final product: the antenna terminal.

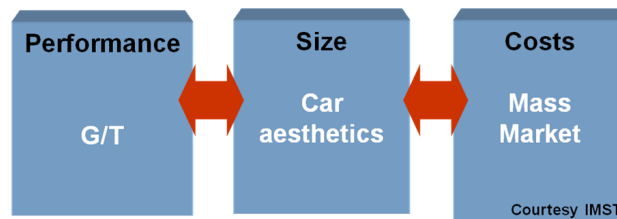


Figure 1.2. NATALIA key design parameters. The G/T is an important figure of merit for antennas. It stands for the relation between the antenna *Gain* and the antenna Equivalent Noise *Temperature*.

At early stages of the viability survey, these constraints led to the rejection of mechanically based solutions to achieve both beam steering and polarization tracking. In fact, systems with mechanically moving parts are generally high-profile, bulky, and subject to G-forces [38, 39, 42]. The alternative of a full electronic control of these pointing parameters is approached as a classic phased array design problem [6], which can provide low profile solutions, with no moving parts and high reliability.

The main building blocks of the NATALIA phased array concept are illustrated in *Fig. 1.3*. According to this diagram, the beam pointing and the polarization alignment are based on steering information provided by the *Receiver SubSystem*, that gathers all sensor information (GPS, gyro), to the antenna *Controller* at a certain update rate, that depends on the speed of the car as well as on the required pointing accuracy. Then, the *Controller* reconfigures the *Tracking Units* (TUs), which synthesize the array illumination, accordingly.²

The phased array alternative suffers, however, from the potentially high costs associated to both the **complexity** of its implementation and the **number of active components** (typically GaAs Monolithic Microwave Integrated Circuits -MMICs) required. These are major obstacles to a broad diffusion of phased array technology in the consumer market [41] and constitute, in fact, the main design challenges addressed by the NATALIA concept.

²From now on, the discussion will focus on the *Antenna SubSystem* itself, discarding the *Receiver SubSystem*, the *Controller* and the *Down Converter*, which are out of the scope of this work.

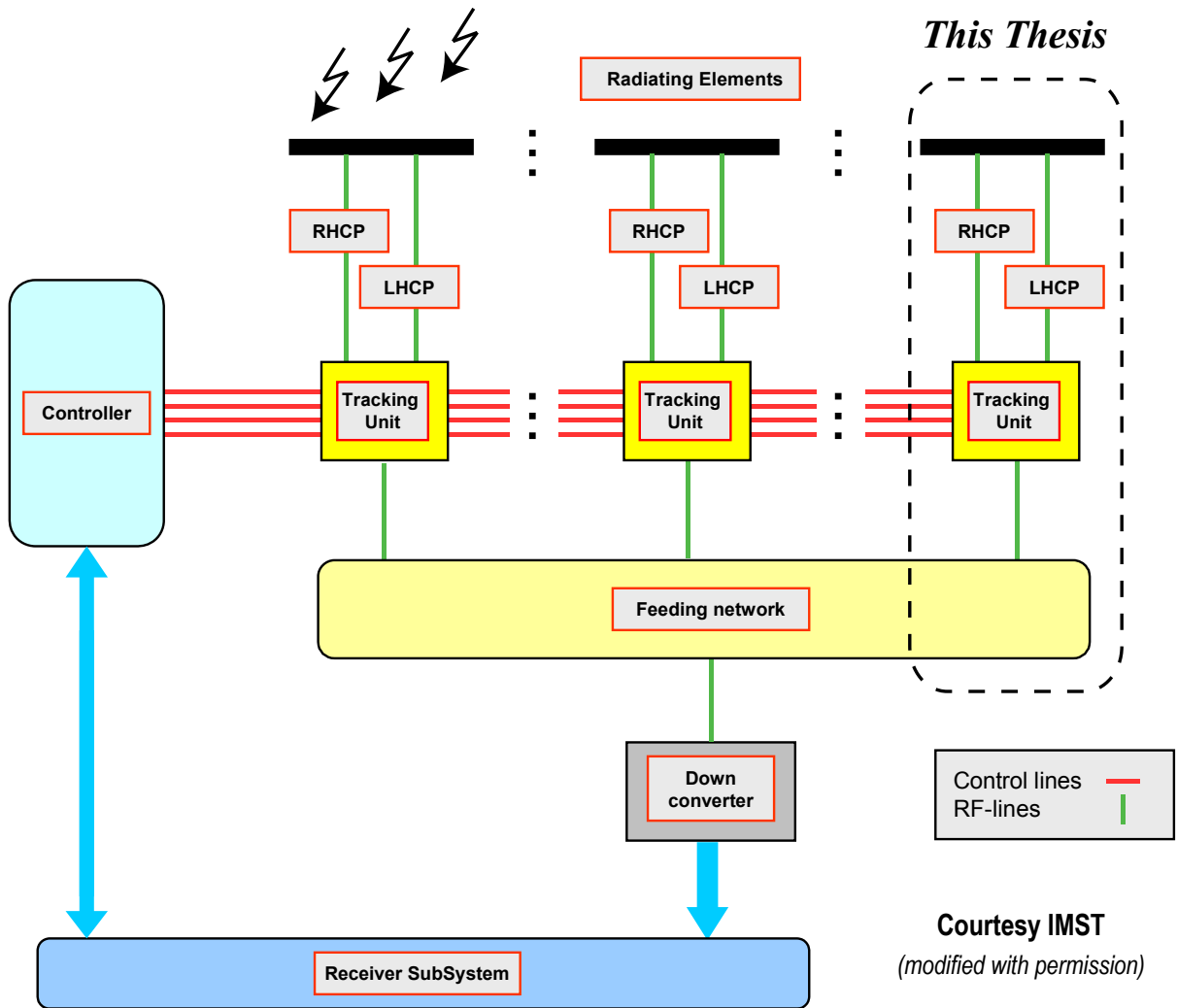


Figure 1.3. Block diagram with key components of the NATALIA concept. Note that the radiating elements have dual circular polarization. $R(L)HCP$ stands for Right (Left) Hand Circular Polarization.

a) The Tracking Unit (TU)

With regard to the issue of the **active components count**, the NATALIA phased array concept tries to optimize the compromise between their number, their complexity and their diversity by merging the amplification, the beam steering and the polarization tracking capabilities within a couple of twin active components. This combination of functionalities takes place at radiating element level, inside the TU, and constitutes the so-called Combined Phase Shifter (CPS) scheme.

According to *Fig. 1.4*, each TU is attached to the two outputs of a radiating element with dual circular polarization and comprises a power combiner and a couple of active components. Each active component is an MMIC that integrates a Low Noise Amplifier (LNA) and a reconfigurable Phase Shifter.

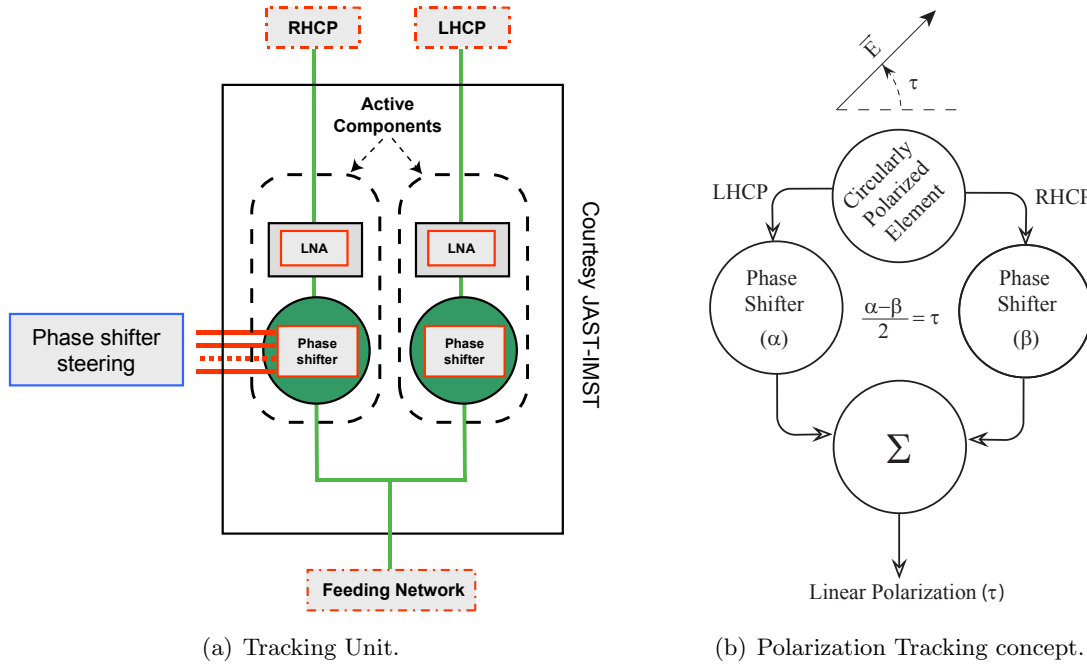


Figure 1.4. Schematic description of the NATALIA Tracking Unit, from [40].

In fact, the use of dual circularly polarized radiating elements within the CPS scheme allows to combine a differential phase shift between the two ports of each element with a phase shift that is common at element level, but progressive over the aperture. Obviously, the progressive phase shift is the responsible of the steering of the beam, while the orientation (tilt, τ in *Fig. 1.4(b)*) of the linearly polarized field received by the antenna is given by half the differential phase shift.³

Another advantage of the CPS scheme is that it can also naturally handle the phasing required to accommodate in the same aperture radiating elements that are rotated with respect to each other. This is done by adding an extra phase shift (phase rotation) at element level to compensate for its relative physical rotation inside the aperture. This degree of freedom is actually used to implement the sequential rotation of all the elements within the array aperture. This sequential rotation is such that it enables a further simplification of the logic in the active components, with the consequent impact on their size and cost,⁴ as well as an important relaxation of the performance requirements at radiating element (RE) level [6].

³A linearly polarized wave can be decomposed into a couple of circularly polarized waves of identical power that rotate in opposite senses [44, Ch. 15].

⁴By the end of 2006, the price of GaAs wafer for customized MMICs was between 1 and 4 US\$/mm², assuming a production of $\approx 2 \times 10^6$ chips/year.

b) The Antenna Aperture. Practical Implementation

Despite all these simplifications, the practical implementation of the NATALIA concept remains rather **complex**, especially within the constraints of size, cost and performance. This practical implementation concerns basically the *array topology*, the *manufacturing technology* and the *interconnections architecture*. For the first part, an in depth study of different array topologies revealed the convenience for the present application of a planar array with its REs arranged in the basis of a densely populated triangular grid, as illustrated in *Fig. 1.5*.

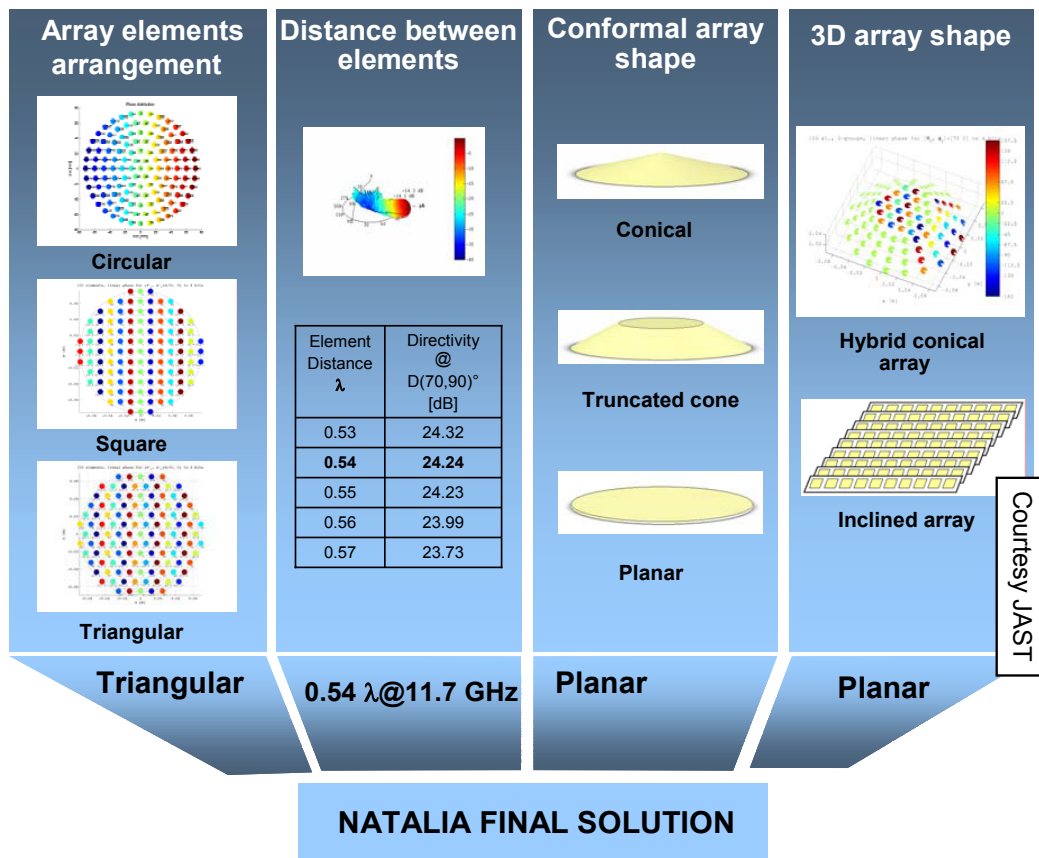


Figure 1.5. NATALIA implementation alternatives and final solution.

In particular, it was found that, despite its reduced effective aperture at low elevation angles, a planar aperture is as efficient as its low profile conformal counterpart, less prone to the appearance of grating lobes and compatible with simpler manufacturing processes.

With regard to the distribution of the elements over the array aperture, the use of a triangular lattice, compared with the circular and rectangular alternatives, minimizes the distance between the REs in all azimuth directions.⁵ This has the advantages of making a better use of the available

⁵The minimization of this distance is, in fact, one of the main requirements for phased arrays with broad scan capabilities.

area that effectively radiates (which provides broader scan capabilities), enhancing the azimuthal symmetry of the array and increasing the pointing resolution. In addition, arrays with triangular lattices can be enlarged more gradually (in groups of 3, 6 and 12 elements) while preserving their symmetry. All this together makes of the triangular lattice one of the best configurations for phased arrays with broad scan capabilities.

The choice of a planar aperture with a triangular lattice, as that illustrated in *Fig. 1.6*, still leaves a several degrees of freedom of great practical importance, which concern the way the REs are grouped, the rotation of the elements within a group and the relative rotation of the groups. As stated before, this degree of freedom may permit the simplification of the active components within the Tracking Unit and the compensation of potential deficiencies at element level. However, as will be seen in the next section, this leeway is constrained by the physical integration of the ensemble TU & RE within the array aperture, especially when its footprint does not have the idealized square shape outlined in *Fig. 1.6*.

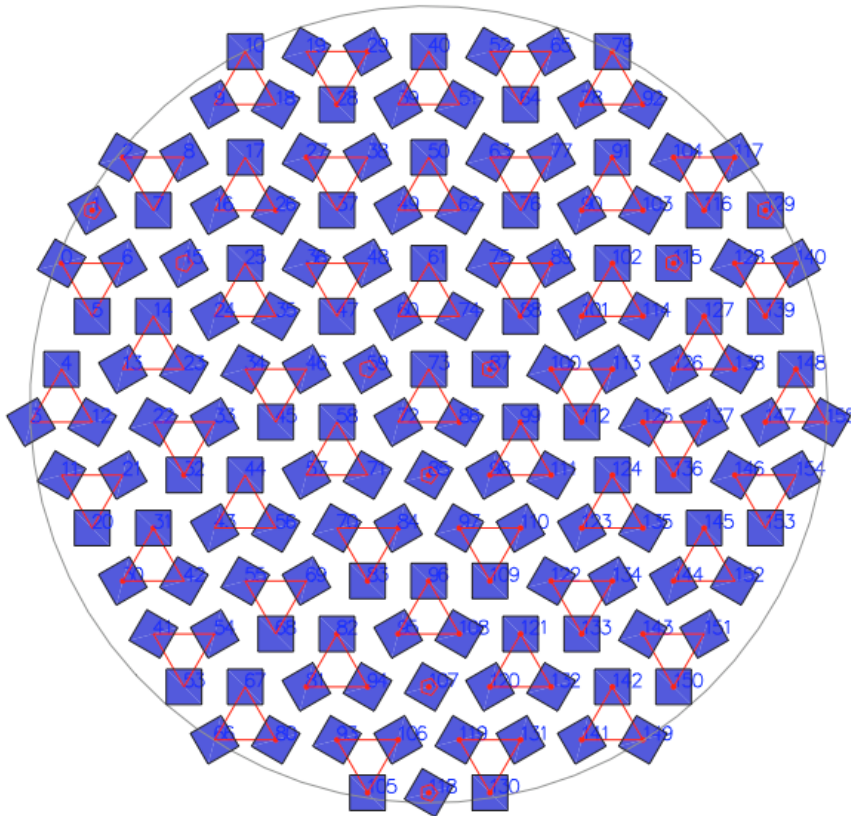


Figure 1.6. NATALIA array lattice with exemplary grouping and sequential rotation, from [40]. Note that there is not a central element and that groups with a single element (marked with a circle in their center) are allowed.

With respect to the *manufacturing technology*, standard Printed Circuit Board (PCB) prevails mainly due to its compatibility with large production volumes, its high yield, its maturity as well as its inherent suitability for low cost, low profile, compact and sturdy architectures [8–13].

In spite of the apparently direct mapping of the planar array topology into a multilayer PCB structure, it is at this point that a careful choice of both the *interconnections architecture* and the particular *fabrication processes* must be carried out in order to minimize certain fundamental risks, namely:

- the high potential complexity associated to the interconnection and control of the REs of the array, which may either severely restrict the technical viability of the whole antenna, or downgrade its performance below acceptable limits,
- the intrinsic performance limitations at microwave frequencies, with regard to other special purpose technologies (such as coaxial or waveguide), of both circuitual and radiating components when implemented in standard PCB technology without high-end materials, and
- the considerable impact the PCB processing details (i.e. the number of processes and their sequence) may have on the fabrication tolerances, the yield, the performance and the cost of the antenna terminal.

The success of this choice relies on the wide experience of the industrial partners in both system design and PCB technology as well as on intensive interaction with several leading PCB manufacturers. The resulting PCB buildup, whose preliminary overview is depicted in *Fig. 1.7*, has been optimized in order to be easy to implement and inexpensive. In particular, the configuration of the vertical interconnections (vias,⁶ hereafter) has been designed to allow the manufacturing of the PCB in one single press and one single metalization (plating) processes.

Once the system architecture and the fabrication technology are properly settled, a more convenient redefinition of the main building blocks of the antenna subsystem can be addressed. This redefinition will enable the identification and solution of further design compromises and thus prepare the way for their integration in the foreseen antenna array. These building blocks are defined as follows:

- the **Elementary Radiating Cell**, which comprises the dual circularly polarized radiating element, in the upper side of the PCB buildup, and, by extension, all the passive components of the TU that are embedded within the PCB core. These passive components are:
 - i) the interconnections between the RE and the TU. As illustrated in *Fig. 1.7*, these interconnections are the couple of twin vias that cross most of the buildup to reach the inputs of the TU-MMICs, which are located in the bottom microstrip layer. These vias are implemented as *through vias*⁷ and will be referred hereafter as *Long Vias*.

⁶ *Via* is an acronym that stands for Vertical Interconnect Access.

⁷ Throughout this document, the term *through vias* stands for those vias whose drill holes pass completely through the PCB buildup. On the other hand, *blind vias* refers to those vias whose drill holes have one of its extremes closed somewhere within the buildup.

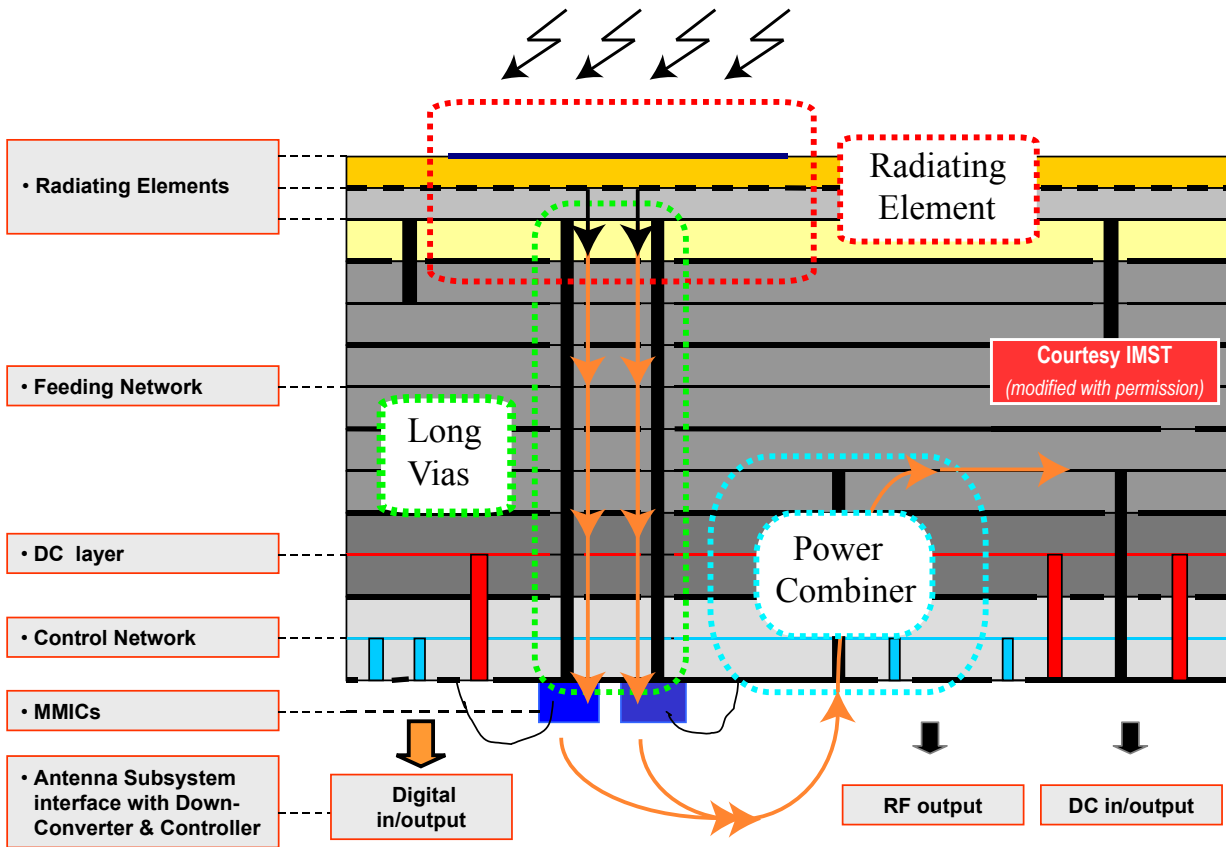


Figure 1.7. Preliminary NATALIA PCB buildup overview (not to scale).

- ii) The *Power Combiner* that connects the outputs of the TU-MMICs to the Feeding Network, as shown in Fig. 1.4. According to Fig. 1.7, the Feeding Network is situated in an intermediate stripline-like layer. This layer is reached by the Power Combiner using a *blind via*.

As will be seen throughout this thesis, the integration of the ERC within the PCB buildup and the array lattice are two issues of major relevance for the design of this building block.

- The **MMIC**, that is a customized design that integrates the LNA and the reconfigurable Phase Shifter. This component constitutes the heart of the TU and is expected to represent more than 80% of the antenna terminal cost price. Its design and prototyping are carried out in parallel with those of the ERC to mitigate the impact of the long delays required for the completion of each foundry run. Besides, to cope with the high cost of each run, the number of iterations is minimized.
- The **Feeding Network** is conceived as a passive corporate network connecting the output of all TUs to the input of the *Down-Converter* (recall Fig. 1.3). In addition to the minimization of its loss, another important design constraint is related to the situation of this network within

the PCB buildup. In fact, since the network is mostly accommodated in the intermediate layers of the buildup, its routing must be compatible with the distribution over the array aperture of the through vias (the *Long Vias*, for example) used for the implementation of the cells. According to *Fig. 1.7*, this last constraint is also present in the routing of the *Control Network*. In fact, the density of vias over the antenna aperture is expected to be so high that it is advisable not to start the routing of these two networks until the design of the ERC architecture and the arrangement of its replicas within the array aperture (i.e. the sequential rotation) are frozen.

The present thesis deals with the development of the Elementary Radiating Cell (ERC). Due to the cross-cutting nature of the array basic building block, the understanding of the trade-offs that underlie the design of the ERC calls, in the first place, for a basic knowledge of the whole antenna solution, at both functional and technological levels. A more detailed description of the role of the ERC as well as of its design guidelines will then provide a deeper overview of the remaining components of the antenna array and highlight design issues that are not evident at this stage.

c) The Elementary Radiating Cell. Technical Requirements

Each one of the radiating cells that compose the antenna array must deliver to the feeding network a conveniently amplified version of the linearly polarized DBS signal emitted by the corresponding broadcasting GEO satellite. With regard to the cell coordinate system, both the angle of incidence and the polarization tilt of the incoming signal can be arbitrary, within certain boundaries specified in *Table 1.1*.

In accordance with the technological requirements outlined above, the implementation of this ERC must be compatible with PCB technology, with severe additional restrictions in terms of cost (materials/processes) and overall thickness of the multilayer buildup. The integration of the radiating cell within the array lattice also imposes limitations in the surface to be allocated to each cell, which becomes thus bounded in its three dimensions (see *Table 1.3*).

The compromise between these technological constraints and the EM performance of the ERC is driving most of the design trade-offs. In fact, this compromise is so tight and the technological requirements so restrictive, that, beyond certain fundamental limitations that may apply to the physical structure supporting the cell,⁸ the maximum EM performance that can be achieved at ERC level is expected to be rather limited. How much this performance might be limited in a practical implementation of the cell remains, in fact, a question to be addressed in this work.

On the other hand, some of these functional limitations at element level should be compensated at array level, once the overall performance improvements provided by the foreseen sequential

⁸In analogy, for example, with the fundamental limitations in *bandwidth* and *radiation efficiency* of an antenna with regard to the *volume* occupied by it [3–5], already mentioned at the beginning of the chapter.

rotation are effectively exploited [45, Ch. 13], [46, 47]. Actually, when it comes to provide a quantitative specification of the performance requirements applicable to the RE, one should take into account the array environment in which the element is going to operate.

In this sense, to rigorously take into account the array environment becomes a rather involved task for several reasons. These reasons are related to the fact that the array environment that is “seen” by each one of the REs depends on its location within the array aperture as well as on the sequential rotation implemented. Moreover, the set of feasible sequential rotations depends, in turn, on the shape and dimensions of the ERC, that contains the element. This dependence is exemplified in *Fig. 1.8*, where the feasibility of a couple of sequential rotations is compared for a given footprint of the ERC, which is now assumed to be rectangular, and a given placement of the RE within the cell (off-center). For this particular footprint, the rotation scheme proposed in *Fig. 1.8(a)*, that is leading to the overlapping of the cells, would not permit the physical integration of the ERC within the array aperture and is thus discarded. On the other hand, the scheme implemented in *Fig. 1.8(b)*, that does not fall into ERC overlapping, would be feasible, in principle.

More precisely, a rigorous approach taking into account the array environment would lead, for a given sequential rotation, to the derivation of different performance requirements depending on the placement of each element in the array aperture. In this scenario, the possibilities of unifying the different sets of specifications would be limited to eventual symmetries in the array aperture.⁹ A further unification of these specifications according to the different *regions* that can be defined in the array aperture would be compromised by the fact that, due to the individual rotation of each element, the environments that are “seen” by elements located within the the same *region* (the periphery of the array, for example) may differ substantially.

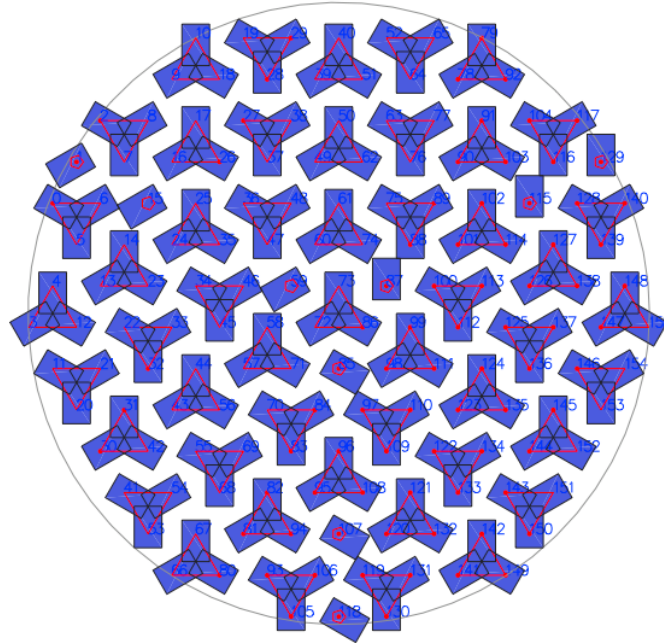
At this point, a convenient simplification step could be to make abstraction of the sequential rotation and assume that the array is infinite.¹⁰ This assumption, though somewhat shaky for the present (medium-size) array, is of great practical importance since it enables the unification of all the performance requirements into a single RE that operates *embedded* into an infinite array.¹¹

Actually, all the performance parameters of this *embedded* element can be straightforwardly transferred to a large (but finite) array, which simplifies considerably the specification and design of the array and of the element. In medium-sized arrays this approach may still provide a valid initial approximation. It is within the context of this rough approximation that one should interpret the performance requirements specified in *Table 1.3* for the Embedded Radiating Element.

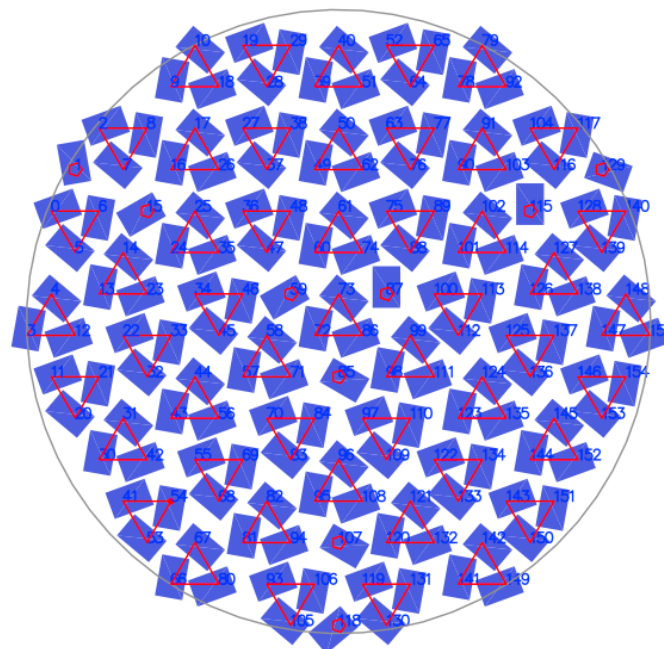
⁹Note the *3-ways* rotational symmetry in the apertures proposed here.

¹⁰In view of this statement, one could wonder if it is really necessary to neglect the sequential rotation when dealing with infinite arrays. More specifically, would it be possible to incorporate a sequential rotation scheme in the analysis of an infinite array?

¹¹Throughout this document, the term *embedded* is equivalent to *array-element* [48, vol.2-Ch.3], in the sense that it applies to a radiating element that is located in *its array environment*, so that all the other elements are present but are *passively terminated* with matched loads. On the other hand, the term *active* is used, as it will be shown later, when all the elements in the array are excited (with an uniform illumination, typically).



(a) The sequential rotation is not compatible with the ERC layout: collision.



(b) The sequential rotation is compatible with the ERC layout. The next step would be to check for the feasibility of the routing of the Feeding / Control Networks.

Figure 1.8. Integration of an ERC with a given shape (rectangular) and dimensions ($0.46 \times 0.30 \lambda_0^2$) within the NATALIA array lattice for two different sequential rotations, from [40].

	Parameter	Requirement
ERC Level	Area	Compatible with the array lattice* and with the routing of the Feeding / Control Networks.
	Thickness	≤ 10 mm
	Technology	Standard PCB, without high-end materials. Simplest processing (single press, single plating).
	Frequency Band	10.7 – 12.75 GHz
Embedded Radiating Element	Directivity	Low - Medium (5 – 7 dB).
	Radiation Pattern	Symmetrical in azimuth.
	Radiation Efficiency	$\geq 80\%$
	Polarization	Dual Circular.
	Axial Ratio	$\lesssim 3$ dB, in the Scanning Range.**
	Return Loss	$\gtrsim 10$ dB
	Port Isolation	$\gtrsim 20$ dB
Long Vias	Mutual Coupling	$\lesssim -20$ dB
	Insertion Loss	≤ 0.8 dB
	Return Loss	$\gtrsim 20$ dB
Power Combiner	Cross Coupling	$\lesssim -20$ dB
	Insertion Loss	$\lesssim 0.6$ dB
	Return Loss	$\gtrsim 20$ dB
	Power Unbalance	$\lesssim 0.5$ dB

$$*A_{\text{O}} (\varnothing_{\text{min}} = 0.54 \lambda_0) \approx 0.25 \lambda_0^2.$$

**360° in az. and 20° – 70° in el. (from broadside).

*** \lesssim and \gtrsim symbols are used for performance parameters whose required values are not explicitly determined from system calculations but estimated from typical expectations.

Table 1.3. Elementary Radiating Cell requirements.

In practice, while the direct measurement of this embedded element performance in a large, but *finite*, array is very advantageous, for its theoretical evaluation it is generally preferred an indirect approach [48, vol.2-Ch.3]. This indirect approach is based on the analysis of an uniformly illuminated *infinite* array (uniform amplitude and linear phase shift), from which the embedded element performance can be derived. This last approach circumvents the computational burden associated to the (direct) analysis of a finite array (that depends strongly on the actual array size) at the expense of the effort required for the derivation of the embedded performance (which does not depend on the array size but on the extension of the scan domain over which the operation of the array is to be evaluated). In fact, the gain in computational cost and accuracy provided by this indirect approach increases with the size of the array to which it is applied.

Furthermore, a preliminary knowledge of the principles of operation of the targeted element may enable a significant reduction of the computational cost associated to the derivation of its embedded performance. This can be achieved if, out of the required scan domain, the infinite array analysis is limited to certain angular sub-regions where the performance of the foreseen array is

expected to be most compromised, for example [49, Ch.3], [50]. The efficiency of this infinite array modeling approach has been proven in the design of high performance REs for broadband wide-scan array antennas [51–56].

The time constraints in the first design iterations prevented, however, a further investigation on the use of the infinite array modeling approach for the present application. Moreover, the effectiveness of this technique might be questioned in the case of a medium-size array (~ 150 elements) whose performance relies, up to a certain extent, on the sequential rotation applied to its elements. Under these conditions, the preferred approach is based, instead, on the modeling of the RE in a stand-alone, *isolated*, configuration. The simplicity of this modeling approach is expected to contribute to the acceleration of the first design stages of the foreseen antenna, that focus on the validation of the array concept and the system architecture. Actually, the work presented here with regard to the RE has been entirely done under this perspective. Later design steps towards the optimization of the antenna overall performance may require the use of more rigorous modeling schemes.

One of the main drawbacks of the last modeling approach is related with the difficulty of finding a proper translation between the performance requirements specified for the embedded element in *Table 1.3* and those applicable to the isolated element. In the absence of a rigorous translation, the fulfillment of the requirements at isolated element level does not guarantee its satisfactory operation within the array environment. Moreover, this translation might lead to a rather vague specification of the isolated element.

To address this uncertainty, the correspondence between these two sets of requirements could be checked during the design of the element by means of a number, hopefully very limited, of analysis of the whole array aperture. Here, the medium-size of the foreseen array may permit this kind of analysis, which is expected to be computationally expensive, but that allows to evaluate the impact of the sequential rotation scheme on the performance of the antenna. In this scenario, the performance of the isolated element is requested to match, or exceed, “as much as possible” the requirements specified for the embedded element. And, in order to support a *reasonable* trust in the convergence of this design approach and to simplify it, the specifications of the isolated element are given under certain general conditions that are discussed next.

Some additional considerations on the Radiating Element Requirements

The radiation pattern of the element must be compatible with the scan requirements specified for the phased array antenna. According to this principle, the RE pattern should present azimuthal symmetry (see *Table 1.3*) and its directivity should be as small as possible, to minimize the scan loss when the array beam is steered throughout its elevation range (i.e. between 20° and 70° from broadside). In this sense, an omni-directional pattern such as that provided, for example, by a vertical “Hertz dipole” over a ground plane, would be well suited for the targeted application,

where no broadside radiation characteristics are specified [57]. Another type of element that could match the array scan requirements is the “Huygens source,” which provides, moreover, a better approximation to the so-called “ideal element pattern.” This ideal pattern is claimed to be compatible with the interesting, though physically unrealizable, property of eliminating the impact that the integration of such an RE within a given array environment would have on its stand-alone performance [48, vol.2-Ch.3], [58, 59].

In fact, when it comes to integrate the RE within an array, its *embedded* radiation pattern,¹² and therefore its directivity, can present considerable differences with regard to the parameters observed for the same element in a stand-alone, *isolated*, configuration. These differences, that concern actually all the performance parameters of the RE, are due to mutual coupling phenomena arising between the elements within the array aperture. A great deal of these differences depend on the array configuration (i.e. element spacing, array lattice) and its prediction can be addressed by using powerful approximations (e.g. the infinite array approximation). Nevertheless, there are still certain details at both array and RE levels that can have a significant impact on the overall behavior of the array antenna and the estimation of such an impact may become rather demanding.

This is the case of the foreseen array antenna, a medium-sized array where the elements are arranged according to a sequential rotation and both (the elements and their rotation) are still design unknowns. For the sake of simplicity, this design challenge is addressed by applying, in a preventive basis, a series of additional performance requirements to the RE. The aim of these requirements is to guide the design of the element in such a way that its behavior, when isolated, is as close as possible to that of an hypothetical “ideal element.” The proximity between the behaviors of these two elements may support a certain degree of confidence in the differences between the performances of the isolated and the embedded elements to be moderate. And, if such differences are expected to be limited, the design of the RE could focus, at least during an initial iteration, only on its stand-alone configuration, which constitutes a simplification of great practical importance.

These additional performance requirements for the isolated RE can be summarized as follows:

- a “conservative” threshold for the inter-element **mutual coupling**, at least within *small* sub-arrays, is set (typically -20 dB, from *Table 1.3*), so that the embedding of the RE could be expected to have no more than a “moderate” impact on its isolated behavior.¹³ This mutual coupling depends mainly on the inter-element spacing, that is typically a heavily constrained design parameter, on the relative orientation (rotation) of the elements and on the radiating element itself, whose design can benefit from broader degrees of freedom.

¹²Here, the reader should recall that the concept of *Embedded* Radiation Pattern is equivalent to that of “Array-Element Pattern” in [48, vol.2-Ch.3]; but here the first term is applied, by default, to a *field* pattern, while the second refers to a *power* one.

¹³Strictly speaking, the definition of this threshold does not provide any guarantee that the RE will operate as desired, but is intended only to reduce the complexity of its design, as a general indication. In fact, the mutual coupling phenomena can be beneficial provided that they are properly taken into account for the design of the RE [52, 54, 56, 60].

- Upper limits for the **directivity** and the **radiation efficiency** of the isolated element are defined. These limits are given by the array configuration and constitute the maximum levels of directivity and radiation efficiency that an “ideal element” could attain when it is operating in an uniformly illuminated (active) infinite array.

In an infinite array, the areas allotted to all elements are equal. For the particular case of a triangular lattice with inter-element spacing d , this area (A_e) would be that of a hexagon whose inscribed circle has a diameter d :

$$A_e = A_{\square} (\varnothing_{\min} = d) = \frac{\sqrt{3}}{2} d^2, \quad (1.1)$$

that, for $d = 0.54 \lambda_0$, becomes $A_e \approx 0.25 \lambda_0^2$.

Under these conditions:

- the upper bound for the directivity is that of an uniformly illuminated surface of area A_e , if the special case of super-directivity is excluded [6, 43]. This would be, in fact, the maximum directivity corresponding to a slice of area A_e out of an uniformly illuminated aperture whose dimensions are large compared to the wavelength (λ) [59, 61]. This directivity (D_e) is given by the expression:

$$D_e = 4\pi \frac{A_e}{\lambda^2}, \quad (1.2)$$

that, for $A_e \approx 0.25 \lambda_0^2$ and $f = f_0$, results in $D_e \approx \pi \approx 5$ dBi.

- And the maximum radiation efficiency is that of an *active* loss-less “ideal element,” as it is defined in [62].

On the one hand, the radiation efficiency that is specified in *Table 1.3* is applied to both *embedded* and *isolated* elements throughout this memoir, and does not take into account the return loss in the ports of the RE. By default, all the allusions to the radiation efficiency that are made in this document refer to this definition:

$$\eta_{\Omega} = \frac{P_{\text{rad.}}}{P_{\text{acc.}}}, \quad (1.3)$$

where

- $P_{\text{rad.}}$: is the power radiated by the antenna, and
- $P_{\text{acc.}}$: is the power accepted by the antenna.

On the other hand, the so-called *active* radiation efficiency (η_A) constitutes by itself a measure of the average reflection coefficient magnitude over the scan domain (all the elements in the array are excited) [61, 62]. This active efficiency is defined as:

$$\eta_A = \frac{P_{\text{rad.}}}{P_{\text{avail.}}}, \quad (1.4)$$

where

$$\begin{aligned} P_{\text{avail.}} : & \text{ is the power available from the generator, and} \\ P_{\text{rad.}} : & \text{ is the power radiated by the antenna,} \end{aligned} \quad (1.5)$$

and its upper bound for an array with triangular lattice and $d = 0.54 \lambda_0$ is $\eta_{A \text{ Max.}} \approx 80\%$ at $f = f_0$ [62, *Fig. 10*].

In fact, it is reasonable to expect that any excess from these maximum values observed in the performance of the isolated RE would be automatically corrected by increased mutual coupling phenomena once the element is introduced in the array. Such excess would constitute, therefore, a first estimation of the magnitude of the deviation between the behaviors of the isolated element and its embedded counterpart. And this deviation from the “ideal behavior” would finally serve to question the validity of the isolated element design.

The present overview of the performance requirements that are applicable to the isolated element concludes with a remark that may considerably simplify its design. This concerns mainly the level of axial ratio (AR) specified in *Table 1.3* for the embedded RE. This level, provided the technological constraints and the remaining performance requirements,¹⁴ may be rather demanding for the isolated RE. Nevertheless, as it has been advanced, the foreseen sequential rotation is expected to contribute to an overall performance improvement at array level, which may permit an effective relaxation of certain performance requirements at (isolated) element level.

In principle, this relaxation seems more evident with regard to the AR of the element, but its quantification remains rather complicated. Actually, it is found that this improvement depends not only on the sequential rotation itself, that at this point remains a design unknown, but also on the mutual coupling phenomena within the array aperture. And, though theoretical estimations that take these phenomena into account reveal improvements of up to 7 dB for certain embedded elements, a reasonable level of AR to aim at during the design of the isolated element should be around 6 – 8 dB. This range is already considered to be compatible with the technological constraints as well as the remaining performance parameters [63].

¹⁴The frequency band, the scan domain and the radiation efficiency, mainly.

1.2 Objectives

The main objective of this thesis is to acquire a deeper experience in the development of phased array antennas for consumer applications, with especial emphasis in the design of their basic component: the radiating element. The thesis aims to cover all the steps of this design process. This process comprises the conception and modeling of the element, but also its implementation and the measurement of its performance.

The contribution, within the EPFL Laboratoire d'Électromagnétisme et d'Acoustique, to the NATALIA project provides an excellent framework to attain the targeted *learning goals*. Associated to this contribution, there are several specific *project driven goals* that concern mainly the technical requirements that are applicable to the building block of the foreseen array antenna.

The satisfaction of these technical requirements is expected to provide a realistic design scenario. An scenario in which a close collaboration between University and Industry should bring out the best, allowing this thesis work to be fruitful for everybody.

The objective of the present memoir is, finally, to provide a reasoned outline of this design process and its results, with the vocation that also the reader could derive some benefit from the resulting document.

1.3 Methodology

As a complement to the design approach outlined in the end of *Section 1.1.2* and anticipating the foundations of the design guidelines that will be thoroughly described in the next chapter, the methodology that guides the design of the Elementary Radiating Cell (ERC) is summarized in this section, as it helps to understand and justify many design decisions taken along the thesis.

According to the practical implementation of the array antenna, the design of the ERC is conceived from the point of view of its integration into the antenna PCB buildup and into the array grid. These two levels of integration (“horizontal” and “vertical”) are not independent, but strongly interrelated and deeply affecting the EM performance of the cell.

As will be shown throughout this work, this conceptual division contributes, on one side, to highlight the compromise between the integration of the element and its EM performance that underlies the design of the ERC. On the other hand, such a division provides the basis to the design process itself, which is approached as an iterative process. This process tries to optimize the intimate relation between performance and integration by aiming sequentially to each one of the two levels of integration involved. These iterations should converge, ideally, on the best EM performance that is compatible with all the integration constraints.

1.4 Outline

This section summarizes the contents of the chapters of the thesis memoir.

Chapter 1 presents the context in which the thesis is carried out and defines the goals of this work.

Essentially, these goals are related to the development of a programmable radiating element (the ERC) for a compact and cost-effective phased array antenna within the framework of the ESA project “NATALIA”. This chapter also provides the basics of the methodological approach used for the development of that work and outlines the contents of the present memoir.

Chapter 2 describes the criteria that guide the design of the ERC. As far as possible, this description is done in such a way that these criteria can be easily applied to other radiating elements of the same class as the ERC, regardless the particular constraints imposed by the targeted application.

Chapter 3 focuses on the way the design guidelines proposed in *Chapter 2* are applied to the development of the ERC. This development is addressed from the point of view of the integration of the ERC within (i) the antenna PCB buildup and (ii) the array lattice.

Chapter 4 is devoted to the assessment of the design results from *Chapter 3*. The performances of the ERC and its components in different configurations are evaluated and contrasted with predictions.

Chapter 5 summarizes the concluding remarks and outlines the possible future research directions inspired by the work presented in this memoir.

Every chapter contains an independent list of references.

1.5 Original Contributions

The work summarized in this memoir has been done in the framework of an ambitious industrial project with precisely defined goals, specifications and time-frames. As in any project of this type, the investigation of potential innovations must be carefully weighed against the inherent risks in affecting the scheduling constraints imposed by the project execution. In other words, many trade-offs have been adopted and it has not been possible to explore some interesting, but lateral, conceptual and/or technological challenges arising during the antenna development process.

These strong constraints have, however, driven the optimization of known concepts and structures up to an unprecedented degree of sophistication. The two key words here are **miniaturization** and **integration**, and the developments in this direction constitute the main original contributions of this thesis.

In particular, the originality of the work presented here resides in the integration of available blocks into an optimized structure, the so-called ERC, that complies with the stringent requirements, in both size and performances, of the global project.

With regard to the planar architecture of the foreseen antenna terminal, the integration of this programmable array cell is made at two levels. At the “horizontal level” the cell is optimized to fit within the grid of the array aperture. While at “vertical level”, all the components of the cell are arranged through the stratified media in such a way that the resulting buildup remains low profile and its fabrication using standard PCB techniques is kept as simple as possible. Of course, this integration is performed so that the compatibility with a satisfying EM performance at ERC level is guaranteed. This design approach is exhaustively presented in *Chapter 2* and *Chapter 3*. Its practical implementation has produced a patent [43].

Finally, the integration of the elementary radiator in the antenna buildup entails several additional challenges where this work has resulted in original contributions. Firstly, extensive design and measurement campaigns have brought to light some EM phenomena (like parallel plate waveguide modes) that, quite unexpectedly, seem to play a very important role in the performance of the foreseen antenna. In this memoir we have advanced some explanations, mostly based on empirical considerations. A full theoretical description of these phenomena and the derivation of a set of guidelines to cope with them remain desirable future developments. Secondly, the need of a simple and reliable characterization of the performance of the different components that are buried in the antenna PCB buildup has led to a series of interesting technological developments. Basically, these developments are related to the conception and implementation of several right angle coaxial-to-stripline transitions that, as described in *Section 3.2.2*, enable competitive compromises between EM performance, ease of manufacturing and robustness.

For a complete list of publications, the reader is referred to the end of of this memoir.

References

- [1] S. J. Dick and R. D. Launius, Eds., *Societal impact of spaceflight*. Washington DC: NASA Office of External Relations, History Division, 2007. [Online]. Available: <http://permanent.access.gpo.gov/lps115997/>
- [2] C. E. Cohen, B. W. Parkinson, J. D. Powell, D. G. Lawrence, B. S. Pervan, and H. S. Cobb, "System and method for generating precise position determinations (GPS)," U.S. Patent 5 572 218, November 5, 1996.
- [3] H. Wheeler, "Fundamental limitations of small antennas," *Proceedings of the IRE*, vol. 35, no. 12, pp. 1479 – 1484, 1947.
- [4] L. J. Chu, "Physical limitations of omni-directional antennas," *Journal of Applied Physics*, vol. 19, no. 12, pp. 1163–1175, 1948.
- [5] R. F. Harrington, "Effect of antenna size on gain, bandwidth and efficiency," *Journal of Research of the National Bureau of Standards-D Radio Propagation*, vol. 64-D, pp. 1–12, 1960.
- [6] R. J. Mailloux, *Phased Array Antenna Handbook*, 2nd ed. London: Artech House, 2005.
- [7] R. C. Hansen, *Phased Array Antennas*. New York: Wiley-Interscience, 1998.
- [8] K. R. Carver and J. W. Mink, "Microstrip antenna technology," *IEEE Trans. Antennas Propag.*, vol. AP-29, pp. 2–24, Jan. 1981.
- [9] D. M. Pozar, "Microstrip antennas," vol. 80, no. 1, Jan. 1992, pp. 79–91.
- [10] J.-F. Zürcher and F. E. Gardiol, "The SSFIP: A global concept for high performance broadband planar antennas," *Electron. Lett.*, vol. 24, no. 23, pp. 1433–1435, Nov. 1988.
- [11] —, *Broadband patch antennas*. Boston: Artech House, 1995.
- [12] R. J. Mailloux, J. F. McIlvanna, and N. P. Kernweis, "Microstrip array technology," *IEEE Trans. Antennas Propag.*, vol. AP-29, no. 1, pp. 25–37, Jan. 1981.
- [13] D. M. and D. H. Schaubert, Eds., *Microstrip Antennas. The Analysis and Design of Microstrip Antennas and Arrays*. New York: IEEE Press., 1995.
- [14] R. F. Harrington, *Field Computation by Moment Methods*. MacMillan, 1968.
- [15] A. Peterson, S. Ray, and R. Mittra, *Computational Methods for Electromagnetics*. IEEE Press/Oxford University Press, 1998.
- [16] J. R. Mosig, "Integral equation techniques," in *Numerical techniques for microwave and millimeter-wave passive structures (ch. 3)*, T. Itoh, Ed. New York: Wiley, 1989.
- [17] J. R. Mosig and F. E. Gardiol, "Analytical and numerical techniques in the Greens functions treatment of microstrip antennas and scatterers," in *Inst. Elect. Eng. Microwave Antennas and Propagation*, vol. 130, Mar. 1983, pp. 175–182.
- [18] K. A. Michalski and J. R. Mosig, "Multilayered media Greens functions in integral equations formulations," *IEEE Trans. Antennas Propag.*, vol. 45, pp. 508–519, Mar. 1997.
- [19] R. Garg, P. Barthia, I. Bahl, and A. Ittipiboon, *Microstrip Antenna Design Handbook*. Boston: Artech House, 2001.
- [20] A. Henderson and J. James, "Improved microstrip flat-plate array for domestic DBS reception," in *Antennas and Propagation Society International Symposium*, vol. 24, Jun. 1986, pp. 565–568.
- [21] —, "Low-cost flat-plate array with squinted beam for DBS reception," *Microwaves, Antennas and Propagation, IEE Proceedings H*, vol. 134, no. 6, pp. 509 –514, december 1987.
- [22] J. Huang, "Microstrip antennas for commercial applications," in *Microstrip Antennas. The Analysis and Design of Microstrip Antennas and Arrays*, D. M. Pozar and D. H. Schaubert, Eds. New York: IEEE Press., 1995, pp. pp. 371–379.

- [23] M. E. Bialkowski and P. W. Davis, "Radial line slot antenna," U.S. Patent 6 124 833, September 26, 2000.
- [24] A. Zaghloul, R. Gupta, E. Kohls, L. Sun, and R. Allnutt, "Low cost flat antennas for commercial and military SATCOM terminals," in *MILCOM 2001 - IEEE Military Communications Conference*, no. 1, Oct. 2001, pp. 795–799.
- [25] K. Sakakibara, Y. Kimura, J. Hirokawa, M. Ando, and N. Goto, "A two-beam slotted leaky waveguide array for mobile reception of dual-polarization DBS," *Vehicular Technology, IEEE Transactions on*, vol. 48, no. 1, pp. 1–7, Jan. 1999.
- [26] S.-C. Gao, L.-W. Li, M.-S. Leong, and T.-S. Yeo, "Integrated multibeam dual-polarised planar array," in *IEE Proceedings in Microwaves, Antennas and Propagation*, vol. 148, no. 3, Jun. 2001, pp. 174–178.
- [27] Y. J. Cheng, W. Hong, and K. Wu, "Millimeter-wave substrate integrated waveguide multibeam antenna based on the parabolic reflector principle," *IEEE Trans. Antennas Propag.*, vol. 56, no. 9, pp. 3055–3058, Sept. 2008.
- [28] M. Ettorre and R. Sauleau, "Dual-layer optimized pill-box antenna for applications in the millimeter-wave range," in *5th ESA Workshop on Millimetre Wave Technology and Applications & 31st ESA Antenna Workshop*, ESA/ESTEC, Noordwijk, The Netherlands, Jun. 2009.
- [29] A. C. Densmore and V. Jamnejad, "A satellite-tracking K and Ka-band mobile vehicle antenna system," *IEEE Trans. Veh. Technol.*, vol. 42, no. 4, pp. 502–513, Nov. 1993.
- [30] F. Hules, G. Streelman, and H. Yen, "A direct broadcast satellite reception system for automotive OEMs," in *IEEE Antennas and Propagation Society International Symposium*, vol. vol. 1B, 2005, pp. 80–83.
- [31] S. Y. Eom, S. H. Son, Y. B. Jung, S. I. Jeon, S. A. Ganin, A. G. Shubov, A. K. Tobolev, and A. V. Shishlov, "Design and test of a mobile antenna system with tri-band operation for broadband satellite communications and DBS reception," *IEEE Trans. Antennas Propag.*, vol. 55, no. 11, pp. 3123–3133, Nov. 2007.
- [32] (2008, Feb.) Datron Product Information Sheet. Datron Advanced Technologies Inc. [Online]. Available: <http://www.turbosurf.com/CruiseTV-STS.html>
- [33] (2008, Feb.) MotoSAT Product Information Sheet. MotoSAT Systems. [Online]. Available: <http://www.motosat.com/>
- [34] (2008, Feb.) Satellites in Motion(R) catalog. Satellites in Motion(R). [Online]. Available: <http://www.satellitesinmotion.com/>
- [35] R. Azadegan, "A Ku-band planar antenna array for mobile satellite TV reception with linear polarization," *IEEE Trans. Antennas Propag.*, vol. 58, no. 6, pp. 2097–2101, 2010.
- [36] (2008, Feb.) NATALIA (New Automotive Tracking Antenna for Low-cost Innovative Applications) Project. European Space Agency. [Online]. Available: <http://telecom.esa.int/telecom/www/object/index.cfm?fobjectid=27952>
- [37] ESA, "Patch Antenna for Mobile Receive Only Terminals. Appendix 1: Statement of Work," Invitation To Tender AO/1-4482/03/NL/US, Sep. 2003.
- [38] R. Baggen, S. Vaccaro, and D. L. del Río, "Mobile Ku-band satellite terminal for low-cost applications," in *International URSI Commission B. Electromagnetic Theory Symposium*, Ottawa, ON, Canada, Jul. 2007, pp. 80–83.
- [39] R. Baggen, S. Vaccaro, and D. Llorens, "Design considerations for compact mobile Ku-band satellite terminals," in *proc. EuCAP 2007, 2nd International Conference on Antennas and Propagation*, Nov. 2007.
- [40] D. Llorens, F. Tiezzi, and S. Vaccaro, "Sub-array polarization control using rotated dual polarized radiating elements," Patent US 20 100 253 585, October 7, 2010.

- [41] S. Vaccaro, D. Llorens, R. Torres-Sánchez, and R. Baggen, “Low cost phased array for mobile Ku-band satellite terminal,” in *proc. EuCAP 2010, 4th International Conference on Antennas and Propagation*, Apr. 2010.
- [42] R. Baggen, S. Vaccaro, , D. Llorens, R. Torres-Sánchez, and G. Langgartner, “First prototyping of a compact mobile Ku-band satellite terminal,” in *proc. EuCAP 2010, 4th International Conference on Antennas and Propagation*, Apr. 2010.
- [43] F. Tiezzi, S. Vaccaro, D. Llorens, and R. Torres-Sánchez, “Method and apparatus for a compact modular phased array element,” Patent US 20 110 025 574, February 3, 2011.
- [44] J. D. Kraus, Ed., *Antennas*, 1st ed. New York: McGraw-Hill, 1950.
- [45] J. R. James and P. S. Hall, Eds., *Handbook of microstrip antennas*. London: P. Peregrinus on behalf of the Institution of Electrical Engineers, 1989.
- [46] P. Hall, “Feed radiation effects in sequentially rotated microstrip patch arrays,” *Electronics Letters*, vol. 23, no. 17, pp. 877–878, 13 1987.
- [47] K. Woelders and J. Granholm, “Cross-polarization and sidelobe suppression in dual linear polarization antenna arrays,” *IEEE Trans. Antennas Propag.*, vol. 45, no. 12, pp. 1727–1740, Dec. 1997.
- [48] R. C. Hansen, Ed., *Microwave scanning antennas*. Los Altos, Calif.: Peninsula Publishing, 1985.
- [49] A. Ellgardt, “Wide-angle scanning wide-band phased array antennas,” Ph.D. dissertation, KTH School of Electrical Engineering, Stockholm, Sweden, 2009.
- [50] H. Wheeler, “The grating-lobe series for the impedance variation in a planar phased-array antenna,” *IEEE Trans. Antennas Propag.*, vol. 13, no. 5, pp. 825–827, sep 1965.
- [51] J. Shin and D. Schaubert, “A parameter study of stripline-fed vivaldi notch-antenna arrays,” *IEEE Trans. Antennas Propag.*, vol. 47, no. 5, pp. 879–886, may 1999.
- [52] P. Friedrich, L. Pringle, L. Fountain, P. Harms, D. Denison, E. Kuster, S. Blalock, G. Smith, J. Moloney, and M. Kesler, “A new class of broadband planar apertures,” in *Allerton Antenna Applications Symposium*, Monticello, Illinois (USA), Sep. 2001.
- [53] B. Munk, R. Taylor, T. Durharn, W. Crosswell, B. Pigon, R. Boozer, S. Brown, M. Jones, J. Pryor, S. Ortiz, J. Rawnick, K. Krebs, M. Vanstrum, G. Gothard, and D. Wiebelt, “A low-profile broadband phased array antenna,” in *Antennas and Propagation Society International Symposium, 2003. IEEE*, vol. 2, june 2003, pp. 448–451.
- [54] B. Thors, H. Steyskal, and H. Holter, “Broad-band fragmented aperture phased array element design using genetic algorithms,” *IEEE Trans. Antennas Propag.*, vol. 53, no. 10, pp. 3280–3287, oct. 2005.
- [55] H. Holter, “Dual-polarized broadband array antenna with BOR-elements, mechanical design and measurements,” *IEEE Trans. Antennas Propag.*, vol. 55, no. 2, pp. 305–312, feb. 2007.
- [56] J. Kasemodel, C.-C. Chen, and J. Volakis, “Broadband planar wide-scan array employing tightly coupled elements and integrated balun,” in *Phased Array Systems and Technology (ARRAY), 2010 IEEE International Symposium on*, oct. 2010, pp. 467–472.
- [57] M. Bourry, F. Tiezzi, and S. Vaccaro, “Omni-directional antenna for mobile satellite broadcasting applications,” Patent US 20 090 027 294, January 29, 2009.
- [58] H. Wheeler, “Simple relations derived from a phased-array antenna made of an infinite current sheet,” *IEEE Trans. Antennas Propag.*, vol. 13, no. 4, pp. 506–514, jul 1965.
- [59] D. Pozar, “The active element pattern,” *IEEE Trans. Antennas Propag.*, vol. 42, no. 8, pp. 1176–1178, aug 1994.
- [60] N. Herscovici, B. Tomasic, J. Ginn, and T. Donisi, “Scanning characteristics of aperture coupled fed fragmented microstrip arrays,” in *Antennas and Propagation Society International Symposium, 2009. APSURSI’09. IEEE*, 1-5 2009, pp. 1–4.
- [61] P. Hannan, “The element-gain paradox for a phased-array antenna,” *IEEE Trans. Antennas Propag.*, vol. 12, no. 4, pp. 423–433, jul 1964.

- [62] W. Kahn, "Ideal efficiency of a radiating element in an infinite array," *IEEE Trans. Antennas Propag.*, vol. 15, no. 4, pp. 534 – 538, jul 1967.
- [63] R. Torres-Sánchez, "Evaluation of different candidate Radiating Elements for the NATALIA array," LEMA (EPFL) & JAST Antenna Systems, Lausanne, Switzerland, Tech. Rep., Sep. 2007, (v. 7).

2. Elementary Radiating Cell. Design Guidelines

*If I had eight hours to chop down a tree,
I would spend six sharpening my ax.*

ABRAHAM LINCOLN

2.1 Introduction

Two of the main components of the NATALIA phased array concept are the Dual Circularly Polarized Radiating Element (DCPRE) and the so-called Tracking Unit (TU), as it was explained throughout the previous chapter and depicted in *Fig. 1.3*. The TU consists of a power combiner and a couple of active components (the MMICs), each one of which integrates a LNA and a programmable phase shifter.

The perspective of a more in detail design of the antenna terminal suggests, however, to adopt a different re-grouping of the parts inside those two components. This re-arrangement leads to the definition of two new building blocks: the so-called **Elementary Radiating Cell** (ERC), that is confined to the PCB core, and the **MMICs**, that are to be incorporated into the PCB during the final fabrication stages.

According to this definition, the ERC comprises the DCPRE and all the passive components within the TU. Just as a reminder, these passive components are highlighted in *Fig. 2.1* and described next:

1. the couple of *Long Vias* that link the outputs of the circularly polarized element, which is located in the upper part of the PCB buildup, to the inputs of the MMICs, in the bottom microstrip layer.

2. The *Power Combiner* that connects the outputs of the MMICs to the Feeding Network, which is routed in an intermediate stripline-like layer.

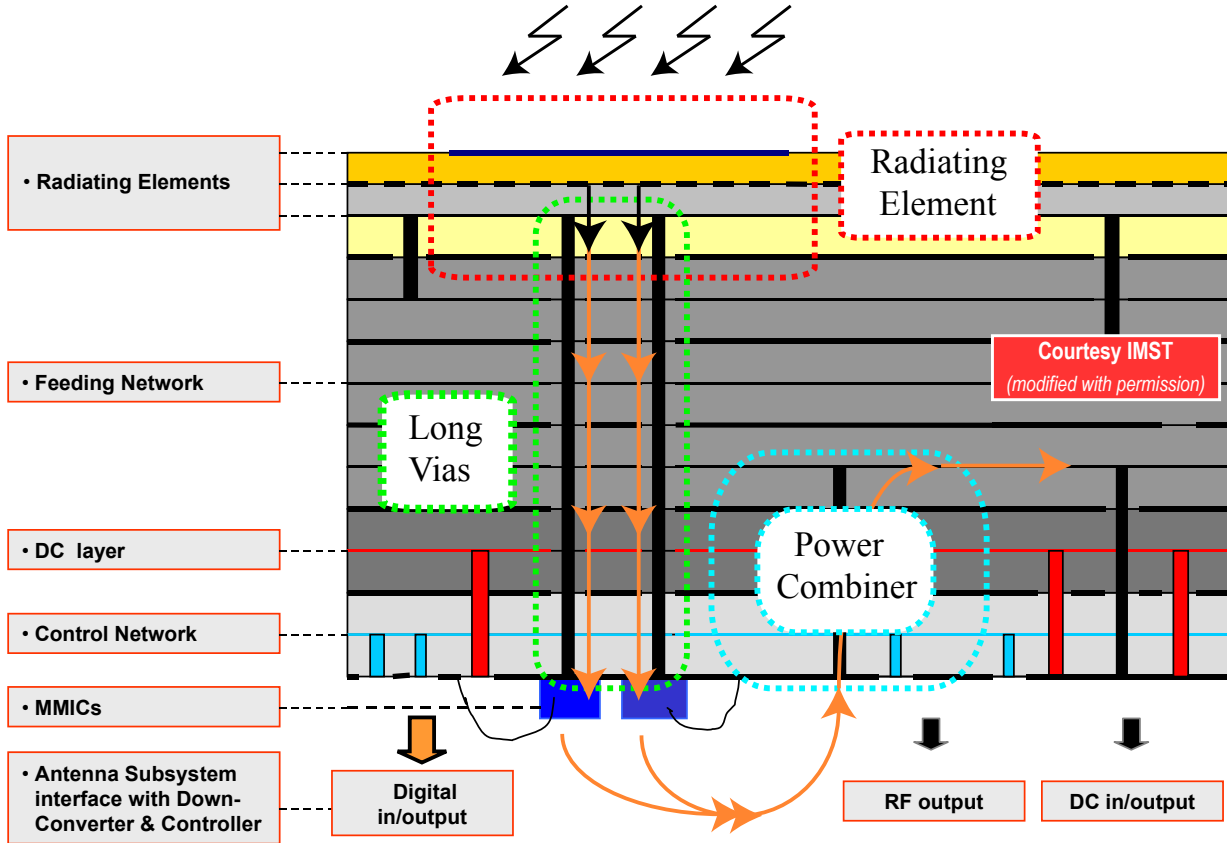


Figure 2.1. Preliminary NATALIA PCB buildup overview (not to scale), with the components of the Elementary Radiating Cell highlighted.

This chapter is based to a large extent on a previous work by the author [1]. It presents the basic concept proposed for the implementation of the DCPRE as well as the main general criteria that guide the design of this antenna element. As far as possible, these criteria are stated in such a way that they should be easily extended to a wide range of radiating elements belonging to the class of the proposed DCPRE, regardless the particular design constraints imposed by the targeted application.

The next chapter will illustrate the way these criteria are applied to the basic DCPRE concept as it is progressively adapted to match the actual design constraints. There, besides the performance requirements, the design constraints will be related to the integration of the ERC inside both the antenna PCB buildup and the array lattice. This integration will also guide the design of the remaining components of the ERC : the *Long Vias* and the *Power Combiner*.

2.2 Design Approach

The design of the DCPRE is based on the combination of a Dual Linearly Polarized Radiating Element and a 3 dB-quadrature coupler. There are structures that are inherently better suited for the radiation of a circularly polarized field and, therefore, not prone to the bandwidth/size limitations generally associated to the quadrature coupler.¹ To the best of the author's knowledge, the two main planar implementations of these structures are the **meander-line polarizer** [3] and the **spiral antenna** [4]. However, both structures are generally limited to the generation of a single circular polarization, which calls into question their suitability for the present application.

In the case, for example, of the spiral antenna, whose integration within the present phased array concept seems more convenient than that of the meander-line polarizer, it must be said that the generation of dual circular polarization at array level has been demonstrated, at the expense of relaxed side-lobe constraints, for a broad-band phased array by interleaving spiral antennas with different polarizations [5]. At radiating element level there have been considerable advances [6], but the quality of the dual circular polarization generated remains somewhat limited in terms of axial ratio, symmetry and bandwidth [7, 8].

With regard to the implementation of the Dual Linearly Polarized Radiating Element (DLPRE), the low-profile characteristics of the **microstrip patch antenna** elements² prevail over the alternatives represented by the **tapered slot** (also named *Vivaldi* or notch) and the **BOR** (Body Of Revolution) elements, that are considerably thicker ($\sim \lambda$), though functionally outstanding for wide-band wide-angle dual polarized array antennas [16–19]. Recent developments based on **Tightly Coupled Dipole Arrays** (TCDAs) are showing very promising wide-band scanning performances with considerably thinner ($\sim \lambda/3$) radiating elements [20]. These elements have single linear polarization and, though the expansion to dual polarization might not significantly increase their overall profile, further thinning down of the elements would be needed to match the actual thickness requirements for the DLPRE ($\sim \lambda/6 - \lambda/4$).

Currently, the radiating elements based on the **Fragmented Aperture Concept** (FAC) constitute one of the most competitive compromises in terms of wide-band scanning performance and low profile (microstrip) implementation [21–23]. In fact, an in depth investigation on the applicability of this concept to the design of the foreseen array is considered of great interest. The design approach for this class of array elements, as for most of the other elements cited above, is

¹Circularly polarized patch antennas can also be designed without adding an external polarizer (the quadrature coupler, in this case), which constitutes an important simplification. The operation principle of these patch antennas is based on the decomposition of the mode excited within the patch cavity into two degenerate orthogonal modes whose relative phase shift is tuned to 90° by means of a series of perturbations, such as slots or truncated segments, in the patch pattern. As it will be discussed in *Section 2.4.2* with regard to the patch miniaturization, this perturbation approach suffers, compared to the use of an external polarizer, from a much smaller bandwidth, mainly with regard to its polarization quality [2, Ch. 4].

²For a description of the different kinds of microstrip antennas, their operation principles, their functional characteristics as well as the most efficient methods used for their theoretical analysis, the reader can find some useful references at the end of the chapter [9–15].

based on the infinite array modeling scheme discussed in *Section 1.1.2*. However, the application of this powerful design scheme is relegated here in favor of the isolated element modeling approach described next, just to accelerate the completion of the first design iterations. Once these design iterations are completed and the array antenna concept proven, such an investigation should be carried out, since it may enable (i) an overall improvement of the actual array performance³ and (ii) an eventual application of the array concept to larger apertures, where the resort to the infinite array modeling scheme (or an equivalent) would become compulsory, anyway.

In the following section, the general design guidelines for the (isolated) microstrip DCPRE are given from the perspective of its evolution from a single to a dual linearly polarized element, and from a dual linear to a dual circular element.

2.3 Design Guidelines

The synthesis of the Radiating Element (RE), according to its planar geometry, can be divided into two tasks:

- the design of its metalization planes, that contain strips, slots, ground planes, etc;
- and the design of its structure in elevation (the so-called *buildup*), that comprises the way the metalization planes and the different dielectric materials in between are superimposed as well as their thicknesses and their electric characteristics.

Though from the point of view of the electrical operation of the RE both tasks are equally important, most of the requirements regarding the antenna installation-integration, its manufacturing and its final cost do fall on the side of the RE buildup.

For the present application, the importance of such requirements motivates that some of the first design choices are related to the RE buildup. Next, the electrical operation will become the main objective of a design process covering, within the degrees of freedom that are still available, both the buildup and the metalization planes of the RE.

As it has just been stated, this approach to the RE synthesis agrees with Prof. D. M. Pozar's view on the first developments of microstrip antennas. According to this view, the main attractiveness of the planar technology for the antenna implementation lied, originally, in its potential to satisfy certain structural and manufacturing requirements [12]. This potential would contribute decisively to encourage a deeper study of the operation principles of microstrip antennas, as well as to the consequent improvement of their electrical performance, which was rather modest for the first prototypes.

³The FAC may allow, in fact, an effective generalization, at array level, of many of the design guidelines proposed here for the isolated element. Certain recent implementations of the FAC seem to point in that direction [23].

2.4 Radiating Element with Single Linear Polarization

2.4.1 Buildup

The RE proposed here is based on the microstrip patch antenna concept. Therefore, its basic structure, visible in *Fig. 2.2*, consists of an arbitrarily shaped thin metal layer, the so-called *patch*, that lies over a dielectric substrate whose opposite face is backed with a ground plane.

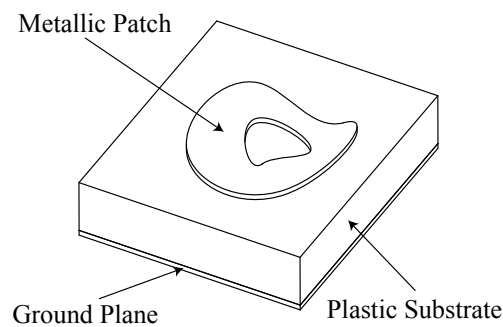


Figure 2.2. Microstrip Patch.

a) Feeding

The buildup of the RE is determined to a large extent by the mechanism used to excite it. This can be appreciated in *Fig. 2.3*, where the most usual approaches are illustrated.

The feeding through a microstrip line that is coplanar to the patch (*edge fed* in *Fig. 2.3*) is the most attractive choice from the point of view of structural simplicity, but its electrical characteristics are rather limited by the compromise between the guiding and the radiation mechanisms (see next section) that arise when the transmission line and the patch lie on the same substrate. On the other hand, the structural complexity associated to the so-called *coaxial* or *probe feeding* may discourage its implementation, especially in the case of “hand-made” fabrication, as the frequency of operation increases [13]. The resort to industrial fabrication techniques, however, can efficiently automatize the implementation of the required vertical connections as metalized holes (vias), at the expense of additional processing steps and/or more stringent design rules.⁴

⁴In this context, additional processing steps have generally a negative impact on the cost of the final PCB as well as in the manufacturing tolerances and, eventually, the production yield. While more stringent design rules, as the use of much longer or thicker vias, can limit considerably the maximum electromagnetic performance that the RE can achieve.

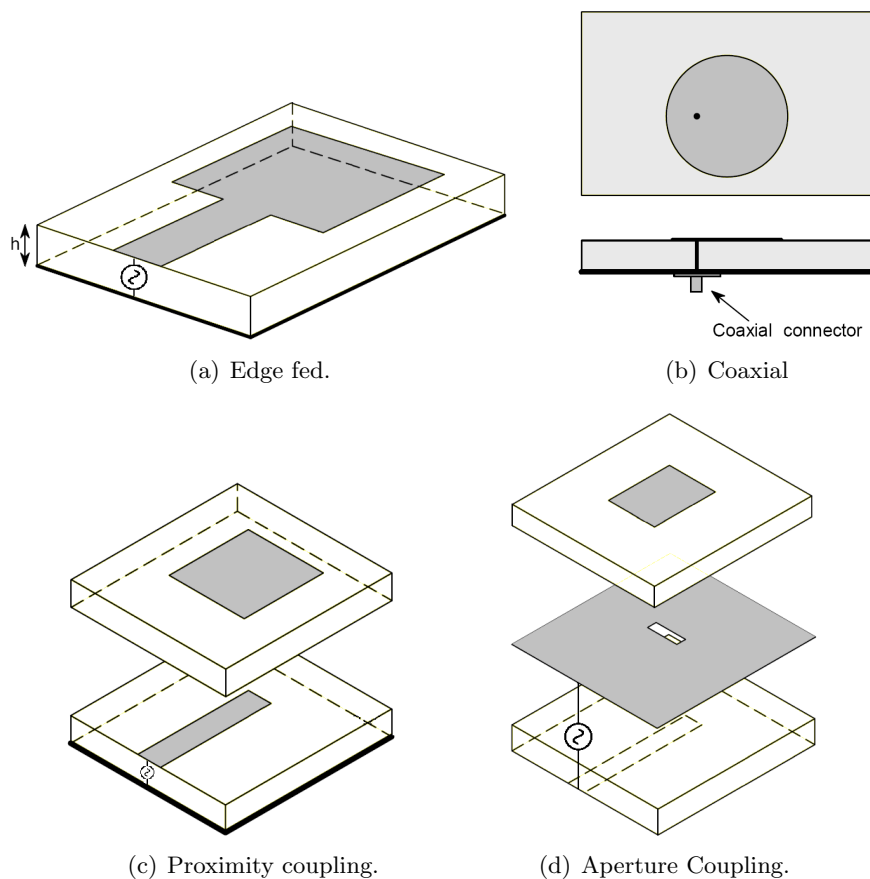


Figure 2.3. Radiating Element Feeding.

Proximity and aperture coupling combine their potentially good electrical characteristics, thanks to the degrees of freedom associated to the use of different dielectrics for the patch and the line, with almost all the advantages of a purely planar technology. The price to pay in this two feeding techniques is a certain increase of their manufacturing complexity, due to the required additional steps of alignment and glueing of the dielectrics. This price, however, may be justified by taking into account that the electrical performances of this kind of REs can be very competitive and that their integration into arrays does not imply an increase of the overall fabrication complexity.

When it comes to compare these two last feeding mechanisms, it must be taken into account that a common practice in the case of aperture coupling is to shield the line by adding another ground plane at a certain distance below the line. This shielding may increase the RE profile noticeably (typically $\lesssim \lambda_0/4 \approx 6.4$ mm) and/or degrade the efficiency of the coupling between the line and the aperture, as it will be discussed in the next section. On the other hand, aperture coupling offers, with regard to proximity coupling, an additional degree of freedom (associated to the aperture geometry) as well as the advantages derived from a complete isolation between the radiating hemisphere and the feeding line. Among these advantages there are the possibility of optimizing each region independently and avoiding undesired interactions between guiding and radiation, that could give rise to spurious radiation from the proximity coupled feeding lines / network [12].

In accordance with these arguments, aperture coupling is found to be the most promising feeding mechanism for the RE of the present application. This element would, therefore, be based on the so-called Aperture Coupled Microstrip Patch Antenna (ACMPA) concept [24] and the design considerations coming next are going to focus on it.

b) Characteristics of the Dielectrics

In the design of microwave planar circuits, the choice of the substrates is one of the key steps, since it determines, beyond the electrical operation, many of the mechanical properties, a great deal of the manufacturing process and a significant part of the cost of the final product.

This claim also applies to the design of microstrip antennas. For these, the specification of the dielectrics acquires a new dimension, because the main propagation mechanism of the EM fields is not only guiding, but it coexists with radiation; just in the same way as the patch coexists with the transmission line feeding it.

In the background, but always present in the stratified media, there are the so-called *surface waves*. This third mechanism, generally unwanted for both the circuit and the antenna designer, is characterized by the propagation of energy in cylindrical wave-fronts guided within the substrate boundaries. These waves may give rise to a significant reduction of the usable signal power, to increased coupling with neighboring structures and, finally, to the radiation of the waves diffracted in the edges where the planar structure is truncated, with a significant increase in the cross-polar and side-lobe levels [13, Ch. 1]. In large phased arrays, the excitation of surface waves can lead to severe limitations of the scan performance and the antenna bandwidth [25,26], [27, vol. 2. Ch.3].

The predominance of one mechanism over the others depends, besides the frequency of operation and the shapes etched in the metalization plane, on the thickness and the electrical characteristics of the substrates. In this way, it happens that while for transmission lines the ideal substrates are generally thin and with relatively high electrical permittivity (ϵ), for the radiating part they should be thick and of low ϵ .

The guiding-radiation duality, necessary for the proper operation of a microstrip antenna, requires, therefore, that the dielectrics composing it satisfy conflicting specifications. That is why, for example, the electrical performance of the antennas in which the patch and the line are lying on the same substrate are so limited. In this kind of antennas, the compromise is usually addressed by using dielectrics with high permittivity, to favor guiding, and thick, to promote radiation, which also leads to an increased excitation of surface waves [13, Ch. 1].

In the case of the ACMPA, with separate substrates for the patch and the feeding line, the operation of the two mechanisms of interest can be optimized independently.

b.1) Radiating Part

Besides favoring the radiation mechanism, the increase of the patch substrate thickness and the reduction of its permittivity can contribute to the increase of the input impedance bandwidth of the RE (see *Section 2.4.3*) and to minimize the surface wave power leakage [28,29].

The two main options to minimize the relative permittivity of the dielectric, the use of air ($\epsilon_{r \text{ ideal}} = 1$) and of artificial foams ($\epsilon_{r \text{ typ.}} \approx 1.07$), require the insertion of a new dielectric layer to hold the etched patch. This carrier layer may also contribute to the protection of the RE against environmental agents such as humidity and ultra-violet radiation, thus acting as a radome. The resulting structure, depicted in *Fig. 2.4*, was proposed by Mr. J-F. Zürcher, who named it SSFIP (Strip - Slot - Foam - Inverted Patch) [30].

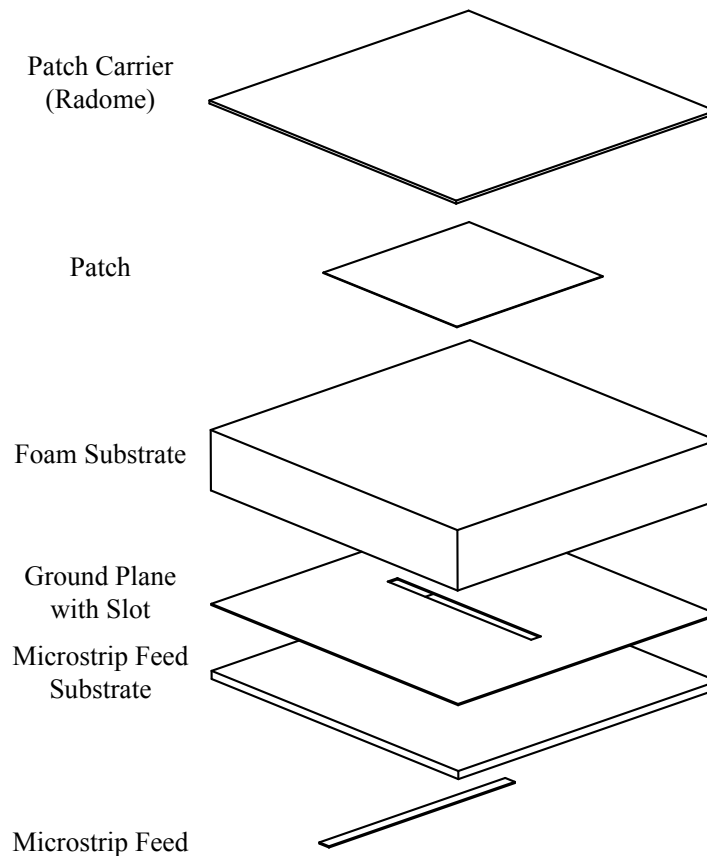


Figure 2.4. SSFIP Buildup.

In this structure, the maximum thickness of the patch (foam) substrate is typically limited by its impact on the antenna profile as well as by the weakening of the coupling between the slot and the patch.

An alternative approach to mitigate the power leakage due to the surface waves is the so-called *cavity backing* technique. Basically, this technique consists in the introduction of a grounded vertical metallic wall around a portion of substrate that lies below the patch. To allow radiation, the cavity defined in this way is open through the gap that separates the periphery of the patch from the wall edges. The inclusion of this metallic wall effectively prevents the propagation of surface waves in the patch substrate and eliminates most of the design constraints imposed by this propagation mechanism. For example, the bandwidth of a cavity backed patch antenna can be enlarged by increasing the thickness of the patch substrate, regardless the value of its permittivity, which becomes, therefore, an additional degree of freedom. And this degree of freedom can be used either to further broaden the bandwidth of the antenna or to contribute to its miniaturization [31].

In practice, the implementation of the cavity generally implies the introduction of a drilled thick metal plate in the antenna buildup. The presence of this thick metal plate can also improve both the mechanical and thermal characteristics of the antenna system.

At the expense of a certain increase in the structural complexity and the weight of the resulting antenna element, the *cavity backing* technique enables, therefore, significant improvements in terms of radiation efficiency and bandwidth at both RE and array levels. At array level, it is worth noticing that this technique can reduce the mutual coupling between the elementary radiators and, therefore, prevent undesired phenomena such as scan blindness [31–36]. On the other hand, the array lattice determines the maximum size of the cavity for each RE, which may represent a limitation for their stand-alone performance.

Finally, the choice of the radome is done according to:

- its carrier and protective roles, and
- its effect in the electrical operation of the antenna; mainly with regard to the loss this superstrate introduces. In this case the goal is not typically to improve the RE operation, but to minimize its degradation. To achieve this, the use of thin dielectrics with low permittivity (to minimize the loss due to surface waves) and low dielectric loss ($\tan \delta$) is advised.

Actually, and to the best of the author's knowledge, the methods used to improve certain electrical characteristics of a printed antenna using this superstrate usually have a negative impact on the cost and the antenna profile, which prevents their use for the present application. In particular, with the techniques typically labeled as '*superstrate loading*' the gain of a patch antenna can be increased (up to values close to 11 dB for a single element), they can contribute to the miniaturization of the RE or reduce its radar cross-section. This technique, however, entails very often a reduction of the radiation efficiency as well as the polarization purity of the antenna element and, in many cases, requires the use of expensive or specially tailored materials (ferrite, chiral materials, etc.) [15, 37].

b.2) Feeding Part

The use of thin substrates with high electrical permittivity for the feeding part of the microstrip patch antenna, which is advised to favor the guiding of the fields, has certain practical implications, not so desirable, that call for a compromise:

- the first issue is that the electrical operation of the lines becomes more sensitive to errors in the drawing of the traces (e.g. under-etching).

It is well known, for example, that to keep constant the transmission characteristics of a microstrip line as the thickness of the substrate (h) is reduced and its relative permittivity (ϵ_r) increases, it is required that the physical dimensions of the line decrease; this is, in fact, the principle of the so-called circuit *miniaturization* process. In this way, however, the relative dimensions of a constant fabrication error, and therefore its impact on the operation of the transmission lines, become bigger. This is illustrated in *Fig. 2.5*.

- The second consequence is that, in general, the tolerance with which the permittivity of a practical dielectric is specified generally increases with the nominal value of ϵ_r . This may introduce a significant level of uncertainty in the operation of the transmission lines. In general, to achieve tolerances of the order of 1% in ϵ_r , it is advised to use substrates with $\epsilon_r \in [2.1, 2.6]$ [15].
- And the third implication is that the use of thin dielectrics, though it reduces spurious radiation from the line, also means higher transmission loss. Typical recommended values for h are between $0.01 \lambda_0$ and $0.02 \lambda_0$ ([0.26 mm, 0.51 mm], for the present application) [29].

An important limitation of microstrip antennas, when it comes to integrate them in an array, is given by the loss in the feeding networks interconnecting them [38]. That is why in this type of applications special attention is paid to the dielectric loss factor ($\tan \delta$) and to the conductivity (σ) of the metalizations, as two important sources of signal attenuation and thermal noise. In this sense, while for the metalizations the choice of a good conductor as copper is quite usual and inexpensive, for the dielectrics the choice gets more complicated, because the impact of $\tan \delta$ on their price is generally considerable.

And last, but not least, the shielding of the circuits in microstrip technology is a good practice to prevent undesired interactions with the environment, to guarantee the predictability of their performance and, in general, to allow a proper integration within complex systems.

This protective measure acquires a particular importance when it is applied to the line feeding an ACMPA, since the slot through which the patch is excited constitutes a discontinuity that is prone to radiate. This radiation may affect the operation of the whole antenna, not only its guiding part, because it can lead to (i) a distortion of the radiation pattern of the antenna, which may no longer be unidirectional, and (ii) a reduction of its effective radiation efficiency. In these antennas,

the shielding is usually accomplished with the insertion of an additional ground plane in the *lower* part of the element buildup, which leads to the definition of a sort of stripline (triplate) structure, as illustrated in *Fig. 2.6*.

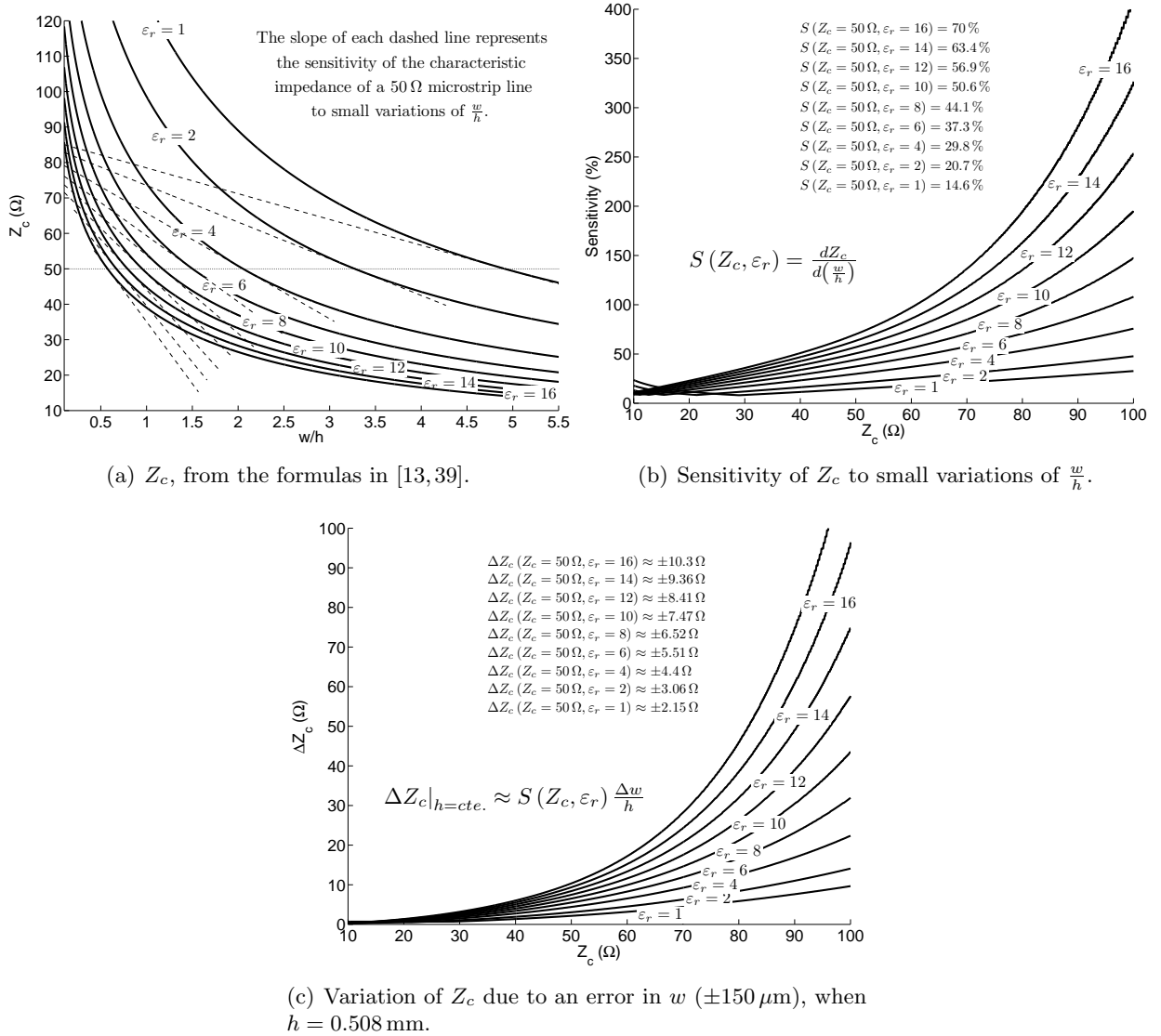


Figure 2.5. Sensitivity of the characteristic impedance (Z_c) of a microstrip line to errors in the definition of its width (w), as a function of the substrate height (h), for different substrate permittivities (ϵ_r). Note that the thickness of the metal strip of the line is assumed to be negligible. From [1].

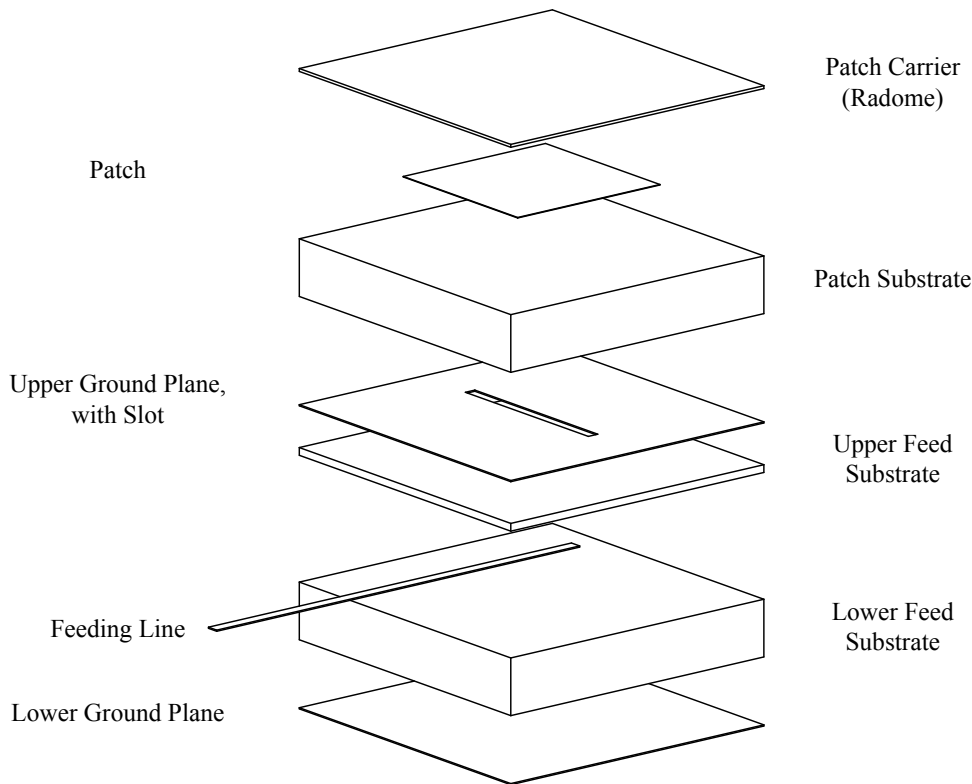


Figure 2.6. Shielded SSFIP (S3FIP) Buildup.

According to [40–44], the use of a stripline for the excitation of an ACMPA requires to take into account the following considerations:

- i) before arriving at the patch to be radiated, a significant proportion of the energy supplied to the triplate structure may be absorbed by Parallel Plate Waveguide Modes (PPWMs). These modes propagate, as cylindrical fronts, between the two ground planes enclosing the feeding line. The most harmful of these modes is usually the fundamental mode. This mode tends to create a difference of potential between both ground planes, does not have a cut-off frequency, and its excitation is related to asymmetries in the triplate structure, as that introduced by the slot in the upper ground plane depicted in *Fig. 2.6*.

An effective technique to diminish the impact of these parasitic modes on the performance of the RE is to insert shorting pins between both ground planes.⁵ If the shorting pins are suitably distributed around the slot, this power leakage can be noticeably reduced. The effectiveness of this technique is illustrated by the simulation results displayed in *Fig. 2.7*, that feature an increase of up to 50 % in the *Radiation Efficiency* of a Shielded SSFIP (S3FIP) element. In practice, the shorting pins define a sort of cavity around the slot, in the same way as it was proposed by Dr. R. J. Mailloux to prevent the mutual coupling, through PPWMs, between the slot elements in an infinite phased array. Furthermore, this approach can be considered to be analogous to the *cavity backing* technique described above [34, 46].

⁵There are other promising techniques to counteract these parasitic modes, such as the use of electromagnetic bandgap substrates [45], but at the time of design they were not found to be suitable for the targeted application, yet.

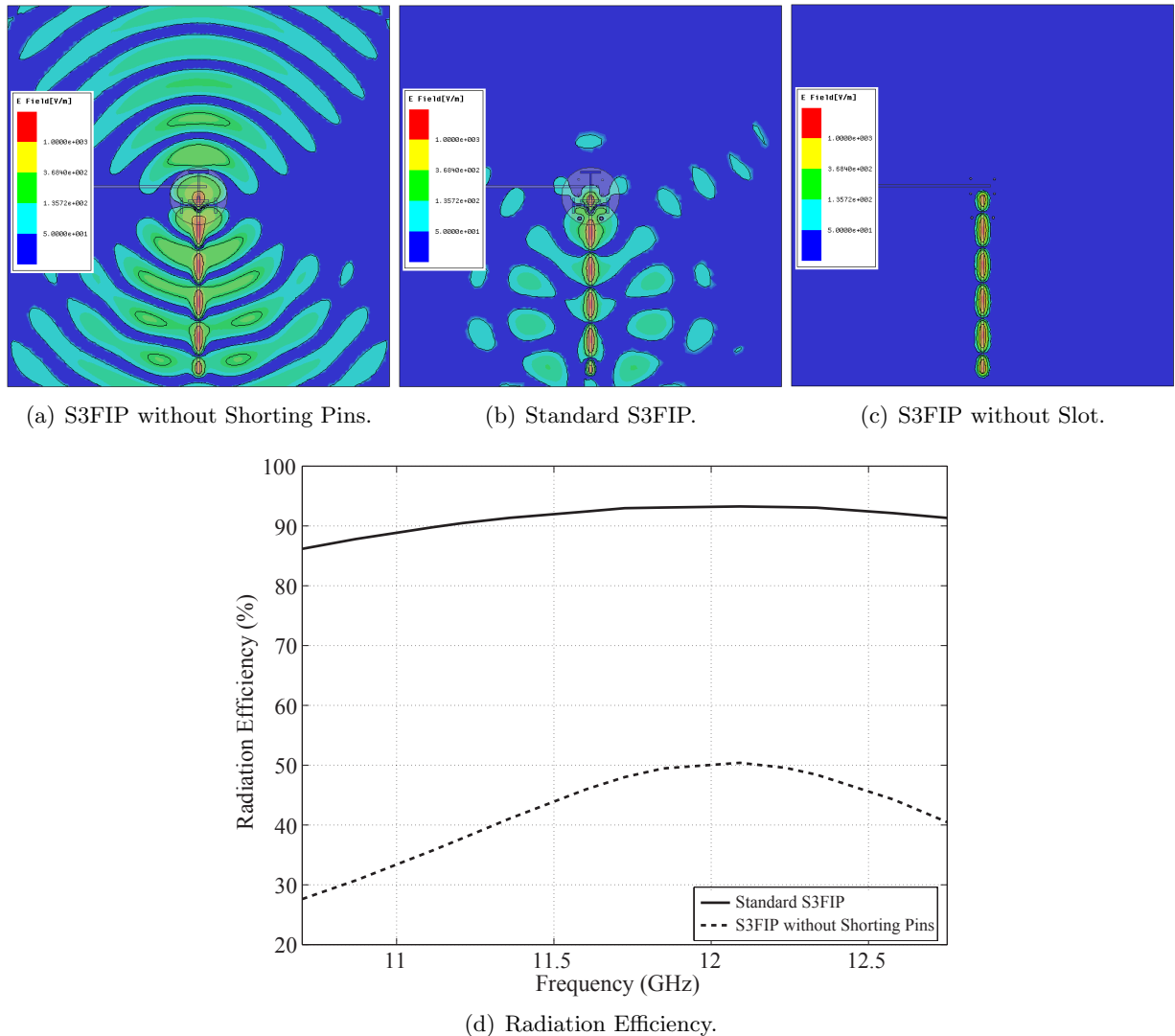


Figure 2.7. Effect of the Parallel Plate Waveguide Modes in the operation of a S3FIP in different configurations: *Standard* (i.e. with Shorting Pins and Slot) vs. *Modified* configurations (without Shorting Pins or without Slot). The triplate structure is an asymmetric stripline with $\epsilon_r = 3.48$, $h_{\text{up}} = 0.254$ mm (spacing strip-slot) and $h_{\text{down}} = 0.762$ mm (spacing strip-lower ground plane). The simulation results on the top correspond to contour plots of the magnitude of the electric field, evaluated over a surface in the vicinity of the lower ground plane, at 12.75 GHz (the three plots are calculated with *Ansoft HFSSTM* and have the same scale). On the bottom, the Radiation Efficiencies (calculated with *Ansoft DesignerTM*) of the two most representative configurations are compared.

In fact, the optimization of the radiation efficiency of the S3FIP is the main criteria considered here for the placement of the shorting pins. This optimal placement, that depends on the slot shape and the particular triplate buildup, is done under the constraints given by (a) the fabrication technology, (b) the impact of the shorting pins on other performance parameters and (c) the integration of the RE within the ERC.

In the present application, the fabrication technology limits, for example, the diameters of the different kinds of vias used to implement the shorting pins,⁶ and their minimum distance to neighboring slots and traces. Besides the *Radiation Efficiency*, the placement of the shorting pins affects the *Input Impedance* of the RE, which is very sensitive to the fluctuations in the coupling between the feeding line and the slot. And last, the integration of the RE within the ERC may introduce further restrictions in the placement and number of the shorting pins. As will be exemplified by the end of the present chapter, these restrictions are related to (c.1) the limited area available for the RE within the ERC, which applies mainly to *blind vias*, and (c.2) the possibility of collision with traces on the layers the pins are passing through (this essentially concerns *through vias*).

- ii) In an alternative approach, the shielding of the feeding line leads to a split of the induced electric current that should excite the field in the slot between two ground planes. This split results in a reduction of the coupling between the line and the slot, with the consequent degradation of the feeding mechanism of the patch antenna.

This unwanted effect can be compensated by increasing the number of current lines intercepted by the slot. This compensation can be achieved with the design of an appropriate geometry for the slot (as it will be discussed later, in *Section 2.4.2*), and the construction of an asymmetric triplate structure. In fact, as the thickness of the lower feed substrate in *Fig. 2.6* is increased and its dielectric permittivity reduced, the fields tend to concentrate in the upper feed substrate, with the corresponding rise of the current density in the slotted ground plane.

From the considerations above, the design of the slot and the placement of the shorting pins should become more involved as the triplate structure approaches that of a symmetric stripline. On the other hand, the use of shorting pins might not even be necessary for a shielded microstrip ($\epsilon_r, \text{lower substrate} \rightarrow 1$), provided that the lower ground plane is far enough from the feeding strip.

In the case of a shielded microstrip, all the design considerations made at the beginning of this section for the microstrip feeding remain valid, and the distance between the lower ground plane and the slot is typically advised to be $\approx \lambda_0/4$. At radiating element level and for broadside arrays, this distance is considered to be optimal in terms of impedance matching, beam-width and side-lobe level [47], but may lead to the excitation of PPWMs in a scanning array [48]. Moreover, the use of a shielded microstrip to feed the RE may increase its profile noticeably and make its connection with the array logic that lie below the lower ground plane very difficult (recall *Fig. 2.1*). For the present application, this last point is decisive, since for a shielded microstrip the length of the corresponding *Long Vias* would become excessive and their implementation through low ϵ_r dielectrics (as air or foam) is not a standard PCB technique.

⁶Depending on its length, the minimum realizable diameter of a *blind via* can be up to $\times 3$ larger than that of a *through via*.

As an intermediate solution between the stripline and the shielded microstrip approaches, there is the option of using an asymmetric stripline to feed the radiating element.⁷ This feeding scheme typically requires the insertion of shorting pins and is somewhat more sensitive to fabrication tolerances than the shielded microstrip (see *Fig. 2.8*, and compare with *Fig. 2.5*), but can enable a better compromise between cost, antenna profile and performance.

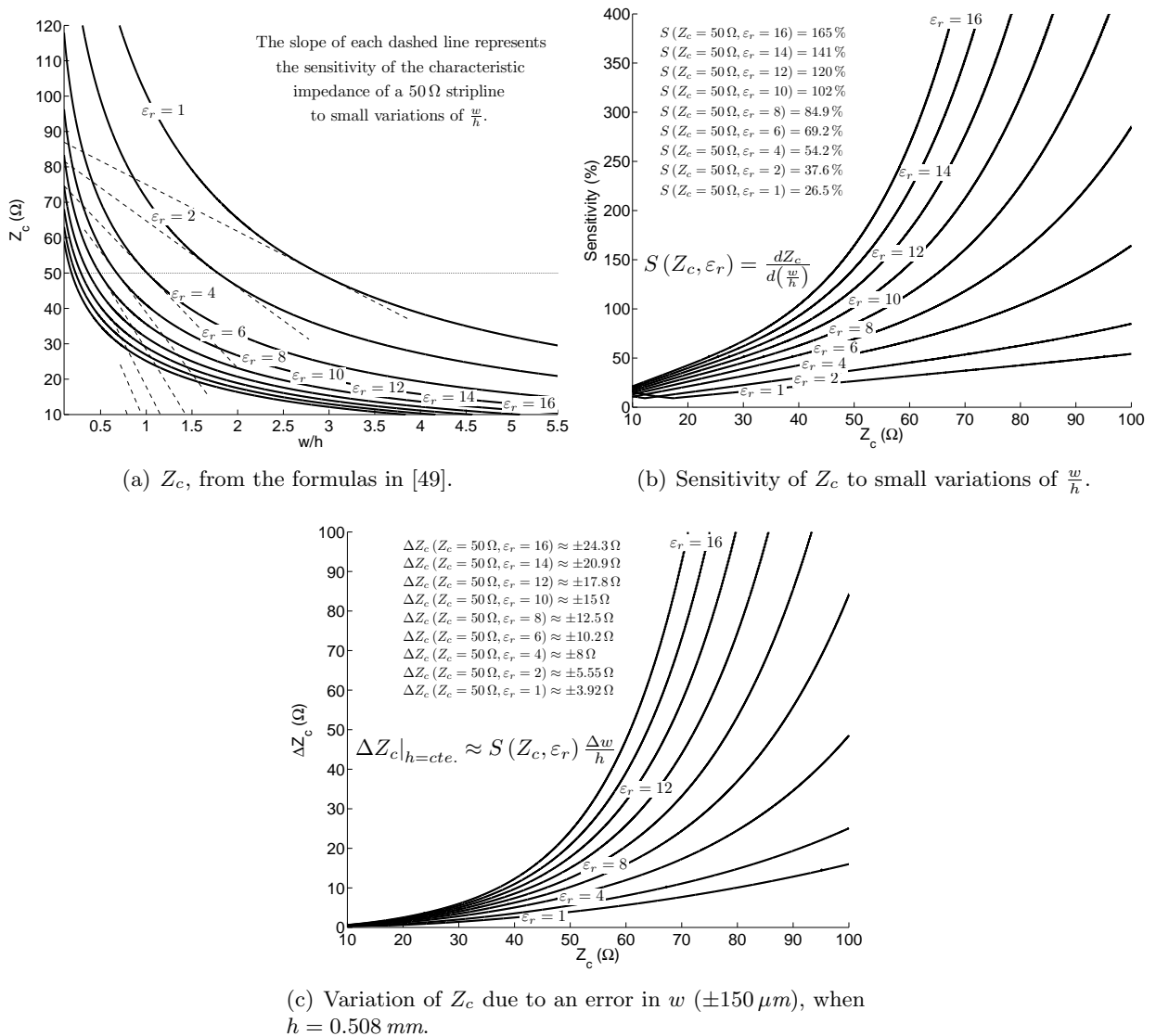


Figure 2.8. Sensitivity of the characteristic impedance (Z_c) of a symmetric stripline to errors in the definition of its width (w), as a function of the substrates height (h), for different substrate permittivities (ϵ_r). Note that the thickness of the metal strip of the line is assumed to be negligible and that the separation between the ground planes equals to $2h$.

⁷The possibility of using different dielectrics for the asymmetric stripline, which would thus become a sort of asymmetric heterogeneous stripline, could provide a valuable degree of freedom for the designer, at the expense of an increased diversity of the materials used in the buildup. This diversity may have a negative impact on the final cost of the antenna buildup and would require special considerations for its assembly, to guarantee, for example, a proper matching of the thermo-mechanical properties of all the dielectrics and the adhesives involved.

2.4.2 Metalization Planes

Next, the design guidelines concerning the metalization planes of a patch antenna are presented. For the sake of simplicity, these guidelines are given for a generic ACMPA, but, in practice, they can be easily extrapolated to the design of other kinds of patch antennas. Two kinds of particular interest are the SSFIP and shielded SSFIP. In fact, as it has been discussed in the previous section, the design of a S3FIP requires some particular considerations, but they are essentially related to the buildup of its feeding part and, therefore, such considerations can be readily incorporated into the statements made here with regard to the metalization planes of the ACMPA.

a) The Patch

Heart of the radiating part of the antenna, the patch can adopt, in principle, any shape. In practice, most patches have shapes that are based on those depicted in *Fig. 2.9*, which are characterized by a certain regularity and symmetry. These two properties ease the intuitive understanding of the basic antenna operation (polarization, directivity, etc) at early design stages, while additional variations of the patch shape, that can arise at later refinement steps,⁸ may require more complex models for the prediction of the antenna electrical operation.

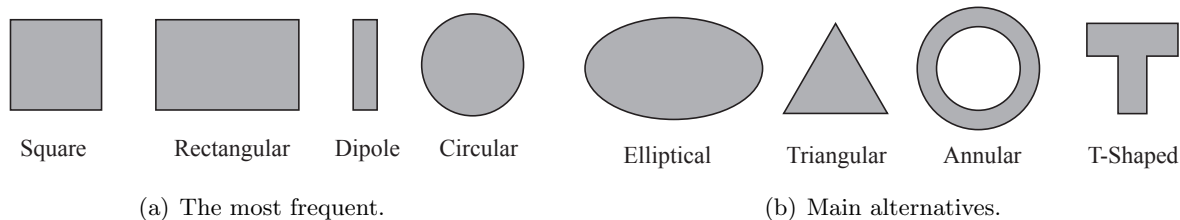


Figure 2.9. Typical patch shapes.

The shapes of the patches of the first microstrip antennas to be proposed and analyzed were rectangular and circular. The wide experience accumulated in the study of these basic shapes,⁹ together with their simplicity and versatility make of patches as those shown in *Fig. 2.9(a)* the main candidates for most of the applications. On the other hand, for more specific purposes the designer may resort to shapes as those depicted in *Fig. 2.9(b)*. The *T-shaped* patch, for example, can contribute to the reduction of mutual coupling in interleaved transmit-receive arrays [50, 51], and a *star-shaped* patch can enable certain degree of beam shaping at element level [52].

Compared to circular shapes, rectangular patches provide the designer with the degree of freedom of an additional dimension and their size is generally smaller (for the same frequency of

⁸Patch miniaturization, multi-frequency operation or certain techniques to generate circular polarization, for example.

⁹See [15] for a complete outlook on the topic.

operation and substrate). On the other hand, circular patches present better azimuthal symmetry, which permits the generation of a circular polarization with better quality, particularly at low elevation angles.

Within rectangular patches, the printed dipole stands out with regard to the high quality of the linear polarization it can generate and its reduced dimensions, which makes of it a very attractive choice for array integration. This compact size constitutes, however, a fundamental limitation for its impedance bandwidth [13, 28, 53].

In fact, the different measures to improve the bandwidth of microstrip antennas result typically in a growth of the effective volume occupied by the radiating element. This is the case, for example, of the patch antennas that increase the thickness of the patch substrate as well as of those that add parasitic elements around the patch, with their mutual resonances properly tuned. As described in [12, 13], these parasitic elements can be:

- coplanar to the patch. Despite its potentialities, the use of these parasites to improve the bandwidth of the radiating element may be problematic, particularly if the element is to be part of an array antenna, since it restricts the inter-element spacing and may accentuate the frequency dependence of certain characteristics of the radiation pattern, as the beam pointing direction or the polarization.
- Or printed in different dielectrics that are superimposed to the patch. This approach leads typically to the so-called *stacked patches* technique, that consists in the superposition over the “active” patch of a certain number of “parasitic” patches of similar dimensions. Despite the consequent increase in both the profile of the radiating element and its structural complexity, this technique remains suitable for array antenna elements and provides additional degrees of freedom that can enhance notably the electrical performance of the RE [54].

On the other hand, techniques aiming at the reduction of the directivity of the radiating element or the mitigation of the inter-element mutual coupling may proceed to a miniaturization of the patch, which can also be a goal by itself. Certain efficient miniaturization techniques, as those applied in the Planar Inverted *F-shaped* Antenna (PIFA) concept [55] and many of its variants [56] require the use of vias for the grounding of the patch, which may involve a significant increase of the manufacturing complexity.

The miniaturization techniques with the most simple practical implementation are probably those that only apply to the patch shape. Typically, these techniques rely on the compensation, at operational level, of a physical down-scaling applied to the patch shape. This compensation may be performed by means of a “virtual” increase of the patch area, as seen by the electric currents resonating over it. In fact, the introduction of slots or notches in certain regions of the patch shape can perturb the flow of these currents in such a way that the length of their “electric path” is effectively increased and their resonance takes place over a smaller conducting area. This

is the principle of operation of the so-called *fractal antennas* [57, 58], and many other antenna concepts [59–61].

Practical limits to this miniaturization technique are coming from the fact that it implies a growth of the current densities in certain parts of the patch, with the consequent increase of the conductor loss and the reduction of the radiation efficiency of the antenna element. And, as it could be expected, the patch miniaturization may also limit the bandwidth of the antenna, mainly because the way the notches perturb the current flow over the patch is, as the current distribution itself, very frequency dependent [62]. Moreover, since the aforementioned operational compensation of the patch down-scaling might be done attending mainly to its input impedance, special attention should be paid to the design of the notches, so that they do not degrade other performance parameters, as the polarization quality of the patch. Ideally, this scaling compensation should apply to all performance parameters, but in practice it may be difficult to prevent an upward frequency-shift of certain parameters, as it will be shown later.

b) The Slot

This aperture in the ground plane shared by the patch and the access line plays a fundamental role in the antenna operation, because it acts as the interface between the radiating part and the feeding of the RE. Since this excitation mechanism was proposed by Prof. D.M. Pozar [24], there have been many design refinements. In particular, the shape of the aperture has evolved to provide improved levels of coupling between the line and the patch as well as reductions in its size.

In this way, the iris-like circular aperture used in the first ACMPAs was succeeded by a rectangular one, that can provide, for the same aperture area, a more intense coupling. For example, slot shaped apertures as those depicted in *Fig. 2.10* can multiply by a factor of 10 the coupling level provided by a circular aperture of the same area [63].

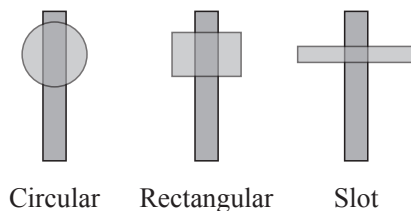


Figure 2.10. Basic aperture shapes.

This coupling improvement can be used to enable, for a given coupling level, the reduction of the aperture size. In turn, this size reduction can contribute to:

- expand the ACMPA functionality, since there would be more area available for additional slots, that could be required, for example, for an antenna with dual polarization,

- reduce the undesired radiation from the aperture, with the consequent improvements in terms of Front-to-Back Ratio (FBR)¹⁰ and radiation efficiency of the ACPMA.
- Alternatively, in the case of a S3FIP, whose FBR is ideally infinite, the use of a smaller slot can help to mitigate the excitation of PPWMs.

In the search of an optimal shape for the aperture, additional modifications on the slot shape have been proposed, leading to further improvements in terms of aperture coupling and size. These improvements are associated to the attainment of a more uniform field distribution over the aperture. Some examples of these improved shapes are given in *Fig. 2.11*.

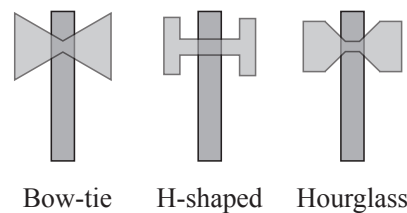


Figure 2.11. Improved aperture shapes.

In fact, the *H-shaped* aperture, also known as *dog-bone*, can provide more than twice the coupling of a slot with the same length, a little bit more coupling than the *Bow tie*, but somewhat less than the *Hourglass*. In practice, for the same coupling level, the use of these structures can lead to a length reduction of up to 30% with regard to the plain slot [63,64].

Examples of antennas that can profit of this slot reduction are those with multi-band, multi-polarization capabilities [65,66], [13, Cap. 6] or broad-band ACMPAs with thick patch substrates. These latter would otherwise require very wide slots -almost resonating- to guarantee a proper coupling level with the patch, with the consequent worsening of the FBR [54], [13, Cap. 3].

It is also worth to note that when the feeding line, the aperture and the patch are centered with regard to each other, their coupling is maximized and the symmetry of the resulting structure is compatible with high levels of polarization purity and radiation pattern symmetry [12,63,67].

c) The Feeding Line

The feeding line of an ACMPA is a microstrip line whose ground plane has an aperture through which the line interacts with the radiating part of the antenna.

¹⁰The FBR is a radiation parameter that quantifies the unidirectionality of an antenna and is expressed as the ratio between the field levels of its main lobe and its back lobe.

In practice, such line stretches a certain distance (L_s) beyond the aperture to end as an open circuit stub, as displayed in *Fig. 2.12(a)*. The stub introduces a tuning parameter that is very useful to achieve a good impedance matching of the ACMPA, but it has certain limitations (basically, it can only compensate the reactive term of the ACMPA input impedance).

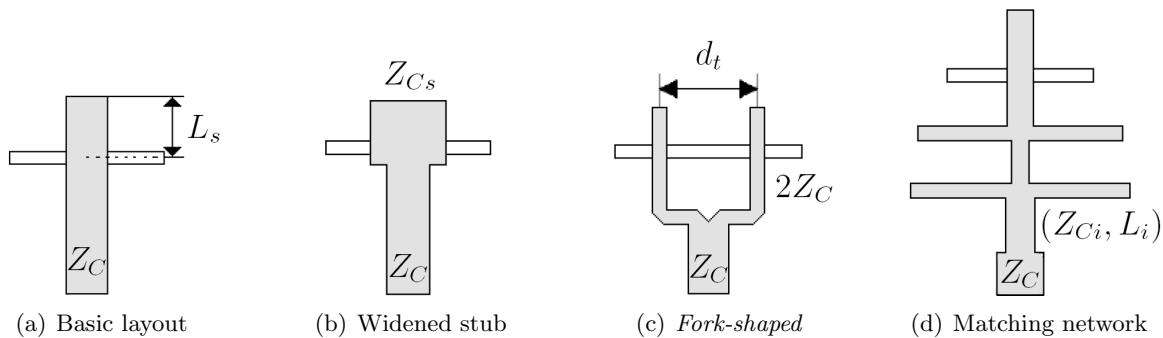


Figure 2.12. The feeding line

In order to match the ACMPA over a wider bandwidth, several variations of the basic layout of the feeding line have been proposed. These variations, essentially, introduce additional tuning parameters. In the case, for example, of the *Fork-shaped* access line, an increase in the tine spacing (d_t) can enhance, through a proper reduction of the coupling between the feeding line and the patch, the matching of the antenna [54].

Another possible option consists in the incorporation of an impedance matching network between the access line and the slot, as proposed in [68] and illustrated in *Fig. 2.12(d)*. Though very powerful, this technique may imply a considerable consumption of printed circuit area as well as an increase of the feeding insertion loss.

2.4.3 Parametric Study

The goal of this section is to complete and make more explicit the design guidelines given up to now. With this purpose, the analysis of a representative antenna, the so-called *Reference Antenna*, is carried out. This particularization should not prevent, however, this analysis to highlight the main qualitative relations between the constitutive parameters of an arbitrary ACMPA¹¹ and its functionality.

This parametric analysis is based on the theoretical modeling of the *reference antenna* at different levels. In fact, explicit and simplified theoretical models are combined with use of more accurate, and more computationally expensive, modeling tools, such as the so-called ‘*Full Wave*’ software tools. These advanced modeling tools use numerical techniques for an efficient solution of the Maxwell’s Equations in stratified media [14, 54, 67, 69].¹²

¹¹Regardless, for example, of whether its feeding line is shielded or not.

¹²The ‘*Full Wave*’ software tool used in the present parametric study is *Ansoft EnsembleTM*, a commercial package that is particularly well-suited for the electromagnetic analysis of the 2.5 D geometries considered here.

a) The Reference Antenna

The present parametric study is inspired by the work of Mr. P. L. Sullivan in [67] and the ACMPA proposed in that work is taken again as the *reference antenna*. This ACMPA is described in *Fig. 2.13* and it has already been used as a touchstone for many methods of EM analysis [48,67,69], which endorses the validity of the guidelines to be derived next.

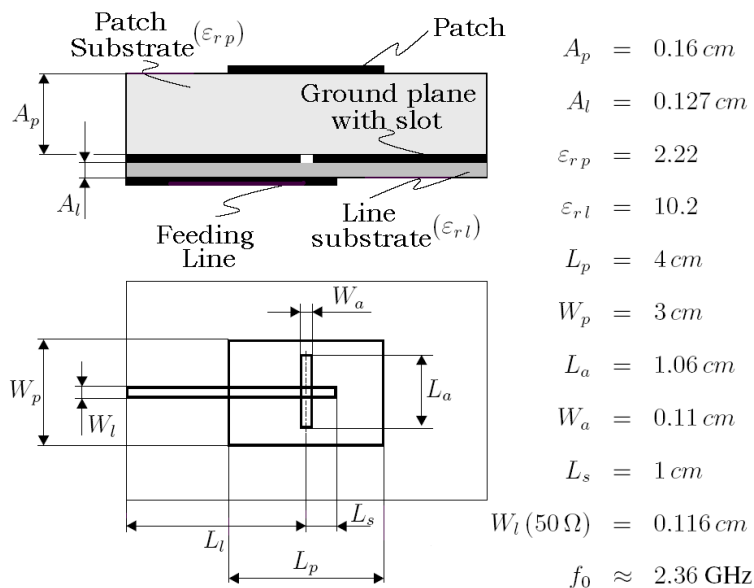


Figure 2.13. The Reference Antenna.

b) Functional Characteristics under study

From the operational point of view, one of the most important limitations of microstrip antennas is their reduced bandwidth. This limitation, that is related to the resonant nature of the antenna structure as well as to the reduced volume occupied by it, is usually given by the antenna input impedance.¹³ Moreover, the input impedance of patch antennas shows a considerable sensitivity to the variation of most of the constitutive parameters of the RE [12, 28, 68].

As a result, one of the main design goals is the improvement of the input impedance bandwidth and the impedance matching levels. This improvement should exceed the minimum limits imposed by the requirements widely enough for the resulting antenna to keep, despite the tolerances associated to its construction (i.e. materials and processes), a satisfying operation within the frequency band of interest [13]. The remaining functional characteristics, most of them related to the far field properties of the antenna and whose variation with frequency is generally smoother, are typically evaluated and adjusted in a subsequent design iterations.

¹³If the patch is assumed to be operating in a single-mode regime.

Within this design approach, the present study is going to focus on the input impedance of the radiating element. This impedance, or equivalently, this reflection coefficient¹⁴ is a near field characteristic that, besides the bandwidth and the matching, provides very important information about the resonance frequency and the coupling between the line and the patch of the ACMPA.

Fig. 2.13 shows two convenient representations of the reflection coefficient. The first one, displayed in *Fig. 2.14(a)*, can be used to give a clear vision of the impedance matching level within the frequency band of interest and, under certain conditions, also of the resonance frequency. And the second representation, visible *Fig. 2.14(b)*, provides both magnitude and phase information, offering a broader perspective of the evolution in frequency of both the input impedance and the reflection coefficient.

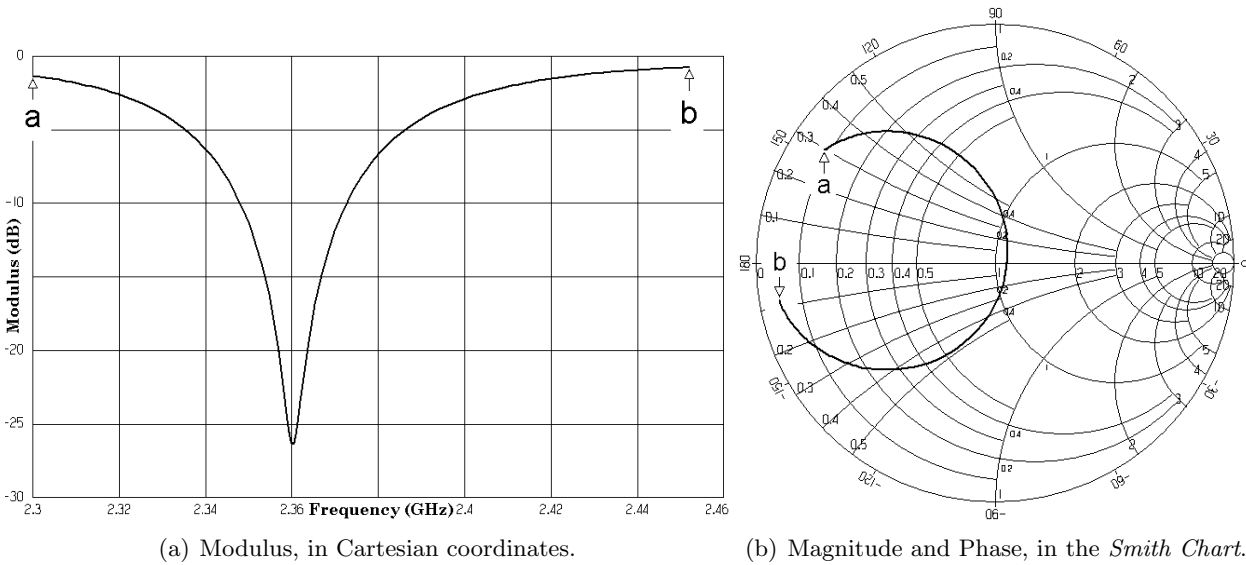


Figure 2.14. Reflection coefficient at the input of the Reference Antenna, as depicted in *Fig. 2.13*. By default, the reference impedance equals the characteristic impedance of the feeding line ($Z_0 = Z_c = 50 \Omega$) and the reference plane of the reflection coefficient is shifted along this line up to the slot center (a shift of L_l in *Fig. 2.13*).

In fact, the loops that the input impedance of this class of antennas trace in the *Smith Chart* can provide information about:

- **the frequency and the resistance of resonance**, f_0 and R_0 respectively, that satisfy the relation

$$\text{if } f = f_0 \Rightarrow \left\{ \begin{array}{l} \text{Real}(Z_{in}) = R_0 \\ \text{Imag}(Z_{in}) = 0 \end{array} \right\} \Rightarrow Z_{in} = R_0$$

and are given by the intersection between the impedance loop and the real axis of the Smith Chart [48, 69].¹⁵

¹⁴Given a reference impedance (Z_0), the relation between impedance (Z) and reflection coefficient (Γ) is: $\Gamma = \frac{Z - Z_0}{Z + Z_0}$.

¹⁵In [11, Fig. 12] an alternative definition for the resonance frequency is given: the frequency at which the real part of the impedance reaches its maximum.

When the loop is centered in the *Smith Chart* real axis, as it is the case -approximately- for the reference antenna, the resonance frequency coincides with the frequency at which the modulus of the reflection coefficient is minimum [67]. This coincidence allows to easily determine the resonance frequency using plots as the one given in *Fig. 2.14(a)*.

- **The resonance type.** In the vicinity of the ACMPA resonance frequency, the equivalent circuit that results from the shunt connection of the slot, of small electrical size, and the patch behaves as a shunt resonant circuit,¹⁶ whose frequency response corresponds to that plotted in *Fig. 2.14(b)*.

This behavior, however, begins to change as the slot grows and approaches its resonance size ($\lambda/2$). This is, for example, what happens when, in order to improve the bandwidth of an ACMPA, the thickness of the patch substrate and the slot length are increased. In this case, the coupling between the resonance of the slot and that of the patch may result in a considerable reduction of the radius of the impedance loop around the center of the Smith Chart. Typically, this small impedance loop would be part of a wider arc with a certain series behavior -see [54, Fig. 2(a)] as well as *Fig. 2.29(f)*, *Fig. 2.29(l)* and *Fig. 2.29(r)*.

- **The impedance bandwidth**, that is defined as the frequency range, around the resonance frequency, in which the distance between the impedance loop and the center of the Smith Chart keeps below the maximum level allowed for the reflection coefficient (S_{max}).

This is why designs with improved impedance bandwidth often present impedance loops that tend to match circles whose center is close to the center of the Smith Chart and that have a radius bounded by S_{max} .

For microstrip antennas, that are typically narrow band, the bandwidth is usually expressed in relative terms, in such a way that if f_1 and f_2 are, respectively, the lower and the upper extremes of the frequency band, the percentage bandwidth is given by:

$$\text{Bandwidth (\%)} = 100 \frac{f_2 - f_1}{(f_2 + f_1)/2}. \quad (2.1)$$

- **The intensity of the coupling**, through the slot, between the patch and the feeding line, also known as *coupling factor*, increases with the radius of the impedance loop and the value of the resonance resistance [67].

There is, hence, a compromise between the level of matching that can be achieved within a frequency band and the coupling mechanism between the line and the patch of the ACMPA. This compromise can be illustrated with regard to both the radiating and feeding part of an ACMPA as follows:

- On the one hand, as the thickness of the patch substrate is increased to improve the bandwidth, and despite the growth of the slot, the patch-slot coupling mechanism begins

¹⁶In fact, according to [12, 70], the equivalent circuit of the slot is a *shunt RLC*, whose dominant component below the slot resonance frequency is inductive. On the other hand, the equivalent circuit of the patch excited by an equivalent magnetic current is a *series RLC*. If, instead, the patch were excited by an electric current (i.e. edge fed or proximity coupling in *Fig. 2.3*), the patch would be more accurately modeled as a *shunt RLC* circuit.

to diminish and the radius of the impedance loop is reduced. Besides, as the length of the slot increases, and approaches its resonant size, it begins to become an efficient radiator. This may entail, for example, a worsening of the ACMPA FBR, as highlighted by the first two antennas in *Table 2.1*.

	Bandwidth*	FBR within the band
Reference Antenna	0.6%	> 21 dB
Thick patch substrate and near-resonating slot [54]	21%	> 12 dB
<i>Stacked Patches</i> [54]	20%	> 18 dB

* $S_{max.} = -14$ dB

Table 2.1. Bandwidth and FBR comparison for three exemplary ACMPA.

- On the other hand, as discussed in *Section 2.4.1*, the shielding of the transmission line that feeds an ACMPA may lead to a considerable reduction of the coupling between the line and the slot. This coupling reduction is evidenced not only by a decrease in the radiation efficiency of the antenna, but also by a narrowing of its impedance loop and its shift towards the left of the Smith Chart. In this case, the introduction of shorting pins around the slot to mitigate the excitation of PPWMs within the triplate structure may lead to strong fluctuations in the reactive part of the antenna input impedance as well as to a widening of the impedance loop. This widening corresponds, typically, to a restoration of the coupling between the feeding line and the slot.

It is also worth to note that, as illustrated in *Table 2.1*, the *Stacked Patches* technique can constitute a promising alternative to reach an equilibrium between bandwidth and FBR, since the slot does not need to be coupled to such a distant patch and the role of secondary resonator is assumed by a parasitic patch.

c) Constitutive Parameters under study

Next, the focus is on the study of how the variation of certain constitutive parameters of the reference antenna affects its input impedance. Unless otherwise stated, this variation is restricted to a single parameter at a time, while the values of the remaining parameters are kept equal to those specified in *Fig. 2.13*.

c.1) The Patch

The **patch length** is one of the parameters to which the resonance frequency of the ACMPA (f_0) is most sensitive. In fact, from the condition of lengthwise resonance in the cavity defined below the patch, the relation between f_0 and the effective length of the patch ($L_{p\text{ effective}}$) can be stated as:

$$f_0 = f / L_{p\text{ effective}} = \frac{\lambda_{\text{patch}}}{2},$$

where λ_{patch} represents the wavelength of the electric field resonating within the patch cavity.

If the patch is modeled as a stretch of microstrip line with length L_p , width W_p and its two extremes (the radiating edges) in open circuit, this resonance condition can be rewritten more explicitly as:

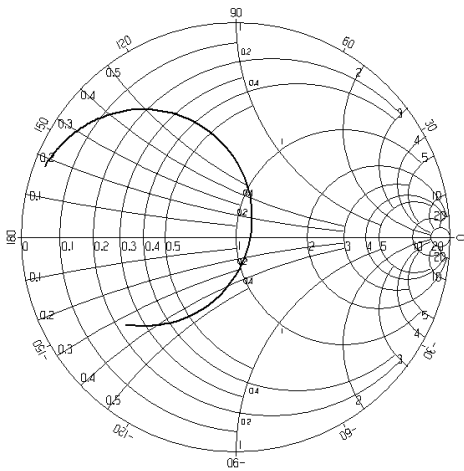
$$\begin{aligned} f_0 = f / L_{p\text{ effective}} = L_p + 2\Delta L_p &= \frac{\lambda_g}{2} \\ \Downarrow \\ f_0 &= \frac{c_0}{2(L_p + 2\Delta L_p)\sqrt{\epsilon_{\text{eff}}}} \end{aligned} \quad (2.2)$$

where

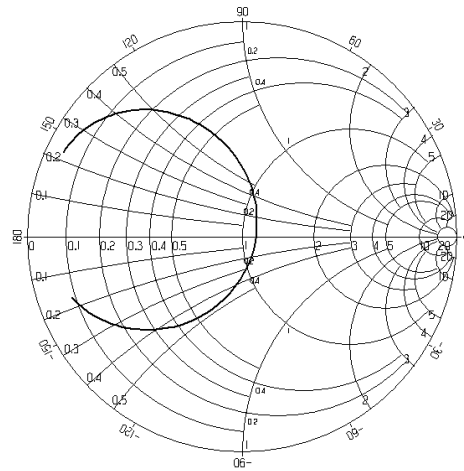
- ΔL_p : is the equivalent length extension of the open circuit microstrip line to take into account the effect of the fringing fields,
- λ_g : represents the guided wavelength in the microstrip line and
- ϵ_{eff} : is the effective dielectric permittivity,
according to the definitions given in [39, 71].

As it can be observed in *Fig. 2.15* and *Fig. 2.16*, the inverse relation between the resonance frequency and the patch length predicted by (2.2) is confirmed by the ‘*Full Wave*’ modeling of the ACMPA.

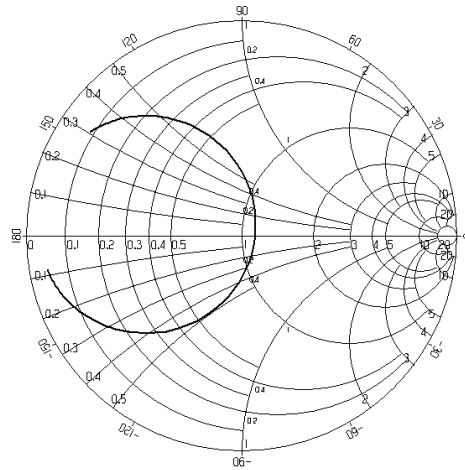
For his part, the **patch width** affects, basically, the *coupling factor*, while the resonance frequency stays almost constant. *Fig. 2.17* illustrates how the *coupling factor* increases as the non-radiating edges of the patch approach the extremes of the slot.



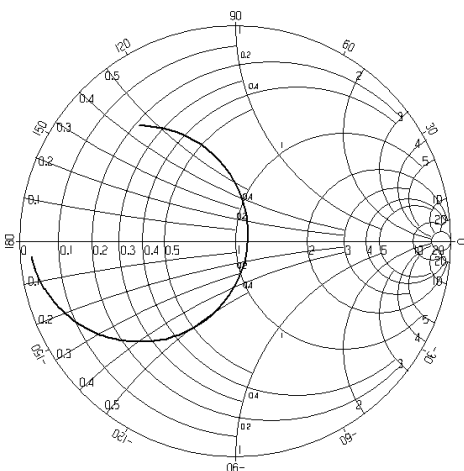
(a) $L_p = 3.9$ cm and $f_0 = 2.416$ GHz.



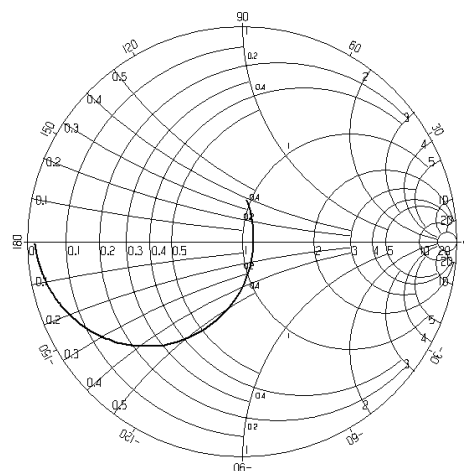
(b) $L_p = 3.95$ cm and $f_0 = 2.387$ GHz.



(c) $L_p = 4$ cm and $f_0 = 2.359$ GHz.



(d) $L_p = 4.05$ cm and $f_0 = 2.335$ GHz.



(e) $L_p = 4.1$ cm and $f_0 = 2.306$ GHz.

Figure 2.15. ACMPA input impedance for different patch lengths.

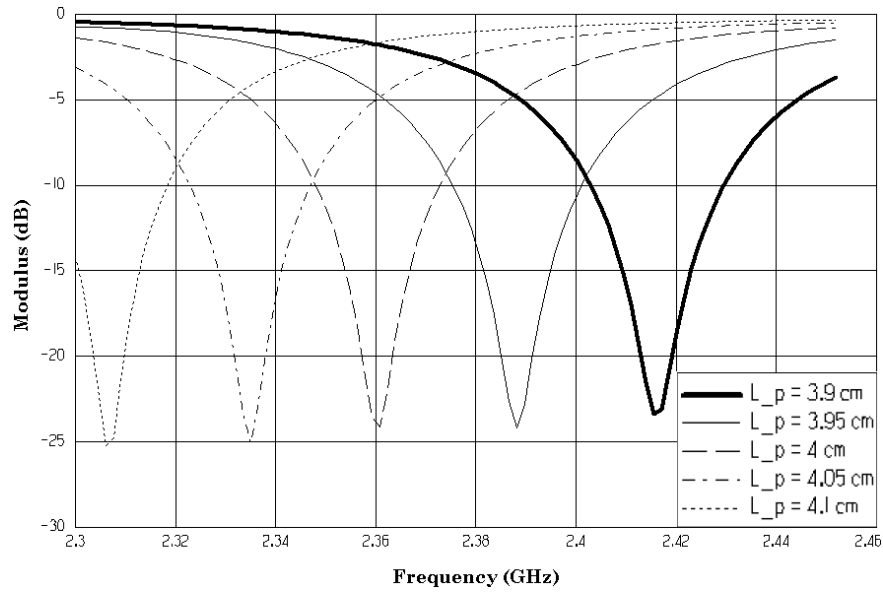


Figure 2.16. Impedance matching of the ACMPA for different patch lengths.

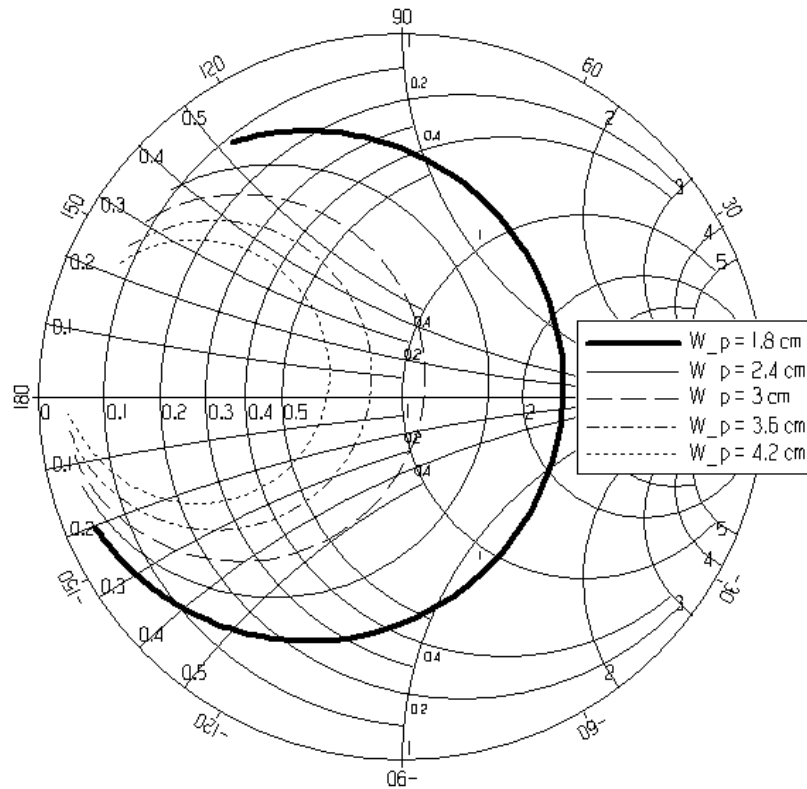


Figure 2.17. ACMPA input impedance for different patch widths.

c.2) The Patch Substrate

In an analogous way to the patch length, the variation of the patch substrate **permittivity** (ϵ_{rp}) has a noticeable impact on the resonance frequency of the antenna. The inverse relation between f_0 and ϵ_{rp} is made clear in (2.2)¹⁷ and *Fig. 2.18*. In other words, the reduction of the

¹⁷Recall that $\epsilon_{\text{eff}} = f(\epsilon_{rp})$.

resonance frequency is related to the increase of the electrical length of the patch as the permittivity of the substrate increases.

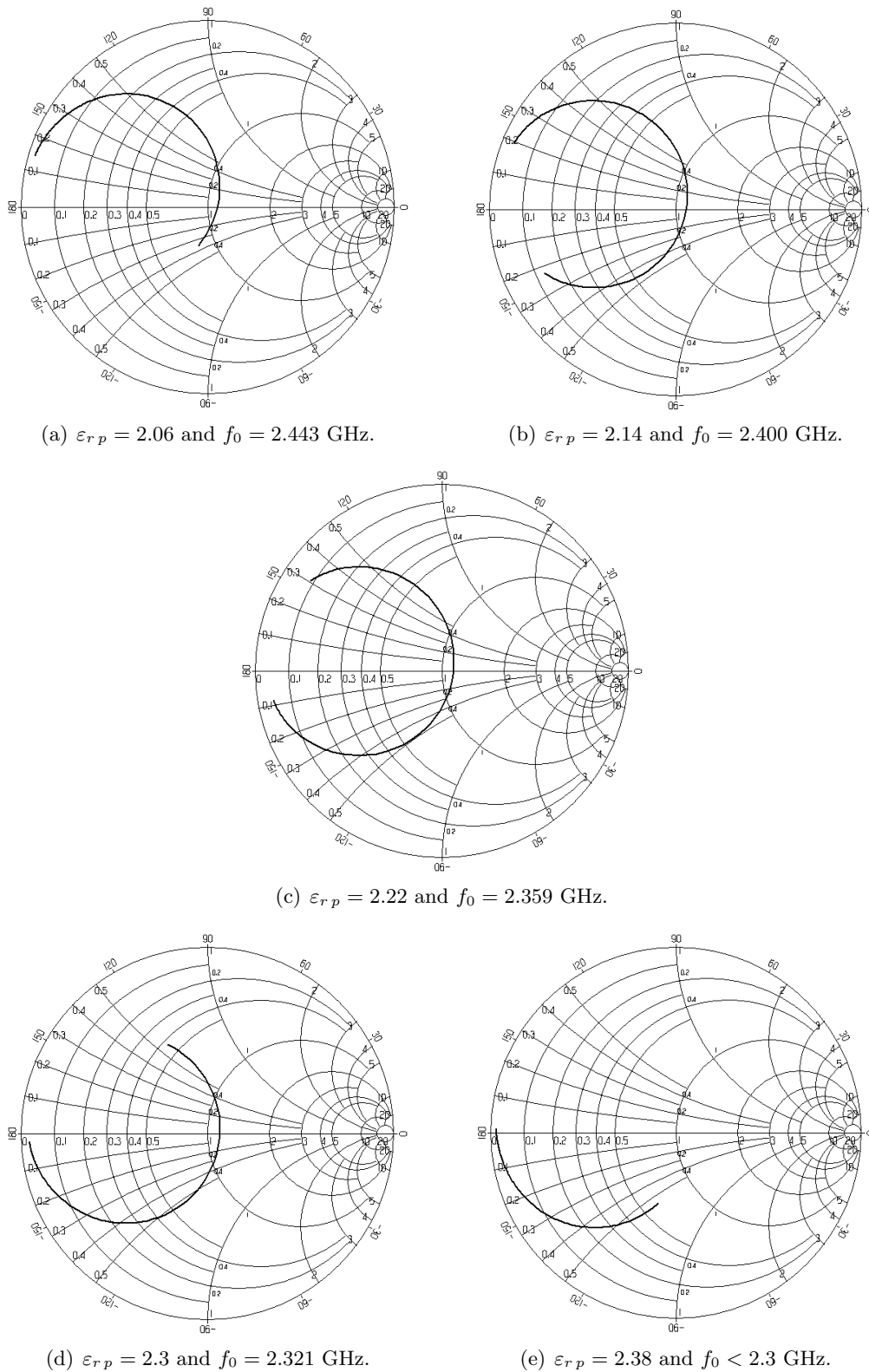


Figure 2.18. ACMPA input impedance for different patch substrate permittivities.

The **thickness** of the patch substrate (A_p) also affects, though in a much slighter fashion, its electrical length. The increase of the coupling factor as the patch and the slot come closer is actually much more significant than the variation of the resonance frequency, as evidenced by *Fig. 2.19*.

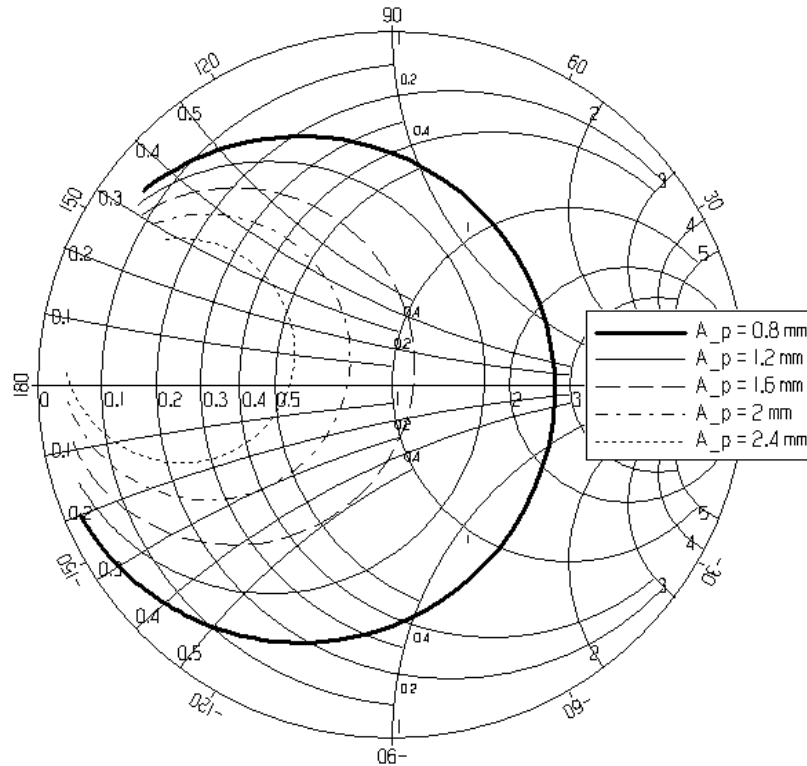


Figure 2.19. ACMPA input impedance for different patch substrate thicknesses (A_p).

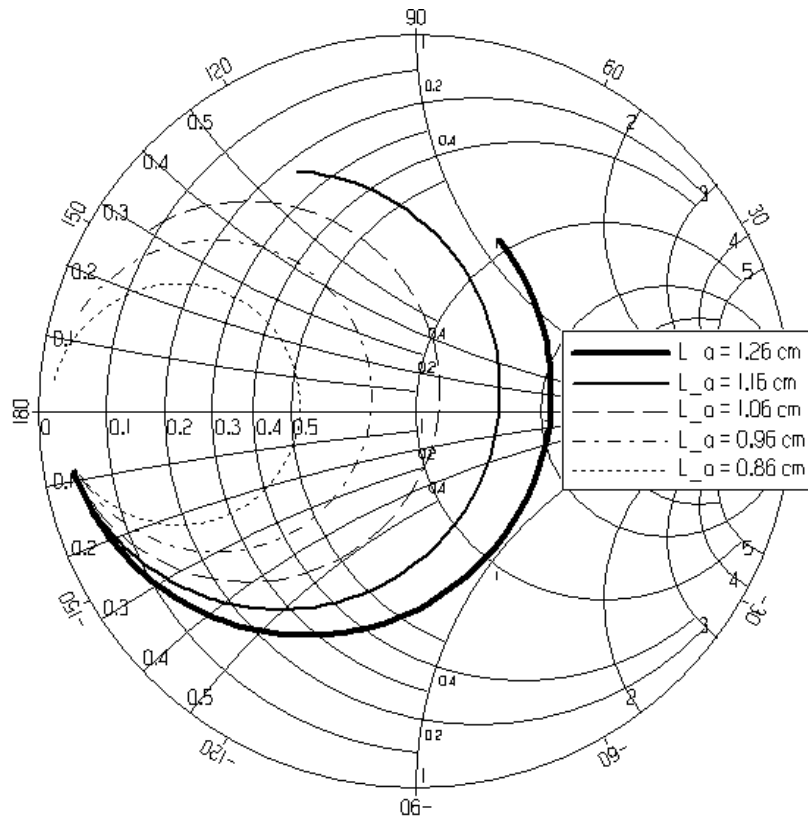
c.3) The Slot

Fig. 2.20 highlights that the effect of an increase of the **slot length** is a strengthening of the coupling factor and the reduction of the ACMPA resonance frequency.¹⁸ This parameter is found to be, after the patch length and its substrate permittivity, one of the parameters with the highest impact on f_0 .

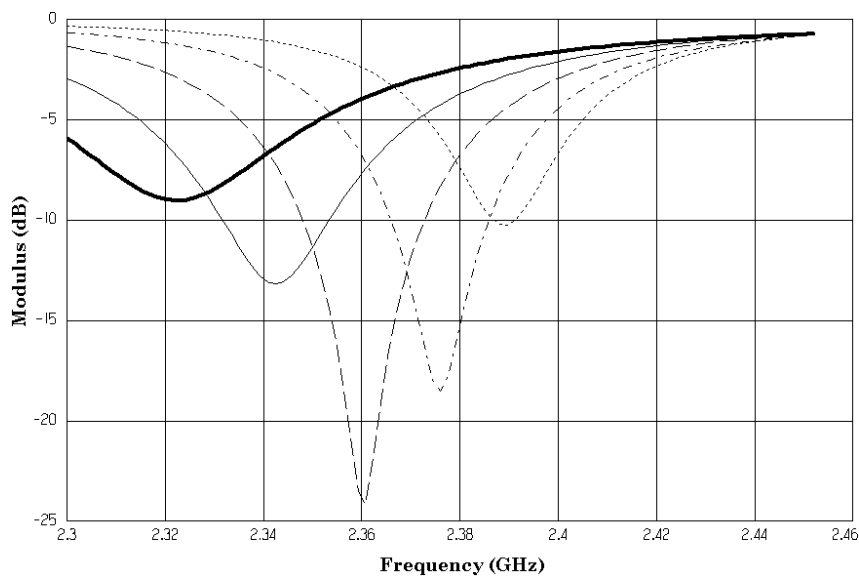
According to *Section 2.4.2*, the use of a *H-shaped* slot may be advantageous. Therefore, this shape is included in the present study by adding a couple of stubs of length L_d to the slot of the reference antenna, as shown in *Fig. 2.21(b)*.

Fig. 2.21 illustrates the functional equivalence existing between the length of the original slot and that of the stubs in the *H-shaped* slot. In both cases, the increase of these lengths leads to a higher coupling factor and a lower resonance frequency.

¹⁸The slot width has a similar effect, though weaker, on the coupling factor.



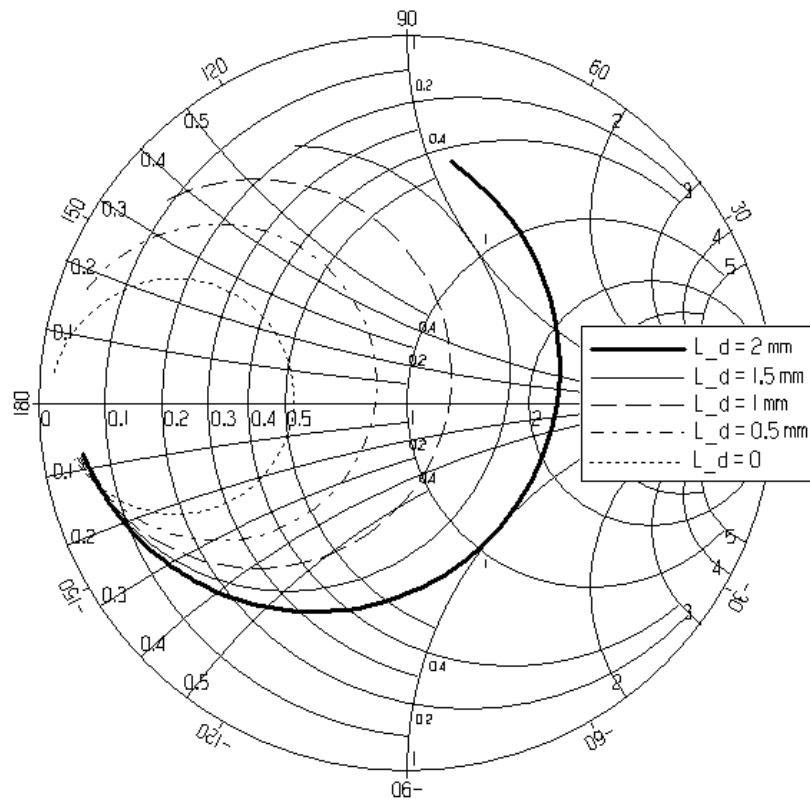
(a) Input impedance.



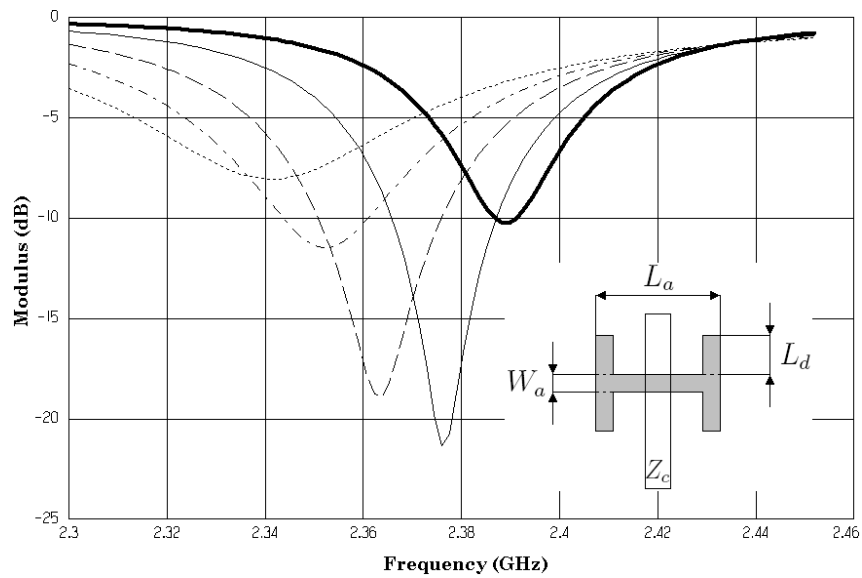
(b) Impedance matching.

Figure 2.20. Effect of the slot length.

At this point it is worth recalling that all the mechanisms presented here, that govern the coupling factor / input impedance of an ACMPA, also hold for shielded SSFIPs. These principles can, in fact, be very useful to address the strong coupling fluctuations associated to the shielding of the S3FIP access line.



(a) Input Impedance in the Smith Chart.



(b) Reflection Coefficient in Cartesian coordinates.

Figure 2.21. Effect of the stub length (L_d) in a H -shaped slot. In this case the reference antenna is that of Fig. 2.20(a) with the shortest slot ($L_a = 0.86$ cm and $L_d = 0$).

c.4) The Feeding Line

From the model in *Fig. 2.22*, it becomes clear that, after the shift of the impedance reference plane up to the center of the slot, the input impedance of the ACMPA can be written as:

$$Z_{in} = Z_{\text{Two-Port Slot + Patch}} - jZ_c \cot(\beta L_s \text{ effective}) \quad (2.3)$$

where

$$L_s \text{ effective} = L_s + \Delta L_s \quad \text{and}$$

ΔL_s : the equivalent length extension of the open circuit microstrip line to take into account the effect of the fringing fields, according to the definitions in [39, 71].

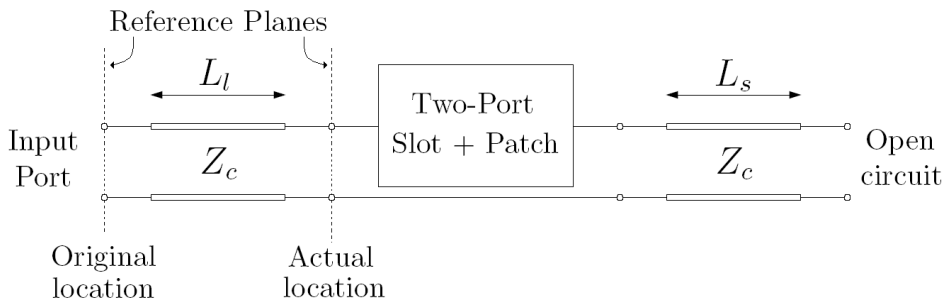


Figure 2.22. Equivalent circuit of the ACMPA feeding line, from [48].

As predicted by (2.3), the Smith Chart in *Fig. 2.23* illustrates how a variation of the **length of the open stub** leads, basically, to a displacement of the ACMPA impedance loop along the circles of impedance with constant real part. This displacement corresponds, actually, to a variation of the reactive component of the input impedance.

In order to evaluate the response of the input impedance to the variation of the **feeding line width**, this variation has been isolated -as far as possible- from the side-effects of the change in the open stub reactance and the feeding line characteristic impedance. The process followed to attain this goal is summarized next:

- i) according to *Fig. 2.24*, several models of the reference antenna with different feeding line widths and with ports in the two extremes of each line are defined and simulated,
- ii) for each model, both reference planes are shifted along the access line to make them coincide in the center of the slot. In this way the responses of the different “Slot + Patch Two-Ports” are *de-embedded*.

- iii) The input impedances are then obtained by loading each two-port with the input impedance of an isolated open stub of the same length and width of the stub in the reference antenna, and
- iv) the different input impedances are represented in the same Smith Chart, normalized with regard to the same characteristic impedance (50Ω).

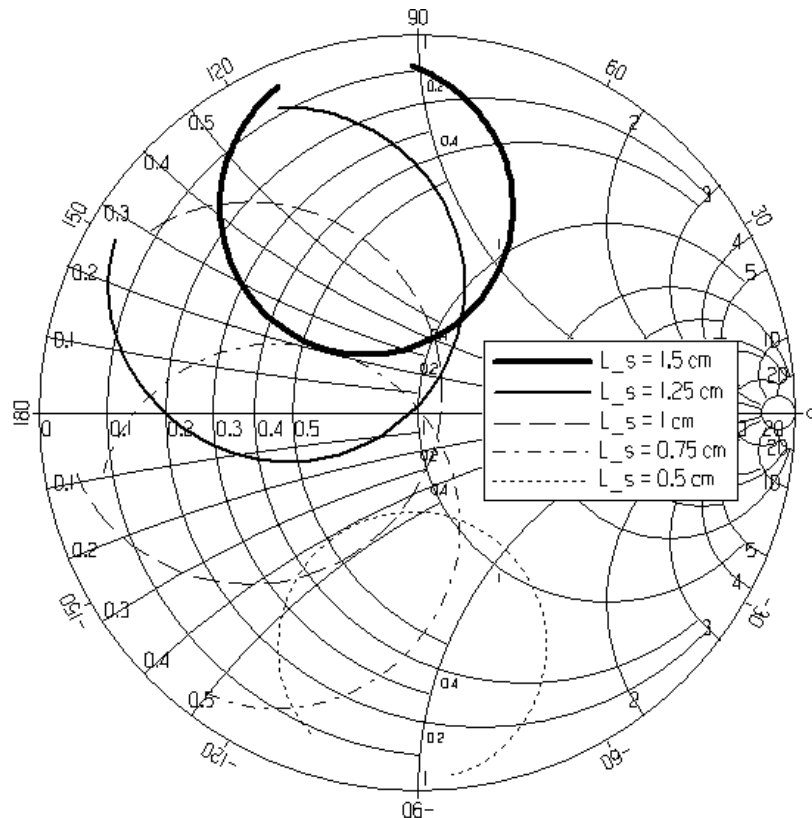


Figure 2.23. ACMPA input impedance for different lengths of the feeding line open stub.

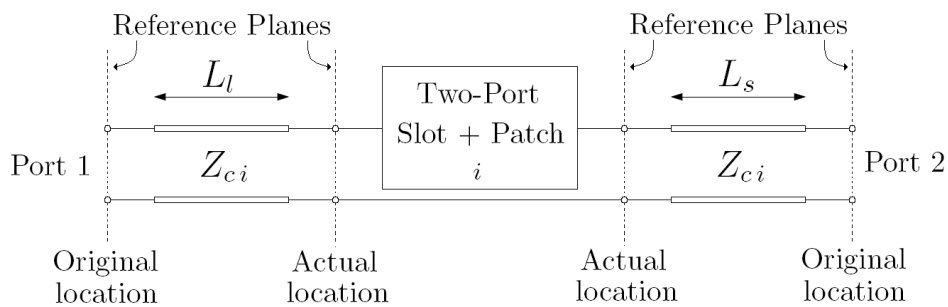


Figure 2.24. The feeding line as a two-port.

Fig. 2.25 gathers the results of this process and evidences the slight reduction of the coupling factor that follows an increase of the feeding line width, in agreement with the proposition in [54].

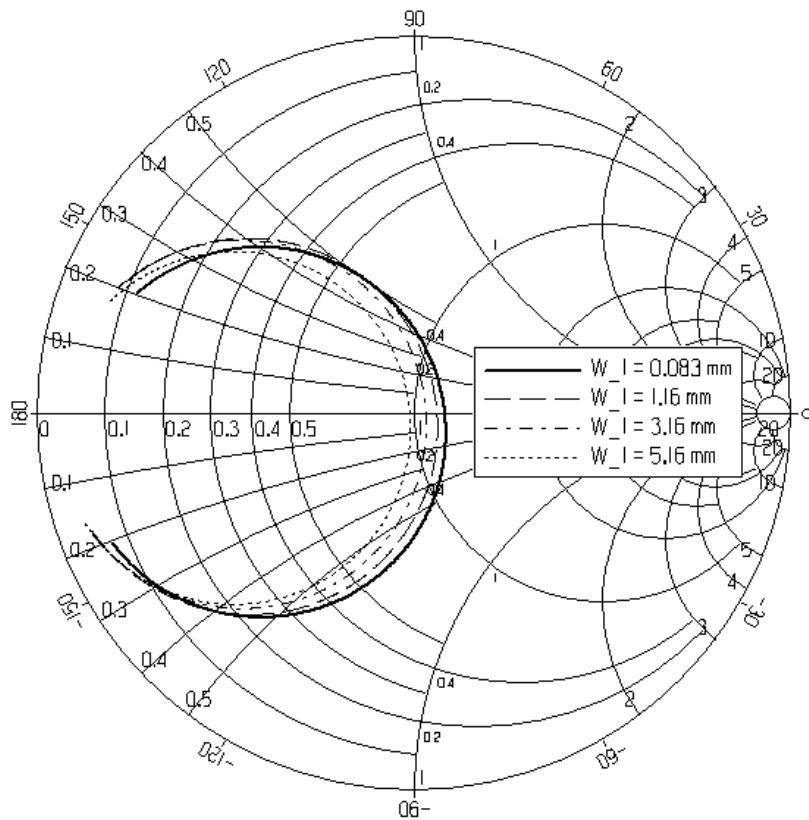


Figure 2.25. ACMPA input impedance for different widths of the feeding line.

Another modification of the feeding line that can provide a higher control of the coupling factor, also suggested in [54], consists in the simultaneous excitation of the slot from its two extremes with a couple of parallel strips that join the main access line of a *Fork-shaped* arrangement, as it is depicted in *Fig. 2.26*. There is, in fact, an inverse relation between the coupling factor and the **tine separation** (d_t), as illustrated in *Fig. 2.27*.

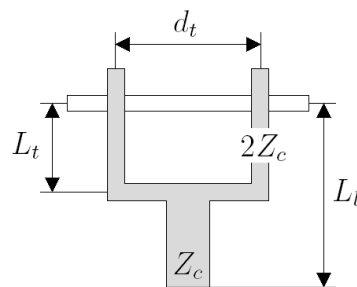


Figure 2.26. *Fork-shaped* feeding line.

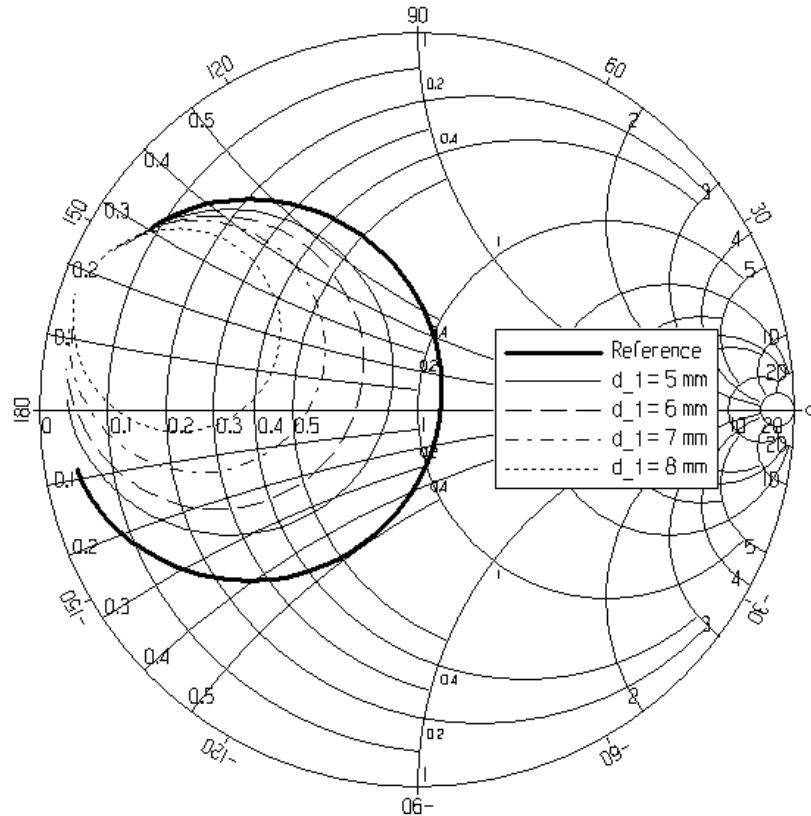


Figure 2.27. ACMPA input impedance for different tine separations. The physical length of the tine is kept constant ($L_t = 5$ mm), and the electrical length of the stub remains equal to that of the reference antenna. In analogy with the previous results, the reference plane is shifted a distance L_l through a (virtual) line whose characteristic impedance matches that of the main access line ($Z_c = 50 \Omega$).

c.5) The Feeding Line Substrate

The response to an increase of the feeding line **substrate permittivity** is a strengthening of the coupling factor, as it can be appreciated in *Fig. 2.28(a)*, and a reduction of the resonance frequency. This response can be attributed to the increase of the electrical length of the slot, since the results follow a similar trend, though much slighter, to that observed when the slot is physically elongated [67].

With regard to the feeding line **substrate thickness**, *Fig. 2.28(b)* highlights the way the coupling factor is weakened as the line and the slot are moved away from each other. On the other hand, the evolution of the imaginary part of the input impedance reveals a slight reduction of the resonance frequency as the substrate gets thicker.

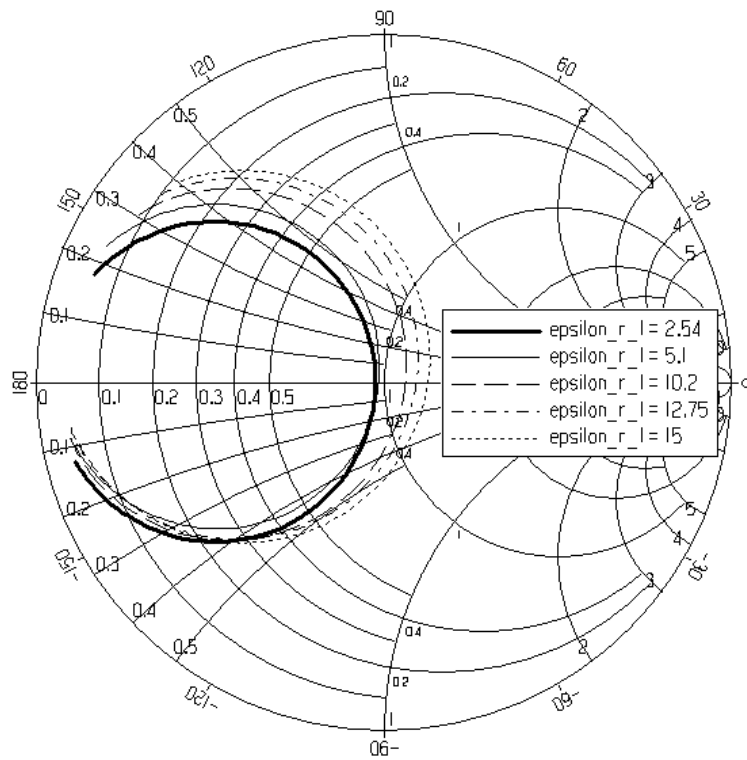
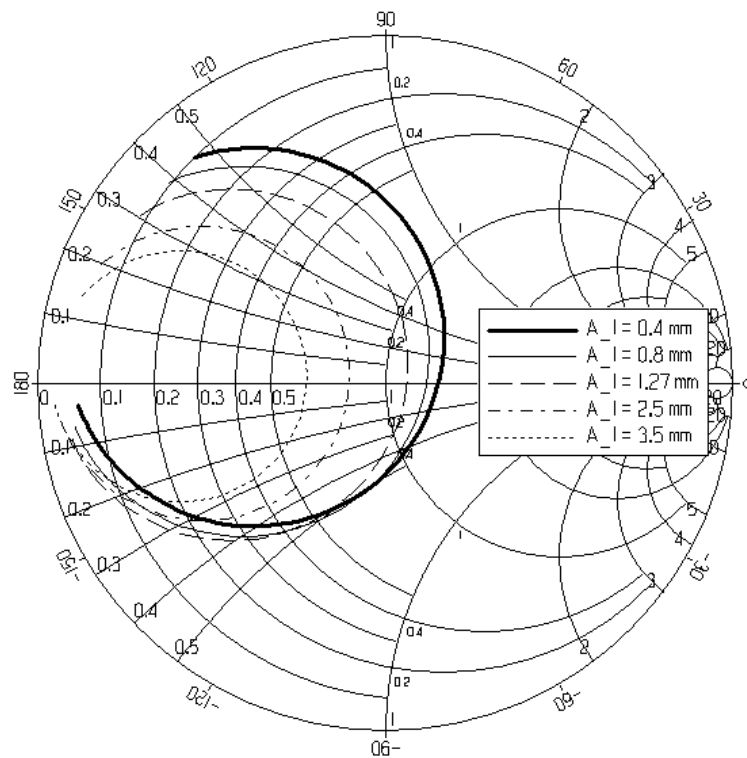
(a) Substrate permittivity (ϵ_{r_l}).(b) Substrate thickness (A_l).

Figure 2.28. ACMPA input impedance for different values of the feeding line substrate permittivity and thickness. The characteristic impedance of the different feeding lines and the electrical length of their stubs are kept equal to those of the reference antenna with the corresponding adjustments in the line width (W_l) and the stub length (L_s).

d) Application Example

A number of qualitative design relations have been deduced from the parametric study in the previous section. Next, the goal is to exemplify the way in which these relations can be used to mold, according to certain design requirements, the functionality of a given initial prototype.

Here, the initial prototype is the reference antenna depicted in *Fig. 2.13* and the design process focuses on the improvement of the impedance bandwidth of this antenna. The evolution of such design process, whose starting point is the performance curves displayed in *Fig. 2.14*, is illustrated throughout *Fig. 2.29*. For the sake of clarity, the development of this process has been expanded in three iterations, one for each column. The rationale behind this sequence is outlined in the paragraphs that follow.

According to the previous section, a bandwidth enlargement can be visualized over the Smith Chart as the combination of two transformations:

- a shift of the input impedance loop center towards the center of the Smith Chart and
- a reduction in the radius of the impedance loop.

These impedance transformations are actually the overall effect that the adjustment of the constitutive parameters of the RE is trying to reproduce.

The joint analysis of *Fig. 2.17*, *Fig. 2.19* and *Fig. 2.20(a)* reveals that there is a compromise between the two desired transformations, especially if only individual variations of the corresponding constitutive parameters are considered. This example shows how the effects of different parameters of the ACMPA can be combined to reproduce both transformations simultaneously.

From *Fig. 2.14(a)*, it is clear that the impedance loop center must be brought to the right of the Smith Chart. The main alternatives to do this imply an increase of the coupling factor. These alternatives are:

- the reduction of the patch substrate thickness, that is dismissed because it conflicts with the bandwidth broadening principle itself and with the promotion of the patch radiation mechanism,
- the reduction of the patch width, that would contribute to the reduction of the patch directivity due to the shortening of its radiation edges, and
- the elongation of the slot, that may imply an FBR degradation.

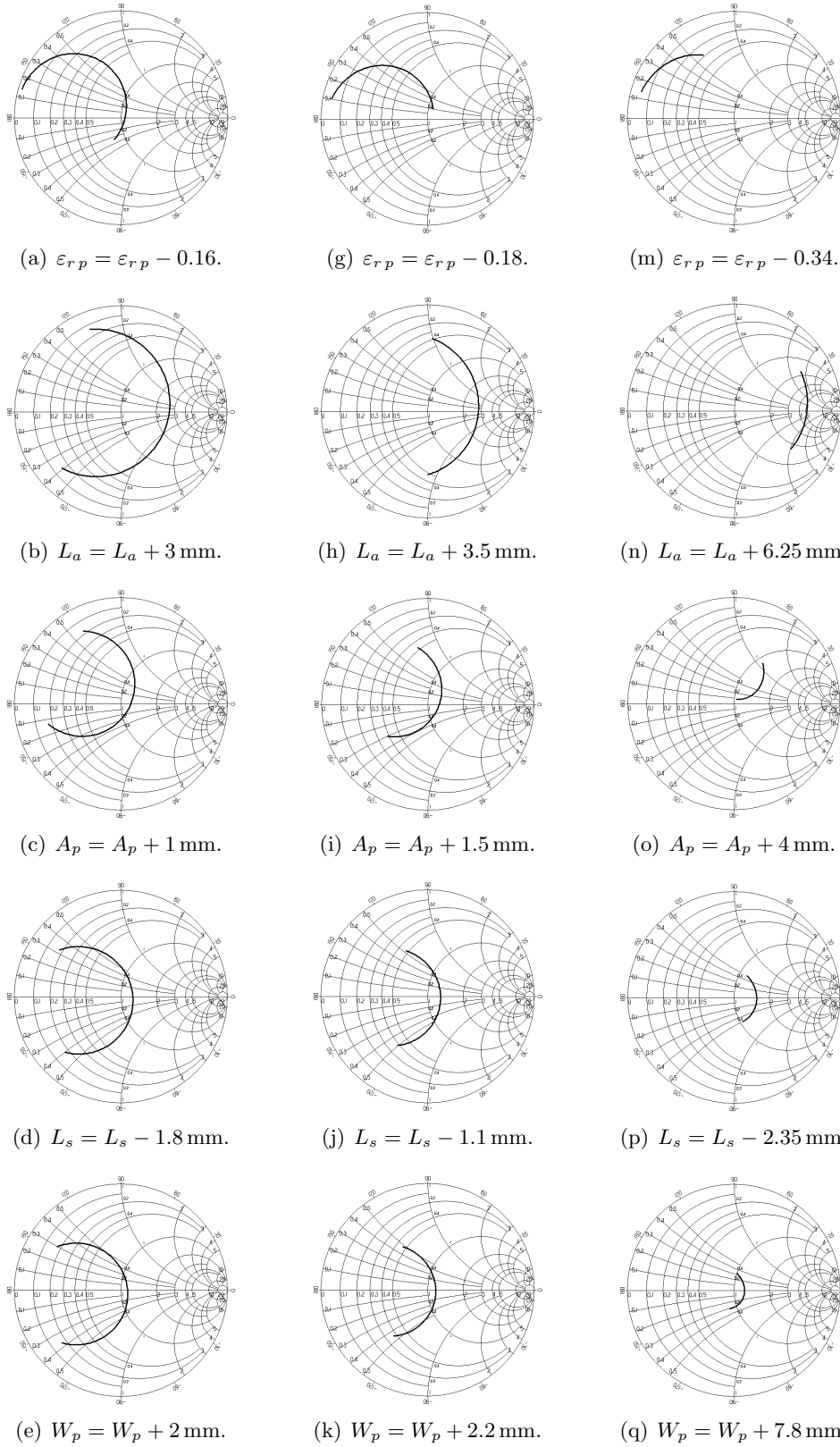
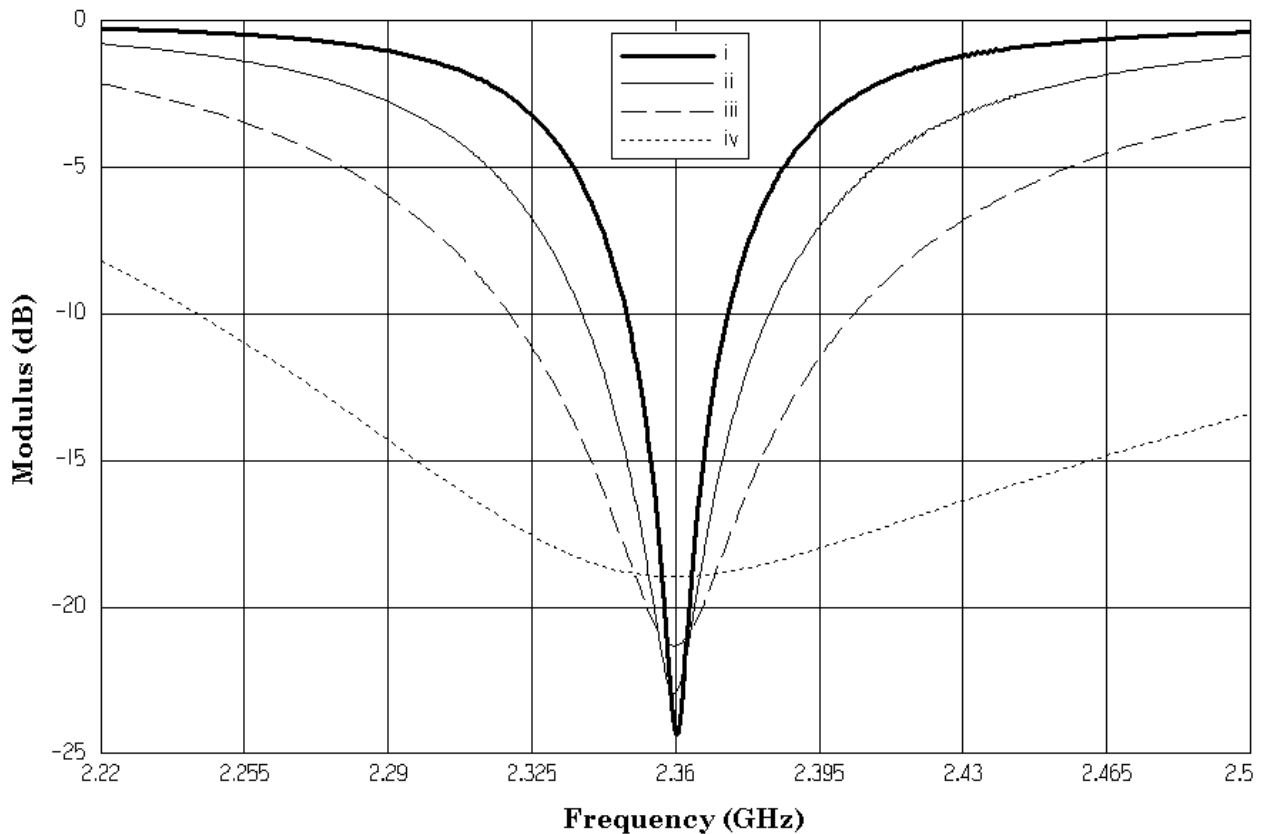
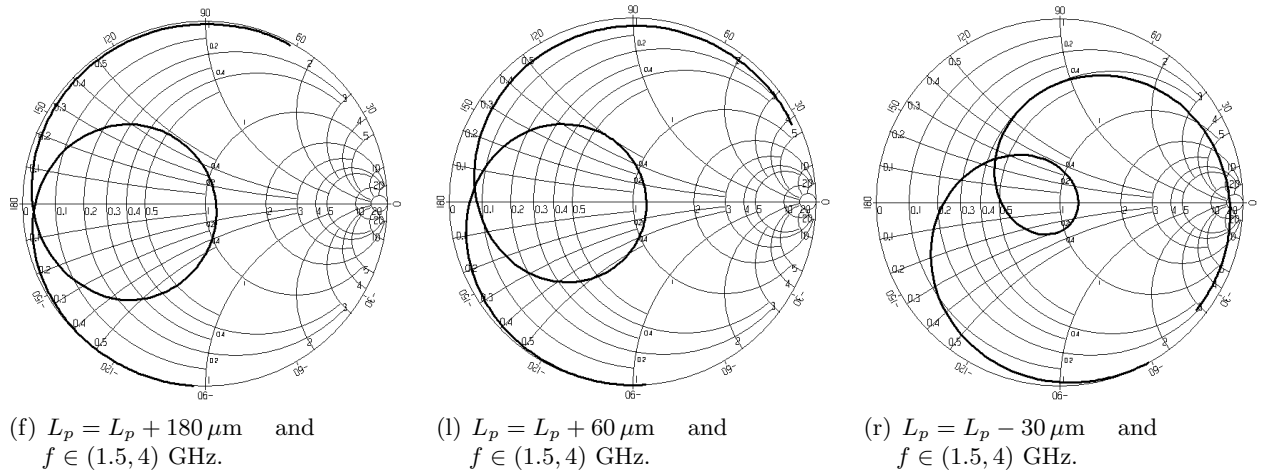


Figure 2.29. Reference antenna bandwidth improvement process, with $f \in (2.3, 2.452)$ GHz.



(s) Reference antenna impedance matching -i- together with those from Fig. 2.29(f) -ii-, Fig. 2.29(l) -iii- and Fig. 2.29(r) -iv-.

Figure 2.29. Reference antenna bandwidth improvement process (contd.)

From these two options, the slot elongation is preferred, since the coupling factor is more sensitive to the slot length than to the patch width and because in further design steps the plain long slot can be readily substituted with a smaller *H-shaped* one, with improved FBR characteristics.

In the present example, the drop in the resonance frequency that is expected to follow the elongation of the slot is prevented with an initial upwards shift of such frequency. With this aim, between the alternatives of reducing the patch length or the substrate permittivity, the latter, that favors the radiation mechanism, is privileged. The result of these actions can be observed in the plots within the two first rows of *Fig. 2.29*.

To reduce the radius of the impedance loop, the coupling factor is diminished compensated by means of an increase of the distance between the patch and the slot, as shown in *Fig. 2.29(c)*, *Fig. 2.29(i)* and *Fig. 2.29(o)*. The inductive component that arises with this action is compensated with a shortening of the feeding line stub, as it can be seen in *Fig. 2.29(d)*, *Fig. 2.29(j)* and *Fig. 2.29(p)*.

Before proceeding to the fine tuning of the resonance frequency by varying the patch length, the relative insensitivity of this frequency to the patch width is seized to perform further reduction of the coupling factor, as illustrated in *Fig. 2.29(e)*, *Fig. 2.29(k)* and *Fig. 2.29(q)*.

At this point it also becomes evident how the bandwidth broadening is also associated to a gradual reduction of the total length, over the Smith Chart, of the impedance loop within the targeted frequency span.

The progressive reduction of the impedance loop radius and its shift towards the center of the Smith Chart can be more clearly appreciated over a wider frequency span, as displayed in *Fig. 2.29(f)*, *Fig. 2.29(l)* and *Fig. 2.29(r)*. In the light of these last plots, it can be stated that this bandwidth broadening phenomena is the result of an intensified coupling between the resonances of the patch (the small loop, in the center) and that of the slot (the broad loop), as already proposed in *Section 2.4.3* and [54].

The outcome of this whole process is the enlargement of the input impedance bandwidth of the ACMPA, as summarized in *Fig. 2.29(s)*.

The increase of the antenna overall volume that underlies this bandwidth improvement is achieved, basically, by enlarging the distance between the patch and the slot, which had to be elongated accordingly. The price to pay with this approach is typically a rise of the radiation from the slot, that can lead to a reduction of the FBR of the radiating element, as shown in *Table 2.2*.

	Bandwidth*	FBR in the band	FBR(f_0)
Reference Antenna	1.1%	> 21 dB	21.8 dB
Antenna from <i>Fig. 2.29(f)</i>	1.9%	\geq 21 dB	21 dB
Antenna from <i>Fig. 2.29(l)</i>	3.4%	> 19 dB	19.8 dB
Antenna from <i>Fig. 2.29(r)</i>	13.8%	> 15 dB	17.4 dB

* $S_{max.} = -10$ dB

Table 2.2. Compromise between bandwidth and FBR.

2.5 Radiating Element with Dual Linear Polarization

By virtue of their common planar structure, the design of the Dual Linearly Polarized Radiating Element (DLPRE) is addressed in an analogous way as it was done in *Section 2.4* for its Single Linear Polarization counterpart (the so-called SLPRE).

In this way, the first design considerations, that concerns both the manufacturing & structural issues and the electrical operation of the microstrip antenna, are focusing on the RE buildup. Conversely, the tailoring and tuning of the metalization planes, as well as other parameters of the buildup not yet fixed, would be carried out giving priority to the electrical operation of the element, in the final steps of the design process described next.

2.5.1 Buildup

The design of the DLPRE is addressed just as an expansion of the functionality of the SLPRE. And, since both radiating elements are based on microstrip technology, all the considerations made throughout *Section 2.4.1* and *Section 2.4.2* with regard to the SLPRE structure and its electrical operation should remain essentially valid.

a) Feeding

The ports giving access to the RE are, in this case, two: one for each polarization state. However, the way these ports excite the microstrip patch can be, basically, the same proposed for the SLPRE ; namely : edge fed, coaxial, proximity and aperture coupling.

The considerations made before about each one of these excitation mechanisms remain valid, too. And the aperture coupling remains, therefore, as the most convenient excitation mechanism for the radiating element of the present application.

For example, to make an ACMPA with single linear polarization radiate also with the orthogonal polarization, it would suffice to add another couple feeding line & slot similar to that of the original antenna, but rotated by 90° with respect to it. In this way, two orthogonal modes simultaneously resonating lengthwise and widthwise within the cavity defined between the patch and the ground plane could be excited. For a rectangular patch on the XY plane, these modes would be the TM_{10} and TM_{01} ; while for a circular patch, the modes involved would be two orthogonally rotated versions of its fundamental mode, the TM_{11} .

The placement, within the buildup, of the new access line may give rise to different architectures for the radiating element. These architectures can be classified, essentially, into two groups, depending on whether the antenna access ports are contained or not in the same metalization plane.

a.1) Coplanar Feeding

The possibility of routing the new line on the same substrate layer where the line associated to the orthogonal polarization lies is structurally simple. This approach, however, may lead to a competition between the two lines feeding the radiating element.

This competition, on the one hand, results in the fact that both lines can no longer access the center of the cavity defined below the patch, which entails:

- a potential degradation of the coupling with the patch [12, 48, 67]
- and the need to take special steps in order to keep the symmetry of the radiating element excitation. This symmetry plays, in fact, a very important role in terms of polarization purity, port isolation and radiation pattern shape [12, 13, 63, 72].

Two important approaches to achieve this symmetry are based on particular arrangements of the slots below the patch. These approaches correspond to the centered *Double Cross* and the offset *T-shaped* slot configurations [13, Ch. 6], [66, 73], which are depicted in *Fig. 2.30*.

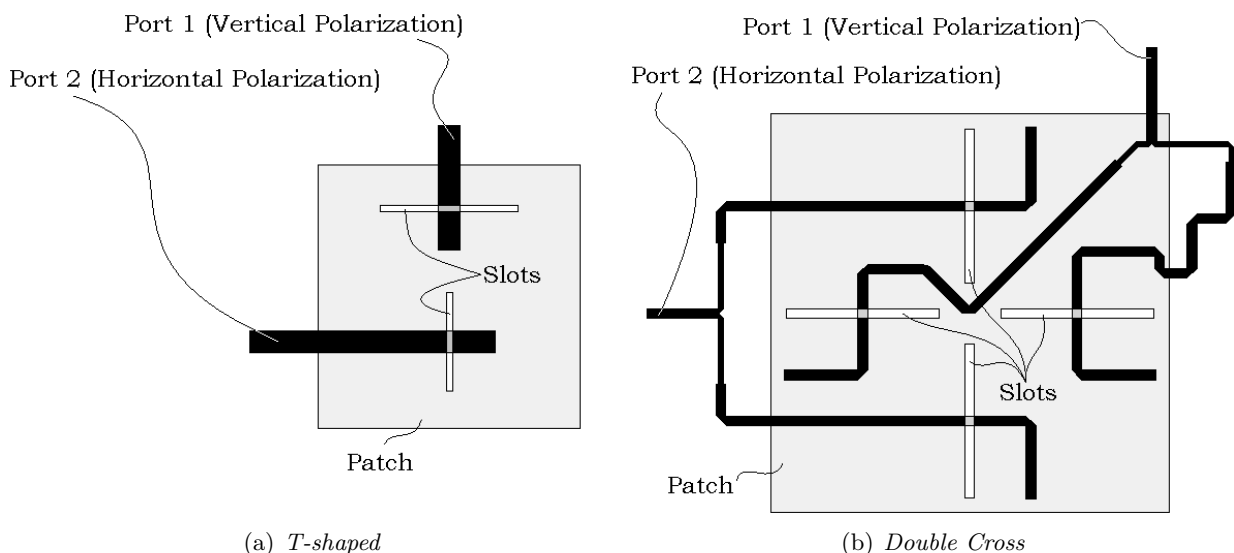


Figure 2.30. Layouts of two square Dual Linearly Polarized ACMPAs with different arrangements of the slots.

The good levels of port isolation that can be achieved with these two configurations, exemplified in *Table 2.3*, contrast with their potentially limited impedance bandwidth. This limit is related to the degradation of the coupling mechanism between the access lines and the

patch. The reduction of the overall slot length, typically required in these feeding schemes,¹⁹ contributes to this coupling degradation and makes difficult the broadening of the impedance bandwidth via an increase of the patch substrate [13,72].

	Port Isolation		Impedance Matching	
	S_{ij}	Bandwidth	S_{ii}	Bandwidth
<i>T-shaped</i> [73]	< -30 dB	> 20 %	≤ -10 dB	≈ 10 %
<i>Double Cross</i> [13]	< -20 dB	> 16.7 %	≤ -10 dB	≈ 6.5 %

Table 2.3. Performance of two Dual Linearly Polarized ACMPAs with symmetric excitation.

As shown in *Table 2.4*, this bandwidth limitation can be overcome, at the expense of an increased structural complexity, with the *stacked patches* technique, that does not require the use of large slots to excite the patches.

	Impedance Matching	
	S_{ii}	Bandwidth
<i>T-shaped</i> [66]	≤ -10 dB	> 20 %
<i>Double Cross</i> [13]	≤ -10 dB	≈ 19 %

Table 2.4. Bandwidth improvement using the *stacked patches* technique.

On the other hand, the line traces in this feeding architecture must share the surface available in their metalization plane, which, beyond a certain complexity in their routing, may compromise the integration of the radiating element in an array. This integration, with the corresponding limitation in PCB area per element and the consequent increase of the density of traces in the shared layer, may actually be prone to the emergence of undesired coupling between the different feeding lines. These undesired interactions may degrade the performance of the array antenna, especially with regard to the port isolation and the polarization purity.

In particular, for broadband arrays with dual linear polarization capabilities, whose beam-forming networks are typically incorporate to prevent the beam squint, this density of traces, which grows fast with the number of elements, can be prohibitively high.

¹⁹In these schemes, besides a significant increase of printed circuit area consumption, the price to pay for an improved bandwidth using bigger slots can be a degradation of the symmetry of the radiation pattern, among others [74].

a.2) Multilayer Feeding

The competition between the lines accessing the DLPRE can be circumvented if they are routed in different layers. This approach may enable important enhancements in terms of antenna performance and array integration, at the expense of a certain increase in the structural complexity of the multilayer structure.

There are several possible implementations of this multilayer feeding. Next, some of the implementations that could be compatible with the practical realization of the foreseen DLPRE are presented.

The implementation whose buildup is represented in *Fig. 2.31* is characterized by the fact that both feeding lines, printed in different metalization layers, are sharing the same side of a common ground plane. In this ground plane there is a cross slot through which the feeding lines can be coupled to the patch, in the opposite side of the common ground plane. The buildup also shows that both feeding lines can reach the center of their slot, which can be centered below the patch too. This centering of the different metalization layers is one of the advantages of the multilayer feeding, since the resulting structure clearly improves the symmetry of the *T-shaped* configuration and can provide a better coupling with the patch than the *Double Cross* excitation. These two improvements are compatible with enhanced radiation characteristics (recall *Section 2.4.2*) and broader impedance bandwidth.²⁰

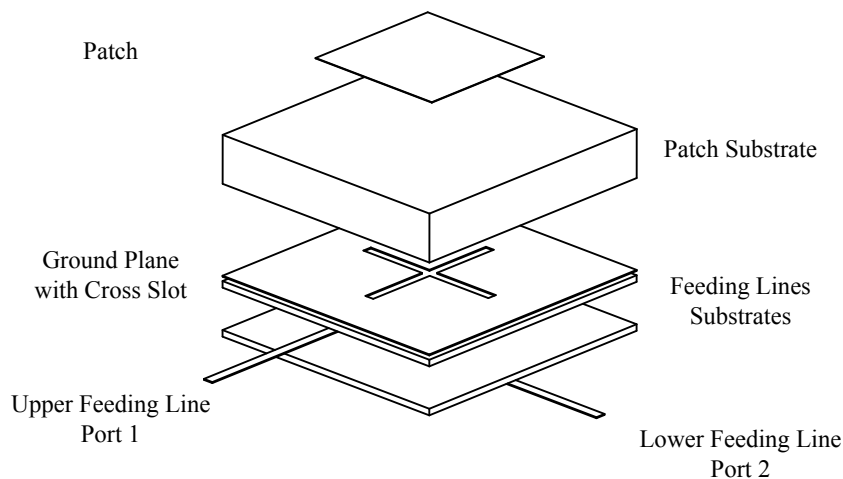


Figure 2.31. Dual Linearly Polarized ACMPA with multilayer feeding. Both feeding lines are below a common ground plane.

²⁰For example, a radiating element designed with this topology and the *stacked patches* technique has shown very good impedance matching and port isolation ($S_{ii} < -10$ dB, $S_{ij} < -21$ dB), symmetric radiation patterns and very low cross-polarization levels over a bandwidth in excess of 22% [75], [13, Ch. 6].

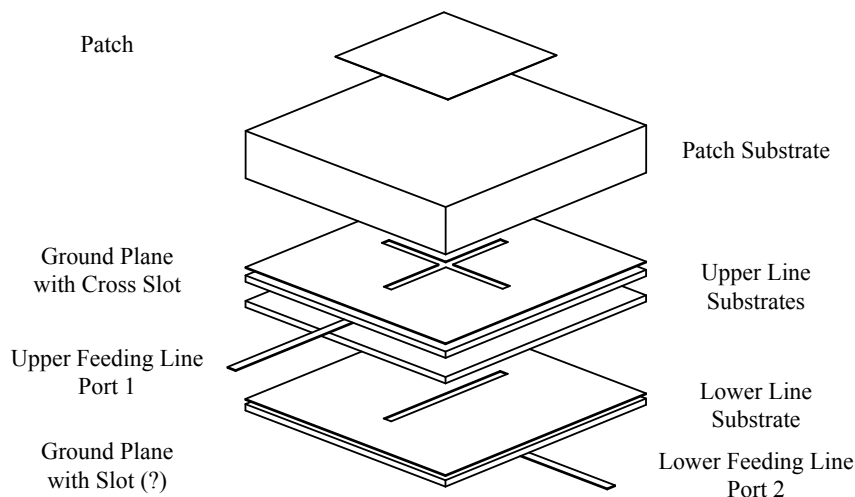
Moreover, with regard to the array integration, the multilayer feeding can make a more efficient use of the area allotted to each element in the array lattice, thanks to the superposition of the lines and the merging of the coupling slots. In this sense, however, the structure in *Fig. 2.31* can suffer from undesired couplings between lines in these two layers, especially if these layers are to contain densely packed feeding networks.

This drawback can be addressed by inserting a ground plane between both feeding layers, which would lead to structures such as the couple depicted in *Fig. 2.32*. The first structure (*Fig. 2.32(a)*) is only hypothetical, but would be optimal in the sense that both feeding lines could be separated from the radiating part of the antenna. This first structure would require at least one of the feeding lines (the *upper line*) to be a stripline. This implies that the considerations outlined in *Section 2.4.1* should be taken into account, with the particularity that a proper coupling between the patch and the *lower feeding line* through a couple of stacked apertures should also be guaranteed, which does not seem to be evident, however. This last drawback is not present in the second, more realistic, structure proposed in *Fig. 2.32(b)*, that combines a proper isolation of the feeding lines / networks with the relative structural simplicity of the buildup illustrated in *Fig. 2.31*.

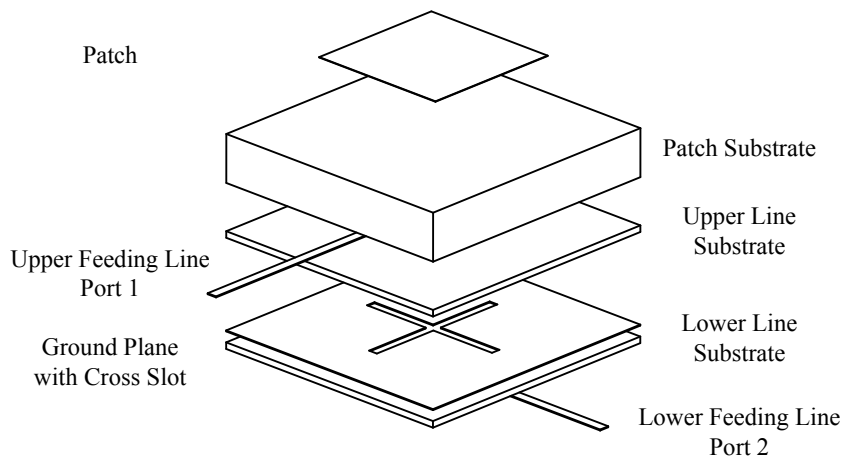
The main particularity of this last dual feeding approach concerns the upper access line, whose location between the patch and the slotted ground plane resembles the feeding mechanism used to excite proximity coupled patches. In practice, the design considerations that can be applied to these two feeding schemes should be quite similar, but the presence of the slot in the common ground plane adds an important degree of freedom. In fact, the distance between the patch and the line is no longer limited by their capacitive coupling, but by its combination with the inductive coupling through the equivalent magnetic current in the slot. This inductive coupling can be much stronger than the capacitive one, to the point that in many cases the operation principle of this feeding mechanism can be reduced to that of an ACMPA [76–79].

A proper balance between these capacitive and inductive coupling mechanisms can enable the design of broadband DLPREs (e.g. $S_{ii} \leq -10$ dB and $S_{ij} < -34$ dB within a 21% frequency band), without resorting to the *stacked patches* technique [80].

However, the fact that the radiating and the feeding parts of the antenna are not as clearly separated as they would be in the basic ACMPA, makes this feeding structure susceptible to spurious radiation. The adverse effects of these emissions in the symmetry of the radiation pattern, the polarization quality and, even, the port isolation of a DLPRE can become critical if, when it comes to integrate the RE in a dual polarized array antenna, special precautions are not taken in the design of the upper feeding network [81–84].



(a) Both feeding lines are below the patch ground plane.



(b) One of the feeding lines is over the patch ground plane.

Figure 2.32. Dual Linearly Polarized ACMPA with multilayer feeding. The feeding lines are separated by a ground plane.

b) Characteristics of the Dielectrics

The considerations made in *Section 2.4.1* with regard to the dielectric materials of both the radiating and the feeding parts of the SLPRE hold also for the DLPRE.

In fact, the main additional consideration for the design of the DLPRE with multilayer feeding depicted in *Fig. 2.32(b)* would apply to its upper feeding line. The substrate of this feeding line should promote the guiding mechanism over radiation to mitigate possible spurious emissions from the line. For this reason, the permittivity of this substrate ($\epsilon_{r \text{ upper line}}$) should be chosen, at least, as high as the permittivity of the (unshielded) microstrip feeding of the basic ACMPA (typically $\epsilon_{r \text{ ACMPA}} \in [2.1, 2.6]$).

2.5.2 Metalization Planes

As it has just been done for its buildup, the same design criteria presented for the SLPRE in *Section 2.4.2* are applicable to the metalization planes of the DLPRE. Moreover, the qualitative relations deduced from the parametric study presented in *Section 2.4.3* also hold for the DLPRE and their application will considerably benefit from the fact that the level of isolation between its two ports is expected to be quite high.

In fact, this high level of isolation will permit, at preliminary design stages, an almost independent adjustment of the electrical operation of the two polarization states of the DLPRE, as if they were two independent SLPREs. In this sense, the only constraints shared by both polarization states will be given by the relative placement of the feeding lines & slots with respect to the patch center as well as by the final shape and dimensions of the patch they are exciting. These shared constraints can be effectively taken into account in subsequent design steps, where the fine tuning of the electrical performances of the actual DLPRE will require a more complete simulation model.

2.6 Radiating Element with Dual Circular Polarization

As stated in *Section 2.2*, the Dual Circularly Polarized Radiating Element (DCPRE) is to be composed by a DLPRE and a 3dB-quadrature coupler.

Among all the feeding architectures reviewed in the previous section, when it comes to join the feeding lines of the DLPRE through a planar 3dB-quadrature coupler to synthesize a DCPRE, the structural simplicity of the so-called *coplanar feeding* techniques, which does not require additional vertical connections, takes precedence over the more compact and symmetric *multilayer* alternatives.

Between the two coplanar feeding techniques proposed, the one using a *T-shaped* arrangement of the slots is preferred to the *Double Cross*, since the first one is considered to consume much less PCB area, for a given minimum line-width, while providing equal or even better electrical performances (recall *Table 2.3* and *Table 2.4*).

With regard to the choice of the 3dB-quadrature coupler implementation, the three main candidates considered here are the *Branch Line*, the *de Ronde* and the *Lange* hybrids, as illustrated in *Fig. 2.33*.

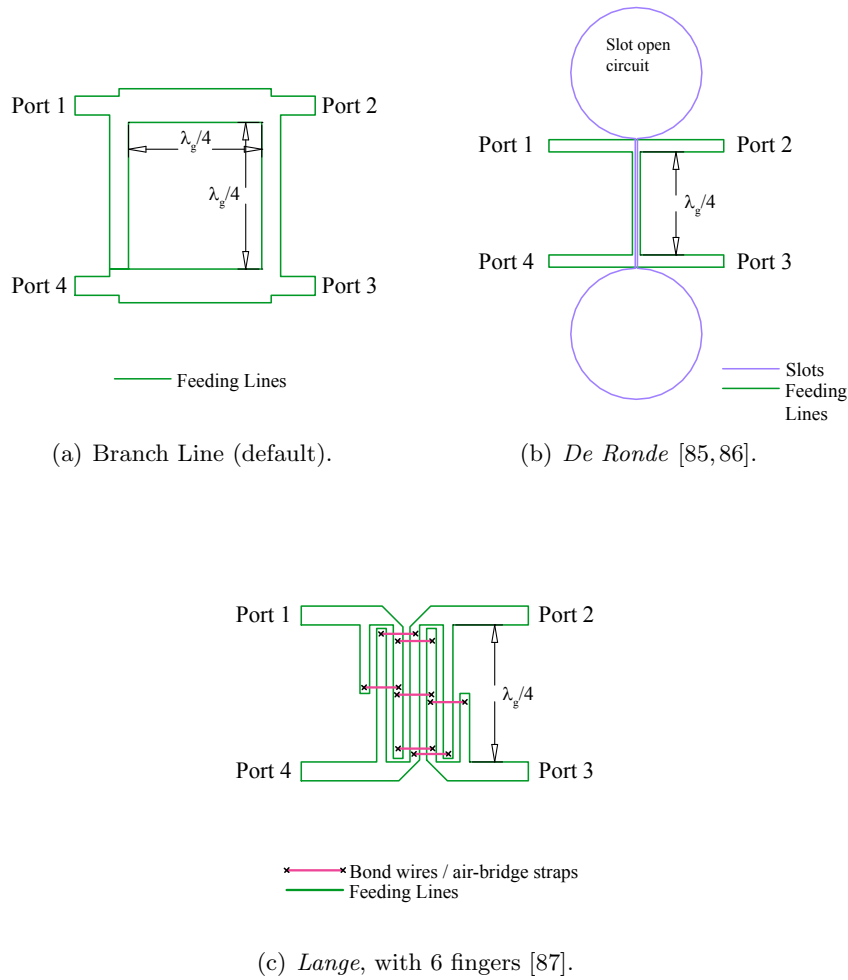


Figure 2.33. Different architectures of 3 dB-quadrature couplers.

The *Lange* coupler is the most compact of the three candidates, but requires tight tolerances in the etching of the inter-digitated lines, which may be out of reach for the standard PCB processes envisaged,²¹ as well as bridges to interconnect the lines, which makes of this coupler the most complex of the three candidates. The next in terms of structural complexity is the *de Ronde* coupler, since it is composed of a strip line coupled to an open ended slot-line that is printed in a common ground plane. The slot-line structure should normally lie in the ground plane of the the radiating patch, which may degrade the isolation between the feeding and the radiating parts of the ACMPA / S3FIP. Besides, the overall PCB area occupied by the slot-line open ends can be considerable. After these considerations, the advantageous compromise between size and structural simplicity provided by the Branch Line hybrid prevails over the higher electrical performances of the other two candidates.

²¹The minimum clearance allowed by the targeted manufacturers is $\approx 150 \mu\text{m}$, with an etching tolerance around $\pm 17 \mu\text{m}$, which, depending on the substrate material, can constitute a severe restriction for the design of the coupled lines.

At this point, the relevance of the PCB area constraints in the design of the RE can be further highlighted if a particular case of interest is considered. For the targeted application, it can be anticipated that such is the case of an S3FIP with dual linear polarization, asymmetric stripline feeding and six shorting pins, to mitigate the PPWM power leakage. This radiating element is depicted in *Fig. 2.34*. As proposed above, the excitation of the two orthogonal modes below the circular patch of this element (TM_{11} modes) is made through a couple of *dog-bone* slots arranged in a *T-shaped* configuration. And these slots are fed by a pair of striplines that are lying on the same metalization plane.

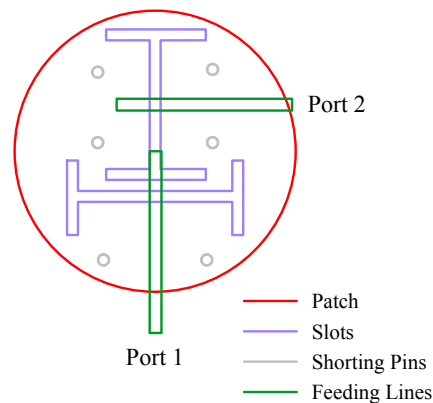
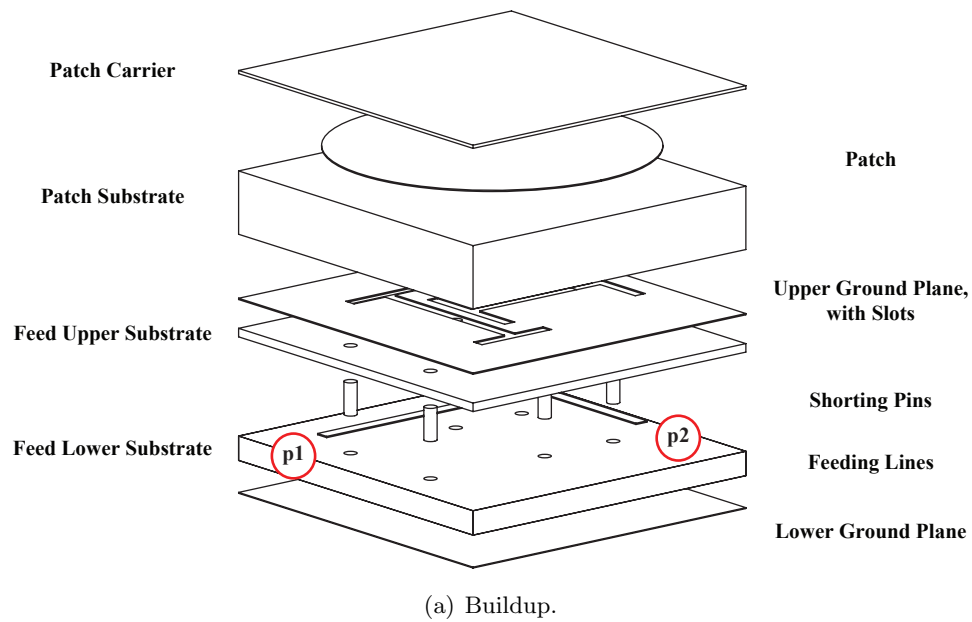


Figure 2.34. Dual Linearly Polarized S3FIP with asymmetric stripline feeding, six shorting pins and circular patch (Preliminary version).

This RE has been designed, according to the criteria presented so far, to match the requirements specified by the targeted application, as summarized in *Table 1.3*. And, though it corresponds to one of the first developments of the element (the so-called *Candidate #0*), this element can already serve to illustrate the importance of the PCB area issue from the perspective of the integration of the quadrature coupler, as stated above.

Fig. 2.35 illustrates how the PCB area occupied by the DLPRE feeding (lines, slots & shorting pins) conditions the way the branch line hybrid is connected to it. In general, the most efficient (compact) filling of the hexagonal cell area imposed by the triangular array lattice would be achieved with a radial growth of the ERC around the DLPRE.

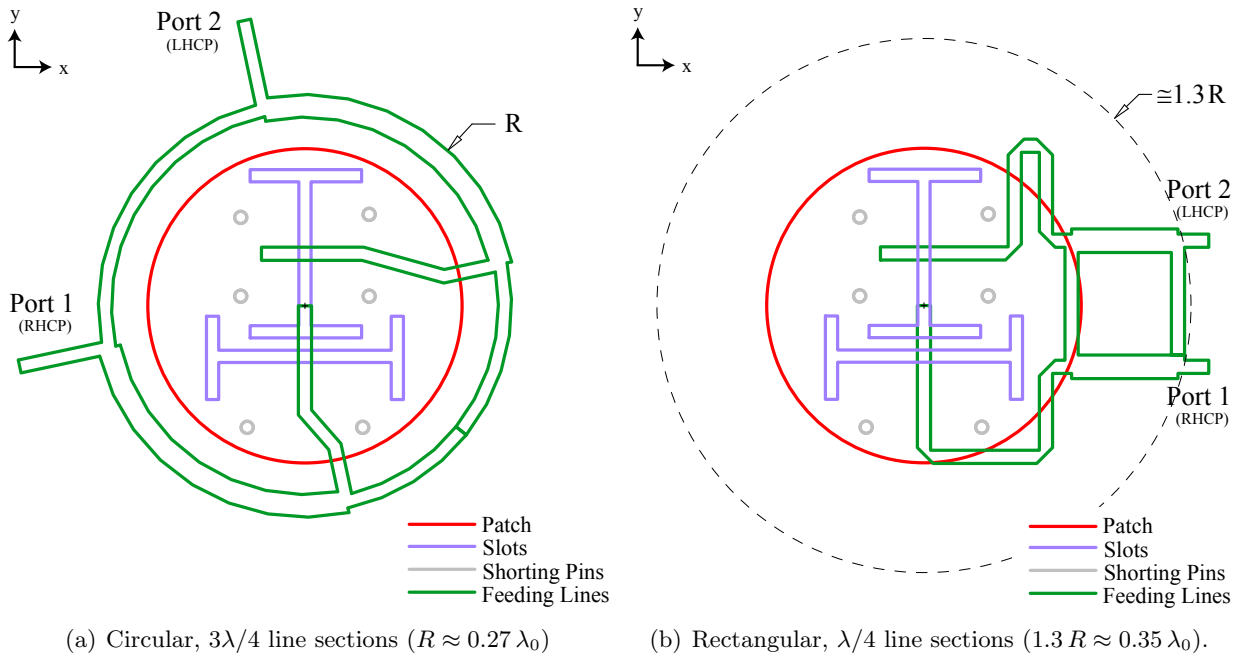


Figure 2.35. Layout Outline of a Dual Circularly Polarized S3FIP with two different implementations of the Branch Line Coupler (Radial vs. Lineal growth schemes). The overall size increase with the Lineal growth scheme is $\sim 30\%$.

A natural implementation of this radial growth could be to deploy the quadrature coupler around the DLPRE feeding, as depicted in *Fig. 2.35(a)*. However, the area occupied by the actual S3FIP feeding requires the use of a “large” ($3\lambda/4$) branch line to embrace it,²² which would prohibitively reduce the operational bandwidth of the hybrid with regard to its “standard” ($\lambda/4$) implementation [90]. In fact, it was found that the bandwidth compliance of the DCPRE using a “standard” branch line was already rather tight and the use of a two-sections branch-line to improve the DCPRE frequency response was even considered [91], but the etching accuracy limitations and the cell size constraints finally advised against this possibility.

²²A more compact feeding architecture may permit the use of an hybrid of “standard” size encircling it, which would pave the way for significant size / performance improvements. Though far from the aperture coupling scheme discussed here, the use of *probe feeding* is considered to be a promising alternative for the implementation of such a compact excitation structure. Actually, this encircling approach has been successfully applied to the feeding of dipole elements in TCDAs [20] and should be extensible to patch antennas, especially if it is combined with the *stacked patches* technique. The stacked patches technique allows, in fact, the use of a thinner, not necessarily foam-based, substrate for the lower patch, with the consequent reduction of the feeding vias length and their associated inductance, which facilitates the impedance matching of the RE in a broader frequency band. In this type of antennas, however, the coupling between the pair of probes that would feed the patch may require special attention, and their industrial implementation might be more complex than the “single press” process envisaged for the present application [88,89].

The most convenient configuration for the present application is found, therefore, to be given by the straight concatenation of the DLPRE with a “standard” branch line, as shown in *Fig. 2.35(b)*. This figure also illustrates a common approach to equalize the phases of the two orthogonal modes that resonate below the patch, prior to their combination in the quadrature coupler. This phase equalization takes into account the different distances between each one of the slots and the patch phase center as well as for possible differences in the length of the feeding lines, as they are routed from the slot center to the coupler ports. In fact, this routing can be severely conditioned by the feeding layout of the DLPRE, and the required phase equalization is usually achieved with the introduction of a “true time” delay section of a proper *length* in one of the DLPRE access lines.

In the case of the S3FIP shown in *Fig. 2.35(b)*, the arrangement of the slots & the shorting pins leads to a somewhat intricate tracing of the feeding lines. This routing determines most of the additional delay length introduced by the tight meander in the line that excites the vertical slot. In practice, a starting value for the length of this meander is given by the condition of equal length for the two access lines of the DLPRE. This length is then refined attending to the quality of the circular polarization over the whole scanning range of the foreseen array (360° in azimuth and from 20° to 70° in elevation), within the frequency band of interest.

References

- [1] R. T.-S. Sánchez, “Two beam printed antenna array for satellite reception,” Master Thesis Report (in Spanish), Escuela Técnica Superior de Ingenieros de Telecomunicación de la Universidad de Málaga, Málaga, España, Mar. 2006, Report summary available at http://www.coit.es/pub/ficheros/p_astra_dfb74c86.pdf?PHPSESSID=4e27a815b4815581fe4a579d9c5fd977.
- [2] J. R. James and P. S. Hall, Eds., *Handbook of microstrip antennas*. London: P. Peregrinus on behalf of the Institution of Electrical Engineers, 1989.
- [3] L. Young, L. Robinson, and C. Hacking, “Meander-line polarizer,” *IEEE Trans. Antennas Propag.*, vol. 21, no. 3, pp. 376 – 378, may 1973.
- [4] W. L. Curtis, “Spiral antennas,” *Antennas and Propagation, IRE Transactions on*, vol. 8, no. 3, pp. 298 –306, may 1960.
- [5] R. Guinvarc’h and R. Haupt, “Dual polarization interleaved spiral antenna phased array with an octave bandwidth,” *IEEE Trans. Antennas Propag.*, vol. 58, no. 2, pp. 397 –403, feb. 2010.
- [6] N. Stutzke and D. Filipovic, “Broadband two-arm dual-mode dual-polarized spiral antenna,” in *Antennas and Propagation Society International Symposium, 2005 IEEE*, vol. 1B, july 2005, pp. 414 –417.
- [7] K. Hirose, Y. Shimazawa, Y. Uchikawa, and H. Nakano, “Dual circularly polarized spiral and loop antennas backed by a conducting plane reflector,” in *Antennas and Propagation Society International Symposium, 2008. AP-S 2008. IEEE*, july 2008, pp. 1 –4.
- [8] C. Chen and E. Yung, “Dual-band dual-sense circularly-polarized CPW-fed slot antenna with two spiral slots loaded,” *IEEE Trans. Antennas Propag.*, vol. 57, no. 6, pp. 1829 –1833, june 2009.
- [9] C. A. Balanis, *Antenna Theory: Analysis and Design*. John Wiley & Sons Inc., 1996.
- [10] W. F. William and F. Richards, “Microstrip antennas,” in *Antenna Handbook : Theory, Applications and Design*, Y. T. Lo and S. W. Lee, Eds. Kluwer Academic Pub., May 1988.
- [11] K. R. Carver and J. W. Mink, “Microstrip antenna technology,” *IEEE Trans. Antennas Propag.*, vol. AP-29, pp. 2–24, Jan. 1981.
- [12] D. M. Pozar, “Microstrip antennas,” vol. 80, no. 1, Jan. 1992, pp. 79–91.
- [13] J.-F. Zürcher and F. E. Gardiol, *Broadband patch antennas*. Boston: Artech House, 1995.
- [14] J. R. Mosig, “Integral equation techniques,” in *Numerical techniques for microwave and millimeter-wave passive structures (ch. 3)*, T. Itoh, Ed. New York: Wiley, 1989.
- [15] R. Garg, P. Barthia, I. Bahl, and A. Ittipiboon, *Microstrip Antenna Design Handbook*. Boston: Artech House, 2001.
- [16] J. Shin and D. Schaubert, “A parameter study of stripline-fed vivaldi notch-antenna arrays,” *IEEE Trans. Antennas Propag.*, vol. 47, no. 5, pp. 879 –886, may 1999.
- [17] T.-Y. Yun, C. Wang, P. Zepeda, C. Rodenbeck, M. Coutant, M. yi Li, and K. Chang, “A 10- to 21-GHz, low-cost, multifrequency, and full-duplex phased-array antenna system,” *IEEE Trans. Antennas Propag.*, vol. 50, no. 5, pp. 641 –650, may 2002.
- [18] H. Holter, “A new type of antenna element for wide-band wide-angle dual polarized phased array antennas,” in *Phased Array Systems and Technology, 2003. IEEE International Symposium on*, oct. 2003, pp. 393 – 398.
- [19] —, “Dual-polarized broadband array antenna with BOR-elements, mechanical design and measurements,” *IEEE Trans. Antennas Propag.*, vol. 55, no. 2, pp. 305 –312, feb. 2007.
- [20] J. Kasemodel, C.-C. Chen, and J. Volakis, “Broadband planar wide-scan array employing tightly coupled elements and integrated balun,” in *Phased Array Systems and Technology (ARRAY), 2010 IEEE International Symposium on*, oct. 2010, pp. 467 –472.

- [21] P. Friedrich, L. Pringle, L. Fountain, P. Harms, D. Denison, E. Kuster, S. Blalock, G. Smith, J. Moloney, and M. Kesler, "A new class of broadband planar apertures," in *Allerton Antenna Applications Symposium*, Monticello, Illinois (USA), Sep. 2001.
- [22] B. Thors, H. Steyskal, and H. Holter, "Broad-band fragmented aperture phased array element design using genetic algorithms," *IEEE Trans. Antennas Propag.*, vol. 53, no. 10, pp. 3280 – 3287, oct. 2005.
- [23] N. Herscovici, B. Tomasic, J. Ginn, and T. Donisi, "Scanning characteristics of aperture coupled fed fragmented microstrip arrays," in *Antennas and Propagation Society International Symposium, 2009. APSURSI'09. IEEE*, 1-5 2009, pp. 1 –4.
- [24] D. M. Pozar, "Microstrip antenna aperture-coupled to a microstripline," *Electron. Lett.*, vol. 21, no. 2, pp. 49–50, Jan. 1985.
- [25] D. M. Pozar and D. H. Schaubert, "Scan blindness in infinite phased arrays of printed dipoles," *IEEE Trans. Antennas Propag.*, vol. AP-32, pp. 602–610, Jun. 1984.
- [26] D. Pozar and D. Schaubert, "Analysis of an infinite array of rectangular microstrip patches with idealized probe feeds," *IEEE Trans. Antennas Propag.*, vol. 32, no. 10, pp. 1101 – 1107, oct 1984.
- [27] R. C. Hansen, Ed., *Microwave scanning antennas*. Los Altos, Calif.: Peninsula Publishing, 1985.
- [28] D. M. Pozar, "Considerations for millimeter wave printed antennas," *IEEE Trans. Antennas Propag.*, vol. AP-31, no. 5, pp. 740–747, Sep. 1983.
- [29] ——. (2006, Feb.) A review of aperture coupled microstrip antennas: History, operation, development, and applications. aperture.pdf. University of Massachusetts. Amherst, MA. [Online]. Available: <http://www.ecs.umass.edu/ece/pozar/aperture.pdf>
- [30] J.-F. Zürcher and F. E. Gardiol, "The SSFIP: A global concept for high performance broadband planar antennas," *Electron. Lett.*, vol. 24, no. 23, pp. 1433–1435, Nov. 1988.
- [31] F. Zavosh and J. Aberle, "Single and stacked circular microstrip patch antennas backed by a circular cavity," *IEEE Trans. Antennas Propag.*, vol. 43, no. 7, pp. 746 –750, jul 1995.
- [32] —, "Improving the performance of microstrip-patch antennas," *Antennas and Propagation Magazine, IEEE*, vol. 38, no. 4, pp. 7 –12, aug 1996.
- [33] N. Karmakar, "Investigations into a cavity-backed circular-patch antenna," *IEEE Trans. Antennas Propag.*, vol. 50, no. 12, pp. 1706 – 1715, dec 2002.
- [34] F. Zavosh and J. Aberle, "Infinite phased arrays of cavity-backed patches," *IEEE Trans. Antennas Propag.*, vol. 42, no. 3, pp. 390 –398, mar 1994.
- [35] B. Brynjarsson and T. Syversen, "Cavity-backed, aperture coupled microstrip patch antenna," in *Antennas and Propagation, 1993., Eighth International Conference on*, vol. 2, 1993, pp. 715 –718.
- [36] S. Yang and A. Fathy, "Cavity-backed patch shared aperture antenna array approach for mobile dbS applications," in *Antennas and Propagation Society International Symposium 2006, IEEE*, july 2006, pp. 3959 –3962.
- [37] F. Bilotti and L. Vegni, "Chiral cover effects on microstrip antennas," *IEEE Trans. Antennas Propag.*, vol. 51, no. 10, pp. 2891–2897, Oct. 2003.
- [38] R. J. Mailloux, J. F. McIlvanna, and N. P. Kernweis, "Microstrip array technology," *IEEE Trans. Antennas Propag.*, vol. AP-29, no. 1, pp. 25–37, Jan. 1981.
- [39] E. O. Hammerstad and O. Jensen, "Accurate models for microstrip computer-aided design," in *Microwave symposium Digest, 1980 IEEE MTT-S International*, may 1980, pp. 407–409.
- [40] R. C. Hall and J. R. Sanford, "Performance enhancements for aperture coupled microstrip antennas," in *IEEE APS Symp. Dig.*, Chicago, IL, Jul. 1992, pp. 1040–1043.
- [41] P. Brachat and J. M. Baracco, "Dual-polarization slot-coupled printed antennas fed by stripline," *IEEE Trans. Antennas Propag.*, vol. 43, no. 7, pp. 738–742, Jul. 1995.
- [42] M. Yamamoto and K. Itoh, "Behavior of parallel plate mode in a slot-coupled patch antenna with stripline feed," in *IEEE Antennas Propagat. Symp. Dig.*, 1998, pp. 932–934.

- [43] A. Bhattacharyya, O. Fordham, and Y. Liu, "Analysis of stripline-fed slot-coupled patch antennas with vias for parallel-plate mode suppression," *IEEE Trans. Antennas Propag.*, vol. 46, no. 4, pp. 538–545, feb. 2007.
- [44] *Advanced Design System 2008 Documentation. Radiation Patterns and Antenna Characteristics for Momentum*, Agilent Technologies, Jun. 2011. [Online]. Available: http://cp.literature.agilent.com/litweb/pdf/ads2008/mom/ads2008/Radiation_Patterns_and_Antenna_Characteristics_in_Momentum.html#RadiationPatternsandAntennaCharacteristicsinMomentum-Polarization
- [45] J. Shumpert, W. Chappell, and L. Katehi, "Parallel-plate mode reduction in conductor-backed slots using electromagnetic bandgap substrates," *IEEE Trans. Microw. Theory Tech.*, vol. 47, no. 11, pp. 2099–2104, nov 1999.
- [46] R. J. Mailloux, "On the use of metallized cavities in printed slot arrays with dielectric substrates," *IEEE Trans. Antennas Propag.*, vol. 35, no. 5, pp. 477–487, may 1987.
- [47] Y. Yoshimura, "A microstripline slot antenna," *IEEE Trans. Microw. Theory Tech.*, vol. MTT-20, pp. 760–762, Nov. 1972.
- [48] D. M. Pozar, "A reciprocity method of analysis for printed slot and slot-coupled microstrip antennas," *IEEE Trans. Antennas Propag.*, vol. AP-34, no. 12, pp. 1439–1446, Dec. 1986.
- [49] S. Cohn, "Problems in strip transmission lines," *Microwave Theory and Techniques, IRE Transactions on*, vol. 3, no. 2, pp. 119–126, 1955.
- [50] R. Manrique, R. Torres-Sánchez, C. Domínguez, F. Tiezzi, and J. R. Mosig, "Design and prototyping of a microstrip transmit-receive array antenna for mobile Ku-band satellite terminals," in *proc. EuCAP 2010, 4th International Conference on Antennas and Propagation*, Apr. 2010.
- [51] F. Tiezzi, S. Vaccaro, and D. Llorens, "Hybrid single aperture inclined antenna," Patent US 20 100 328 161, December 30, 2010.
- [52] A. Pal, A. Mehta, D. Mirshekar-Syahkal, and P. Massey, "Doughnut and tilted beam generation using a single printed star antenna," *IEEE Trans. Antennas Propag.*, vol. 57, no. 10, pp. 3413–3418, oct. 2009.
- [53] R. F. Harrington, "Effect of antenna size on gain, bandwidth and efficiency," *Journal of Research of the National Bureau of Standards-D Radio Propagation*, vol. 64-D, pp. 1–12, 1960.
- [54] S. D. Targonski, R. Waterhouse, and D. M. Pozar, "Design of wide-band aperture-stacked patch microstrip antennas," *IEEE Trans. Antennas Propag.*, vol. 46, no. 5, pp. 1245–1251, Sep. 1998.
- [55] Y.-X. Guo, M. Chia, and Z. N. Chen, "Miniature built-in multiband antennas for mobile handsets," *IEEE Trans. Antennas Propag.*, vol. 52, no. 8, pp. 1936–1944, aug. 2004.
- [56] M. Bourry, F. Tiezzi, and S. Vaccaro, "Omni-directional antenna for mobile satellite broadcasting applications," Patent US 20 090 027 294, January 29, 2009.
- [57] J. Gianvittorio and Y. Rahmat-Samii, "Fractal antennas: a novel antenna miniaturization technique, and applications," *Antennas and Propagation Magazine, IEEE*, vol. 44, no. 1, pp. 20–36, feb 2002.
- [58] D. Werner and S. Ganguly, "An overview of fractal antenna engineering research," *Antennas and Propagation Magazine, IEEE*, vol. 45, no. 1, pp. 38–57, feb 2003.
- [59] S. Bokhari, J.-F. Zurcher, J. Mosig, and F. Gardiol, "A small microstrip patch antenna with a convenient tuning option," *IEEE Trans. Antennas Propag.*, vol. 44, no. 11, pp. 1521–1528, nov 1996.
- [60] J. Huang, "Miniaturized UHF microstrip antenna for a Mars mission," in *Antennas and Propagation Society International Symposium, 2001. IEEE*, vol. 4, 2001, pp. 486–489.
- [61] T. Tanaka, M. Takahashi, and K. Ito, "Study on the radiation characteristics of a miniaturized circularly polarized circular sector patch antenna," in *Antennas and Propagation Society International Symposium 2006, IEEE*, july 2006, pp. 1561–1564.
- [62] A. Skrivervik, J.-F. Zurcher, O. Staub, and J. Mosig, "PCS antenna design: the challenge of miniaturization," *Antennas and Propagation Magazine, IEEE*, vol. 43, no. 4, pp. 12–27, aug 2001.

- [63] D. M. Pozar and S. D. Targonski, "Improved coupling for aperture-coupled microstrip antennas," *Electron. Lett.*, vol. 27, no. 13, pp. 1129–1131, Jun. 1991.
- [64] V. Rathi, G. Kumar, and K. P. Ray, "Improved coupling for aperture coupled microstrip antennas," *IEEE Trans. Antennas Propag.*, vol. 44, no. 8, pp. 1196–1198, Aug. 1996.
- [65] K.-L. Wong, H.-C. Tung, and T.-W. Chiou, "Broadband dual-polarized aperture-coupled patch antennas with modified H-shaped coupling slots," *IEEE Trans. Antennas Propag.*, vol. 50, no. 2, pp. 188–191, Feb. 2002.
- [66] S. Gao, P. G. L. W. Li, and P. S. Hall, "Wide-band dual-polarized microstrip patch antenna," *Electron. Lett.*, vol. 37, no. 20, pp. 1213–1214, Sep. 2001.
- [67] P. L. Sullivan and D. H. Schaubert, "Analysis of an aperture coupled microstrip antenna," *IEEE Trans. Antennas Propag.*, vol. AP-34, no. 8, pp. 977–984, Aug. 1986.
- [68] H. F. Pues and A. R. V. de Capelle, "An impedance-matching technique for increasing the bandwidth of microstrip antennas," *IEEE Trans. Antennas Propag.*, vol. 37, no. 11, pp. 1345–1354, Nov. 1989.
- [69] A. Ittipiboon, R. Oostlander, and Y. M. M. Antar, "A modal expansion method of analysis and measurement on aperture-coupled microstrip antenna," *IEEE Trans. Antennas Propag.*, vol. 39, no. 11, pp. 1567–1574, Nov. 1991.
- [70] G. A. Kyriacou, A. A. Mavrides, O. Breinbjerg, and J. N. Sahalos, "A design procedure for aperture coupled microstrip antennas based on approximate equivalent networks," in *Proceedings of AP2000 Millennium Conference on Antennas & Propagation*, Davos, Switzerland, 2000, pp. 50–56.
- [71] E. O. Hammerstad, "Equations for microstrip circuit design," in *Microwave Conference, 1975. 5th European*, sept. 1975, pp. 268–272.
- [72] S. D. Targonski and D. M. Pozar, "Design of wideband circularly polarized aperture coupled microstrip antennas," *IEEE Trans. Antennas Propag.*, vol. 41, no. 2, p. 214220, Feb. 1993.
- [73] M. E. Bialkowski and H. J. Song, "Investigations into a power-combining structure using a reflect array of dual-feed aperture-coupled microstrip patch antennas," *IEEE Trans. Antennas Propag.*, vol. 50, no. 6, pp. 841–849, Jun. 2002.
- [74] S. Hienonen, A. Lehto, and A. V. Risnen, "Simple broadband dual-polarized aperture-coupled microstrip antenna," in *Proc. IEEE Antennas and Propagation Soc. Int. Symp. Dig.*, Orlando, Florida, Jun. 1999, p. 12281231.
- [75] M. Edimo, A. Sharaia, and C. Terret, "Optimized feeding of dual polarized broadband aperture-coupled printed antenna," *Electron. Lett.*, vol. 28, pp. 1785–1787, 1992.
- [76] M. Yamazaki, E. T. Rahardjo, and M. Haneishi, "Construction of a slot-coupled planar antenna for dual polarization," *Electron. Lett.*, vol. 30, no. 22, pp. 1814–1815, Oct. 1994.
- [77] J. R. Sanford and A. Tengs, "A two substrate dual polarized aperture coupled patch," in *Proc. IEEE Trans. Antennas and Propagation Symp. Digest*, 1996, p. 15441547.
- [78] L. Bekraoui, "Low cost broadband microstrip antenna for satellite-TV reception," in *Proc. IEEE Antennas and Propagation Soc. Int. Symp. Dig.*, vol. 2, Orlando, Florida, Aug. 1999, pp. 916–919.
- [79] K. Ghorbani and R. B. Waterhouse, "Dual polarized wide-band aperture stacked patch antennas," *IEEE Trans. Antennas Propag.*, vol. 52, no. 8, pp. 2171–2174, Aug. 2004.
- [80] S. Gao and A. Sambell, "Dual-polarized broad-band microstrip antennas fed by proximity coupling," *IEEE Trans. Antennas Propag.*, vol. 53, no. 1, pp. 526–530, Jan. 2005.
- [81] P. Hall, "Feed radiation effects in sequentially rotated microstrip patch arrays," *Electronics Letters*, vol. 23, no. 17, pp. 877–878, 13 1987.
- [82] P. S. Hall and C. M. Hall, "Coplanar corporate feed effects in microstrip patch array design," in *Proc. IEE*, vol. 135, no. 3, Jun. 1988, pp. 180–186.
- [83] R. Torres-Sánchez, F. P. Casares-Miranda, E. Márquez-Segura, and P. Otero, "Printed array with dual lineal polarization for satellite reception," in *XXI Simposium Nacional de la URSI*, in Spanish.

-
- [84] —, “Symmetry, XPD, and port isolation in an ACMPA array with dual linear polarization,” *Microwave Opt. Technol. Lett.*, vol. 49, no. 7, pp. 1722–1727, Jul. 2007.
- [85] B. Schiek, “Hybrid branchline couplers – a useful new class of directional couplers,” *IEEE Trans. Microw. Theory Tech.*, vol. 22, no. 10, pp. 864 – 869, oct 1974.
- [86] K. Gupta, R. Garg, and I. J. Bahl, *Microstrip lines and slotlines*. Boston: Artech House, 1979.
- [87] J. Lange, “Interdigitated stripline quadrature hybrid (correspondence),” *IEEE Trans. Microw. Theory Tech.*, vol. 17, no. 12, pp. 1150 – 1151, dec 1969.
- [88] A. Garcia-Aguilar, J. M. Inclan-Alonso, J. M. Fernandez-Gonzalez, and M. Sierra-Perez, “Printed antenna for satellite communications,” in *proc. EuCAP 2010, 4th International Conference on Antennas and Propagation*, 2010.
- [89] A. Garcia-Aguilar, J. M. Inclan-Alonso, L. Vigil-Herrero, J. M. Fernandez-Gonzalez, J. Sanmartin-Jara, and M. Sierra-Perez, “Dual-polarized planar antenna for satellite communications at X-band,” in *32nd ESA Antenna Workshop on Antennas for Space Applications*, ESA/ESTEC, Noordwijk, The Netherlands, Oct. 2010.
- [90] C. Toker, M. Saglam, M. Ozme, and N. Gunalp, “Branch-line couplers using unequal line lengths,” *IEEE Trans. Microw. Theory Tech.*, vol. 49, no. 4, pp. 718 –721, apr 2001.
- [91] M. Muraguchi, T. Yukitake, and Y. Naito, “Optimum design of 3-dB branch-line couplers using microstrip lines,” *IEEE Trans. Microw. Theory Tech.*, vol. 31, no. 8, pp. 674 –678, aug. 1983.

3. Elementary Radiating Cell. Design Process

*Je ne cherche pas à suivre la trace des anciens,
je cherche ce qu'ils ont eux-mêmes cherché.*

MATSUO BASHŌ

3.1 Introduction

According to the guidelines outlined in the previous chapter, the design of the Elementary Radiating Cell (ERC) can be divided into two steps: (i) the integration of the ERC within the antenna PCB buildup and (ii) its integration within the array lattice. The first part will define the basics of the ERC multilayer structure and the second will govern, basically, the design of its different metalization layers.

It must be recalled that this is just a conceptual division, since these two activities are intimately linked through the electromagnetic (EM) performance of the ERC and the structural constraints of the array antenna. And, therefore, every design step will imply an update at both buildup and layout levels. This conception, however, is found to be useful for the goal of this chapter, that is to provide a reasoned description of the process followed in the design of the ERC.

The present chapter describes the way the aforementioned design guidelines are applied to the design of the *circularly polarized element*, from its proof of concept up to the fulfillment of the actual design constraints. In this process, besides the performance requirements, the design constraints are strongly related to the ERC integration. The way these constraints guide also the design of the *Long Vias* and the *Power Combiner* is briefly illustrated by the end of the chapter, where an outline of the design and refinement of a complete model of the ERC is finally provided.

3.2 Integration within the Antenna PCB Buildup

As will be shown throughout the remainder of this memoir, the excitation of the Radiating Element (RE) constitutes one of the major issues for both its design and evaluation. In this sense, the integration of the RE within the antenna buildup does not constitute an exception.

Among all the techniques to feed the microstrip RE that are considered in *Section 2.4.1*, the so-called *aperture coupling* is considered to be the most advantageous for the present application.

An important advantage of this excitation mechanism is the separation that it provides between the radiating and the feeding parts of the RE. Additionally, and with regard to the PCB architecture that is proposed in *Fig. 2.1*, the integration of the RE to the antenna buildup requires:

- a new shielding layer to prevent possible undesired interactions between the RE feeding and the remaining components of the array, which are embedded in the lower layers of the PCB stack.
- To permit the inclusion of reliable connections, through the different layers of the buildup, between these components and the RE. Here, such connections are implemented by the *Long Vias* and the *Power Combiner*.

The combination of these two requirements with the need of a proper coupling between the feeding lines and the radiating patch, leads to the choice of a thin asymmetric stripline to feed the RE. As already discussed in *Section 2.4.1*, this excitation scheme may require the insertion of shorting pins between the two ground planes of the triplate structure to mitigate the power leakage associated to the excitation of undesired modes. These shorting pins are actually placed in the vicinities of the slots that couple the feeding lines of the RE with the patch, where the most harmful of these undesired modes (the fundamental Parallel Plate Waveguide Mode -PPWM-), is excited.

In principle, these shorting pins are implemented as *through vias*, which, according to the PCB manufacturing process, permits to minimize their diameter. In practice, as the diameter of the shorting pins is reduced, the optimization of their placement gets simplified. This is because, at the actual design stage, such optimization only concerns, besides the EM performance of the RE, the area occupied by the layout of the element (recall *Fig. 2.35*).

With regard to the stripline feeding of the RE, preliminary design steps towards the determination of a proper multilayer assembly are conducted. Within the set of dielectric materials advised by the industrial partners, which are summarized in *Table 3.1*, these preliminary design

steps consider different asymmetric stripline configurations, both homogeneous and heterogeneous. And, under the constraint of an overall stripline thickness $\lesssim 1$ mm,¹ it is found that an aspect ratio for the thicknesses of the two dielectrics involved ($h_{\text{down}}/h_{\text{up}}$, recall *Fig. 2.6* and *Fig. 2.7*) of 3 – 4 : 1 can provide a proper coupling between the feeding line and the patch as well as acceptable guiding characteristics for the transmission line, while remaining compatible with the foreseen manufacturing process. Though no significant performance variations are observed between the REs designed with the different feeding assemblies:

- the choice of materials with the highest electrical permittivity results privileged due to the need of minimizing the area occupied by the RE feeding, at the expense of an increased sensitivity to manufacturing tolerances.
- Only homogeneous stripline assemblies are retained, which contributes to the simplification of the buildup manufacturing as well as to the reduction of the diversity of the materials involved. This simplification may have a positive impact on the final cost of the PCB core.

Commercial name	ε_r	$\tan \delta$
RT/duroid [®] 5890	2.1	0.0005
Arlon [™] DiClad 880	2.2	0.0009
Ultralam [®] 2000	2.5	0.0022
RO4003C [™]	3.38*	0.0027
RO4350B [™]	3.48	0.0037

* 3.38 is just a nominal value. The manufacturer typically advises to use $\varepsilon_r = 3.55$, instead.

Table 3.1. Characteristics of the dielectrics tested for the S3FIP feeding.

Concerning the radiating part of the element, the SSFIP (Shielded - Strip - Slot - Foam - Inverted Patch) structure is judged to address conveniently the bandwidth requirements. An example of the resulting S3FIP element is depicted in *Fig. 3.1*. This element is in fact the initial version, the so-called *Candidate #0*, of a series of developments carried out during a First Design Iteration [1].

As will be shown next, this design iteration is undertaken to explore for possible improvements in the performance of a basic S3FIP prototype prior to its practical implementation. The fabrication of prototypes of the radiating element, isolated and within a triangular sub-array, is intended to provide *preliminary proofs* for both the RE feeding and the polarization tracking concepts [2]. Finally, the RE feeding proof of concept would validate the **Integration** of the element in the antenna PCB *Buildup*. And this validation would then enable a second design iteration, this time towards the integration of the RE within the *Array Lattice*.

¹The overall thickness of the stripline feeding is $\sim 1/6$ the thickness of the antenna PCB buildup.

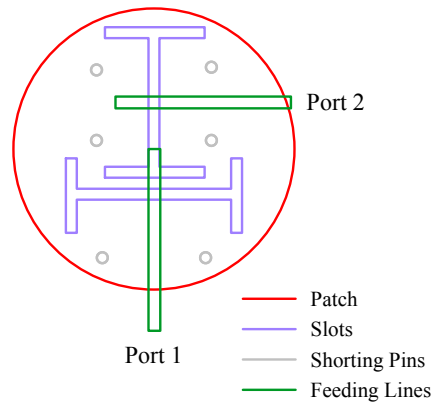
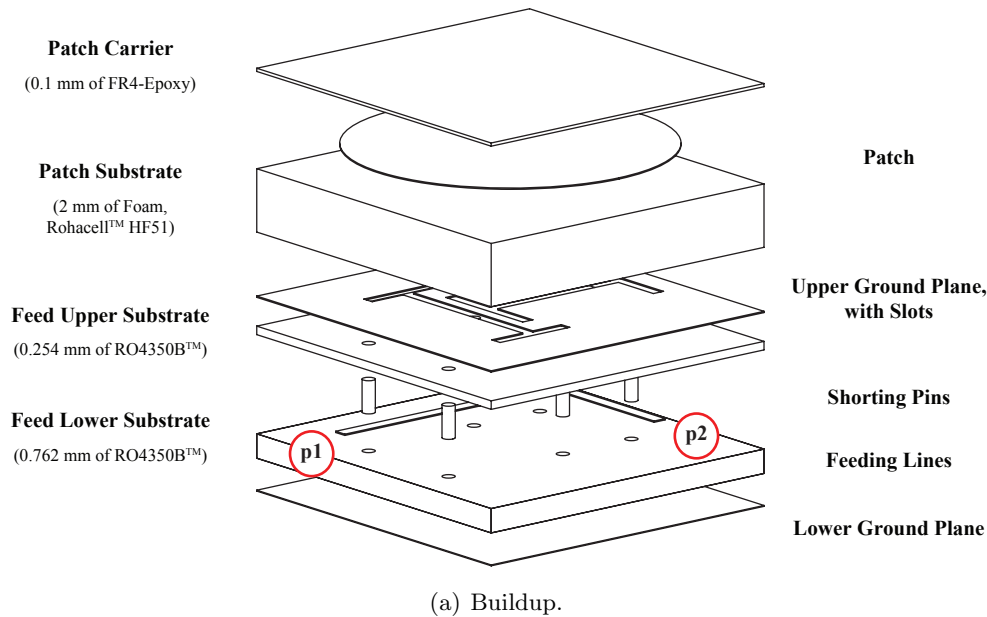


Figure 3.1. Dual Linearly Polarized S3FIP element with asymmetric stripline feeding and circular patch. Preliminary version or *Candidate #0*.

3.2.1 First Design Iteration

Once a proper feeding architecture for the RE has been determined, the next design steps focus on the radiating part of the RE buildup. With this purpose, a series of elements with different radiating parts are designed and their EM performances, compared.²

²This activity is entirely based on simulation results. At this level, the reliability of such results is supported by a careful definition of the corresponding simulation models as well as by the cross-check of the predictions delivered by the different *Full Wave* software tools used to analyze those models. Both commercial and “home-made” software tools are used. Here, the commercial software tools involved are *Ansoft Ensemble™*, *Agilent ADS Momentum*, *Ansoft Designer™* and *Ansoft HFSS™*. The first three tools are based, as their “home made” counterparts (originally developed at LEMA), on numerical methods especially well-suited for the resolution of Maxwell’s Equations in stratified media (2.5D problems), while the last software tool can address more general 3D EM problems.

The main design constraint is given by the overall thickness of the radiating part buildup, that should not exceed ≈ 2.5 mm. For the sake of simplicity, the dielectric materials are limited to foam and polypropylene (low and medium permittivity, respectively) and their minimum thickness step is fixed to 0.5 mm. This simplification is very convenient for the design approach used here, that is essentially manual. In fact, the amount of parameters (both performance and constructive) involved, as well as the difficulties found in the definition of a proper weighting scheme to quantitatively evaluate the “overall suitability” of the different candidate elements prevented a complete automation of this design process.

As it is proposed in *Section 2.4.3*, the design of the different elements concentrates, primarily, on the **scattering parameters** (impedance matching and port isolation) of the Dual Linearly Polarized Radiating Element (DLPRE). This activity is guided to a large extent by the qualitative relationships presented in *Section 2.4.3* as well as by other more particular relations that are deduced during the process of manual refinement of the RE scattering parameters. Then the **radiation efficiency** of the element is evaluated and, eventually, the position of the shorting pins adjusted to improve this efficiency. Depending on the impact these adjustments may have on the scattering parameters of the DLPRE, either a new manual refinement or an automatic fine tuning of the element performance could be carried out. Actually, as the number of structural parameters of the RE is increased, like it may happen when the *stacked patches* or certain miniaturization techniques are applied, the role of this automatic fine tuning becomes more important.

When the design process of the DLPRE has converged, the design of the Dual Circularly Polarized Radiating Element (DCPRE) concentrates, basically, on the quality of the circular polarization generated, that is quantified by its level of **Axial Ratio** (AR). The issue of the area occupied by the DCPRE feeding (i.e. the hybrid and the meander line) is also addressed in this process, but less strictly, since at this design stage this issue is not yet a priority.

Finally, the different candidate elements resulting from this design process are introduced in several small sub-array configurations, where their embedded behaviors are evaluated. These sub-arrays are considered to be representative of the environment that the RE would “see” once it is introduced in the final array aperture and may, therefore, provide a first estimation of the impact that such embedding would have on the performance of the isolated element.

The results of this design iteration and the underlying rationale that is leading to each new antenna concept are summarized next. For the sake of brevity, and with regard to the element performance requirements specified in *Table 1.3*, only the *worst* results for the most critical performance parameters are displayed here, since the remaining parameters stay amply within the specifications [1]. Moreover, this summary is limited to 4 of the most representative RE candidates (i.e. from *Candidate #0* up to *Candidate #3*). The description of each element as well as its performance parameters considered here are displayed according to the template given in *Fig. 3.2*.

These results are going to confirm that most of the aforementioned critical performance parameters are strongly related to each other. And, though no optimum candidate clearly satisfying all the performance requirements related to these parameters is going to be found, a comparative analysis of the performances of the different elements will reveal valuable design trade-offs for the forthcoming development stages.

a) *Candidate #0*

With the basic S3FIP architecture illustrated in *Fig. 3.1*, *Candidate #0* constitutes the starting point of this design iteration. As shown in *Fig. 3.3*, the main weaknesses that this element presents for the targeted application are:

- The considerable **asymmetry in the radiation pattern** of the linearly polarized element and the consequent peaks in the AR of its circularly polarized counterpart, which may degrade the polarization tracking capabilities of the array. In this sense, it is illustrative to note how the ripple shown by the DLPRE pattern in the vicinities of $(\theta, \phi) = (-70^\circ, 90^\circ)$ leads to a pronounced peak of the AR that is located in the same direction of observation.³

This asymmetry is attributed to the combination of the offset feeding of the patch through its *Port 1* and the use of a relatively big patch, but the contribution of the near-resonant slot should not be excluded. In fact, for *Port 2*, whose smaller slot is centered with regard to the direction of resonance of the mode that it excites, this asymmetry is less pronounced. This will also be the case for the next RE candidate, in which the use of a smaller patch (while keeping almost the same size of the slot) will contribute to mitigate this asymmetry.

At this point it is worth to recall from *Section 2.5.1* that centered feeding structures such as that proposed in *Fig. 2.32(b)* and [3] show typically an improved symmetry of the radiation pattern. For these structures, the patch size and the spurious radiation from the uncovered line -the *upper feeding line* in *Fig. 2.32(b)*, for example- are considered to be the main causes of the pattern asymmetry [4, *Fig. 3.19(a)* and *Fig. 3.25(a)*].

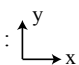
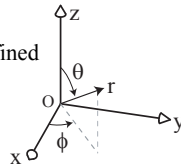
However, an overall compensation of this asymmetry as well as of its impact on the AR are expected to take place once the RE is embedded in an array where the all the elements are sequentially rotated. Such compensation is observed in several full-wave simulations of the whole array, as shown in *Fig. 3.4*.

³ $(\theta, \phi) = (70^\circ, 270^\circ) = (-70^\circ, 90^\circ)$.

Exploded view of the **Multilayer Buildup** of the Radiating Element :

- Dielectric Materials.
- Shorting Pins.
- Metallization Planes.

Layout of the Linearly Polarized Radiating Element :

<ul style="list-style-type: none"> - Layout Outline color code : <ul style="list-style-type: none"> — Upper Patch — Lower Patch — Slots — Shorting Pins — Feeding Lines - Patch Dimensions (<i>radius</i>). - Port Naming. - The layout is over the <i>XY</i> Plane. <p style="text-align: center;">Element Coordinate System : </p>	<p>Normalized Field Pattern of the Linearly Polarized Radiating Element</p> <ul style="list-style-type: none"> - Superimposed Elevation Cuts. - Copolar Component (in continuous line) and Xpol. (dashed) according to <i>Ludwig's third definition</i>. - The Angles (θ, ϕ) are defined according to the Element Coordinate System as : <p style="text-align: center;"><i>- Port 1 excited.</i></p> 
↓	↘
<p>Directivity of the Linearly Polarized Radiating Element</p> <ul style="list-style-type: none"> - The Directivity of the Radiating Element is displayed together with the Equivalent Directivity (D_e) that is associated to the <i>Array Lattice</i>. - As defined in <i>Chapter 1</i>, (1.1) and (1.2): $D_e = 4\pi \frac{A_e}{\lambda^2}, \quad \text{with } A_e = \frac{\sqrt{3}}{2} d^2.$	<p>Radiation Efficiency of the Linearly Polarized Radiating Element</p> <ul style="list-style-type: none"> - As it is defined in <i>Chapter 1</i>, (1.3): $\eta_\Omega = \frac{\text{Power Radiated}}{\text{Power Accepted}}$ <ul style="list-style-type: none"> - In the computation of the Radiated Power, given the high Polarization Purity of the different elements, no distinction is made between the contributions of the Copolar and the Xpol. components of the field.

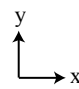
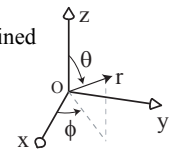
<p>Layout of the Circularly Polarized Radiating Element</p> <ul style="list-style-type: none"> - Layout Outline color code as for the Linearly Polarized Radiating Element. - Port Naming. - The layout is over the <i>XY</i> Plane. <p style="text-align: center;">Element Coordinate System : </p>	<p>Axial Ratio of the Circularly Polarized Radiating Element</p> <ul style="list-style-type: none"> - Superimposed Azimuthal Cuts within the elevation scan. - The Axial Ratio is as defined in <i>Appendix B</i>, (B.12). - The Angles (θ, ϕ) are defined according to the Element Coordinate System as : <p style="text-align: center;"><i>- Port 1 excited.</i></p> 
<p>Outline Layout of the Embedded Linearly Polarized Radiating Element</p> <ul style="list-style-type: none"> - As in the foreseen array, the replicas of the Radiating Element are disposed in a triangular lattice with an inter-element spacing of 0.54λ at 11.725 GHz. - The (7) replicas are sequentially rotated. The rotation angle is 120°. 	<p>Mutual Coupling between the Linearly Polarized Radiating Elements within the array of sequentially rotated replicas</p>
↓	↘
<p>Directivity of the Embedded Linearly Polarized Radiating Element</p> <ul style="list-style-type: none"> - The Directivity of the Radiating Element when surrounded by a ring of 6 sequentially rotated matched replicas. - The 6 replicas are <i>passively terminated</i> with matched loads. 	<p>Radiation Efficiency of the Embedded Linearly Polarized Radiating Element</p> <ul style="list-style-type: none"> - The Radiation Efficiency of the Radiating Element when surrounded by a ring of 6 sequentially rotated replicas. - The 6 replicas are <i>passively terminated</i> with matched loads.

Figure 3.2. Template with the description of the critical performance parameters of the candidate elements in different configurations: isolated (by default) and embedded. These critical performance parameters are summarized from *Fig. 3.3* to *Fig. 3.8*.

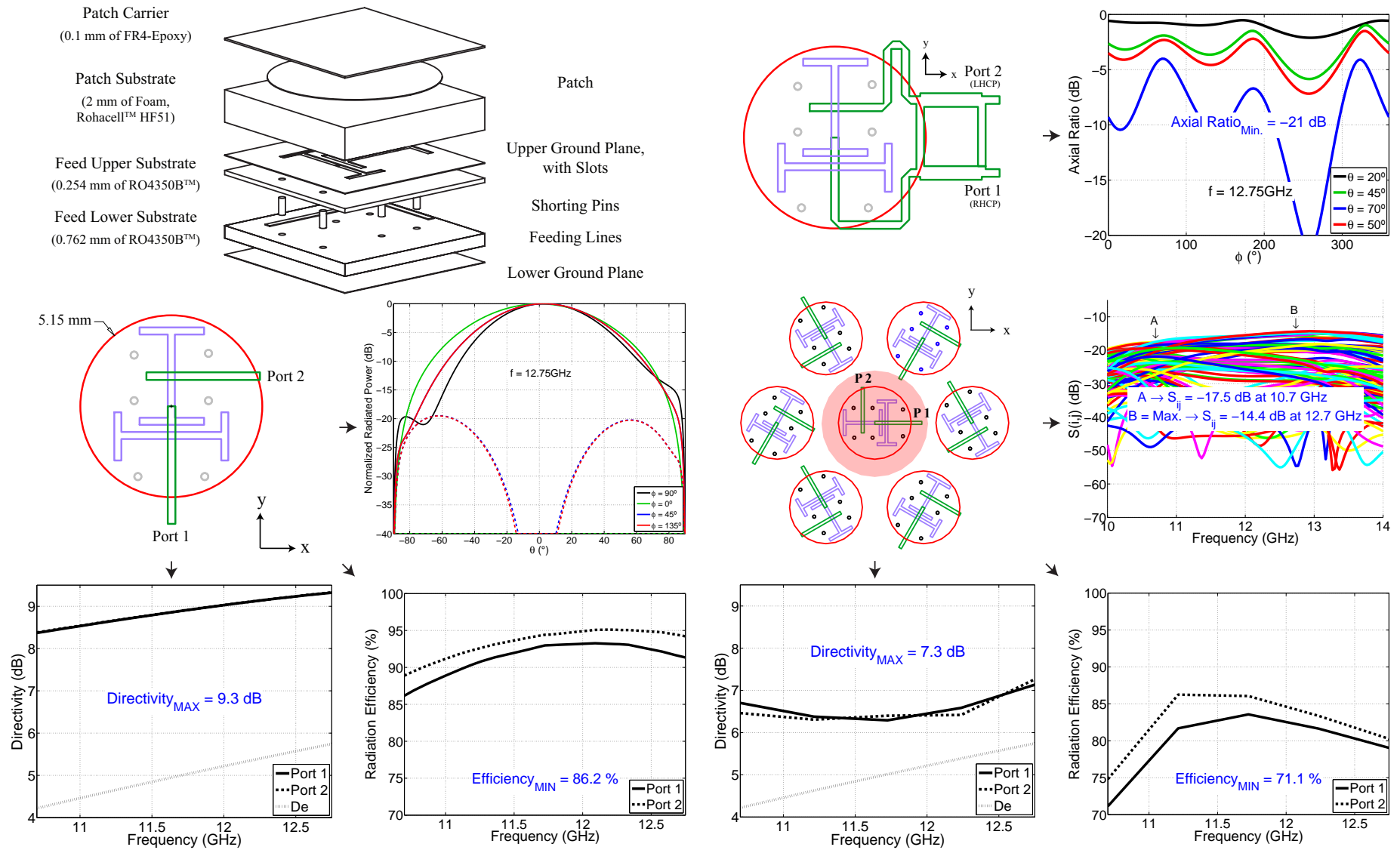


Figure 3.3. Critical performance parameters summary for Candidate #0.

It has also been observed that the embedding of the RE within smaller arrays with sequential rotation leads to an overall improvement of the element symmetry and its embedded AR.⁴ Actually, within a basic sub-array configuration of 7 elements, the worst-case AR of the embedded DCPRE is already found to improve between ~ 7 and 9 dB (see *Fig. 3.5*). Nonetheless, for small arrays, in which the variability of the embedded characteristics of the different elements is potentially high, the evaluation of the AR over the scan domain is more meaningful if it is carried out with *all* the elements excited. In this sense, it is important to note that, unlike the *embedded* AR, for the evaluation of this *active* AR in every scan direction, the phase progression applied to the illumination of the elements should be adjusted accordingly.

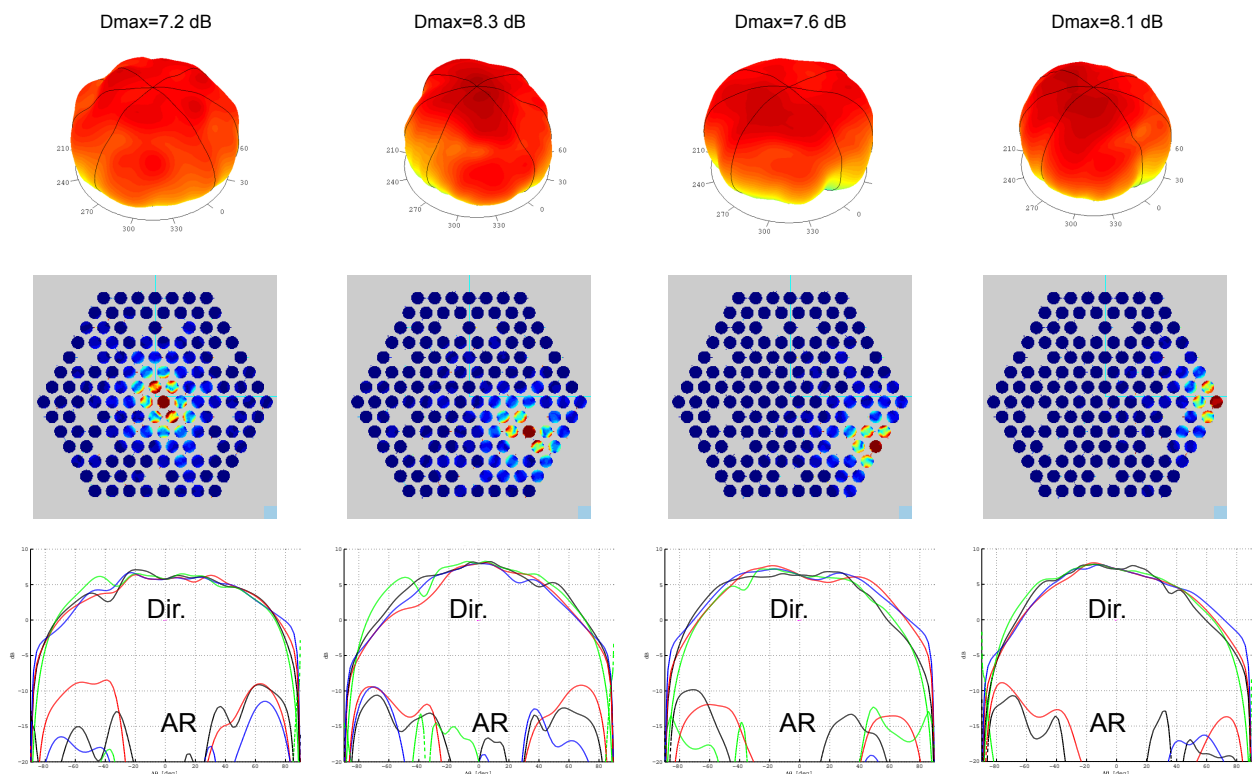


Figure 3.4. Embedded element patterns of the Linearly Polarized *Candidate #0* at 12.75 GHz. The patterns, that are displayed in the first and third rows, correspond to four different locations within the array aperture. The corresponding electric surface currents over the array elements are illustrated in the second row. In this middle row, the excited patch that corresponds to each pattern is identifiable by the color (red) assigned to the maximum of the current on its surface. All the remaining patches in the array are passively terminated with matched loads. These results have been obtained from a full-wave simulation of a preliminary version of the whole array (138 elements), where the elements are sequentially rotated. Note that there is no central element and that groups with a single element are not allowed, leading to the corresponding “holes” in the array layout. All coupling and loss effects are included in the simulation, together with the complete model of the DLPRE (substrates, vias, etc). The substrates and the ground planes are assumed to be of infinite extent. The code for the full wave simulation has been developed by Dr. D. Llorens (*JAST Antenna Systems*) and the image is also courtesy of him, from [5].

⁴Recall that, as defined in *Section 1.1.2*, the *embedded* AR assumes that only one element is excited, while all the other elements in the (sub)-array are passively terminated with matched loads.

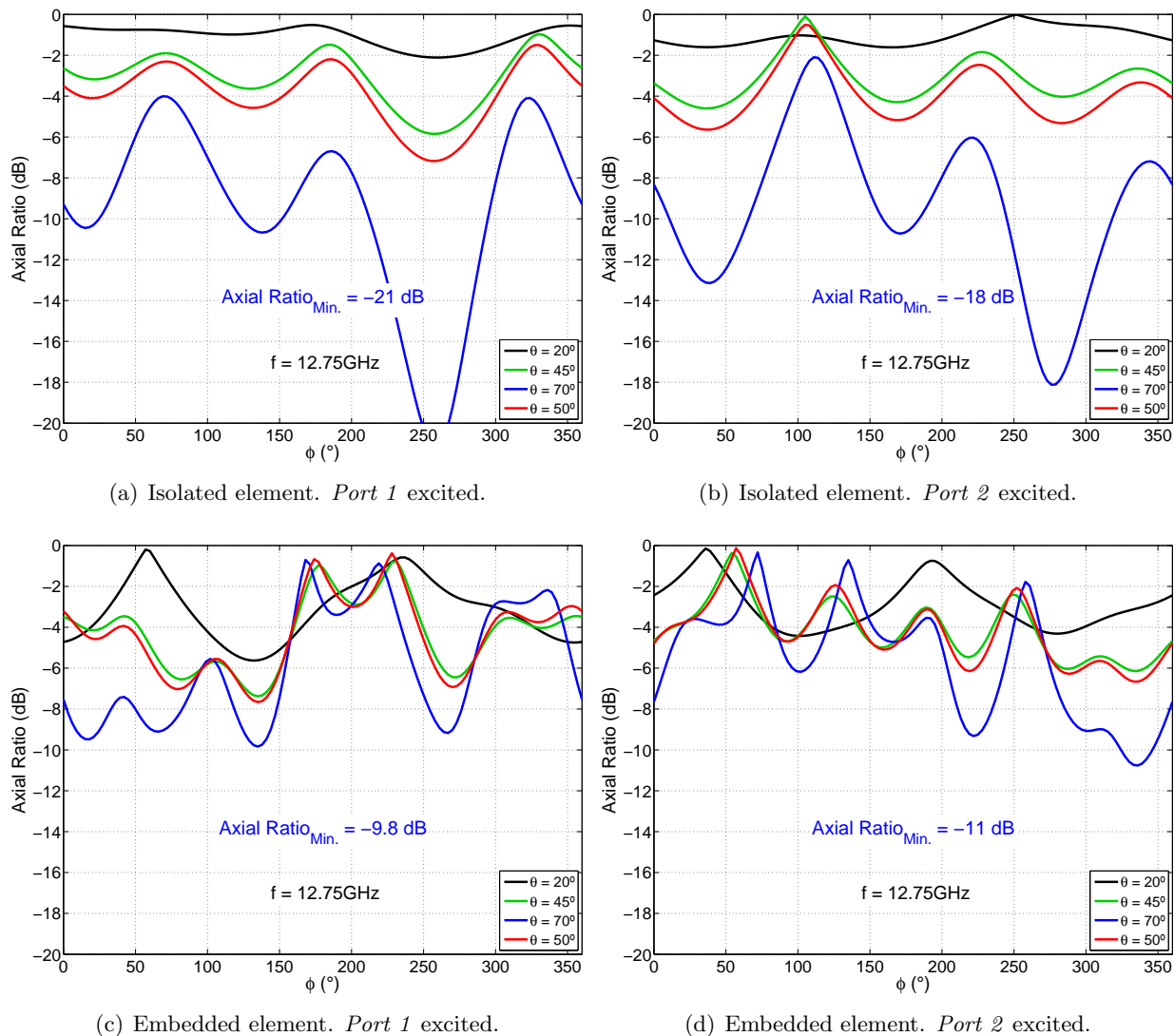


Figure 3.5. Axial Ratio of the Circularly Polarized *Candidate #0*. Superimposed Azimuthal Cuts within the elevation scan at 12.75 GHz, that is the most critical point of the frequency band. The angles (θ, ϕ) are defined according the Coordinate Systems specified in *Fig. 3.2* and *Fig. 3.3*. Note that, as it happens for the DLPRE, the coordinate system for the embedded version of the DCPRE is rotated 90° with regard to that of its isolated counterpart.

- The **excessive directivity** of the isolated element (9.3 dB at 12.75 GHz), that is not compatible with the low elevation scanning requirements and is rather far from the directivity given by the lattice of the foreseen array: recall (1.2), that yields a maximum directivity of ≈ 5.3 dB at 12.75 GHz. According to the considerations made by the end of *Section 1.1.2*, this excess in directivity bodes pronounced mutual coupling phenomena within the array antenna, which could call into question the validity of the present design approach, that focuses on the *isolated* element (recall *Section 1.1.2*). In these conditions, such phenomena may severely limit the performance of the *embedded* element and of the whole array.
- The high level of **mutual coupling** with its neighboring elements (up to -14.4 dB) when embedded into the basic sub-array configuration of 7 elements. This level of mutual coupling is related with the significant reduction in directivity (~ 2 dB) and radiation efficiency ($\sim 15\%$) observed for the embedded element.

b) *Candidate #1*

In order to reduce the directivity of *Candidate #0*, the patch size is scaled down by increasing the permittivity of its substrate. As displayed in *Fig. 3.6*, this maneuver has the following consequences:

- a reduction of ≈ 1 dB in directivity is observed.
- The ripple in the radiation pattern of the DLPRE has disappeared. However, a certain degree of asymmetry is still noticeable and the AR of the DCPRE shows some peaks of about ~ 8 dB.
- In the sub-array configuration, the level of mutual coupling with its neighboring elements is now reduced to ≈ -16.6 dB and the corresponding variations in directivity and radiation efficiency are also relatively small (≈ 0.7 dB and $\approx 3\%$, respectively). This reduction of the mutual coupling is attributed, basically, to the miniaturization of the patch.
- However, the embedded radiation efficiency of this element is still close to that of *Candidate #0* ($\sim 70\%$). This reduced efficiency is attributed mainly to a more severe surface wave power leakage, which is associated to the increase of the permittivity of the patch substrate.

c) *Candidate #2*

With the aim to improve the surface wave efficiency, the patch substrate is made thinner, and, to keep the bandwidth of the original element, a second proximity coupled patch with a thin foam substrate is added to the stack up, leading to the *stacked patches* configuration depicted in *Fig. 3.7*. The main trends observed in the performance of the RE are as follows:

- the level of directivity remains below ≈ 8.5 dB, quite close to that of *Candidate #1*.
- The symmetry of the radiation pattern is significantly improved and the AR of the circularly polarized element is better than ~ 7 dB.
- In the sub-array configuration, the level of mutual coupling with its neighboring elements is almost the same observed for *Candidate #1* (-16.7 dB), but the corresponding variations in directivity and radiation efficiency have increased (up to 1.7 dB and $\sim 6\%$, respectively).
- The most remarkable weakness of the actual element is, in fact, its reduced level of radiation efficiency when embedded in the sub-array configuration, whose lowest value is $\sim 75\%$.

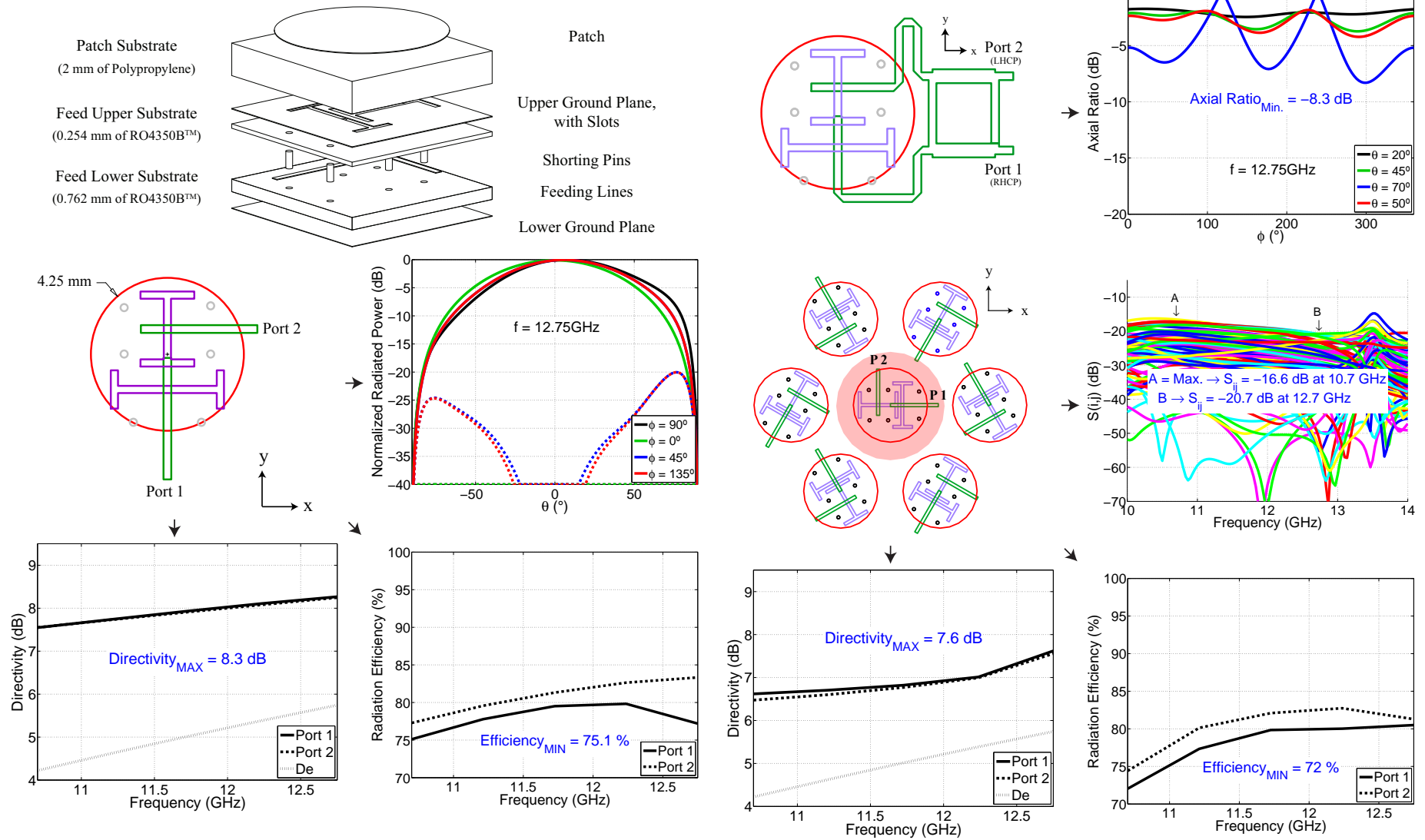


Figure 3.6. Critical performance parameters summary for Candidate #1.

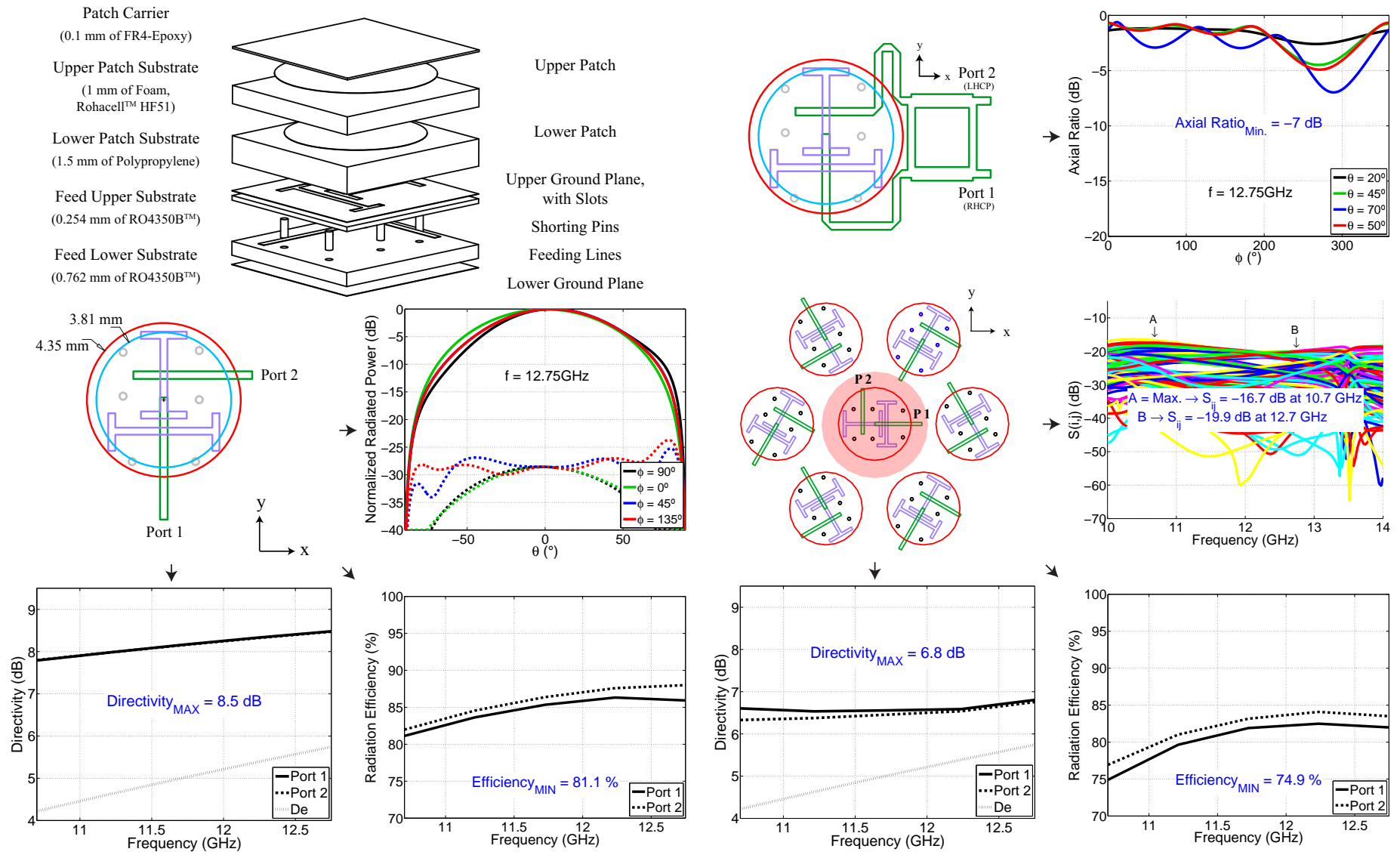


Figure 3.7. Critical performance parameters summary for Candidate #2.

d) *Candidate #3*

In order to further improve the radiation efficiency of the element with regard to *Candidate #2*, the lower patch substrate is made even thinner, while the foam substrate thickness is increased. With this stacked patches configuration, *Fig. 3.8* reveals that:

- the level of directivity increases up to ≈ 8.9 dB, only ≈ 0.6 dB below that of *Candidate #0*.
- The symmetry of the radiation pattern suffers a noticeable degradation and the axial ratio of the circularly polarized element has a peak of ~ 10 dB.
- In the sub-array configuration, the level of mutual coupling with its neighboring elements rises up to -15.8 dB, which has a significant impact on the corresponding variations in directivity and radiation efficiency (2.1 dB and $\sim 9\%$, respectively).
- However, the level of embedded radiation efficiency is the highest observed up to now ($\sim 79\%$).

3.2.2 Proof of Concept

a) Radiating Element Candidates Update

Among the candidate elements proposed in the previous section, one of the most simple ones is chosen to proceed with the empirical assessment of the concepts proposed for the RE feeding and the polarization tracking at sub-array level. This radiating element is based on *Candidate #1*, with certain modifications on the dielectrics of its multilayer buildup. The comparison of the buildups in *Fig. 3.6* and *Fig. 3.9* reveals the nature of such modifications, that are made according to the materials on stock by the time of prototyping, in order to further speed up the implementation of the element and the sub-array.

Though the time constraints for this design stage did not allow to complete the optimization of the new radiating element (*Updated Candidate #1*, hereafter), its performance is not too far from that of *Candidate #1*. For this reason, *Updated Candidate #1* is considered to be good enough for the intended proof of concept.

As will be shown next, this last consideration is also supported by the results of a preliminary investigation on the application of the *cavity backed* technique to improve the design of the element. Among other interesting results, this investigation reveals that *Updated Candidate #1* is actually matching, and even exceeding, the performances of a couple of basic cavity backed elements that are designed under the same structural constraints that the element without cavity.

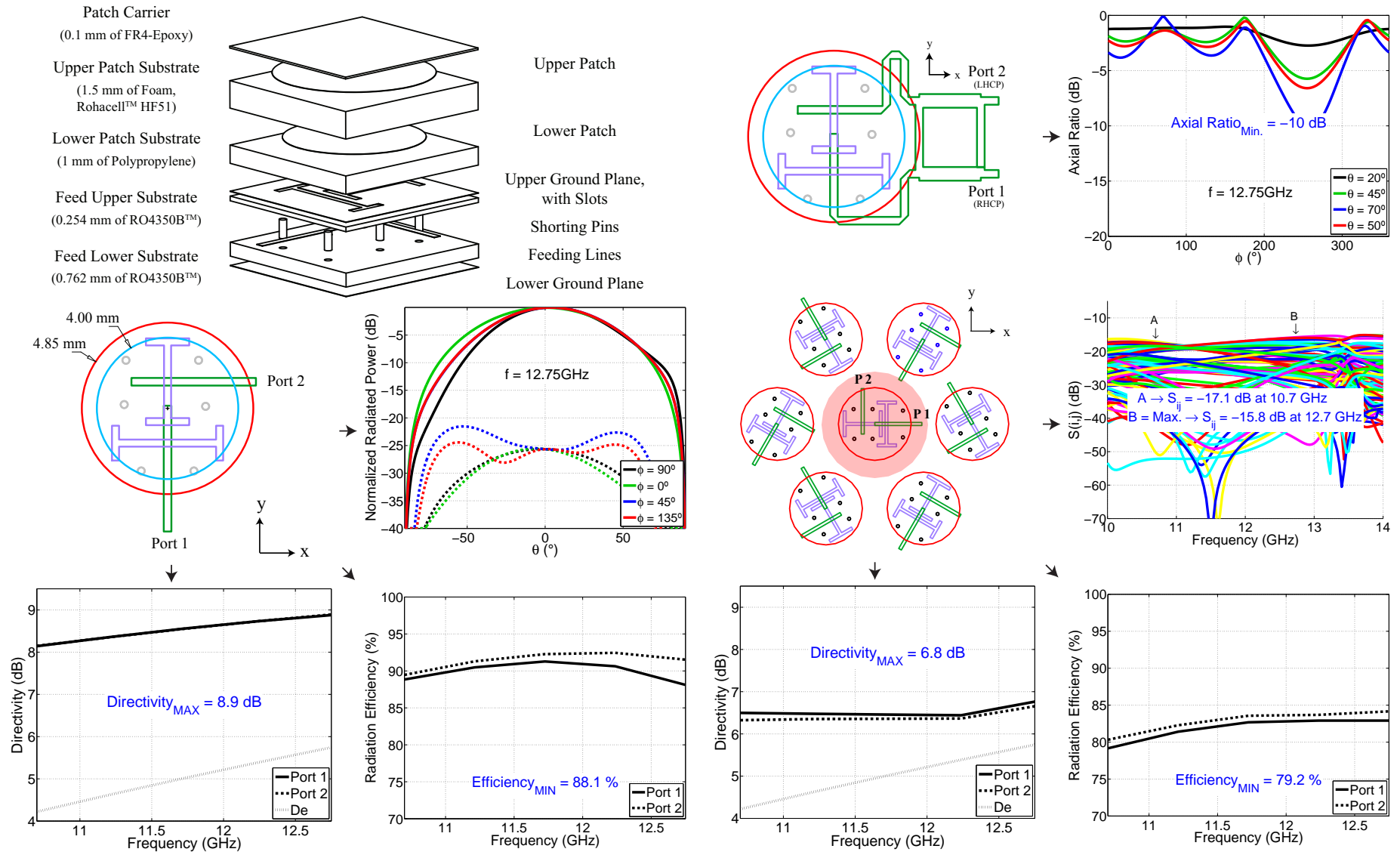


Figure 3.8. Critical performance parameters summary for Candidate #3.

a.1) Updated Candidate #1

The basic structure of *Updated Candidate #1*, displayed in *Fig. 3.9*, is composed of four layers of metalization (the patch, the slotted ground plane, the feeding lines and a shielding ground plane), three kinds of dielectric materials, whose electric characteristics are summarized in *Table 3.2*, and six metallic posts (shorting pins), which vertically cross part of the stack and connect both ground planes. For the sake of simplicity, certain auxiliary layers (as the the glue layers in between the stripline dielectrics -35 μm of VliesofixTM- and around the patch substrate -50 μm of 3MTM 300LSE) are not shown in the exploded view of the buildup.

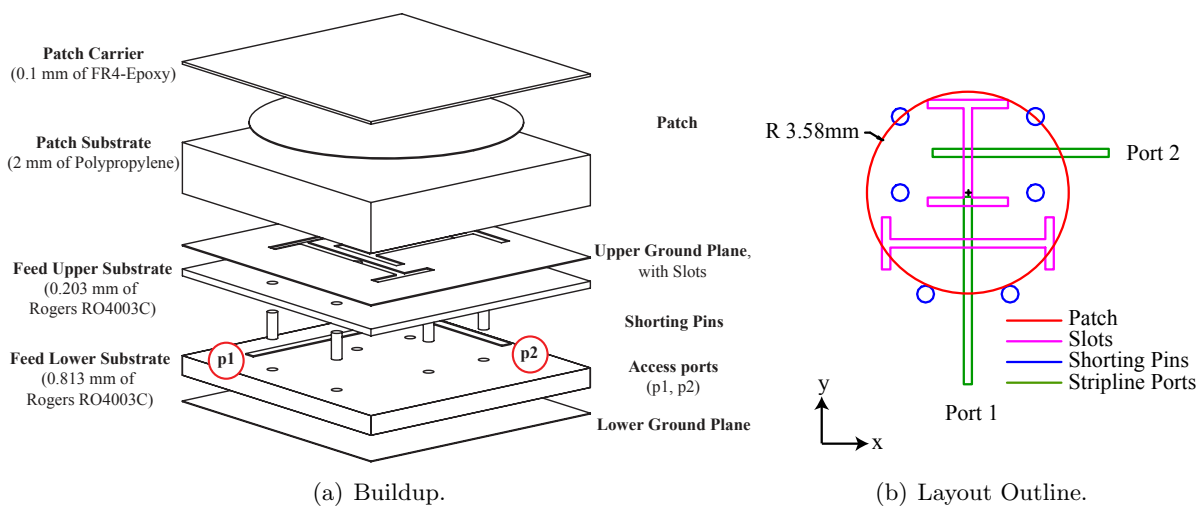


Figure 3.9. *Updated Candidate #1* Structure.

Commercial name	ϵ_r	$\tan \delta$
FR4-Epoxy	4.4*	0.02
3M TM 300LSE	2.2*	0.035
Polypropylene	2.18*	0.0042
RO4003C TM	3.55	0.0027
Vliesofix TM	2.33*	0.0013

* Estimated values.

The most critical incertitude is associated to Polypropylene, for which $\epsilon_{r\text{-typ.}} \in (2, 2.3)$.

Table 3.2. Characteristics of the dielectrics materials of *Updated Candidate #1*.

As its predecessor, *Updated Candidate #1* suffers mainly from the power leakage due to the surface waves that propagate in the patch substrate.⁵ In order to mitigate this power leakage, the possibility of applying the *cavity backing* technique is judged to deserve some attention. Due to time constraints, only a perfunctory investigation in this direction is carried out.

a.2) *Cavity Backed Candidates*

For the present application, the maximum size of the cavity is determined by the array lattice, that allots to each element a hexagon whose minimum diameter (given by the inter-element spacing) is $0.54 \lambda_0 \approx 13.8$ mm. This, together with their manufacturing simplicity, advises the use of cylindrical cavities. Moreover, a minimum wall thickness of ≈ 1 mm is left between neighboring cavities to guarantee a certain mechanical solidity of the resulting metallic honeycomb. This leads to a maximum cavity radius of 6.4 mm.

The design approach used here can be readily anticipated by inserting the patch substrate of *Updated Candidate #1* in such a cavity and observing its impact on the input impedance of the RE. This is illustrated in *Fig. 3.10* for a cavity of 6.2 mm radius. The figure reveals that, according to the broadening of the impedance loops observed, the insertion of the cavity should increase, up to a certain extent, the coupling between the feeding lines and the patch. This phenomenon is consistent with the reduction of the power absorbed by the surface waves, in an analogous way as it happens when the power leakage due to PPWMs is mitigated by inserting shorting pins in the feeding part of an S3FIP.

On the other hand, the noticeable shift of the impedance loops towards the left of the Smith Chart that accompanies their broadening reveals also that, for the actual element, an increasing proportion of the energy coupled to the patch is not actually radiated, but stored in the cavity itself. Actually, as the radius of the cavity approaches that of the patch, the cavity tends to close and, therefore, the impedance loops tend to go towards the outer contour of the Smith Chart, as it would correspond to a purely reactive load.

In practice, the cases studied here are restricted to patches over propylene or foam substrates within cavities whose overall height does not exceed the thickness of the patch substrate of *Updated Candidate #1* (2 mm). Under these conditions, it is found that a broadband operation of the RE, in terms of impedance matching, can be achieved when the radius of the cavity is close to its maximum (6.2 – 6.4 mm). This approach is, in fact, compatible with impedance loops of moderate radius, that can be conveniently reduced and shifted to the right of the Smith Chart by using some of the techniques proposed in *Section 2.4.3*.

⁵One of the the most critical performance parameters of *Updated Candidate #1* remains its radiation efficiency. The most realistic models of this element consider (among others) an increased value of the permittivity of the patch substrate (polypropylene in *Table 3.2*) and a reduced conductivity of the metalization layers, which accentuates this weakness. In fact, these models predict a minimum level of radiation efficiency close to 62% [6], that is considerably below ($\sim 8 - 13\%$) the efficiency estimated for *Candidate #1* [2,7]. In this sense, it must be said that, besides a better design of the element, this last estimation is based on a simpler element model of *Candidate #1* and on a lower value of the polypropylene permittivity, with the consequent reduction of the power leakage due to surface waves in the patch substrate.

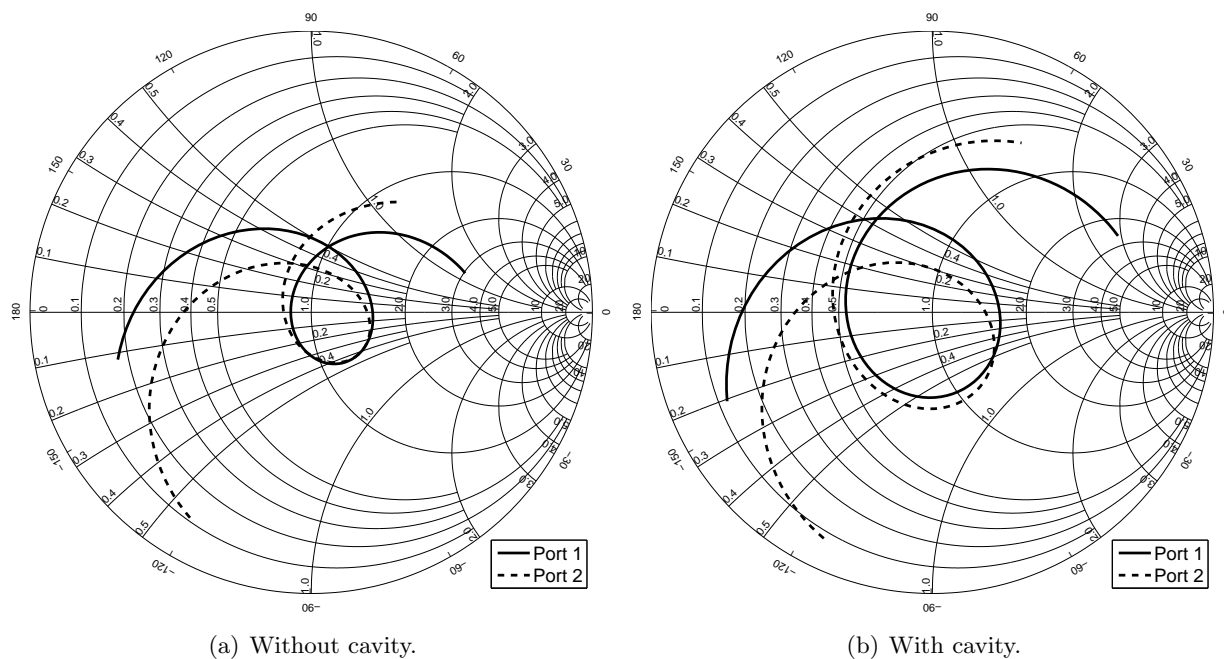


Figure 3.10. Effect of the inclusion of a *backing cavity* in the input impedance of *Updated Candidate #1*. As usual, the reference planes for the impedance are shifted along the feeding lines up to the center of the slots and the normalization impedance is the characteristic impedance of the lines (50Ω).

For example, the design of the couple of cavity-backed elements depicted in *Fig. 3.11* is based, essentially, on a weakening of the *coupling factor* by means of the reduction of the size of the slots and an increase of the width of the feeding lines in the vicinity of the slots. The shift of the impedance loops towards the right of the Smith Chart is achieved, basically, with a small tuning circuit that consists on a couple of symmetric shunt open stubs.⁶

The impedance matching characteristics of the resulting DLPRE cavity-backed elements are shown in *Fig. 3.12*, where an effective reduction of the radius of the impedance loops and their centering in the Smith Chart can be appreciated. The compliance with the matching requirements remains, however, rather tight.⁷ For microstrip antennas this is an important limitation, since it makes the resulting design too sensitive to manufacturing tolerances.

The introduction of the cavity leads to a considerable improvement in terms of radiation efficiency with regard to *Updated Candidate #1*, whose minimum level is close to 62%. According to *Fig. 3.13*, this improvement is around 16 – 18%, which highlights the important role of the surface waves in the performance of the RE. However, the improvement in terms of mutual coupling is negligible [2]. In fact, an investigation of the coupling mechanisms between two adjacent replicas of each one of the 3 candidate elements considered here reveals that, in all cases, most of the mutual

⁶In principle, it would suffice with a single open stub. However, in view of its proximity to the slot, a symmetric configuration for this matching network is preferred to maintain the excitation of the slot as symmetric as possible.

⁷Unlike the port isolation characteristics, that exceed largely the specifications (better than 40 dB from 9 up to 14 GHz). This high level of isolation is attributed, mainly, to the arrangement of the feeding slots (recall *Section 2.5.1*).

coupling takes place through the free space over the patches, and not through the patch substrate (via surface waves, for the element without cavity) nor the triplate feeding (via PPWMs) [2].

The most important drawback of the proposed cavity backed elements is related to the shape of their radiation patterns, that suffers from a significant lack of azimuthal symmetry, especially at low elevation angles. This is evident in *Fig. 3.14*, where the patterns of both candidates are compared.

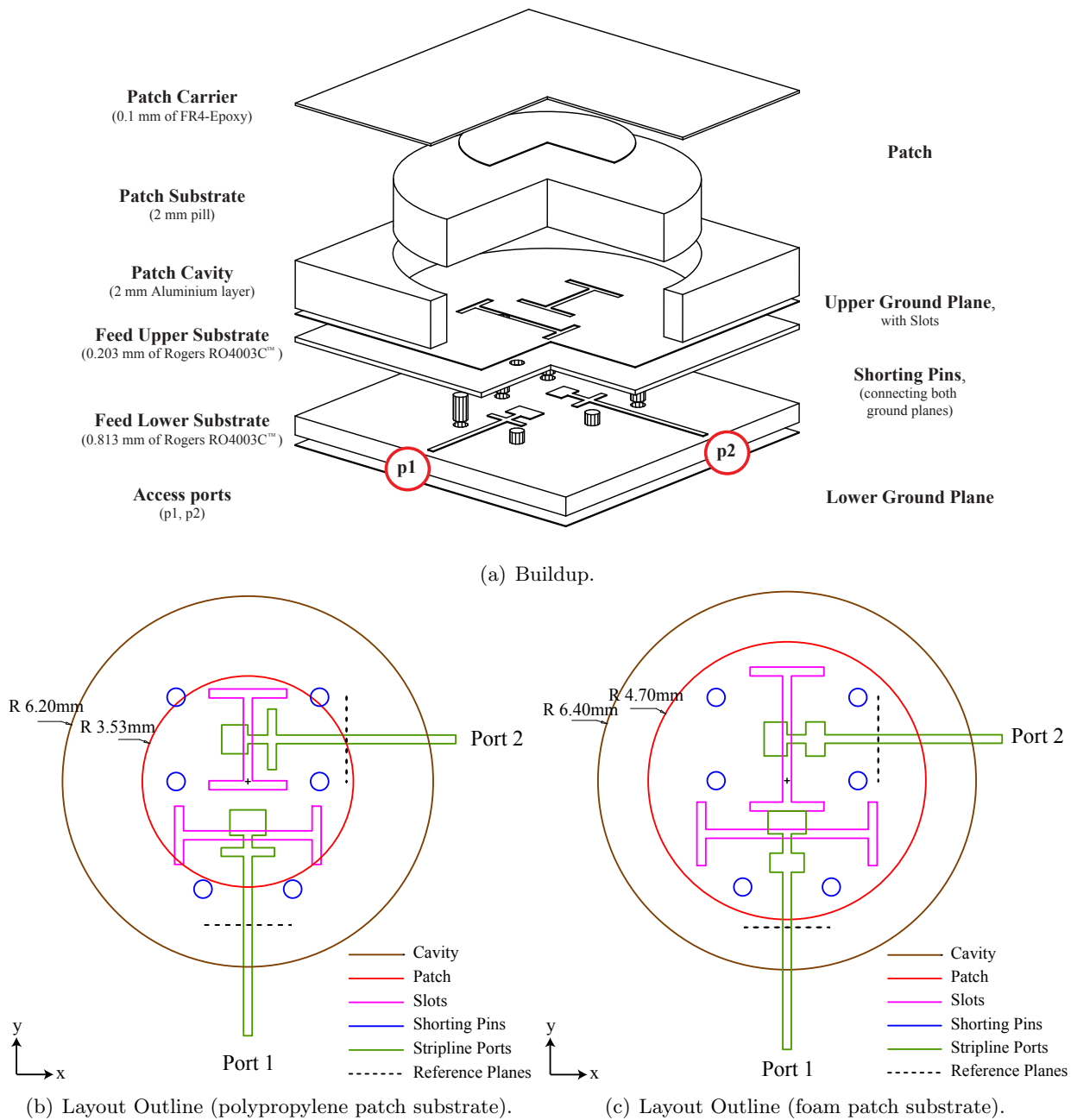
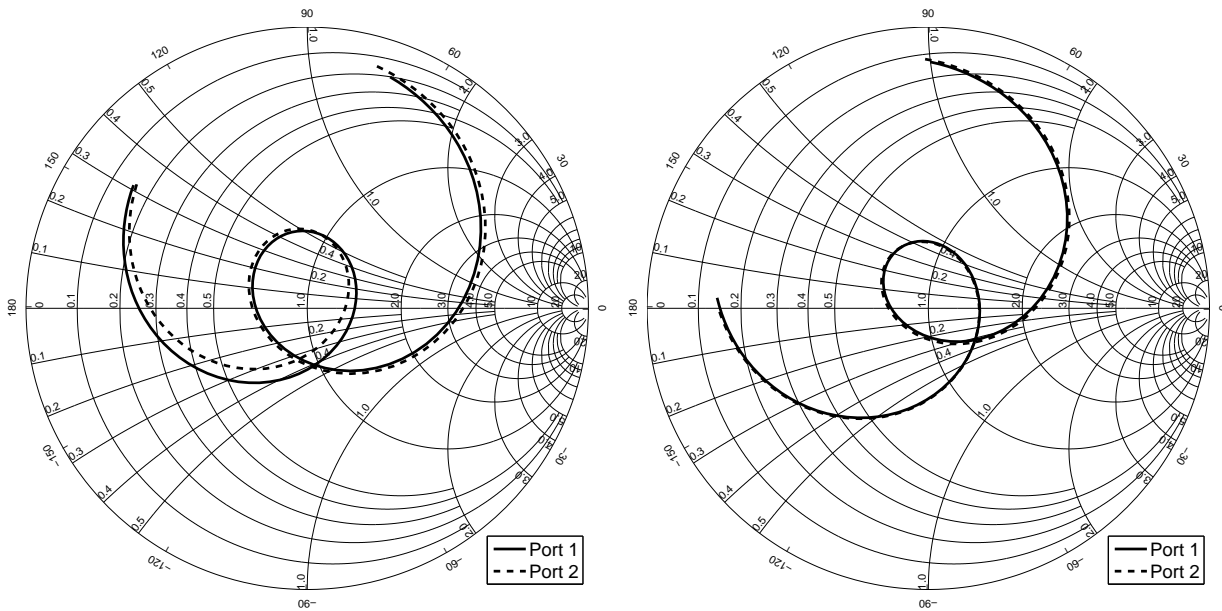
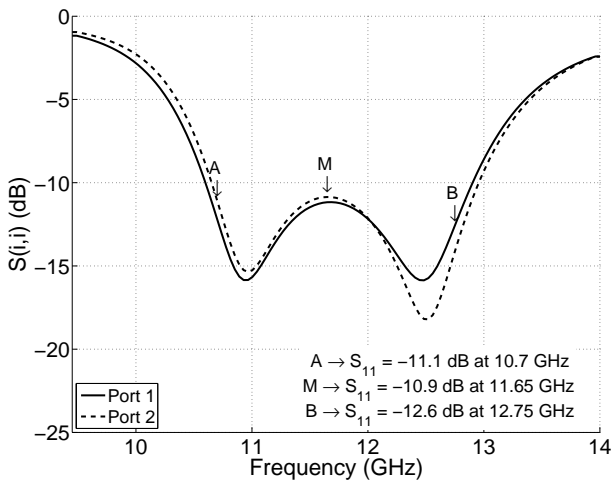


Figure 3.11. Structure of the cavity backed elements: *Candidate #4* (polypropylene-based) & *Candidate #5* (foam-based).

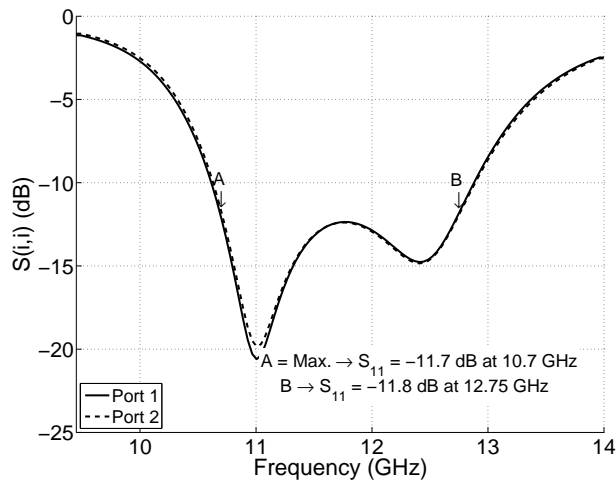


(a) Input Impedance. Candidate #4.

(b) Input Impedance. Candidate #5.



(c) Impedance Matching. Candidate #4.



(d) Impedance Matching. Candidate #5.

Figure 3.12. Impedance matching characteristics of the cavity backed elements. In this case, the location of the reference planes for the input impedances is given by *Fig. 3.11(c)* and *Fig. 3.11(b)*.

This asymmetry has been observed in other cavity backed patch antennas and its mitigation seems to be compatible with the *stacked patches* technique [8,9].⁸ The asymmetry in the patterns of the DLPREs leads, for their circularly polarized counterparts, to the rapid degradation of the AR at low elevation angles that is evidenced in *Fig. 3.15* and [9, Fig. 16].

⁸This is actually a promising path to explore for the present application, also with regard to the limitations in impedance bandwidth (and cavity radius) discussed above. Such an investigation is, however, out of the reach of the perfunctory study intended here.

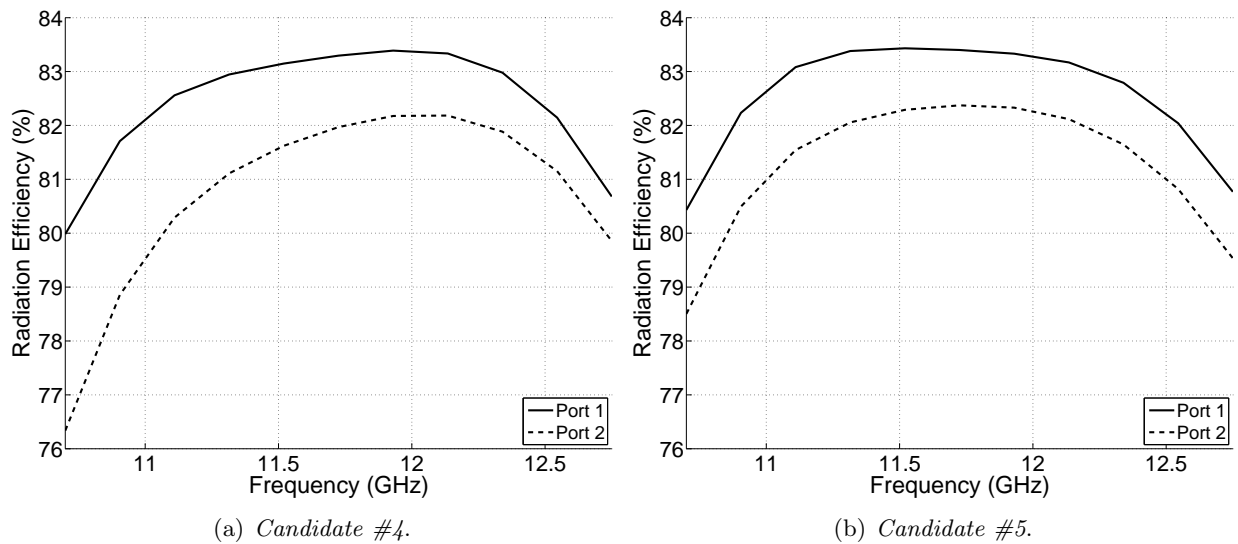


Figure 3.13. Radiation efficiency of the cavity backed elements.

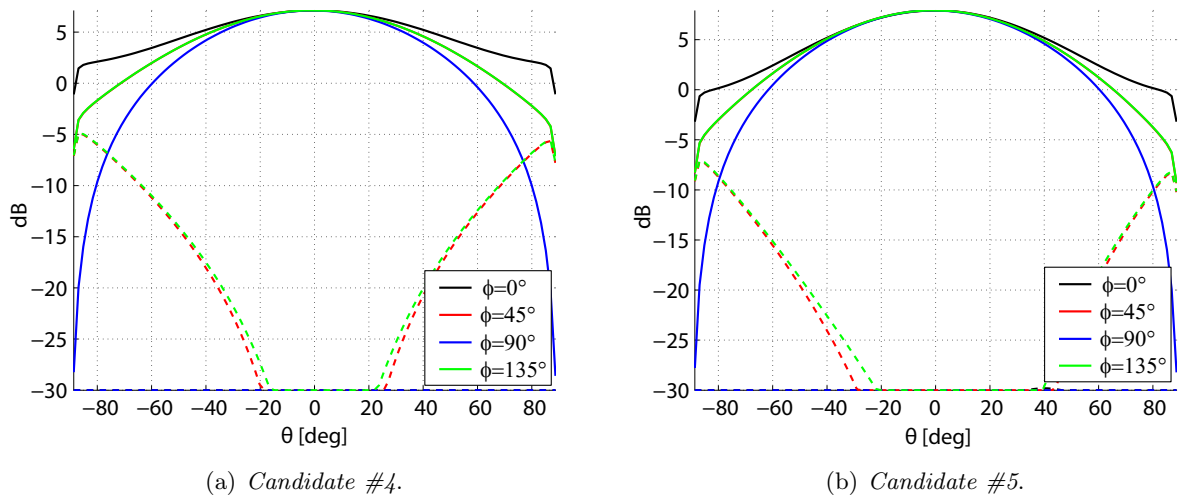


Figure 3.14. Field patterns of the linearly polarized cavity backed elements. Elevation cuts at $f = f_0 = 11.725$ GHz. Port 1 is excited. Co-polar (—) and cross-polar (- -) components.

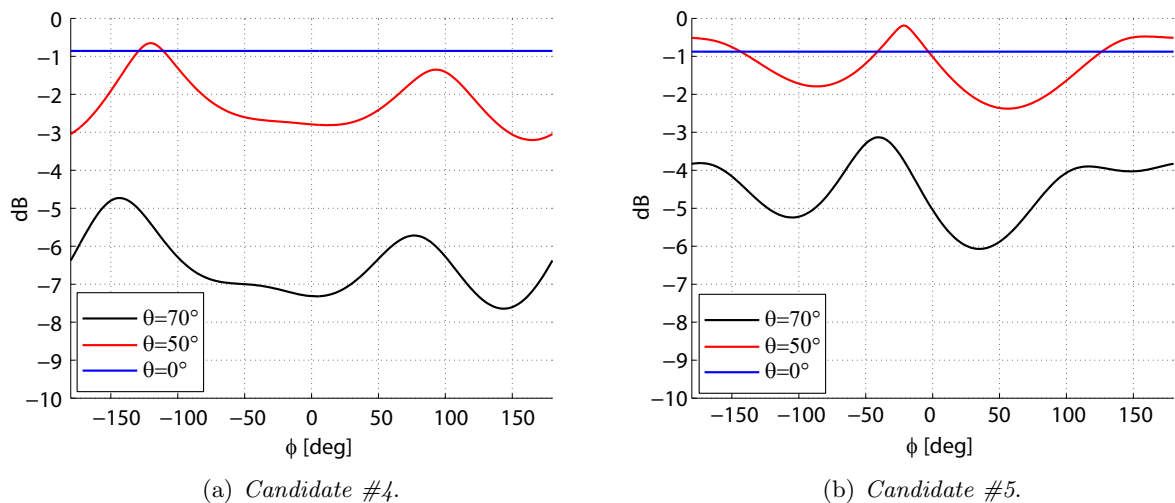


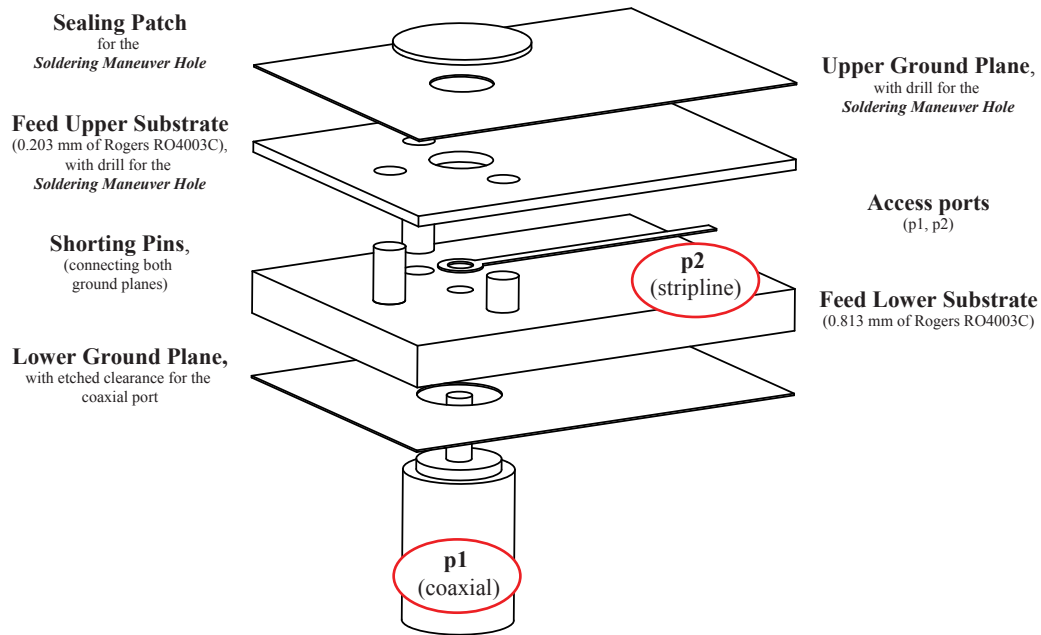
Figure 3.15. Axial ratio of the circularly polarized cavity backed elements. Azimuthal cuts at $f = f_0 = 11.725$ GHz. Port 1 is excited.

b) Radiating Element Feeding

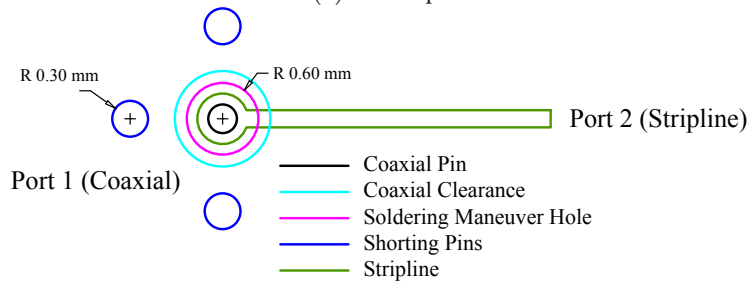
The access to the stripline ports of the RE represents one of the major technological challenges for its practical implementation. This access should be compatible with both ease of prototyping (not far from standard planar processes) and EM performance (using preferably robust and repeatable coaxial connections), not to cast a shadow over the real performance of the element under test.

b.1) Miniature Coaxial-Stripline Transition

The access to the stripline ports of the RE is conceived as a shielded miniature right angle coaxial to stripline transition, whose basic structure is depicted in *Fig. 3.16*. For the sake of simplicity, certain auxiliary layers (as the the glue layer in between the stripline dielectrics, $35 \mu\text{m}$ of VliesofixTM) are not included.



(a) Buildup.



(b) Layout Outline.

Figure 3.16. Miniature Coaxial-Stripline Transition.

This transition, as well as the RE itself, are designed for their manual fabrication using photolithographic process without metalized holes. This choice is made to enable several fast prototyping iterations as well as for the minimization of the diameter of the vertical connections. Actually, it is found that the miniaturization of the transition contributes to improve its performance. In particular, the diameter of the vertical connection that corresponds to the coaxial pin is found to play an important role in the matching of the transition, and its minimization is advised. With regard to the shorting pins, that are intended to guarantee a good electrical contact between the ground planes and to mitigate the deleterious effects of the PPWMs excited in the vicinities of the transition, the minimization of their diameter eases the optimization of their placement.

On the other hand, this manufacturing choice imposes certain constraints in the design of the transition and in the implementation of the vertical connections. These constraints are related, mainly, to the need of the so-called *Soldering Maneuver Hole* (see *Fig. 3.16*) for the connection of the coaxial pin and the use of *conductive glue* (EPO-TEK[®] *H20E* [10]) for the implementation of the shorting pins. The use of this glue allows to minimize the protrusion, over the ground planes, of the shorting pin connections. Such protrusion becomes of considerable practical importance when it comes to accommodate the patch substrate (polypropylene) over the slotted ground plane (see *Fig. 3.17*).

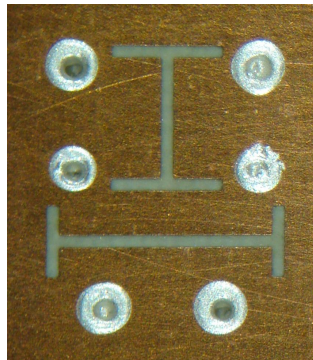


Figure 3.17. Detail of the slotted ground plane of the S3FIP as fabricated. The silver dots correspond to the conductive glue used for the implementation of the shorting pins.

The Soldering Maneuver Hole enables the tinning of the coaxial pin to the stripline pad once the stripline assembly has been properly glued, which simplifies this critical step and prevents the damaging of the coaxial connector. This approach implies, however, the need of “several press processes” if more dielectric layers were to be stacked over the *upper ground plane* in *Fig. 3.16(a)*, as well as to clean out from the maneuver hole all the glue that gets accumulated during the first press process. The reduced size of the maneuver hole and the resilience of the glue make of this cleaning a delicate process, that is briefly sketched in *Fig. 3.18*.

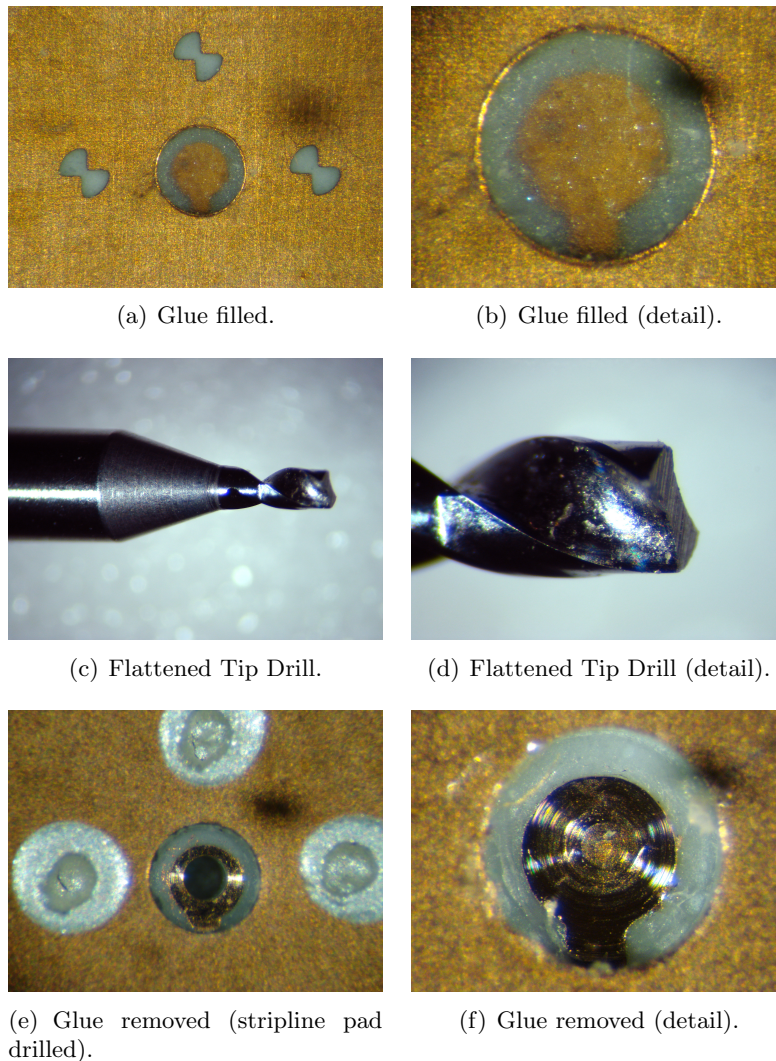
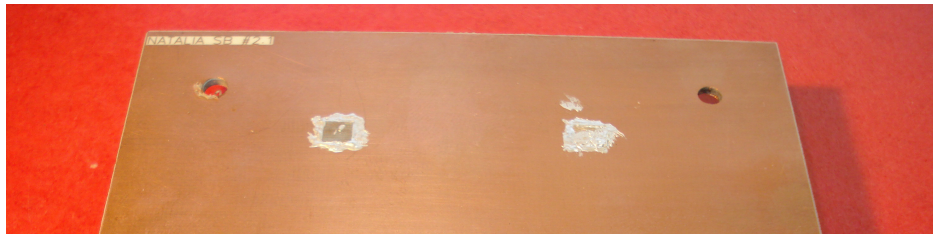


Figure 3.18. Glue removal from the Soldering Maneuver Hole using a Flattened Tip Drill.

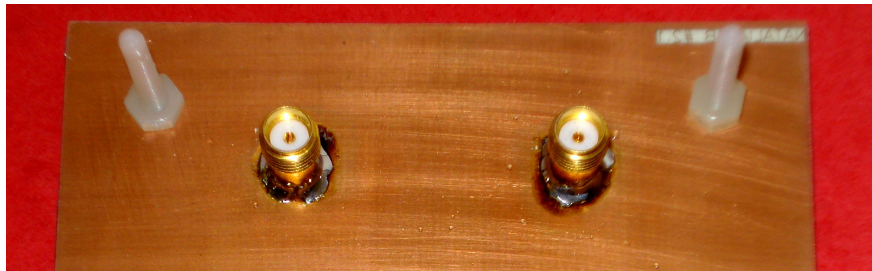
Fig. 3.19 shows an assembled prototype of the coaxial to stripline transition in a back-to-back configuration, ready for the measurement of its performance.⁹ The measured values, displayed in *Fig. 3.20*, keep in reasonable agreement with predicted results, provided the tolerances of the manual fabrication of the transitions. These tolerances are evidenced, for example, by the differences observed between the impedance matching levels at the terminals of the prototype, that should be identical.

The good performance of the transition is assessed by the impedance matching and the insertion loss levels observed for the back-to-back prototype. According to simulation results, these levels should keep better than 22 dB and 0.6 dB, respectively, in the working frequency band of 10.7-12.75 GHz for the transition from coaxial to a stripline whose length is the half of the back-to-back prototype (1.5 cm).

⁹At this point, the decisive contributions of Mr. J.-F. Zürcher (Scientific Associate at EPFL-LEMA) as well as the Printed Circuits Workshop (EPFL-STI-ACI) team to the conception and manufacturing of the transition are duly acknowledged.



(a) Upper Ground Plane view, with sealing for both transitions.



(b) Lower Ground Plane view, with coaxial terminals.



(c) Detail view of the Huber & Suhner 22-SMA-50-0-12/111NE coaxial panel connector.

Figure 3.19. Prototype of the coaxial to stripline transition in a back-to-back configuration, with details of the coaxial connector. The total length of the stripline section is 3 cm.

Actually, the electrical and mechanical performances of the transition are considered to be so promising, that a variation of this transition is developed, this time in collaboration with *JAST Antenna Systems*, for the test of the array Feeding Network as well as other stripline circuits. This variation concerns essentially the suppression of the Soldering Maneuver Hole, which has many technological advantages. In particular, the delicate glue removal operation should be avoided and the compatibility with a multilayer “single press process,” that is also of great practical importance, should be addressed.

The experience gained in the design of this kind of transitions allowed to envisage their industrial fabrication, that is a rather costly and slow prototyping process, with a certain confidence in minimizing the number of iterations. In particular, the possibility of a more efficient implementation of vertical interconnections (vias) offered by an industrial PCB processing is exploited to develop a competitive connector mounting approach for stripline circuits. This approach rivals the classical microstrip edge mounting in simplicity and robustness, at the expense of a performance trade-off.

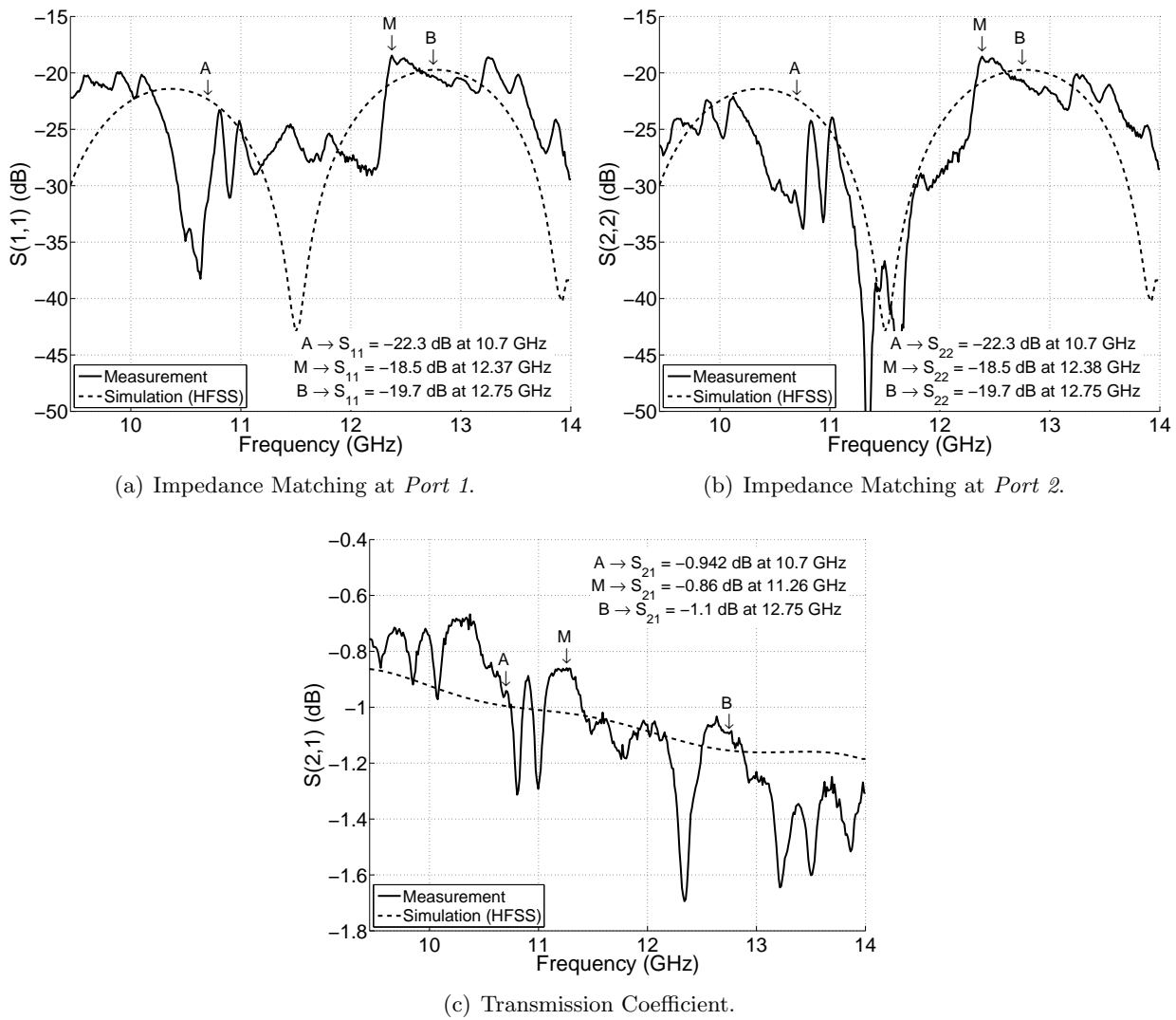


Figure 3.20. Scattering Parameters of the “coax.-stripline-coax.” prototype. The total length of the stripline is 3 cm. Simulated results are obtained using an improved model of the coaxial connector. In [7], the model for the connector does not include, among others, the air gap between the dielectric of the coaxial and the clearance of the *lower ground plane* in Fig. 3.16(a).

This performance trade-off is related to the increase of the diameter of the vertical connection that accesses the stripline. And, as it was expected, this increase leads to a degradation of the impedance matching of the transition. Actually, this thicker vertical connection is implemented as a hollow blind via in whose bosom the pin of the panel connector can be conveniently accommodated, as it can be seen in Fig. 3.21(a). The electric connection within this hollow can be guaranteed by a small dose of conductive glue that is deposited into it before the introduction of the pin of the connector. In practice, the temperature required for the curing of the glue can be attained by heat conduction during the soldering of the body of the connector to ground or by directly heating the outer extreme of the coaxial pin, which enables the “blind mounting” of the connector.¹⁰

¹⁰This procedure should be applied with caution to avoid the degradation of neighboring materials due to over-heating.

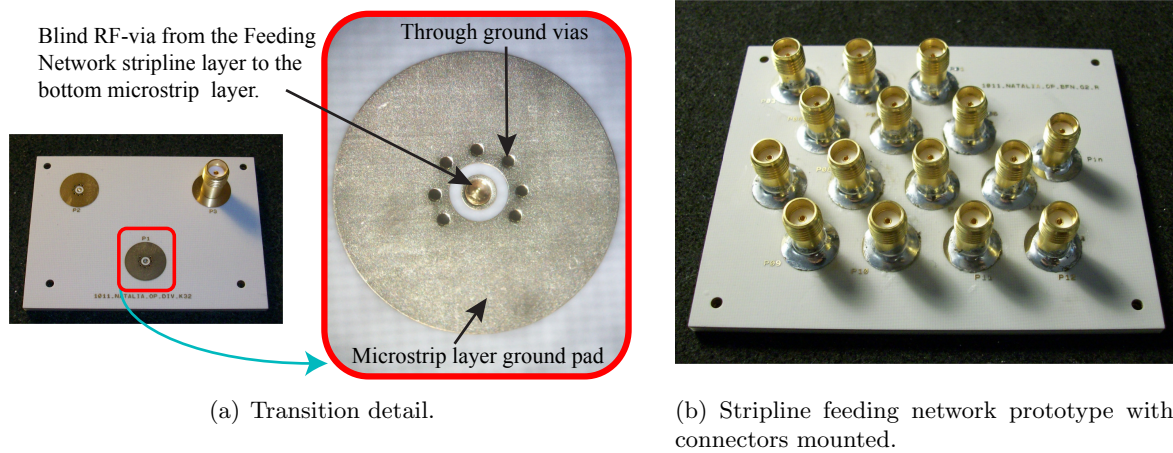


Figure 3.21. Blind mounting of the coaxial to stripline transitions. This image is courtesy of Mr. J. Padilla (*JAST Antenna Systems*), who was deeply involved in the design and fabrication of the feeding network and the transitions themselves.

Another advantage of this transition is that its vertical mounting enables the access to densely packed multi-port devices, as it is the case of the foreseen feeding network. This is illustrated in *Fig. 3.21(b)*, where a prototype of a portion of the array feeding network with all the connectors mounted is shown.

The performance of this transition within a back-to-back configuration is displayed in *Fig. 3.22*. In this case, the concordance between the measured performance and predictions is rather limited. The reasons for this disagreement do not seem evident for the author, who, given the good repeatability of the connections,¹¹ would not attribute these differences to the mounting of the connectors, but rather to the PCB assembly of the transition.

In fact, besides the fabrication tolerances, the modeling of the PCB assembly of the actual transition is considered to suffer, unlike its preceding version, from a limited knowledge of its implementation details. Nonetheless, the measured performance of the back-to-back configuration keeps very promising and supports the expectation that the transitions involved are actually performing well. In particular, the insertion loss of the transition from coaxial to a stripline of 1.5 cm of length should be compatible with the predicted level of 0.7 dB in the working frequency band, which fulfills the prototyping needs.

b.2) Radiating Element Performance

Once the functionality of the coaxial to stripline transition is assessed, the prototyping of the RE can be faced with an acceptable degree of confidence. *Fig. 3.23* shows pictures of the assembled prototype of the DLPRE, where the considerable extension of the prototype board with respect to the patch size is standing out. This oversizing is intended to allow the implementation in the same

¹¹This good repeatability is evidenced by the small differences observed between the return losses measured in both ports of different back-to-back configurations ($S_{11 \text{ meas.}} \approx S_{22 \text{ meas.}}$).

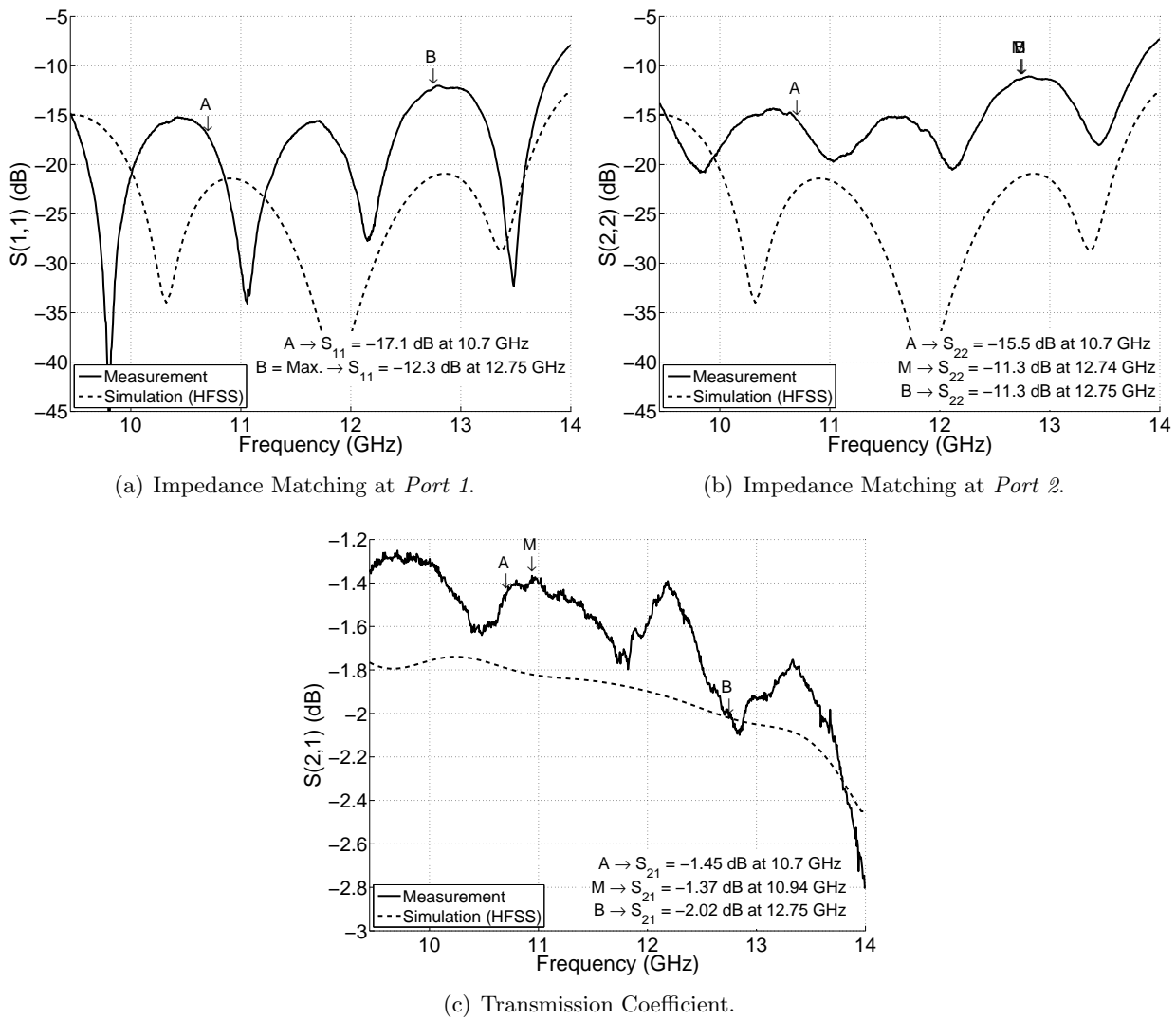


Figure 3.22. Scattering Parameters of the “coax.-stripline-coax.” blind-mounted prototype. The total length of the stripline is 5 cm. Simulation results are obtained using an improved model of the coaxial connector.

board of the prototype to test the transition, which ensures a minimum deviation of the fabrication process used to implement the two couples of transitions involved. This is consistent with the results displayed in *Fig. 3.24*, which evidence a reasonable agreement between measurements and predictions in terms of scattering parameters, provided the uncertainties in the characterization of certain low-cost materials used in the construction of the RE.

On the other hand, the use of such a large board for the prototyping of the RE has some practical implications, as the need of an increased number of shorting pins to permit the proper operation of the triplate structure and the rise of a certain distortion in the shape of the radiation pattern, among others [11,12]. As will be seen next, the last implication is related with the superposition of the waves that are diffracted in the edges of the board. This superposition introduces into the radiation pattern of the element a ripple whose speed increases with the dimensions of

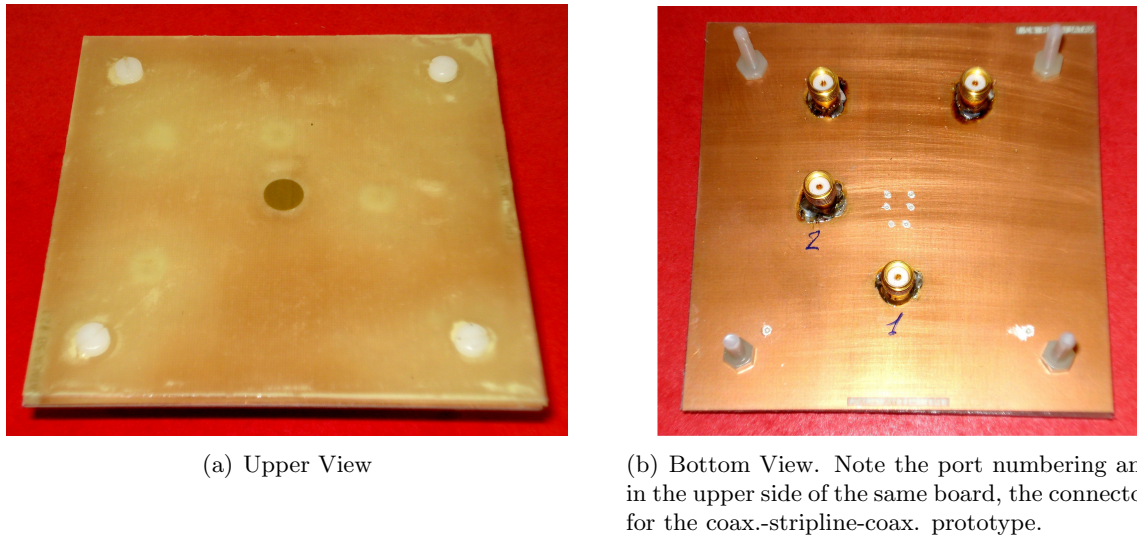


Figure 3.23. Prototype of the linearly polarized *Updated Candidate #1* (recall *Fig. 3.9*). Note, in the bottom view of the prototype, the port numbering and, in the upper side of the same view, the connectors for the coax.-stripline-coax. prototype, which is implemented in the same board.

the prototype sample. Here, this distortion is considered secondary, since its effect is expected to become less noticeable with the arraying of the element.

Actually, as it is illustrated in *Fig. 3.25* and *Fig. 3.26*, the size of the board affects the ripple of the element pattern mainly in its *E Plane*, while in the *H Plane* it is the pattern directivity which seems more perturbed. It is also interesting to note that, as it was observed for the previous candidates, the *E Plane* of *Port 1* ($\phi = 90^\circ$) always presents, in the region $\theta < 0$, an asymmetry whose magnitude increases with the frequency. In terms of performance, the polarization purity of the linearly polarized element, with an Cross-Polarization Discrimination (XPD) ≥ 20 dB all over the scan domain, must also be highlighted.

With regard to the efficient mitigation of the power leakage due to PPWMs in a large (but finite) triplate structure, measurement results seem to indicate that the need of an increased number of shorting pins was not emphasized enough by the time of prototyping.¹² This power leakage is in fact considered to underlie the considerable degradation that, with respect to the theoretical predictions, is observed in the level of gain as the operation frequency increases (see *Fig. 3.27*). This argument is supported by the mitigation of the gain drop that is observed when, due to the arraying of the RE, the number and density of shorting pins are increased, as will be shown in the next section.

¹²Actually, in addition to the shorting pins of the element (6) and the transitions (4×3), only a few more (4) were inserted near the corners of the board.

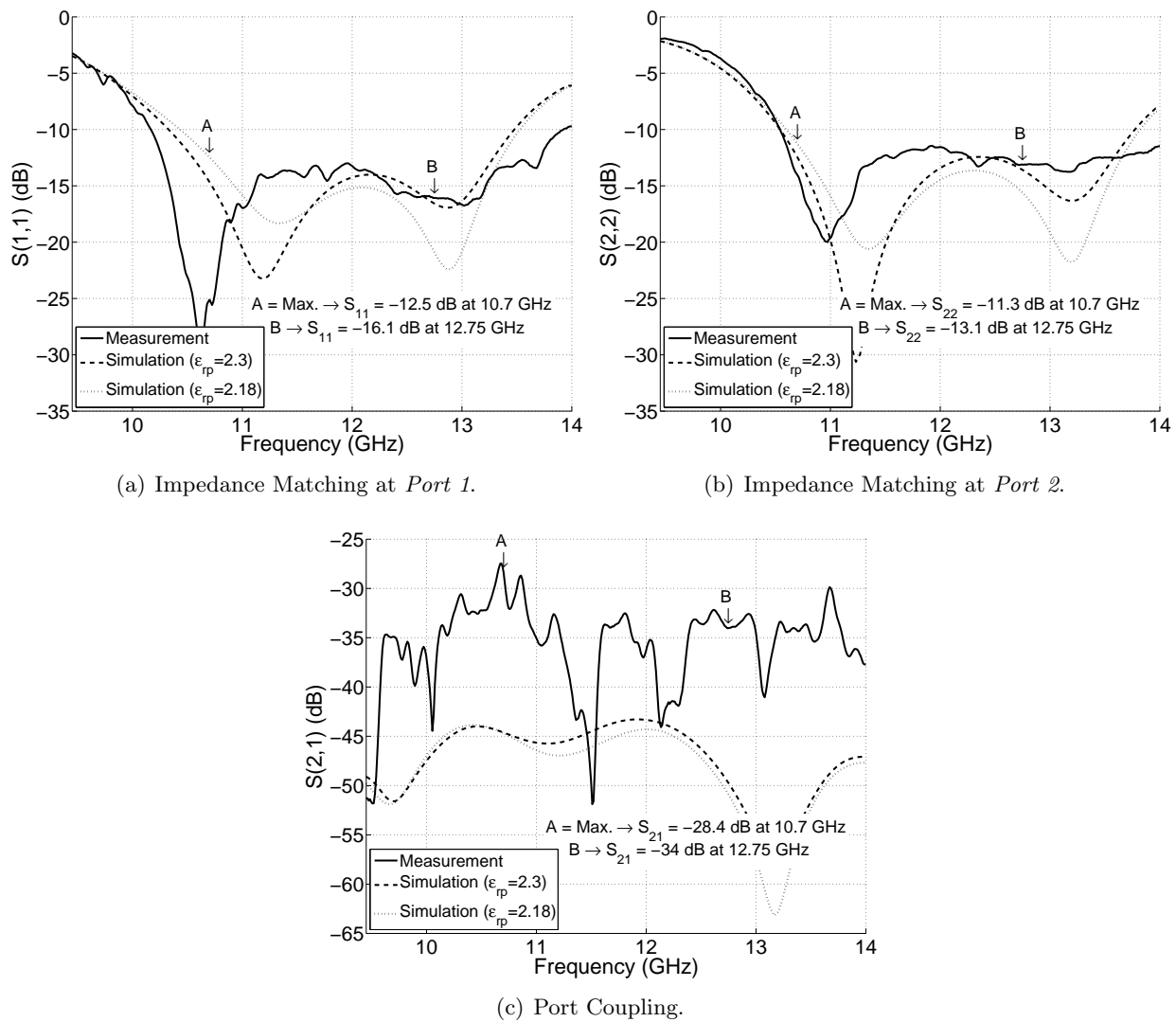


Figure 3.24. Scattering Parameters of *Updated Candidate #1* at its coaxial ports. Simulation results (from HFSS) are obtained using an improved model of the coaxial connector. In the legends, ϵ_{rp} represents the relative permittivity of polypropylene that is used in simulation (cf. *Table 3.2*).

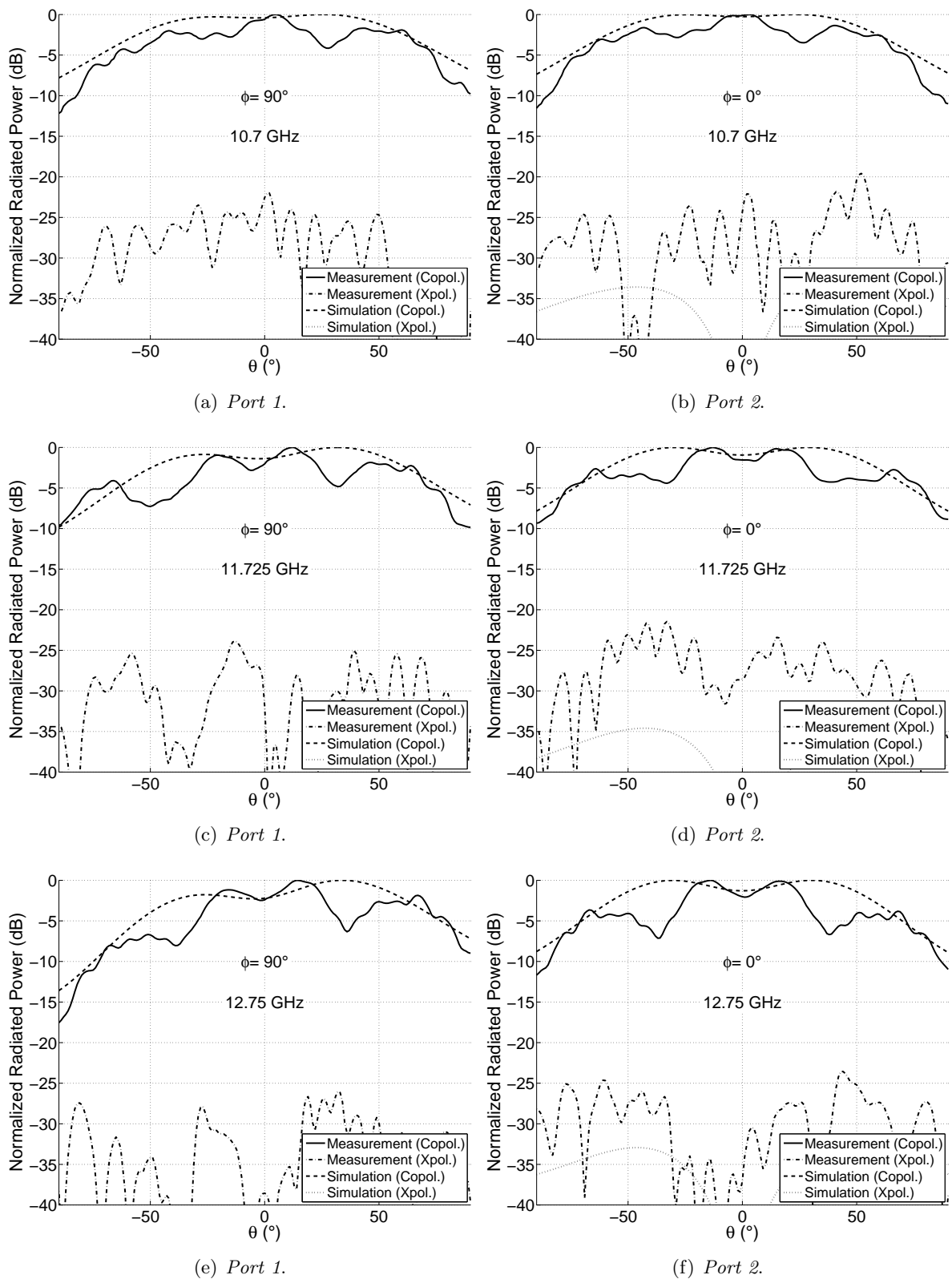


Figure 3.25. Normalized field patterns of *Updated Candidate #1*. Elevation cuts along the *E* Plane at different frequencies. *Port 1* (Vertically Polarized Component) vs. *Port 2* (Horizontally Polarized Component). Simulation results assume a finite ground plane and this plane is smaller than that of the prototype ($1.6\lambda_0 \times 1.6\lambda_0$ vs. $3\lambda_0 \times 3\lambda_0$).

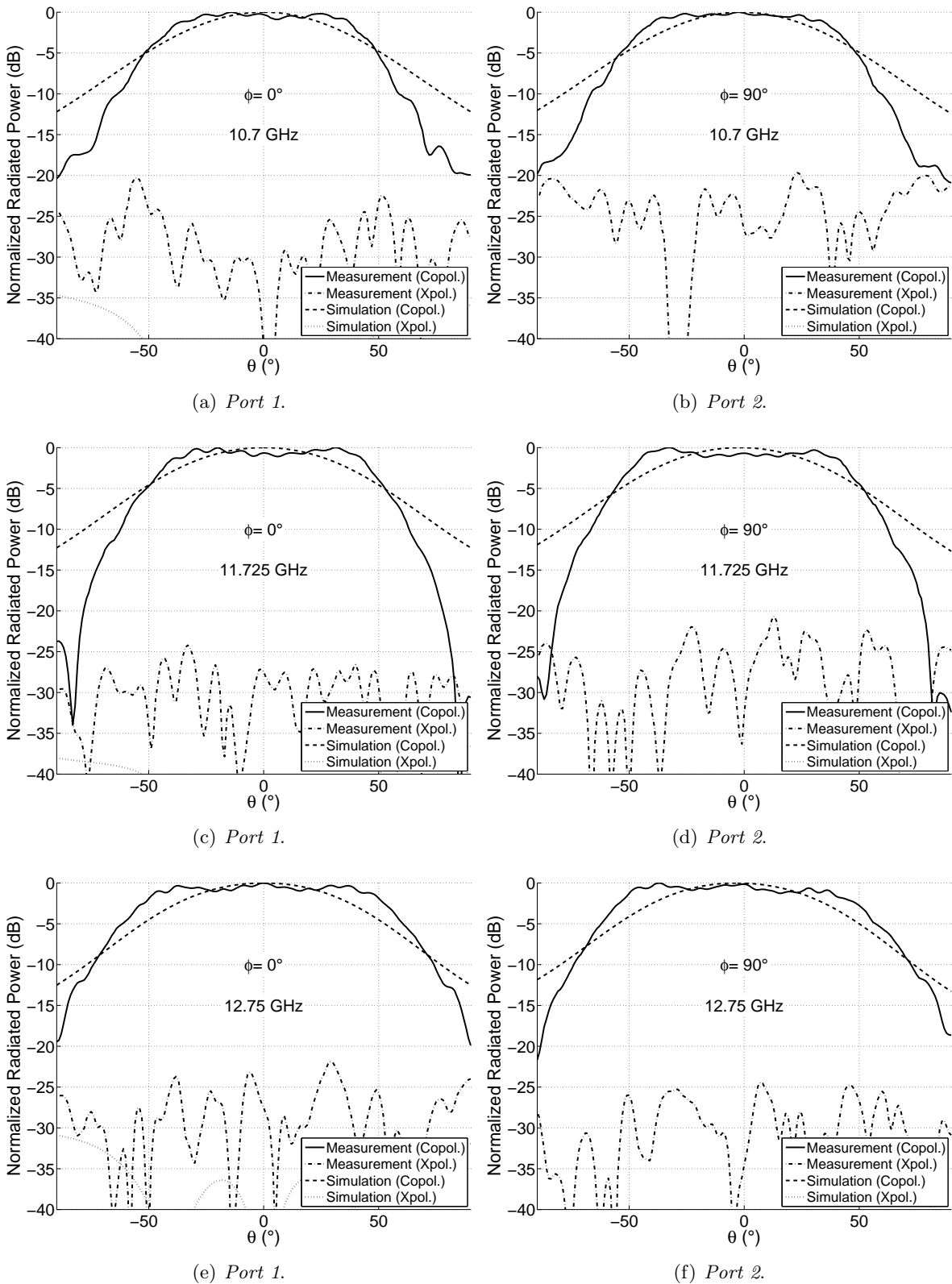


Figure 3.26. Normalized field patterns of *Updated Candidate #1*. Elevation cuts along the *H Plane* at different frequencies. *Port 1* (Vertically Polarized Component) vs. *Port 2* (Horizontally Polarized Component). Simulation results assume a finite ground plane and this plane is smaller than that of the prototype ($1.6\lambda_0 \times 1.6\lambda_0$ vs. $3\lambda_0 \times 3\lambda_0$).

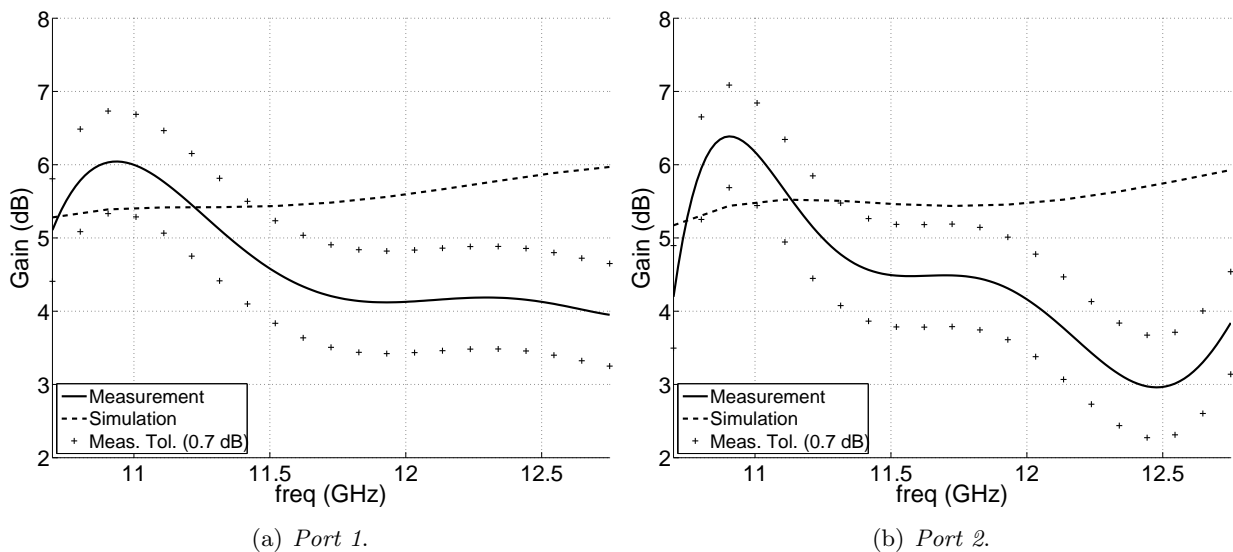


Figure 3.27. Realized gain of *Updated Candidate #1*. Simulation results do not take into account the coaxial connector and assume an infinite ground plane. Simulations with an improved model for the coaxial connector and a finite ground plane (smaller than that of the prototype) show even higher levels of gain in the upper part of the frequency band, which is attributed to an overestimate of the level of power radiated by diffraction in the edges of the board and, therefore, may be somewhat misleading.

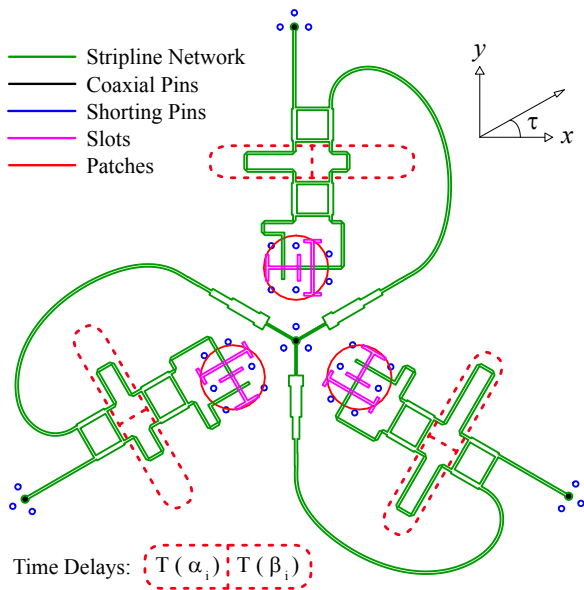
c) Polarization Tracking

Basically, all the results presented above are judged to constitute a valuable empirical assessment of the RE at different levels. In particular, the feeding concept proposed for the S3FIP, the performance of the element and its theoretical modeling are considered to be proven.

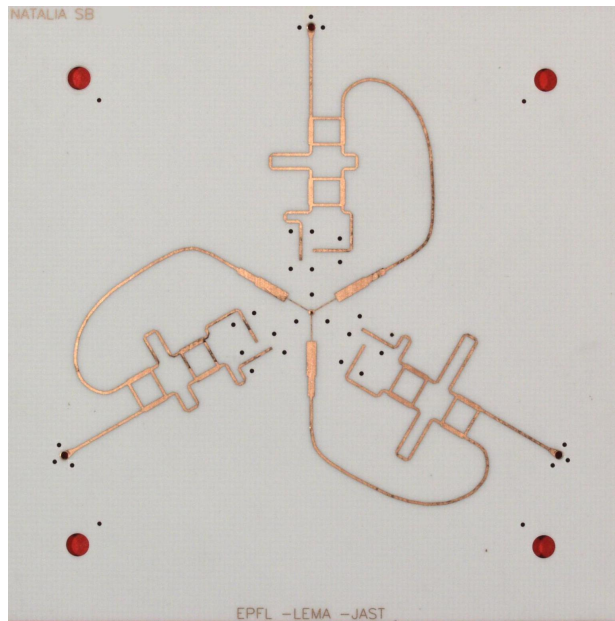
The next steps can therefore focus on the NATALIA array polarization tracking concept. Here, a first empirical verification of this concept is provided. With this aim, a prototype of the basic triangular sub-array group with a fixed tilt angle is implemented and tested.

The layout of the triangular sub-array proposed, together with the reference for the polarization tilt angle (τ), is depicted in *Fig. 3.28(a)*. Up to three miniature coaxial to stripline transitions are visible in the periphery of such layout. In the normal operation of the sub-array, these three ports are connected to 50Ω matched loads and the excitation is applied to a port that is located in the center of the layout. In this way, the outer branch line hybrids operate as Wilkinson power dividers would do, with the technological advantage that there is no need to insert the corresponding resistor within the triplate structure.¹³

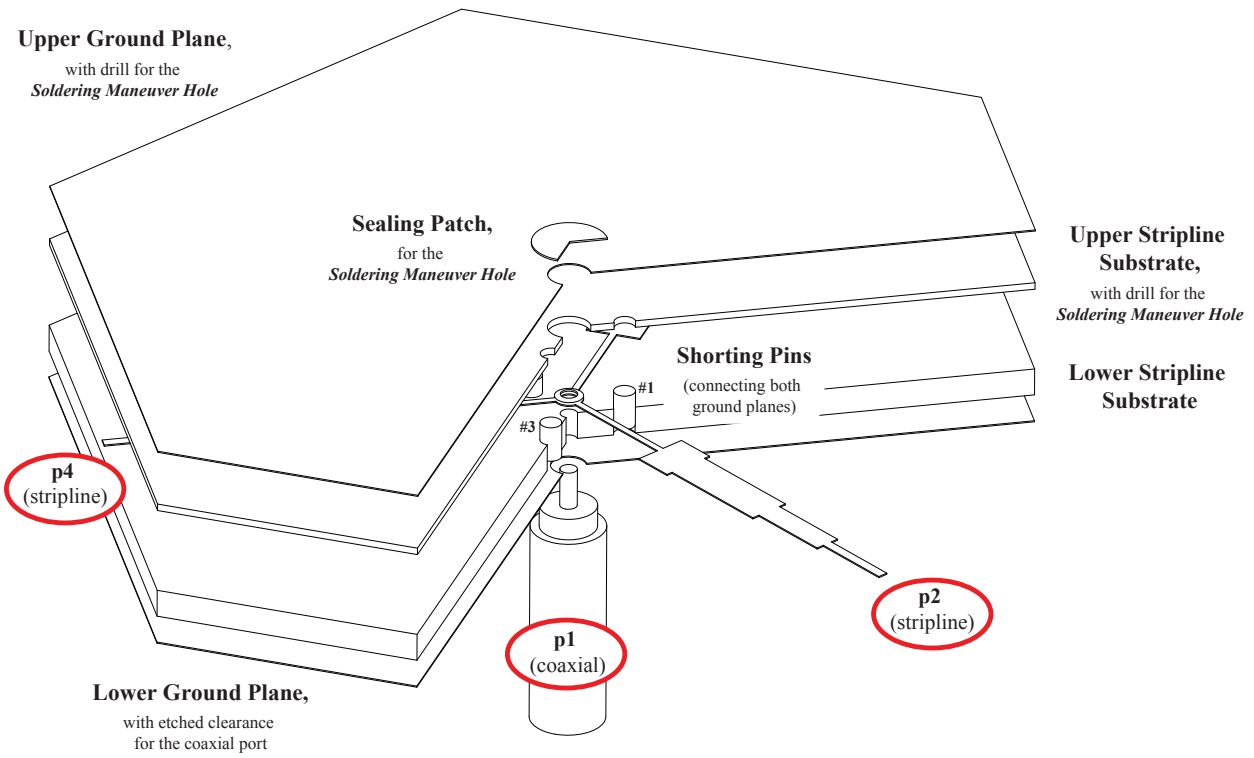
¹³In fact, an initial prototype in which the outer ports are connected to “feed-thru” SMD resistors, instead of coaxial loads, shows a considerable degradation of its performance (with a cross-polar component $\sim 5 - 6$ dB higher). This worsening is attributed, mainly, to the poor matching characteristics provided by the resistors and their grounding.



(a) Sub-array Outline Layout.



(b) Feeding Network prototype.



(c) 3 Ways Power Divider Buildup.

Figure 3.28. Sub-array structure.

For the sake of simplicity, the polarization tracking concept in *Fig. 1.4(b)* is implemented with fixed true-time-delay lines instead of variable phase shifters. These delay lines, highlighted in *Fig. 3.28(a)*, are set to synthesize a linearly polarized field that is parallel to the x axis ($\tau = 0^\circ$).

The central port of the sub-array is made up of a miniature coaxial to stripline transition directly connected to a symmetrical three ways power divider that feeds equally each one of the outer hybrids. The resulting structure is depicted in *Fig. 3.28(c)*. This configuration for the power divider is chosen because of its improved symmetry and its potential applicability to the feeding network of the NATALIA array. The power divider is designed to provide impedance matching in its central port and to minimize the insertion loss through each one of its outputs, as illustrated in *Fig. 3.29*.

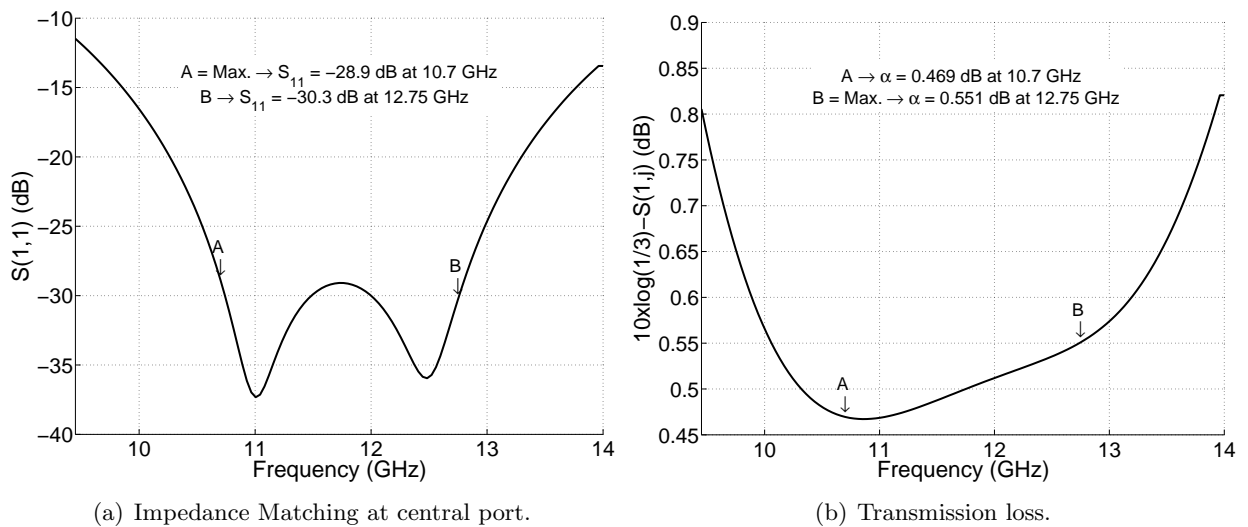


Figure 3.29. Scattering Parameters of the 3 ways power divider in *Fig. 3.28(c)*. Simulation results obtained using an improved model of the coaxial connector.

The sub-array prototyping follows a process analogous to that presented for the isolated element. Some intermediate details of this prototyping are visible in *Fig. 3.30*, and the final result is shown in *Fig. 3.31*.

The measurement of the radiation characteristics of the sub-array provides a satisfactory assessment of the polarization tracking concept. In particular, *Fig. 3.32* evidences the rotation of the polarization plane and the quality of the linear polarization, with a cross-polarization rejection level better than 15 dB all over the frequency band and the scan domain.

Moreover, the agreement with predicted results is very good in terms of both radiation pattern and gain, as confirmed by *Fig. 3.32* and *Fig. 3.33*, which validates the theoretical modeling of the sub-array and the power combiner. The last figure also supports the considerations made above with regard to the reduced gain level observed for the prototype of the isolated element in the upper side of the frequency band.

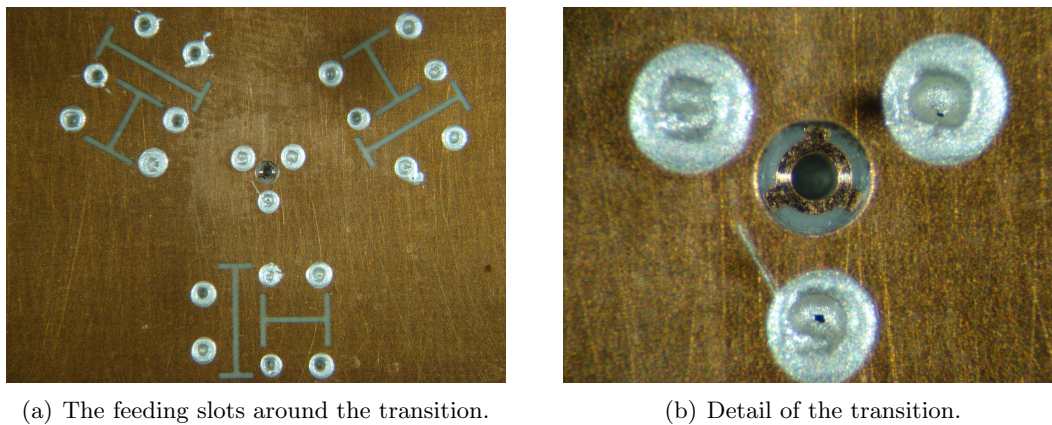


Figure 3.30. The slotted ground plane of the sub-array as fabricated, with detail of the coaxial to stripline transition of the 3 ways power divider in *Fig. 3.28(c)*. The silver dots correspond to the conductive glue used for the implementation of the shorting pins.

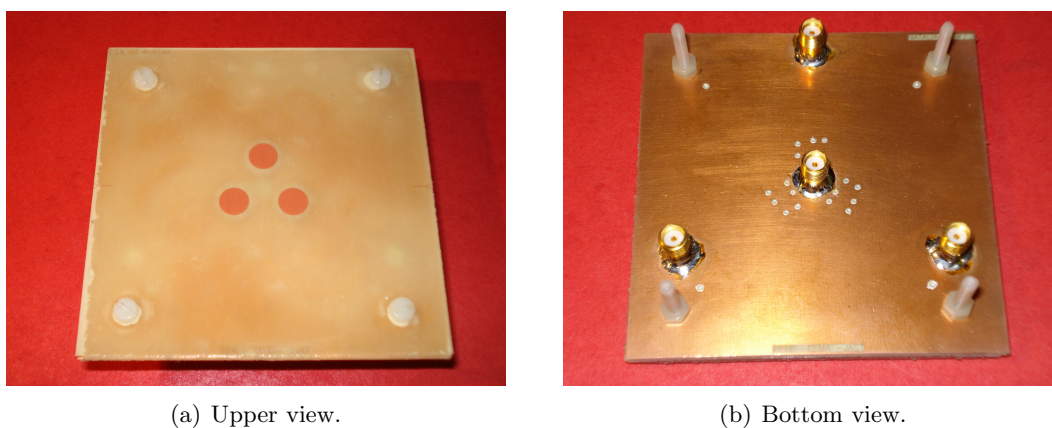


Figure 3.31. Sub-array prototype. Note, in the bottom view, the three ports of the outer branch line hybrids around the central port.

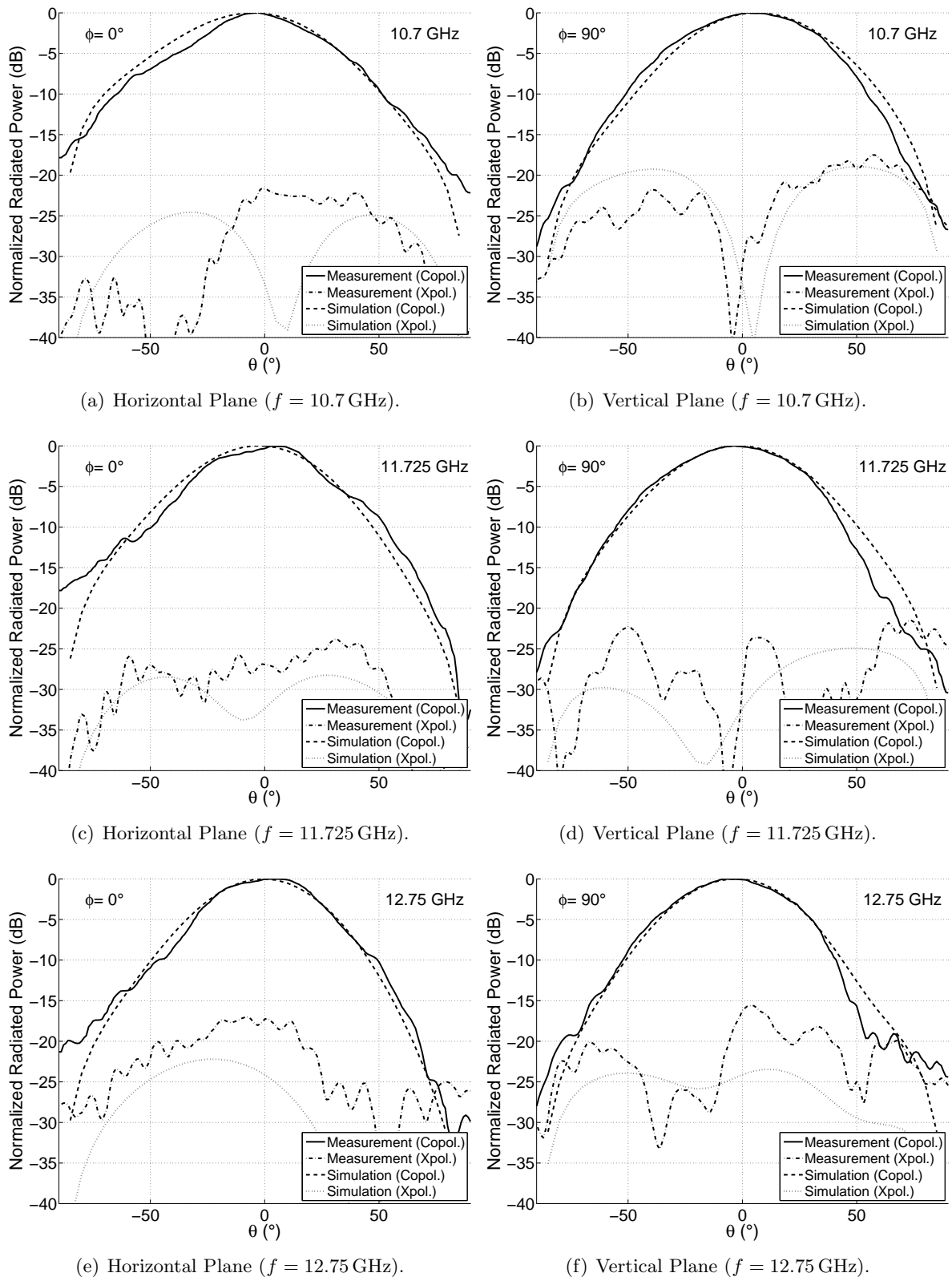


Figure 3.32. Normalized field patterns of the sub-array. Elevation cuts along the Horizontal ($\phi = 0^\circ$) and the Vertical ($\phi = 90^\circ$) Planes at different frequencies. Simulation results assume an infinite ground plane.

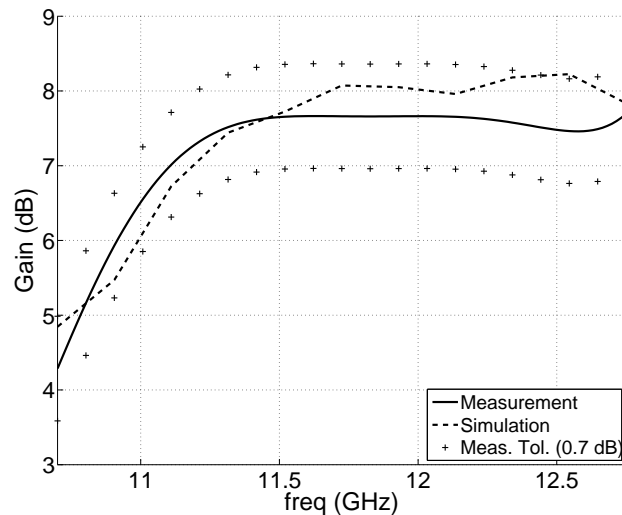


Figure 3.33. Realized gain of the sub-array. Simulation results do not take into account the coaxial connector and assume an infinite ground plane.

3.3 Integration within the Array Lattice

The integration of the Elementary Radiating Cell (ERC) within the array lattice imposes severe restrictions to all its components, namely: the Radiating Element, the Long Vias and the Power Combiner, that must be squeezed in a very limited area. These restrictions are not limited to the antenna aperture, but concern its whole buildup. Actually, in the microstrip layer that, according to *Fig. 3.34*, constitutes the interface between the ERC and the MMICs, a stiff competition for the grid area is established.

On the other hand, the placement of the Feeding Network within an intermediate dedicated stripline layer enables, in principle, an additional flexibility in its design and, therefore, its routing can be envisaged in later development stages.¹⁴ This freedom is, however, relative, since the Feeding Network must fulfill stringent RF requirements, while keeping compatible with the foreseen PCB process. The fabrication process imposes, in fact, the implementation of the Long Vias and the shorting pins of the RE as *through vias*, which will strictly constrain the final routing of this network.

Back to the microstrip layer, the ERC and the MMICs, with all their biasing components, must share the available footprint area with the part of the Control Network that programs and interconnects the MMICs. The routing of these interconnections, that are implemented in a cascade or “daisy chain” basis, depends strongly on the ERC design as well as on the sequential rotation applied to the cells, as it also happens -but to a lesser extent- to the Feeding Network.¹⁴ This dependence is related to the difficulties found to perform an efficient “filling” of the hexagonal cell

¹⁴In practice, the routing of the *Feeding Network* is going to be undertaken only when the remainder of the array antenna design within the PCB core (the ERC, the sequential rotation and the microstrip layer -Control Network included) is frozen.

area imposed by the array lattice. As evidenced in *Section 2.6*, such difficulties suggest instead the definition of a rectangular shape to model the ERC footprint.

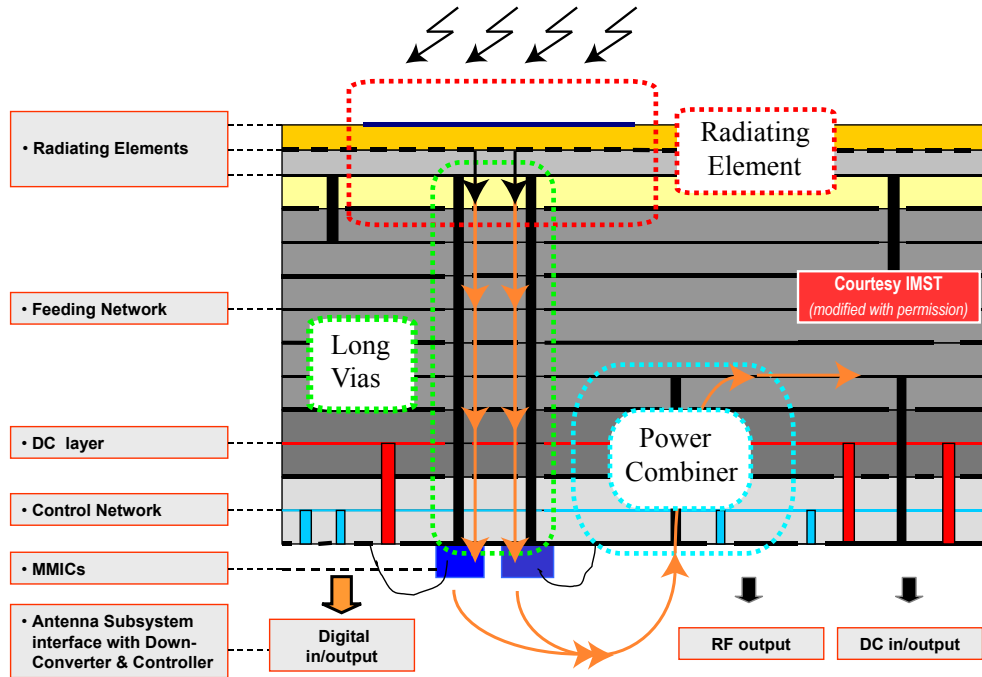


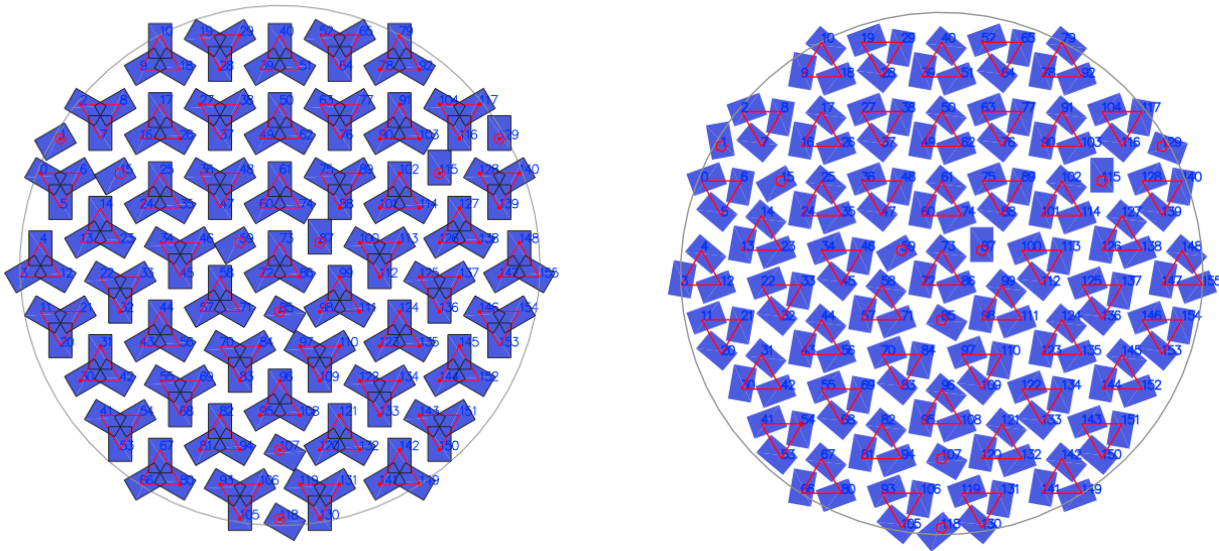
Figure 3.34. Preliminary NATALIA PCB buildup overview (not to scale), with the components of the Elementary Radiating Cell highlighted.

Despite this particularization on the overall shape of the real estate allotted to the ERC, all the inter-relations mentioned above still make very difficult to determine suitable dimensions for this shape. Of course, one should keep in mind that these dimensions also determine the feasibility and the performance of the ERC itself.

Multiple design iterations involving preliminary designs of the ERC components, the sequential rotation, the MMICs arrangement and the Control Network come out into a first estimate of suitable dimensions for this rectangular shape. These dimensions ($\lesssim 12 \text{ cm} \times 8 \text{ cm}$) are close to the refined values proposed in *Fig. 3.35* and allow to envisage a more detailed design of the components within the ERC.

The design of these components, due to the cross-cutting nature of the cell, requires a strong interaction between the teams involved in the design of the PCB, the ERC and the array logic circuits (MMICs biasing & interconnects).¹⁵ Again, several design iterations are required to arrive to a solution that complies with the numerous conflicting constraints involved. These constraints are very varied, covering from the EM performance of the cell and the design rules of the PCB manufacturer, up to the placement of the discrete biasing components and their considerable ratios in terms of cost-size & RF performance.

¹⁵Here, the contributions to the design of the ERC coming from many fruitful exchanges with *IMST GmbH* & *JAST Antenna Systems* teams are duly acknowledged.



(a) The sequential rotation is not compatible with the ERC layout: collision.

(b) The sequential rotation is compatible with the ERC layout. The next step would be to check for the feasibility of the routing of the Feeding / Control Networks.

Figure 3.35. Integration of an ERC with a given shape and dimensions ($0.46 \times 0.30 \lambda_0^2$) within the NATALIA array lattice for two different sequential rotations, from [13].

Next, this design process is illustrated from the perspective of a comparison between the actual design stage of the radiating element (*Updated Candidate #1*) and its more refined version, which is fully integrated into the ERC (the so called *Slitted Element*). In the light of this integration, the rationale for the design of the remaining components of the ERC (the couple of Long Vias and the Power Combiner) will then become more evident.

3.3.1 Radiating Element Description

Before proceeding to the comparison between both versions of the RE, let us first make the acquaintance of *Slitted Element*.

The basic multilayer structure of *Slitted Element*, displayed in *Fig. 3.36(a)*, is composed by five layers of metalization (the couple of stacked patches, the slotted ground plane, the feeding lines and a shielding ground plane), six kinds of dielectric materials, whose electric characteristics are summarized in *Table 3.3*, and six metallic posts (shorting pins), which vertically cross part of the stack and connect two layers of metalization (both ground planes). Around the upper and lower patch substrates there are three glue layers ($50 \mu\text{m}$ of 3MTM 300LSE glue) that, for the sake of simplicity, are not shown. The layout outline of *Slitted Element* as well as of one of its *slitted* patches are depicted in *Fig. 3.36(b)* and *Fig. 3.36(c)*, respectively.

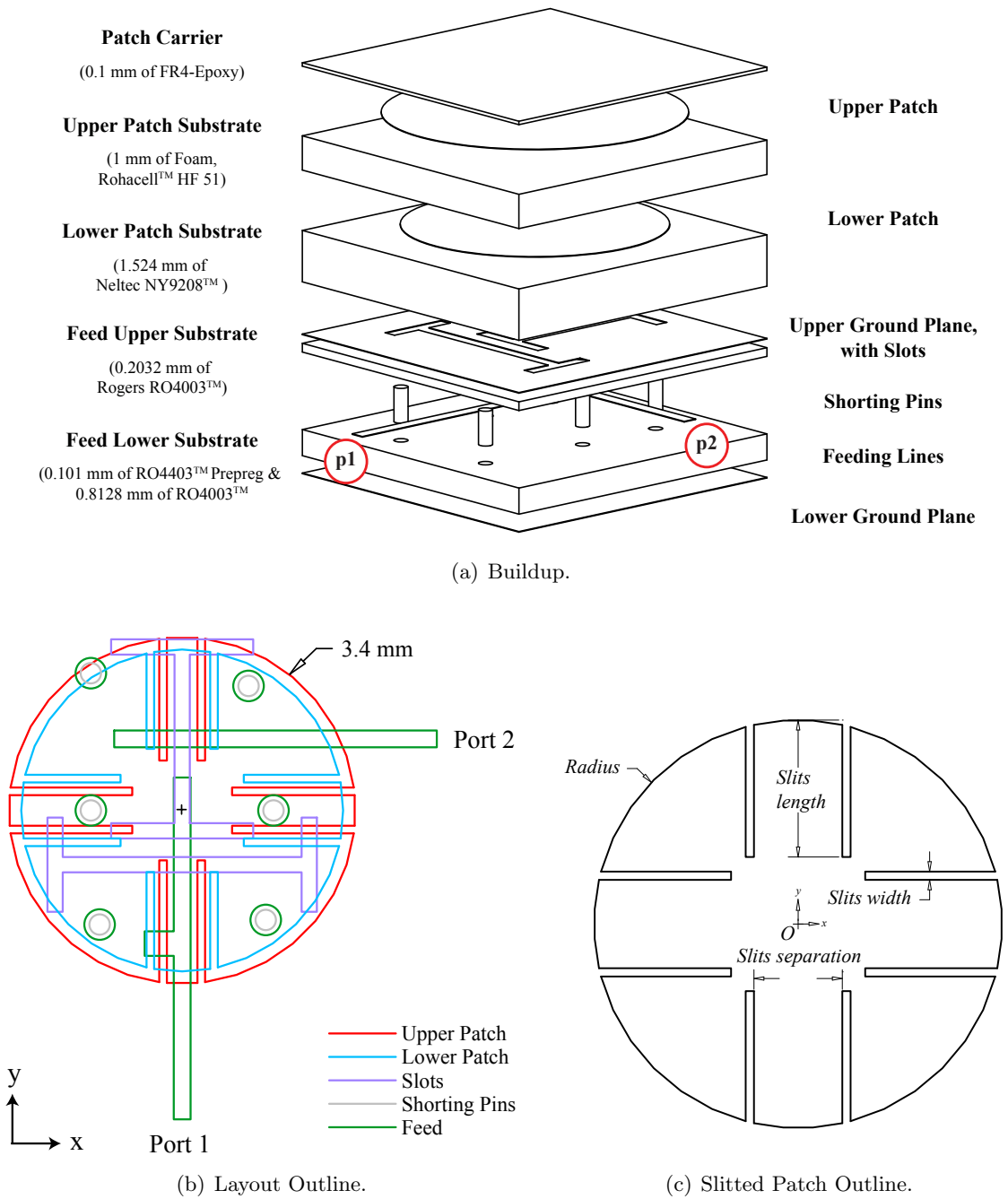


Figure 3.36. *Slitted Element* structure.

Commercial name	ϵ_r	$\tan \delta$
FR4-Epoxy	4.4*	0.02
Rohacell [®] HF51	1.07	0.0041
Neltec NY9208(IM) [™]	2.08	0.0006
3M [™] 300LSE	2.8*	0.04
Rogers Prepreg RO4403 [™]	3.17*	0.005
RO4003 [™]	3.55	0.0027

* Estimated values.

Table 3.3. Dielectric characteristics of *Slitted Element*

3.3.2 Layout Comparison

The layouts of both REs are shown, superimposed, in *Fig. 3.37*. This figure evidences that, apart from a slight reduction of the patch diameter (which is provided by the slits drawn on its perimeter), the main differences between the elements lie in (i) a squeezing of the *Slitted Element* shorting pins around the patch center and (ii) an upwards shift plus a length reduction of the horizontal slot.

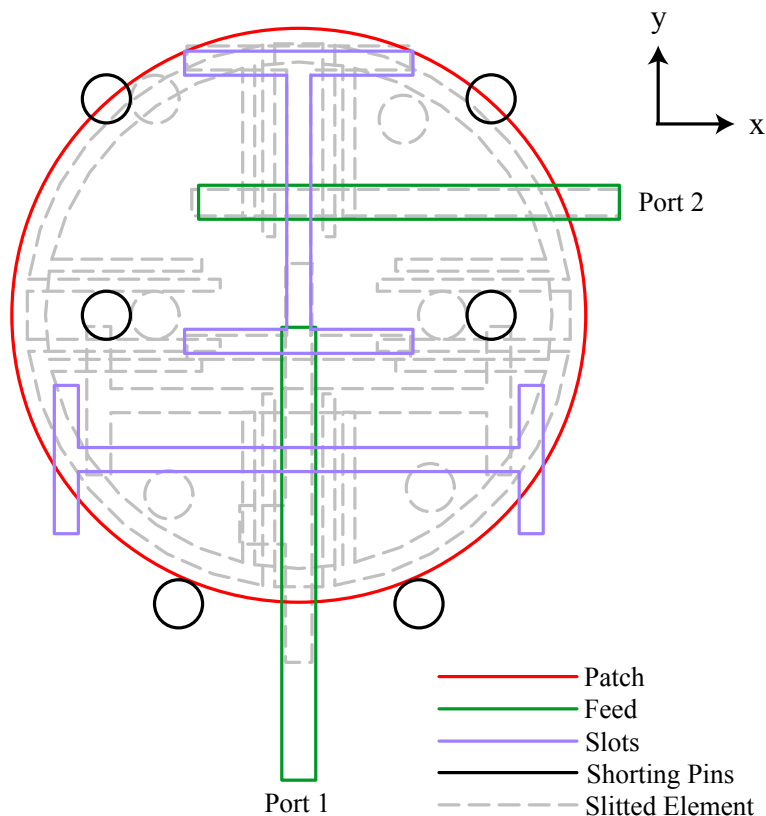


Figure 3.37. Layout of *Updated Candidate #1* (continuous line) compared to that of *Slitted Element* (dashed).

These modifications in the layout of the RE are imposed, as will be illustrated in the next section, by the need to minimize the area occupied by the element into the cell and by the optimal accommodation of the active components into the microstrip layer of the ERC.

However, these modifications are also observed to have a considerable impact on the EM performance of the RE. The compensation of such impact can be addressed by means of a redesign of certain constitutive parameters of the RE for which there are still enough degrees of freedom, as will be shown below, in see *Section 3.3.4*.

3.3.3 Justification of Layout Differences

The justification of the layout differences mentioned above becomes clearer by taking into account the environment in which the radiating element is integrated. If this environment is analyzed gradually, the layout of the DCPRE depicted in *Fig. 3.38* reveals that the DLPRE is rotated with respect to the hybrid¹⁶ and that the latter is squeezed in the horizontal dimension.

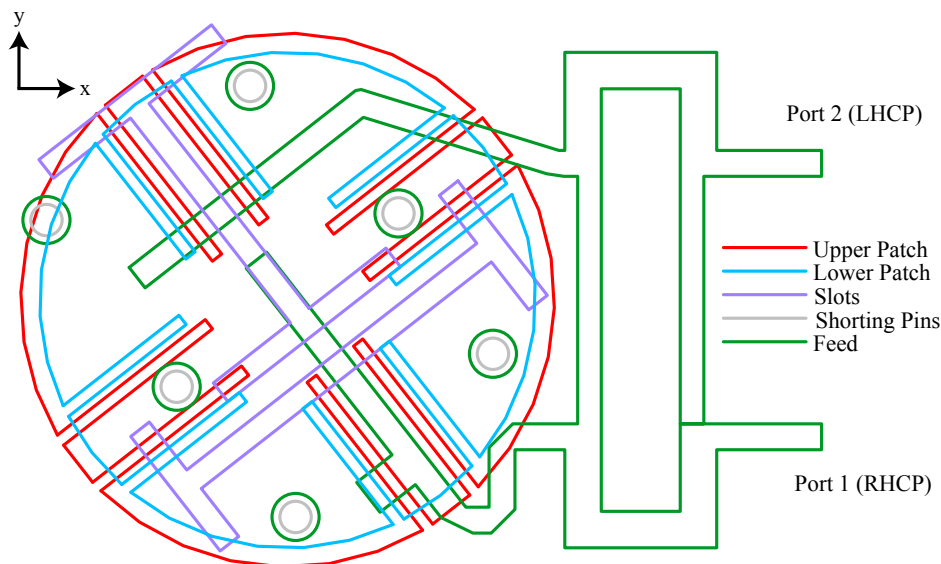


Figure 3.38. Circularly polarized *Slitted Element*. *R(L)HCP* stands for Right (Left) Hand Circular Polarization.

The layout of the circularly polarized *Slitted Element* is compared in *Fig. 3.39* with those corresponding to *Updated Candidate #1*, as it was designed for the proof of concept of the triangular sub-array, and to *Candidate #0*, that provides a more realistic integration benchmark. From this comparison it is possible to realize that the rotation of the DLPRE enables a significant shortening of the meander line used in *Slitted Element* for the phase adjustment of the linear polarizations,¹⁷ which, in turn, allows to move the DLPRE closer to the hybrid. In this way, the area occupied by the DCPRE is effectively reduced.

¹⁶Within the Combined Phase Shifter approach (recall *Section 1.1.2*), the use of programmable phase shifters makes of the physical rotation of the DLPRE a degree of freedom for the design of the ERC.

¹⁷In the case of *Slitted Element*, such a meander is inserted in the line that feeds the “horizontal” slot.

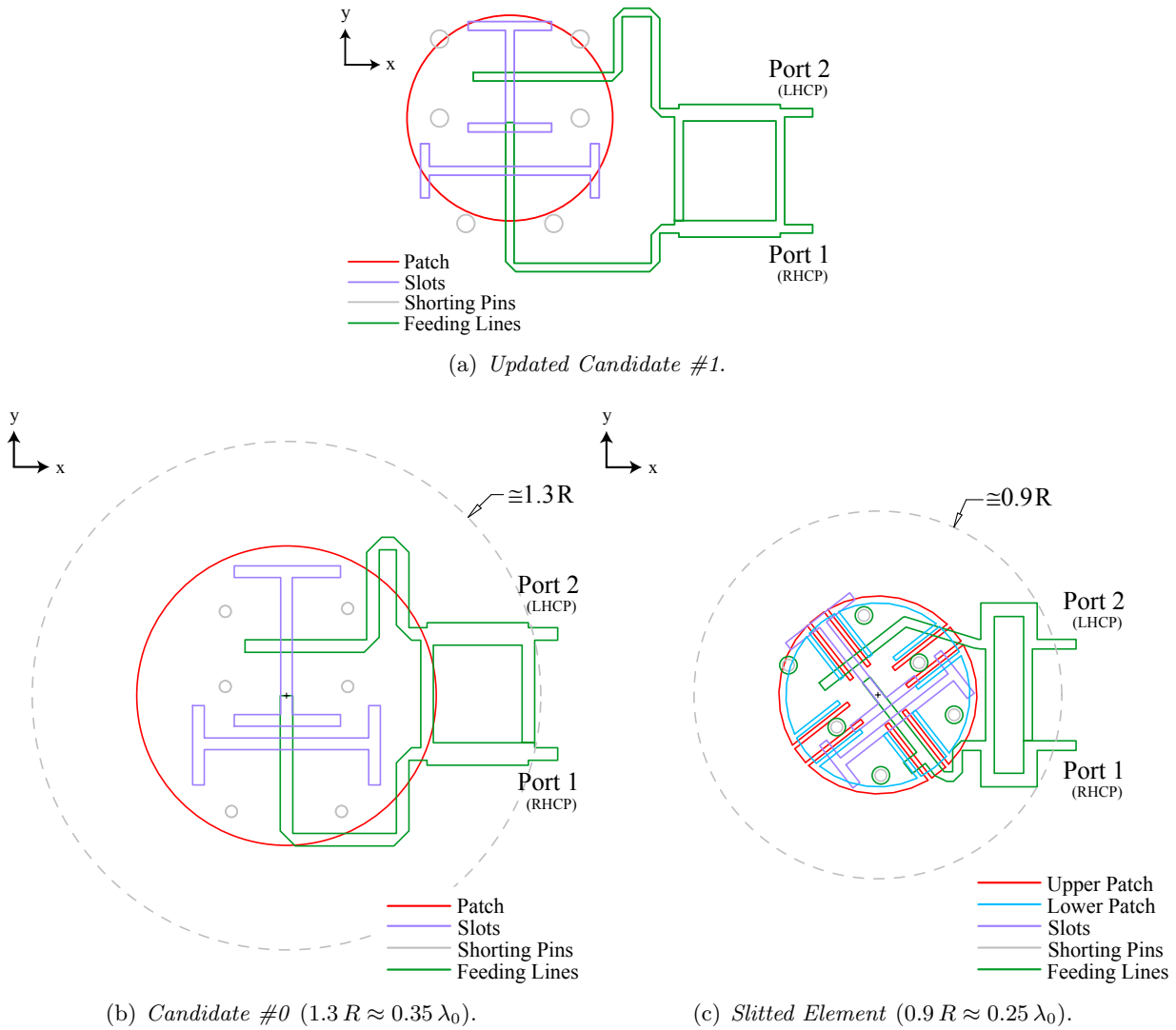


Figure 3.39. Comparison of the layouts of different DCPREs. The overall size reduction attained with *Slitted Element* is $\sim 40\%$ (see also *Fig. 2.35*).

A more in detail analysis of the layouts of the different REs lets also out that, in order to have a positive impact on the DCPRE area, the rotation of the DLPRE has been preceded by (i) a squeezing of the *Slitted Element* shorting pins around the patch center and (ii) an upwards shift plus a length reduction of the “horizontal” slot (recall *Fig. 3.37*)

When it comes to connect the DCPRE with the MMICs, a 3-D view of the ERC can provide a more complete understanding of the integration issues. Such a view is available in *Fig. 3.40*, where the structure of the couple of Long Vias, surrounded each one by a series of shorting pins, can be readily appreciated. See *Fig. 3.41* for a detailed picture of one of the twin Long Vias. In analogy with the shorting pins of the RE, the pins associated to the Long Vias are required to minimize the power leakage due to parasitic modes in the stratified media the vias are going through.

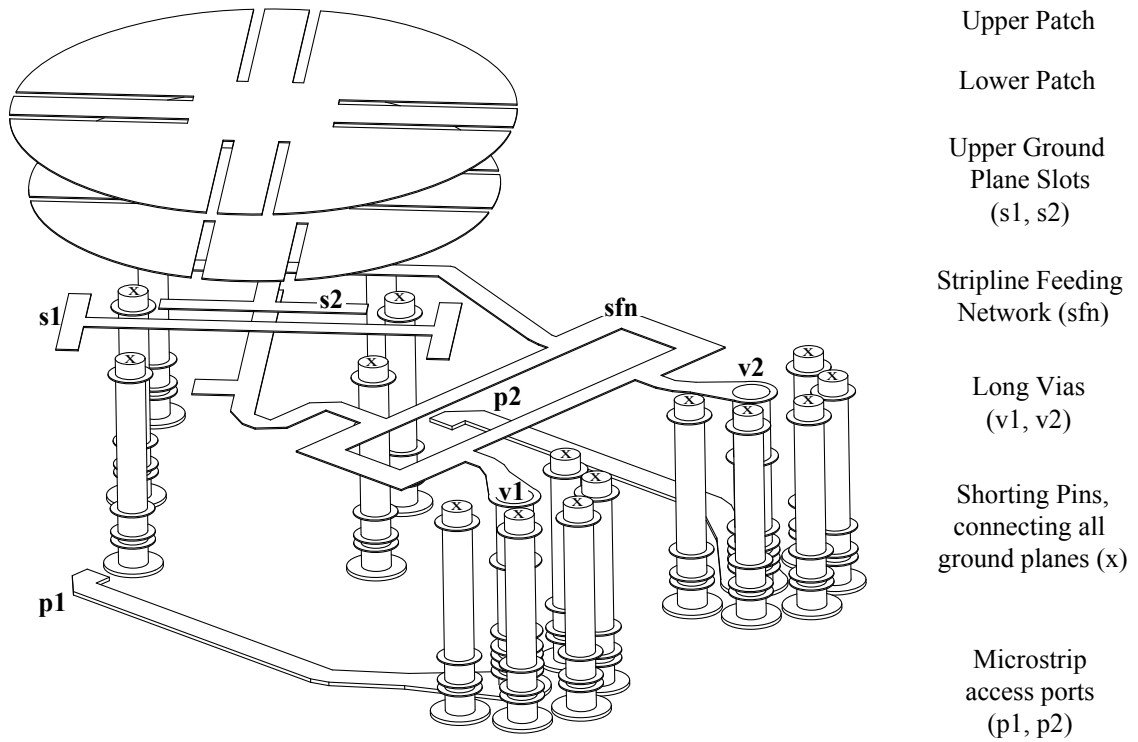


Figure 3.40. Circularly polarized *Slitted Element* with Long Vias included. 3-D view of the metalizations and the slots, as they would lie within the antenna buildup. For the sake of clarity, the substrates and the ground planes in the buildup have been removed.

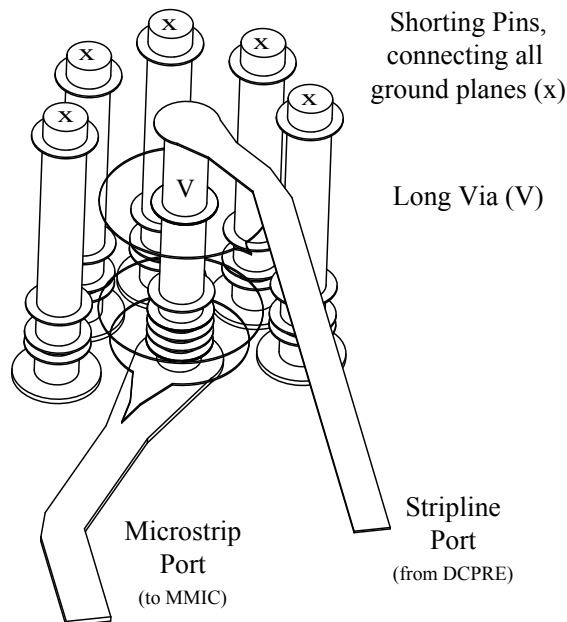


Figure 3.41. Detailed 3-D view of one of the Long Vias. Note the rings corresponding to the clearances in the ground planes the signal via is passing through. The diameter of these clearances, together with the diameter of the signal via and the placement of the shorting pins play an important role in the design of the EM performance of the via.

Here it is also worth to notice that, according to the fabrication rules and to the optimization of the performance of the vias (operating either as signal vias or as shorting pins), their diameters have been minimized. This action, together with the targeted “single press” fabrication process of the PCB, requires, in principle, all these vias to be implemented as *through* vias. This is the reason why the shorting pins of the RE are going through the whole PCB buildup, as well. At this point it becomes more evident the way the implementation of the vias can constrain the deployment of the array Feeding Network, that lies in an intermediate stripline layer and whose routing will therefore have to get round all these vertical connections.

The implementation of the shorting pins of the RE has also relevant implications in the placement of the MMICs and the Power Combiner. These implications can be considered in view of the actual layout of the ERC. In this sense, *Fig. 3.42* shows that the design of the Long Vias and their respective placement with regard to each other and to the Power Combiner are symmetric. This symmetry is important to prevent, as much as possible, any additional unbalance between the two circularly polarized signals received.

With regard to the Power Combiner, it is located just below the patches of the RE and in between the shorting pins of the element to minimize its impact on the cell area. Furthermore, these shorting pins contribute to mitigate the power leakage due to parasitic modes in the stratified media the signal via of the Combiner is going through, in an analogous way to the pins of the Long Vias. This placement of the Power Combiner imposes, however, the meandering of the line that connects the Combiner with the Feeding Network to avoid the shorting pins of the RE (see the stripline *Port 3* in *Fig. 3.42(b)* and *Fig. 3.43*).

In view of *Fig. 3.42(b)*, one may wonder about the need to bring the Power Combiner (and the MMICs) “so far” from the Long Vias. Actually, the corresponding extra length of microstrip-line (notice, in the same figure, the “long” brown traces leading to *Ports 1 & 2*) before the Low Noise Amplifier of each MMIC is just degrading the *Signal-to-Noise Ratio* (G/T, alternatively) of the receiver system. The answer to this question highlights once more the trade-off between EM performance an size that underlays the design of the ERC. As illustrated in *Fig. 3.44*, this “extra length” in the microstrip ports of the Long Vias is required to accommodate, within the area allotted to the ERC, the biasing of the MMICs and their connections to the Control Network. In this way this area gets minimized, and the integration of the ensemble ERC + MMICs within the array lattice, assured.

In the microstrip layout of *Fig. 3.44*, the placement of the microstrip pads of the shorting pins of the RE deserves special attention too. The proximity of some of these grounding pads (the brown circles around the Power Combiner) to the RF inputs of the MMICs (in particular those labeled as #1 and #4) as well as to certain lines of the Control Network reveals that the placement of the RE shorting pins and the rotation of the DLPRE are not only dictated by Radiation Efficiency criteria and the squeezing of the DCPRE, but also by the integration of the MMICs within the cell area. Of course, these layout adjustments will have an impact on the performance of the RE

and this impact has to be evaluated (and, eventually, compensated) after every modification in the ERC floor plan, which evidences the iterative nature of the process leading to the integration the cell within the array lattice.

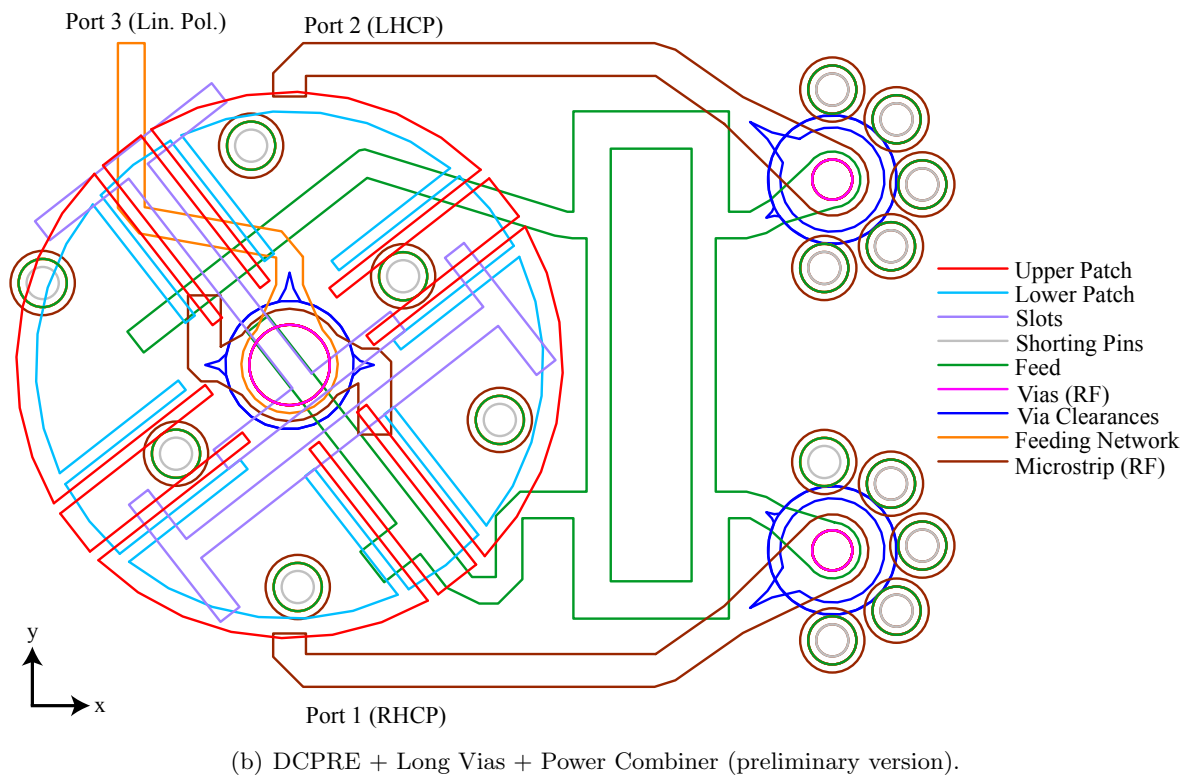
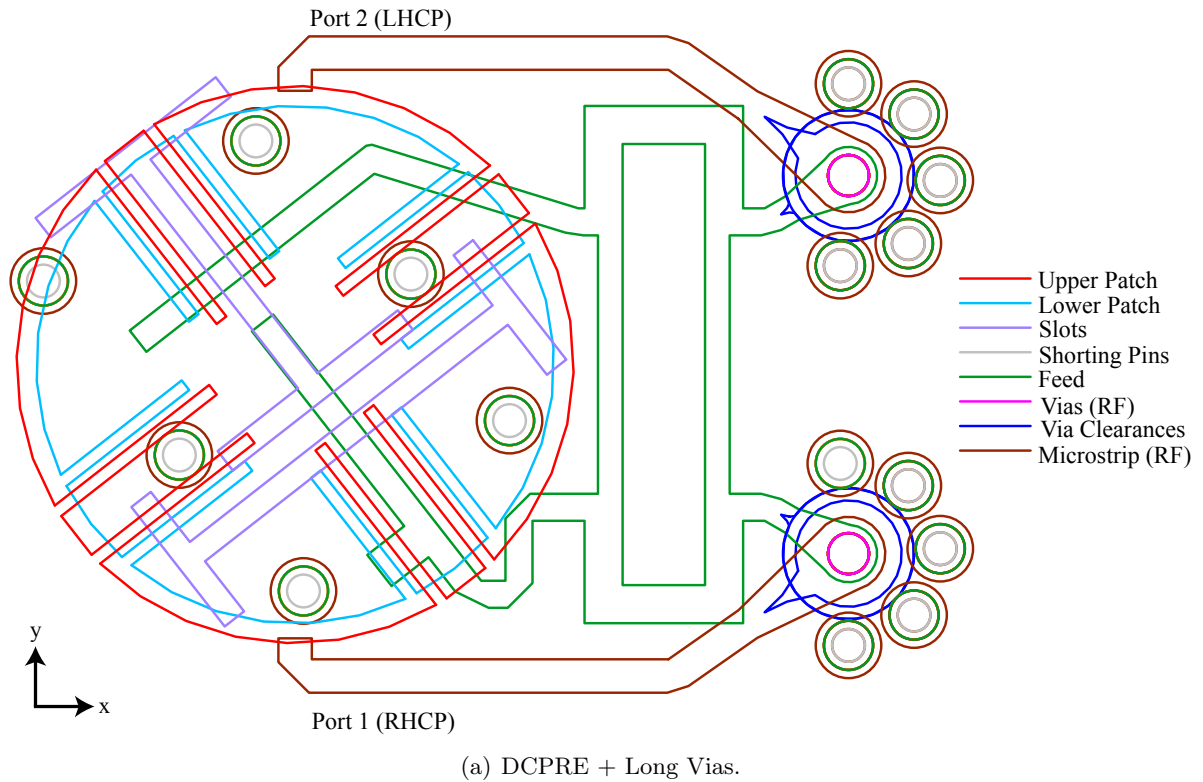


Figure 3.42. Layout outline of the circularly polarized *Slitted Element* with Long Vias included.

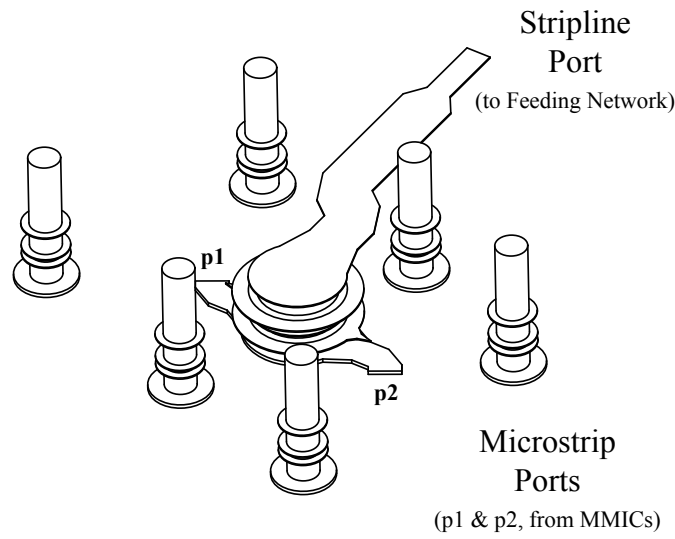


Figure 3.43. Detailed 3-D view of the Power Combiner. Notice the larger diameter of the signal via, that is implemented as a *blind* via, compared to the thinner shorting pins of the radiating element, that are implemented as *through* vias. Observe also that, with regard to the preliminary version of the Power Combiner in *Fig. 3.42(b)*, the Combiner shown here already includes the $\lambda_0/4$ impedance transformer that allows to match the input impedance at its stripline port to 50Ω when its microstrip ports are loaded with the MMICs, whose RF ports are all matched to 50Ω , as well.

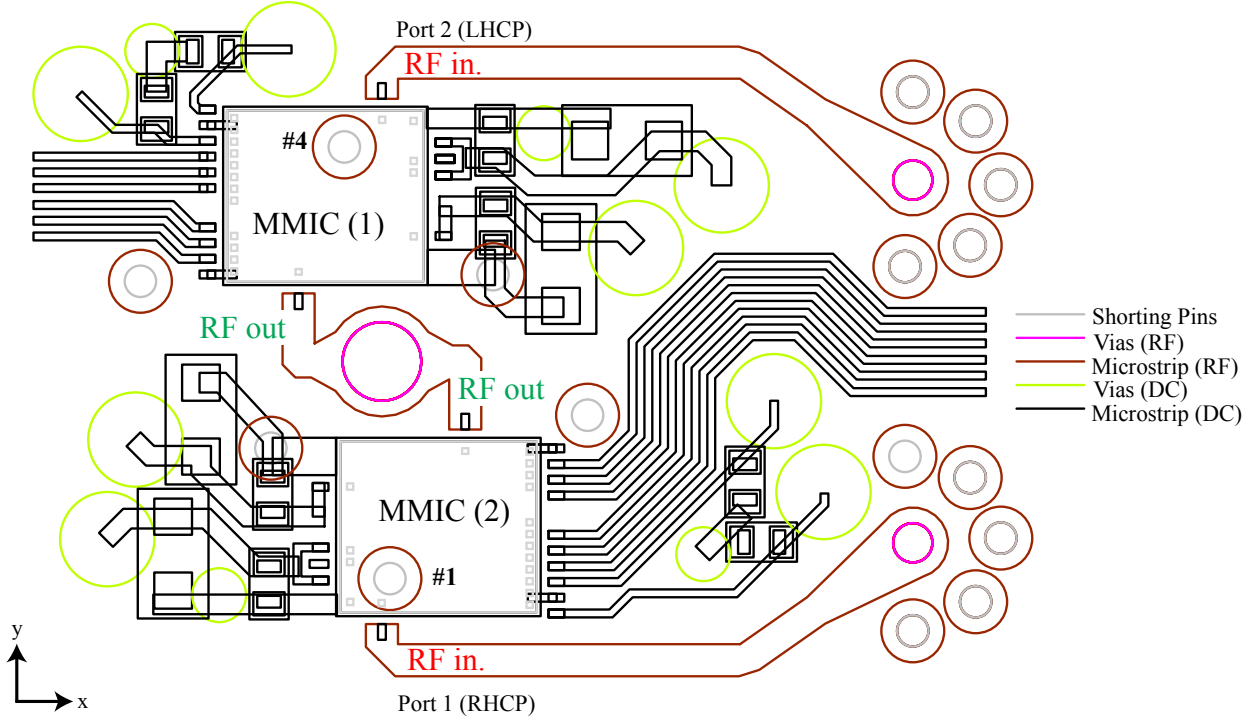


Figure 3.44. Layout outline of the ERC microstrip layer with the footprints of the MMICs and the Input/Output buses of the Control Network included. The different sizes of the pads for the discrete components required for the biasing of the MMICs, as well as the underlying compromise between their EM performance and their cost, are noteworthy too.

Finally, *Fig. 3.45* and *Fig. 3.46* illustrate the degree of integration attained in the different layers of the ERC to comply with the area requirement proposed in *Fig. 3.35* ($0.46 \times 0.30 \lambda_0^2$). This compliance constitutes, indeed, a first successful assessment of the ERC design.

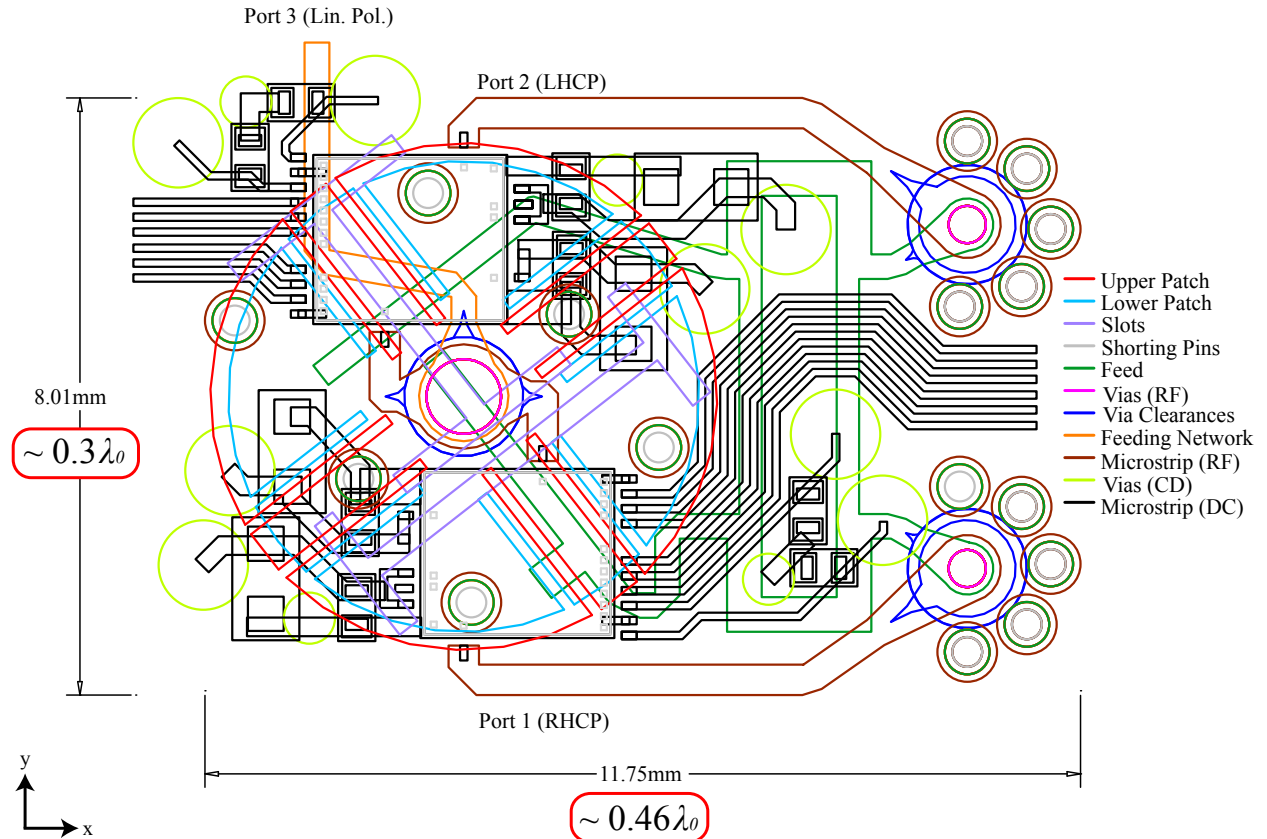


Figure 3.45. Complete layout outline of the ERC, with details of the MMICs and the Control Network.

Just for the sake of illustration, *Fig. 3.47* shows a picture of the microstrip layer of the ERC with the MMICs and biasing components mounted.

3.3.4 Justification of Buildup Differences

As it has been illustrated in the previous sections, the integration of the ERC within the array lattice has required considerable modifications in the layout of the RE, with regard to its original version (*Updated Candidate #1*). These layout modifications have a pronounced impact on the performance of the element. To compensate this impact, a series of measures are taken according to the design guidelines provided in *Chapter 2*. The possibility of improving the original performance levels of *Updated Candidate #1* is also explored.

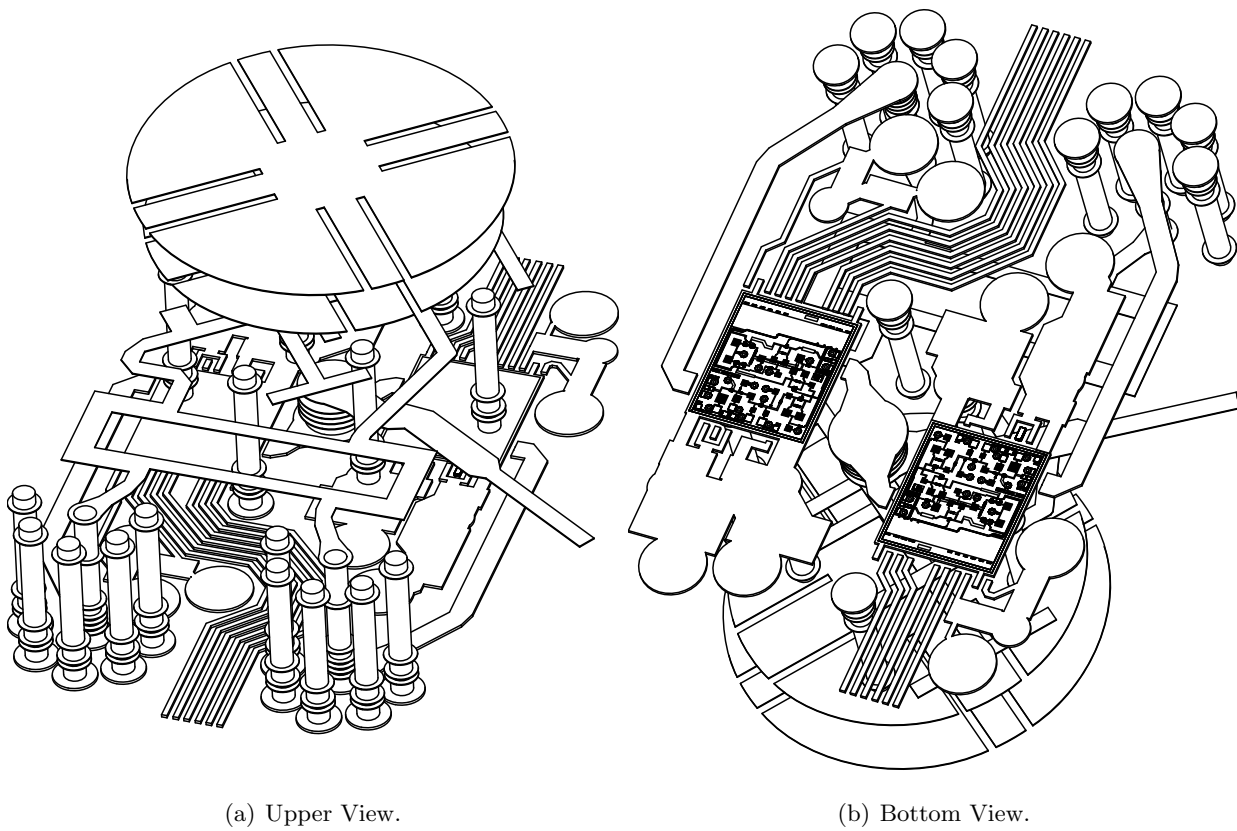


Figure 3.46. 3-D views of the complete ERC, with details of the MMICs and the Control Network.

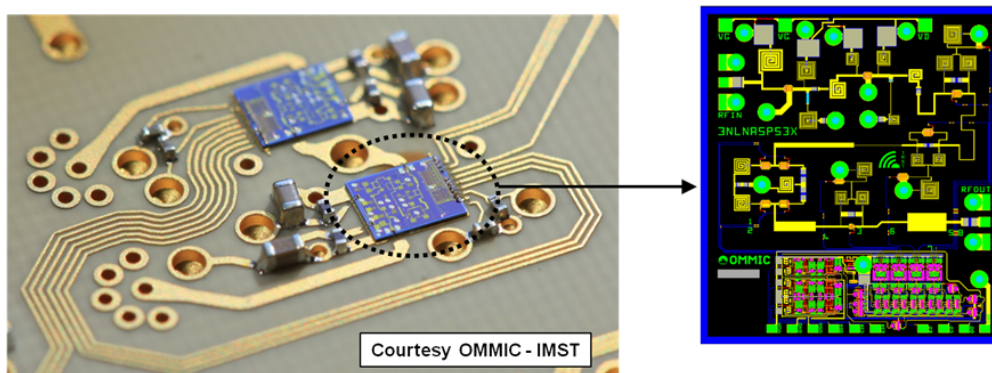


Figure 3.47. Photograph of the microstrip layer of the ERC, from [14].

Basically, the modifications in the layout of the DLPRE are observed to reduce the coupling between the vertical feeding line (*Port 1* in *Fig. 3.36*) and the patch. This coupling reduction is evidenced by the behavior of the the Input Impedance of the RE, whose loops show a marked tendency to narrow down and to shift towards the right part of the Smith Chart as the length of the horizontal slot is reduced and the shorting pins are squeezed around it (recall *Fig. 3.37*).

There are different alternatives to compensate the aforementioned coupling reduction. Essentially, these alternatives are related either with (i) an increase of the permittivity of the patch substrate, which may not be compatible with the maintenance of a reasonable level of radiation efficiency (due to the potential increase of surface wave leakage), or (ii) the use of a thinner substrate for the patch, which implies a reduction of the distance between the patch and the slot.

Though the second approach is, a priori, compatible with reduced levels of surface wave leakage, it may result in a considerable bandwidth drop, due to the overall volume reduction of the RE. This reasoning already connects with that which led to the application of the *stacked patches* technique to the REs conceived during the *First Design Iteration* (*Section 3.2.1*).

In fact, such a bandwidth drop can be compensated by stacking a second resonator over that of the thinned RE and tuning their mutual resonances. Thanks to the additional degrees of freedom provided by this stacked structure, the original performances achieved with *Updated Candidate #1* might be maintained or even improved, while meeting the new integration constraints.

The application of the *stacked patches* technique is thus considered to be worth of being taken up again, since, together with the potential increase of the Radiation Efficiency of the RE, a reduction its directivity and the inter-element mutual coupling are also considered to be feasible.

Actually, it is considered that the miniaturization of the patches, which is successfully achieved by slitting their perimeter, may provide the desired reduction of directivity and of mutual coupling without falling into noticeable degradation of the remaining performance parameters (recall *Section 2.4.2* and the considerations about (1.2)).

The application of all these design guidelines leads to *Slitted Element*, as it has been presented at the beginning of this section, in *Fig. 3.36*.¹⁸ This element is fully compatible with the volume and performance requirements imposed by the integration of the ERC into the foreseen array antenna. The performance comparison between *Updated Candidate #1* and *Slitted Element* is summarized in *Table 3.4*.

¹⁸The amount of constitutive parameters involved in the design of *Slitted Element*, which is evidenced in *Fig. 3.36*, advises the combination of the aforesaid design guidelines with automated optimization routines, such as the Particle Swarm and the DIRECT Algorithms [15–17]. With this purpose, customized interfaces between two commercial *Full Wave* software tools (*Ansoft HFSSTM* & *Ansoft DesignerTM*) and the *MATLAB[®]* codes implementing such algorithms have been developed in collaboration with Dr. R. Golubovic. These routines were intensively used in the final design steps of *Slitted Element* and the *Long Vias*, as well as in other applications [18, 19].

	<i>Updated Candidate #1</i>	<i>Slitted Element</i>
Impedance Matching	-13.1 dB	-11.6 dB
Bandwidth*	23%	21%
Port coupling	< -30 dB	< -30 dB
Max. Directivity	8.1 dB	7.4 dB
Mutual Coupling	-16.9 dB	-17.8 dB
Radiation Efficiency	62%	66%
Axial Ratio**	7.2 dB	6.2 dB

* $S_{ii} \leq -10$ dB.

** 360° in az. and $20^\circ - 70^\circ$ in el. (from broadside).

Table 3.4. Overall performance comparison: *Updated Candidate #1* vs. *Slitted Element*. Simulation Results. For the sake of brevity, and with regard to the element performance requirements specified in *Table 1.3*, only the *worst* values for the most critical performance parameters are displayed here. A more detailed comparison is available in [6].

Besides the overall performance improvement provided by *Slitted Element*, *Table 3.4* and *Fig. 3.48* illustrate that the miniaturization of the patches did succeed in reducing both the mutual coupling (~ 1 dB) and the directivity (~ 0.7 dB) of the RE.

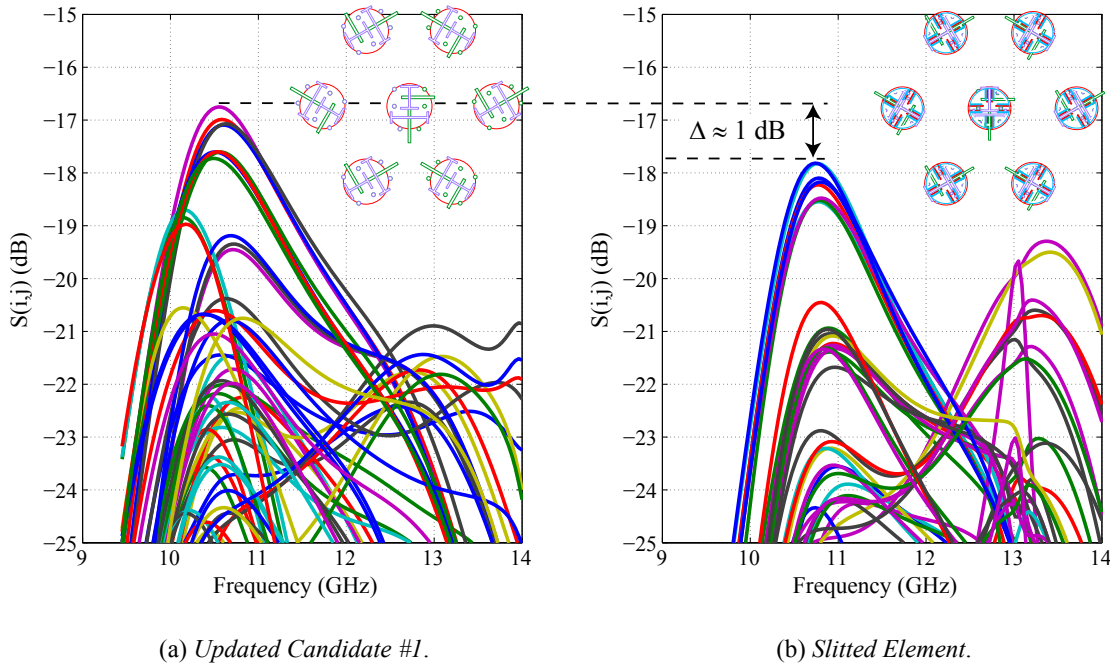


Figure 3.48. Mutual coupling between the linearly polarized elements within a small subarray of 7 sequentially rotated samples (recall *Fig. 3.2* and *Fig. 3.6*). From [6].

3.4 Conclusion

This chapter has described the design process of the ERC. This description highlights the strong compromise that exists between the EM performance of the cell and the structural & technological constraints applying to the foreseen antenna solution. The way this compromise guides the design of the ERC and the solution attained are also illustrated. This solution constitutes a very promising trade-off in terms of performance, fabrication simplicity, cost and size.

With regard to the performance of the radiating element, the compliance with specifications is given by the results in *Table 3.4*, that summarizes the most salient EM characteristics of the DCPRE. A more in depth analysis of these results together with their empirical assessment is provided in the next chapter.

The fulfillment of the remaining design goals, that are related to the PCB fabrication technology and the integration of the ERC within the targeted array antenna, has been demonstrated throughout the present chapter and, finally, it is illustrated in *Fig. 3.49*.

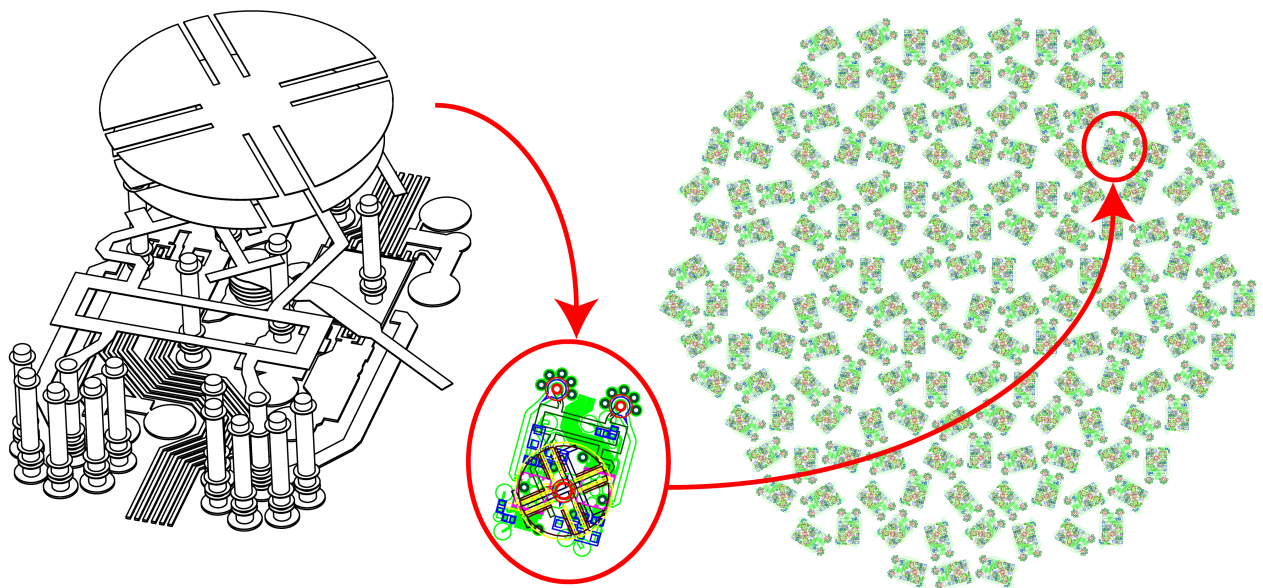


Figure 3.49. Integration of the ERC the Antenna PCB Buildup and into the Array Lattice. The Feeding and the Control Networks are not included in the array layout. The array layout is courtesy of *JAST Antenna Systems*.

References

- [1] R. Torres-Sánchez, “Evaluation of different candidate Radiating Elements for the NATALIA array,” LEMA (EPFL) & JAST Antenna Systems, Lausanne, Switzerland, Tech. Rep., Sep. 2007, (v. 7).
- [2] —, “Proof of concept of the NATALIA radiating element,” LEMA (EPFL), Lausanne, Switzerland, Tech. Rep., Apr. 2008, (v. 4).
- [3] R. Torres-Sánchez, F. P. Casares-Miranda, E. Márquez-Segura, and P. Otero, “Symmetry, XPD, and port isolation in an ACPMA array with dual linear polarization,” *Microwave Opt. Technol. Lett.*, vol. 49, no. 7, pp. 1722–1727, Jul. 2007.
- [4] R. T.-S. Sánchez, “Two beam printed antenna array for satellite reception,” Master Thesis Report (in Spanish), Escuela Técnica Superior de Ingenieros de Telecomunicación de la Universidad de Málaga, Málaga, España, Mar. 2006, Report summary available at http://www.coit.es/pub/ficheros/p_astradfb74c86.pdf?PHPSESSID=4e27a815b4815581fe4a579d9c5fd977.
- [5] D. Llorens del Río and R. Torres-Sánchez, “Full wave simulation status and Evaluation of different radiating element candidates for the NATALIA array,” NATALIA Progress Meeting Update: Teleconference Presentation, JAST Antenna Systems & LEMA (EPFL), Lausanne (Switzerland), Oct. 2007.
- [6] R. Torres-Sánchez, “Integration of the NATALIA Radiating Element: Update & Comparison with the previous candidate,” LEMA (EPFL), Lausanne, Switzerland, Tech. Rep., Feb. 2009, (v. 1.5).
- [7] R. Torres-Sánchez, S. Vaccaro, and J. R. Mosig, “A compact and low cost radiating element for automotive satellite broadcasting reception arrays,” in *30th ESA Antenna Workshop for Earth Observation, Science, Telecommunication and Navigation Space Missions*, ESA/ESTEC, Noordwijk, The Netherlands, May 2008.
- [8] F. Zavosh and J. Aberle, “Single and stacked circular microstrip patch antennas backed by a circular cavity,” *IEEE Trans. Antennas Propag.*, vol. 43, no. 7, pp. 746–750, Jul. 1995.
- [9] N. Karmakar, “Investigations into a cavity-backed circular-patch antenna,” *IEEE Trans. Antennas Propag.*, vol. 50, no. 12, pp. 1706–1715, Dec. 2002.
- [10] “EPO-TEK[®] H20E Technical Data Sheet,” Epoxy Technology, Inc., Jun. 2011. [Online]. Available: <http://www.epotek.com/SSCDocs/datasheets/H20E.pdf>
- [11] J. Huang, “The finite ground plane effect on the microstrip antenna radiation patterns,” *IEEE Trans. Antennas Propag.*, vol. AP-31, no. 4, pp. 649–653, Jul. 1983.
- [12] K.-L. Wong and T.-W. Chiou, “Finite ground plane effects on broad-band dual polarized patch antenna properties,” *IEEE Trans. Antennas Propag.*, vol. 51, no. 4, pp. 903–904, Apr. 2003.
- [13] D. Llorens, F. Tiezzi, and S. Vaccaro, “Sub-array polarization control using rotated dual polarized radiating elements,” Patent US 20 100 253 585, October 7, 2010.
- [14] G. Langgartner, R. Baggen, S. Vaccaro, and D. Smith, “Dedicated GaAs corechip for mobile satellite Ku-band terminals,” in *32nd ESA Antenna Workshop on Antennas for Space Applications*, ESA/ESTEC, Noordwijk, The Netherlands, Oct. 2010.
- [15] J. Robinson and Y. Rahmat-Samii, “Particle swarm optimization in electromagnetics,” *IEEE Trans. Antennas Propag.*, vol. 52, no. 2, pp. 397–407, Feb. 2004.
- [16] B. Fuchs, R. Golubovic, A. K. Skrivervik, and J. R. Mosig, “Spherical lens antenna designs with particle swarm optimization,” *Microwave Opt. Technol. Lett.*, vol. 52, no. 7, pp. 1655–1659, 2010.
- [17] M. Björkman and K. Holmström, “Global optimization using the DIRECT algorithm in Matlab,” in *Advanced Modeling and Optimization*, vol. 1, no. 2, 1999, pp. 17–37.
- [18] S. López-Peña, J. Zürcher, R. Torres-Sánchez, A. G. Polimeridis, and J. R. Mosig, “Modeling and manufacturing of a series of identical antennas for a P-band ice sounder,” in *proc. EuCAP 2010, 4th International Conference on Antennas and Propagation*, Apr. 2010.

- [19] J. Perruisseau-Carrier, F. Bongard, R. Golubovic, R. Torres-Sánchez, and J. R. Mosig, “Contributions to the modeling and design of reconfigurable reflecting cells embedding discrete control elements,” *Microwave Theory and Techniques, IEEE Transactions on*, vol. 58, no. 6, pp. 1621–1628, Jun. 2010.

4. Elementary Radiating Cell Evaluation

The cave you fear to enter holds the treasure you seek.

JOSEPH CAMPBELL, *attributed.*

4.1 Introduction

The design process described in previous chapters concludes with an Elementary Radiating Cell (ERC) that, according to the structure represented in *Fig. 4.1*, satisfies the technological and structural requirements specified for the targeted antenna solution. These requirements are provided in the first chapter of this memoir and summarized, just as a reminder, in *Table 4.1*.

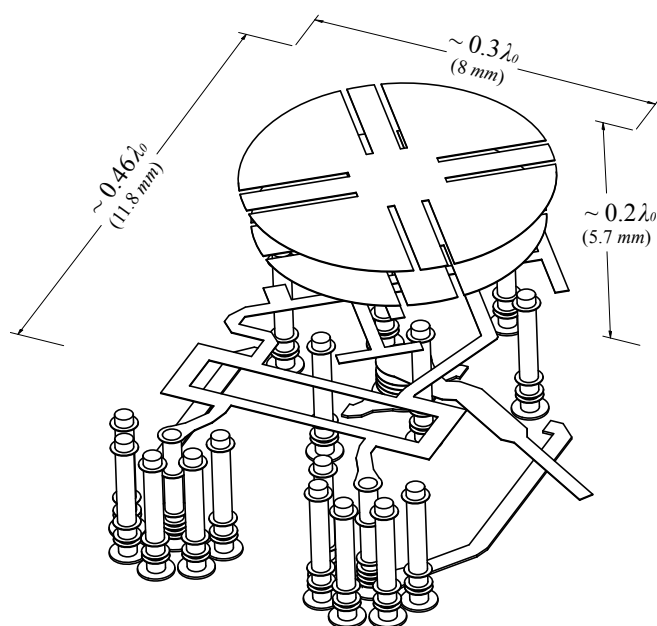


Figure 4.1. 3-D view of the Elementary Radiating Cell, with dimensions.

	Parameter	Requirement
ERC Level	Area	Compatible with the array lattice* and with the routing of the Feeding / Control Networks.
	Thickness	≤ 10 mm
	Technology	Standard PCB, without high-end materials. Simplest processing (single press, single plating).
	Frequency Band	10.7 – 12.75 GHz
Isolated Radiating Element	Directivity	Low - Medium (5 – 7 dB).
	Radiation Pattern	Symmetrical in azimuth.
	Radiation Efficiency	$\geq 80\%$
	Polarization	Dual Circular.
	Axial Ratio	$\lesssim 6 - 8$ dB, in the Scanning Range.**
	Return Loss	$\gtrsim 10$ dB
	Port Isolation	$\gtrsim 20$ dB
Long Vias	Mutual Coupling	$\lesssim -20$ dB
	Insertion Loss	≤ 0.8 dB
	Return Loss	$\gtrsim 20$ dB
Power Combiner	Cross Coupling	$\lesssim -20$ dB
	Insertion Loss	$\lesssim 0.6$ dB
	Return Loss	$\gtrsim 20$ dB
	Power Unbalance	$\lesssim 0.5$ dB

$$*A_{\square} (\varnothing_{\min} = 0.54 \lambda_0) \approx 0.25 \lambda_0^2.$$

**360° in az. and 20° – 70° in el. (from broadside).

*** \lesssim and \gtrsim symbols are used for performance parameters whose required values are not explicitly determined from system calculations but estimated from typical expectations.

Table 4.1. Elementary Radiating Cell Requirements (update to *Table 1.3*).

As it was illustrated throughout the design process of the ERC, the fulfillment of these constructive requirements may entail severe limitations on the electromagnetic (EM) performance of the cell. In fact, the compromise between these two sets of requirements is so tight and the technological constraints so restrictive, that, beyond certain fundamental bounds that may apply to the physical structure supporting the ERC, the maximum EM performance of the cell is expected to be rather diminished. In this scenario, the full compliance with the EM performance requirements specified in *Table 4.1* is not guaranteed.

In particular, the performance levels attained after this design process reveal that the most critical parameters pertain the Radiating Element (RE). The predicted results from *Table 3.4* suggest that these parameters are, in order of relevance, the *Radiation Efficiency* ($\sim 66\%$), the *Mutual Coupling* (-18 dB, approx.) and the *Axial Ratio* (~ 6 dB). The last parameter is expected to improve at array level once the foreseen sequential rotation scheme is implemented. In view of the inter-element spacing, the improvement in terms of mutual coupling seems more involved.

Moreover, given the miniaturization approach used for the mitigation of the mutual coupling, a further improvement in this sense may come into conflict with the radiation efficiency and the bandwidth of the element (recall *Section 2.4.2* and *Section 3.3.4*).

On the other hand, these predictions are already providing a first answer to the question about the performance limitations that could be expected in a practical implementation of the cell, that was posed at the beginning of this thesis. The present chapter is devoted to the empirical assessment of these predicted results, and of the underlying answer. With this aim, the measured performances of the ERC as well as of its components in different configurations are evaluated and contrasted with predictions.

4.2 Fabrication of the prototypes

The present prototyping iteration is undertaken using the industrial PCB process that is targeted for the present application. A complete selection of the different components of the cell as well as several variations of the ERC itself are included in several boards like the one shown in *Fig. 4.2*. In the center of the picture, the circular shape corresponds to a prototype of the whole array aperture. This prototype is intended for the test of the *embedded* cell, which is reviewed in [1]. Around the array aperture, a couple of 4×4 sub-array prototypes is also visible. These sub-arrays are conceived to provide a preliminary assessment of the beam & polarization steering capabilities, as it is summarized in [2,3].

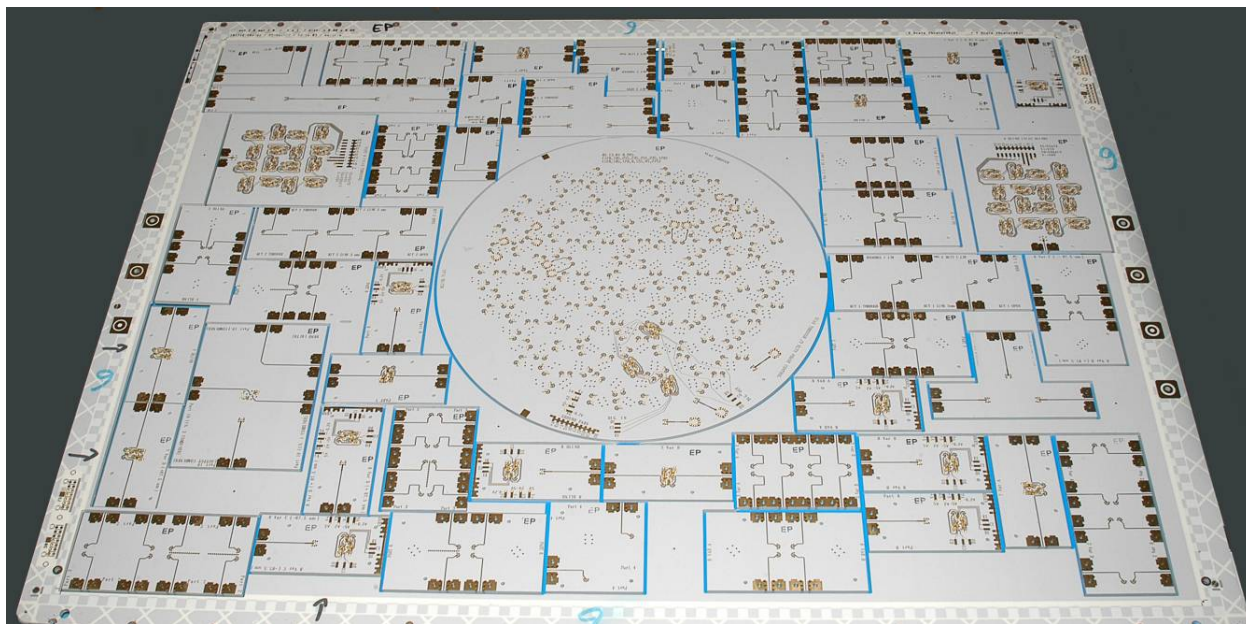


Figure 4.2. Photograph of a complete prototypes board. Image courtesy of *JAST Antenna Systems*.

This chapter deals only with the evaluation of the performances of the *isolated* ERC and its different components.

As a part of this evaluation, the tolerances associated to the manufacturing processes and the materials used for the assembly of the prototypes are taken into account. The effect that these fabrication tolerances may have in the performances of the different prototypes is studied in order to:

- assess the compatibility between the targeted fabrication technology and the ERC concept. If, for example, the sensitivity of the ERC performance to the fabrication tolerances is found to be excessive, such a study may allow to determine in which direction further design refinements could be undertaken or which technological constraints should be relaxed.
- To provide a reference for the degree of agreement between measured results and predictions that, given the fabrication tolerances, could be attained.

4.3 Linearly Polarized Radiating Element

The Dual Linearly Polarized Radiating Element (DLPRE) is the main component of the ERC. The structure of this element and its local coordinate system are provided, as a reminder of *Section 3.3.1*, in *Fig. 4.3*.

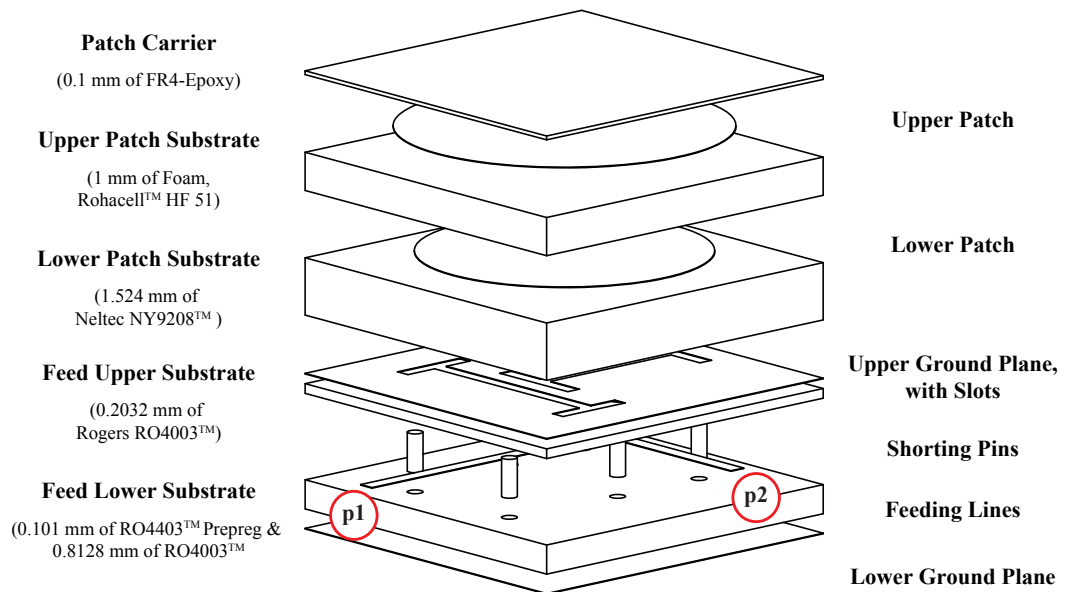
4.3.1 Fabrication Tolerances

The effect of the fabrication tolerances on the performance of the DLPRE is studied in this section. This study is based on the EM modeling of the element with a 2.5D ‘*Full Wave*’ software tool (*Ansoft DesignerTM*), and the fabrication tolerances that are considered relevant for the present study are defined as:

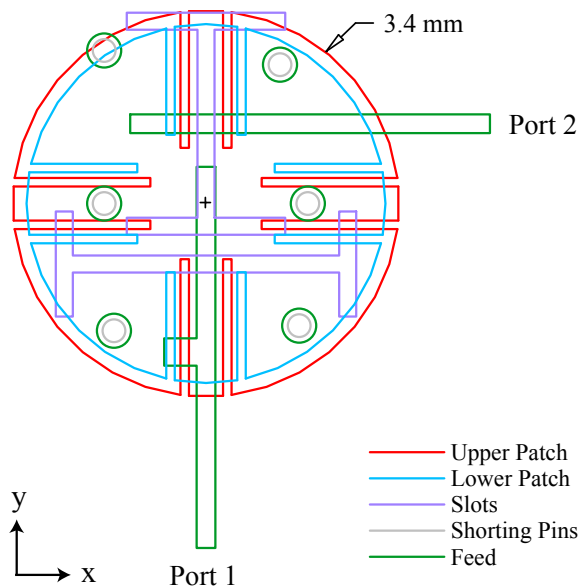
- **etching tolerances:** the estimation of the tolerances in the etching of the different metalization layers that compose the radiating element is $\pm 10 \mu\text{m}$.
- **Alignment tolerances:** the alignment between the different metalization layers that compose the buildup of the element is expected to keep within $\pm 37.5 \mu\text{m}$. The directions in which these miss-alignments take place are not specified.
- **Dielectric permittivity tolerances:** the expected tolerances in the permittivity of the dielectric materials that compose the element buildup are summarized in *Table 4.2*.
- **Dielectric thickness tolerances:** the expected tolerances in the thicknesses of the dielectric materials are shown in *Table 4.3*.

a) Scattering Parameters

The impact of the aforementioned tolerances on the Scattering Parameters (S-Params.) of the RE is evaluated as follows:



(a) Buildup.



(b) Layout Outline.

Figure 4.3. Structure of the linearly polarized element.

1. The S-Params. with the nominal values for all the constitutive parameters of the RE are evaluated. This provides the so-called *Nominal Performance*.

2. The S-Params. with the nominal values for all the constitutive parameters, but for the one that is assumed to be subject to tolerance, are evaluated. This evaluation is repeated taking into account the tolerances in each one of the constitutive parameters under study separately. The way this evaluation is done depends on the parameter whose tolerance is considered:

	ε_r	$\Delta\varepsilon_r$	Source
FR4-Epoxy	4.4	$\pm 10\%$	Estimation
Rohacell [®] HF51	1.07	$\pm 10\%$ *	Estimation
Neltec NY9208(IM) [™]	2.08	$\pm 0.96\%$	Data sheet
3M [™] 300LSE	2.8	$\pm 10\%$	Estimation
Rogers Prepreg RO4403 [™]	3.17	$\pm 10\%$	Estimation
RO4003 [™]	3.55	$\pm 1.5\%$	Data sheet

* with $\varepsilon_r \geq 1$

Table 4.2. Dielectric permittivity *Nominal Values* and *Tolerances* for the radiating element.

	t (mm)	Δt	Source
FR4-Epoxy	0.1	$\pm 10\%$	Estimation
Rohacell [®] HF51	1.0	$\pm 10\%$	Estimation
Neltec NY9208(IM) [™]	1.524	$\pm 10\%$	Estimation
3M [™] 300LSE	0.05	$\pm 10\%$	Estimation
Rogers Prepreg RO4403 [™]	0.101	$\pm 10\%$	Estimation
RO4003 [™] (<i>Upper Feed Substrate</i>)	0.2032	$\pm 12.5\%$	Data sheet
RO4003 [™] (<i>Lower Feed Substrate</i>)	0.8128	$\pm 6.25\%$	Data sheet

Table 4.3. Dielectric layer thickness *Nominal Values* and *Tolerances* for the radiating element.

- **Etching tolerances:** the S-Params. are evaluated only for the extreme values of the etching tolerance in each one of the 4 metalization layers concerned (2^4 evaluations).
- **Alignment tolerances:** the S-Params. are evaluated only for the maximum value of the miss-alignment in each one of the 4 metalization layers of interest. Only 6 possible directions (60° step) of miss-alignment are considered (6^4 evaluations).
- **Dielectric permittivity tolerances:** the S-Params. are evaluated only for the extreme values of the permittivity tolerance in each one of the 6 different dielectric materials integrating the element buildup (2^6 evaluations).

- **Dielectric thickness tolerances:** the S-Params. are evaluated only for the extreme values of the thickness tolerance in each one of the 7 different dielectric layers of the element buildup (2^7 evaluations).
3. Finally, the S-Params. are evaluated when all the constitutive parameters subject to tolerance are allowed to vary simultaneously. In order to avoid a prohibitively high number of evaluations, for each one of the 4 groups of constitutive parameters proposed above only 3 sets of parameter values are considered here (up to 3^4 evaluations). Two of these sets correspond to the extremes (upper and lower) of the domain in which each group of constitutive parameters was swept. The third set of values is chosen as that providing, for each group, the worst level of *Impedance Matching*. This scheme does not guarantee the reproduction of the worst case scenario (the global extreme). However, it is still considered to provide a representative estimation of the combined impact of all these tolerance parameters on the S-Params. of the radiating element.

The relative impacts of these tolerances on the S-Params. of the RE are summarized next:

- the worst value, within the frequency band of interest, of *Impedance Matching* for the *nominal* design is deteriorated by:
 - i) ~ 1.4 dB due to alignment tolerances only (*the smallest impact*),
 - ii) ~ 1.5 dB due to etching tolerances only,
 - iii) ~ 2.4 dB due to dielectric permittivity tolerances only and
 - iv) ~ 4.2 dB due to dielectric thickness tolerances only (*the greatest impact*).

And, as shown in *Fig. 4.4*, the combined impact of all these fabrication tolerances on the impedance matching can be, in the worst case, very important (~ 5.7 dB).

- On the other hand, the worst value, within the frequency band of interest, of *Port Coupling* for the *nominal* design is deteriorated by:
 - i) ~ 0.7 dB due to etching tolerances only (*the smallest impact*),
 - ii) ~ 0.8 dB due to dielectric permittivity tolerances only,
 - iii) ~ 3.4 dB due to dielectric thickness tolerances only and
 - iv) ~ 10.9 dB due to alignment tolerances only (*the greatest impact*).

And, as shown in *Fig. 4.5*, the combined impact of all these fabrication tolerances on the port coupling is not expected to be, in the worst case, so critical (~ 8.7 dB), provided the absolute value of this performance parameter.¹

¹Recall that the criteria used here to select the sweep sub-domains is attending solely to impedance matching. Therefore, the combination of these sub-domains in this last sweep may not guarantee the attainment of the highest degradation of the port coupling. In fact, the level displayed in *Fig. 4.5* (~ 8.7 dB) is not as important as that observed when only the alignment tolerances are considered (~ 10.9 dB).

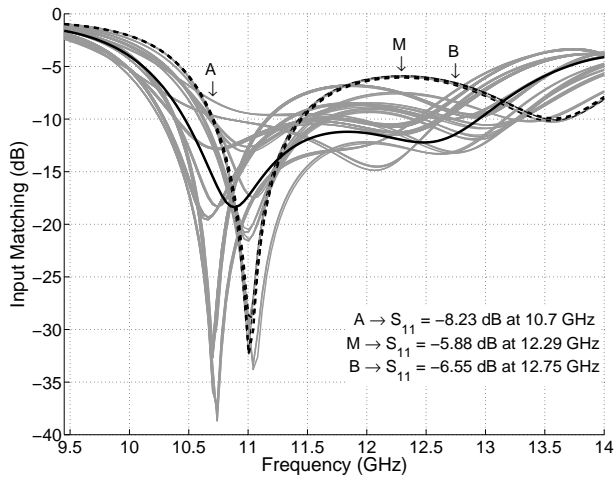
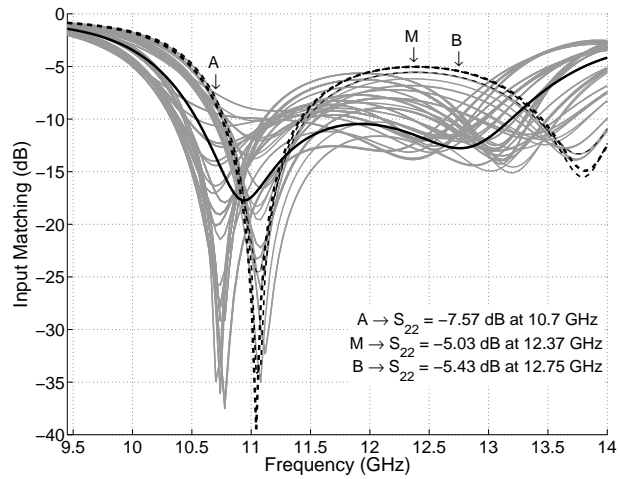
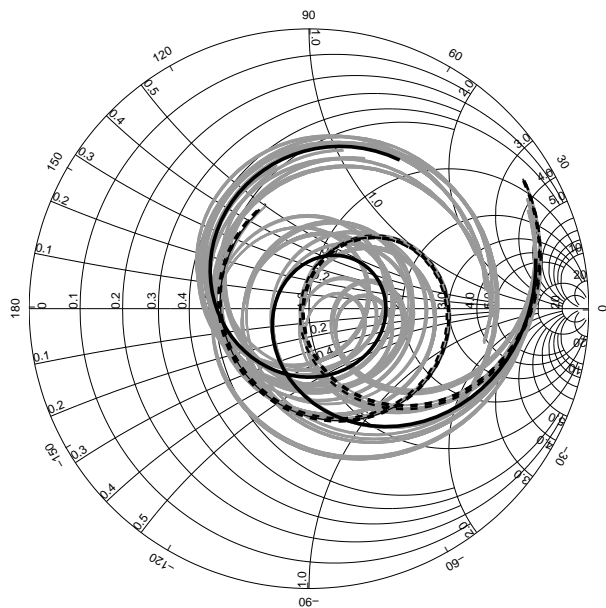
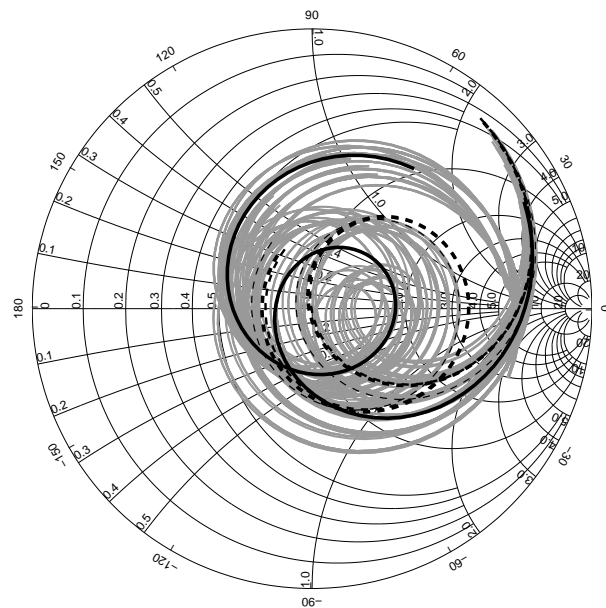
(a) Impedance matching. *Port 1.*(b) Impedance matching. *Port 2.*(c) Input impedance. *Port 1.*(d) Input impedance. *Port 2.*

Figure 4.4. Impact of the fabrication tolerances on the reflection coefficients of the DLPRE. The *nominal* curves (in continuous black line), those obtained for different values of the parameters subject to tolerances (in continuous gray line) and the three cases with *worst Impedance Matching* levels (in dashed black line) are displayed superimposed. Here, the alignment between layers, the etching and the thicknesses & permittivities of the substrates are considered subject to tolerance. From [4].

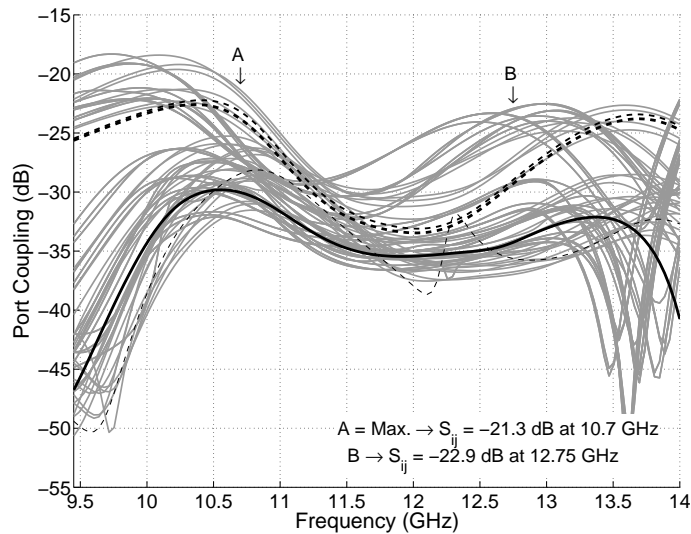


Figure 4.5. Impact of the fabrication tolerances on the port coupling of the DLPRE. The *nominal* curves (in continuous black line), those obtained for different values of the parameters subject to tolerances (in continuous gray line) and the three cases with *worst Impedance Matching* levels (in dashed black line) are displayed superimposed. Here, the alignment between layers, the etching and the thicknesses & permittivities of the substrates are considered subject to tolerance. From [4].

b) Radiation Parameters

The impact of the fabrication tolerances on the Radiation Parameters (Rad. Params.) of the DLPRE is evaluated in a very similar way as it was done for the S-Params. The main difference is coming from the fact that the evaluation, storage and analysis of the Rad. Params. is somewhat more costly. This is basically due to the EM modeling approach (in which the evaluation of Rad. Params. is done after some post-processing steps) and the additional (angular) dimensions involved in radiation problems. This higher cost motivates a less exhaustive evaluation of the impact of these tolerances on the Rad. Params. In order to make this evaluation more representative, the information obtained from the S-Params. analysis described above is reused here.

In particular, for every constitutive parameter subject to tolerance, the maximum number of evaluations of the Rad. Params. is limited to 30. In this way, the 2^4 evaluations associated to the *etching* tolerances are all done. For each one of the other constitutive parameters, however, only the 30 combinations that are observed to provide the worst levels of *Impedance Matching* in the corresponding S-Params. sweep are considered.

The relative impacts of these tolerances on the Rad. Params. of the DLPRE are evaluated only within the scan domain and the frequency band of interest. These impacts can be summarized as follows:

- the worst value of *Cross-polarization* for the *nominal* design is deteriorated by:
 - i) ~ 0 dB due to etching tolerances only (*the smallest impact*),
 - ii) ~ 0.5 dB due to dielectric permittivity tolerances only,
 - iii) ~ 0.5 dB due to alignment tolerances only and
 - iv) ~ 0.8 dB due to dielectric thickness tolerances only (*the greatest impact*).

And, as shown in *Fig. 4.6*, the combined impact of all these fabrication tolerances on the cross-polarization can be moderate (~ 2.3 dB), but is not expected to be critical. Just for the sake of illustration, several elevation cuts of two of the the worst radiation patterns analyzed here are displayed in *Fig. 4.7* and *Fig. 4.8*.

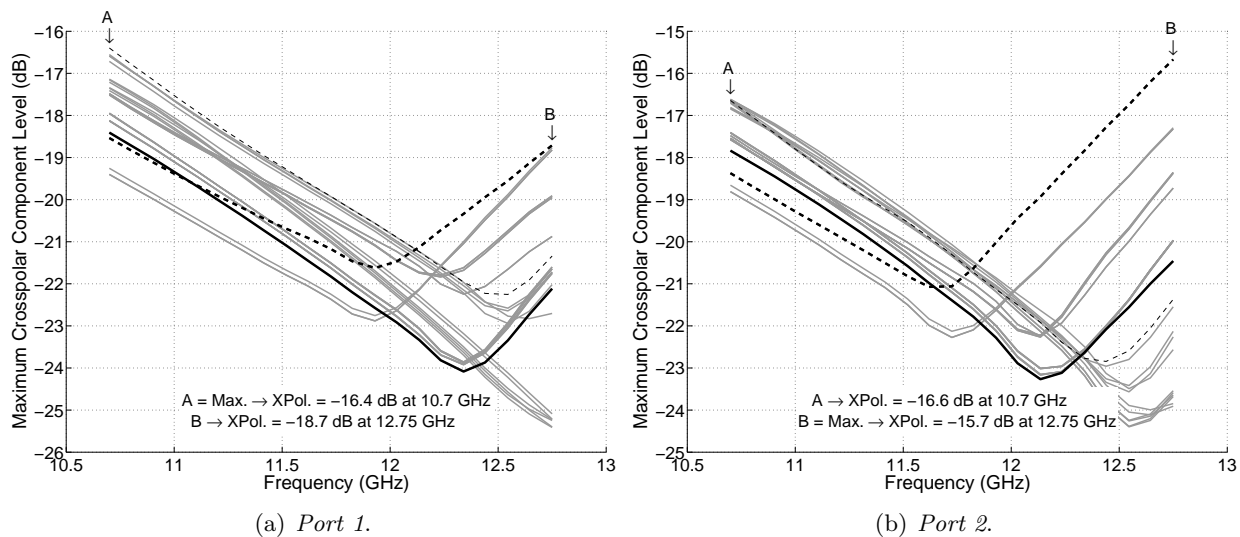


Figure 4.6. Impact of the fabrication tolerances on the Polarization Purity of the DLPRE. Maximum cross-polar component in the scan domain, according to *Ludwig's third definition* [5]. The *nominal* curves (in continuous black line), those obtained for different values of the parameters subject to tolerances (in continuous gray line) and the three cases with *worst Cross Polarization* levels (in dashed black line) are displayed superimposed. Here, the alignment between layers, the etching and the thicknesses & permittivities of the substrates are considered subject to tolerance. From [4].

- On the other hand, the worst value of *Radiation Efficiency* for the *nominal* design is deteriorated by:
 - i) $\sim 0\%$ due to alignment tolerances only (*the smallest impact*),
 - ii) $\sim 0.1\%$ due to etching tolerances tolerances only,
 - iii) $\sim 0.7\%$ due to dielectric permittivity tolerances only and
 - iv) $\sim 0.8\%$ due to dielectric thickness only (*the greatest impact*).

And, as shown in *Fig. 4.9*, the combined impact of all these fabrication tolerances on the radiation efficiency of the element ($\sim 1.7\%$) is not expected to be substantial.

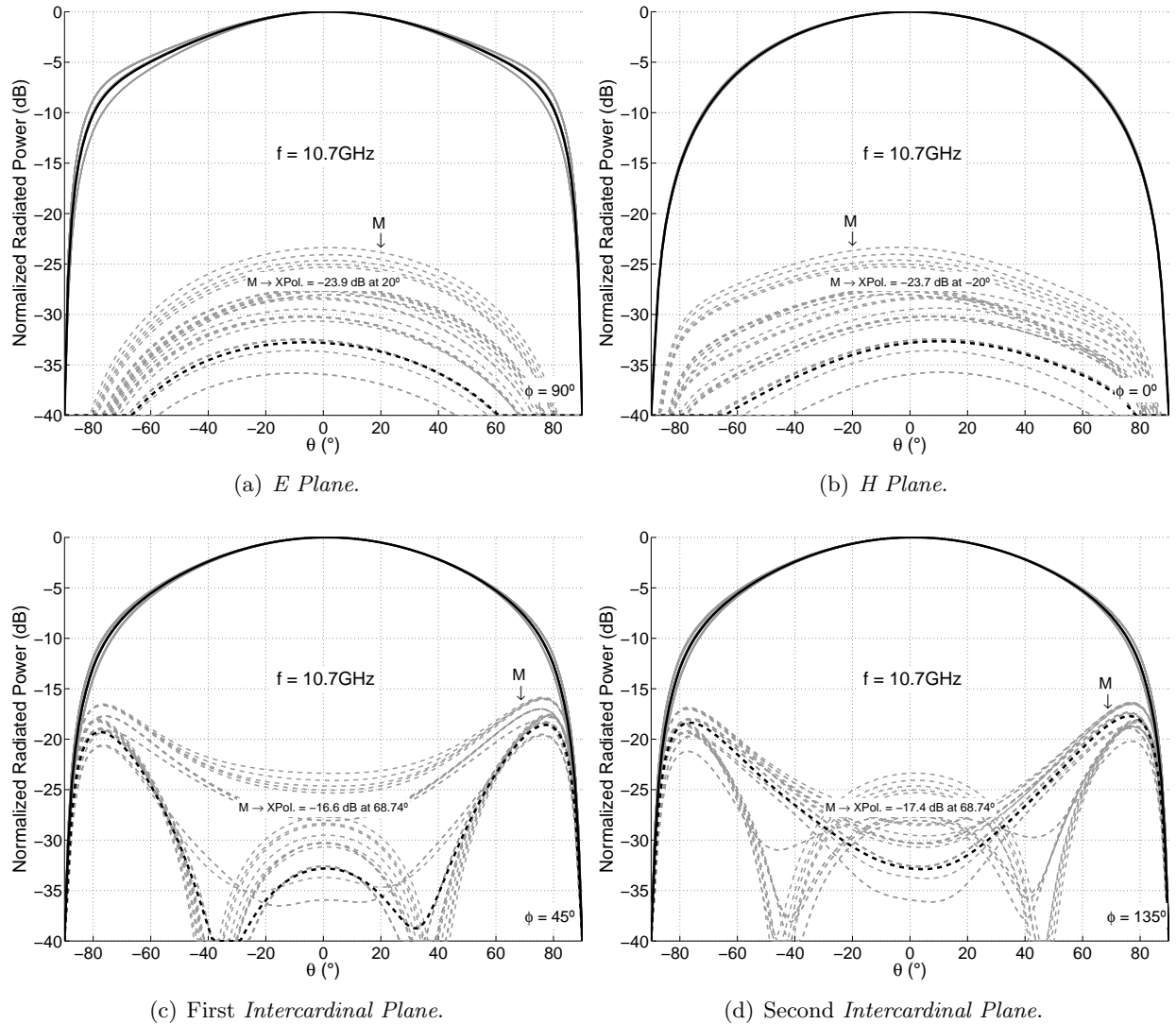


Figure 4.7. Impact of the fabrication tolerances on the Radiation Pattern of the DLPRE. Normalized field patterns of the radiating element (*Port 1* excited). Elevation cuts along the different planes at $f = 10.7$ GHz. Copolar (in continuous line) and Cross-polarized components (dashed) are obtained according to *Ludwig's third definition* [5]. The *nominal* curves (in black) and those obtained for different values of the parameters subject to tolerances (in gray) are displayed superimposed. Here, the alignment between layers, the etching and the thicknesses & permittivities of the substrates are considered subject to tolerance. From [4].

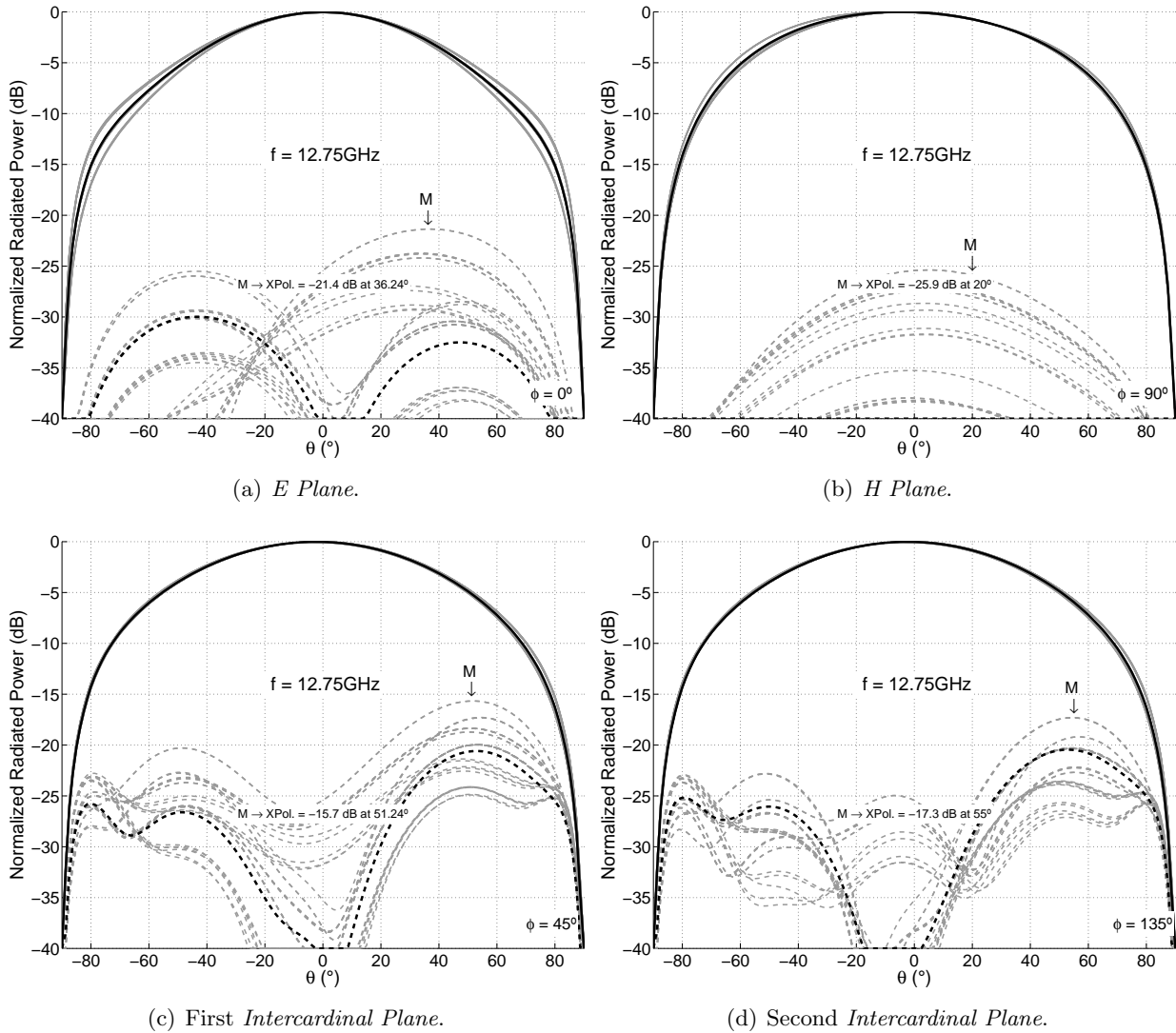


Figure 4.8. Impact of the fabrication tolerances on the Radiation Pattern of the DLPRE. Normalized field patterns of the radiating element (*Port 2* excited). Elevation cuts along the different planes at $f = 12.75$ GHz. Copolar (in continuous line) and Cross-polarized components (dashed) are obtained according to *Ludwig's third definition* [5]. The *nominal* curves (in black) and those obtained for different values of the parameters subject to tolerances (in gray) are displayed superimposed. Here, the alignment between layers, the etching and the thicknesses & permittivities of the substrates are considered subject to tolerance. From [4].

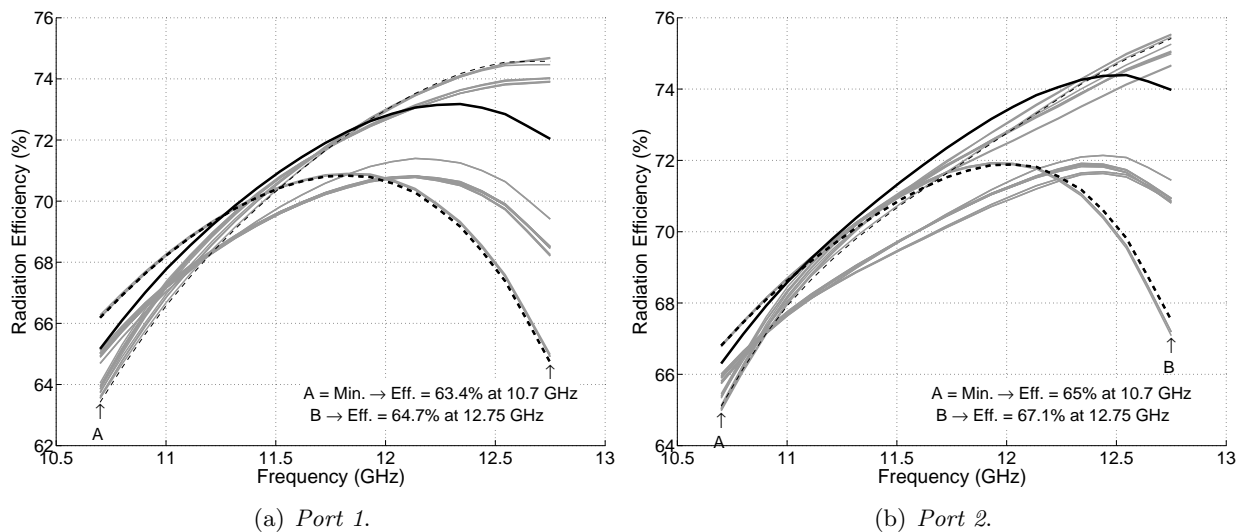


Figure 4.9. Impact of the fabrication tolerances on the radiation efficiency of the DLPRE. The *nominal* curves (in continuous black line), those obtained for different values of the parameters subject to tolerances (in continuous gray line) and the three cases with *worst Cross Polarization* levels (in dashed black line) are displayed superimposed. Here, the alignment between layers, the etching and the thicknesses & permittivities of the substrates are considered subject to tolerance. From [4].

c) Conclusions

The results of this study show that the performance of the DLPRE can be affected considerably by the fabrication tolerances. However, this sensitivity is not considered to be excessive, in general. There is only one case that reveals a dramatic degradation of the performance of the RE. This degradation concerns the impedance matching of the element, which suggests, according to *Section 2.4.3*, that a further oversizing of this performance parameter should be envisaged in future design iterations. To achieve this oversize, given the array lattice constraints, the possibility of allowing a somewhat higher profile for the RE should be explored. On the other hand, it is worth to recall that the results considered here are close to those of a worst case scenario and that the typical performance of the element is, therefore, expected not to be so much degraded.

Another interesting result that can be derived from the present sensitivity analysis is that, apart from the impedance matching of the element, the remaining performance parameters investigated (the radiation efficiency and the polarization purity) show a clear upward frequency-shift in most of the tolerance cases studied here (cf. *Fig. 4.9* and *Fig. 4.6*). This can be attributed to the fact that the miniaturization of the patches, that was done attending mainly to the input impedance of the element, makes the element prone to operate better at higher frequencies (recall *Section 2.4.2*).

4.3.2 Measured Performance

The prototype of the DLPRE is based on the model depicted in *Fig. 4.10*. This figure illustrates also the location of the reference plane and the local coordinate system used for the evaluation of the Scattering and Radiation Parameters, respectively. These references play a fundamental role when it comes to compare measured and predicted performances. In fact, a proper matching of these references in the models and in the prototypes is required to guarantee the coherence of the intended comparison.

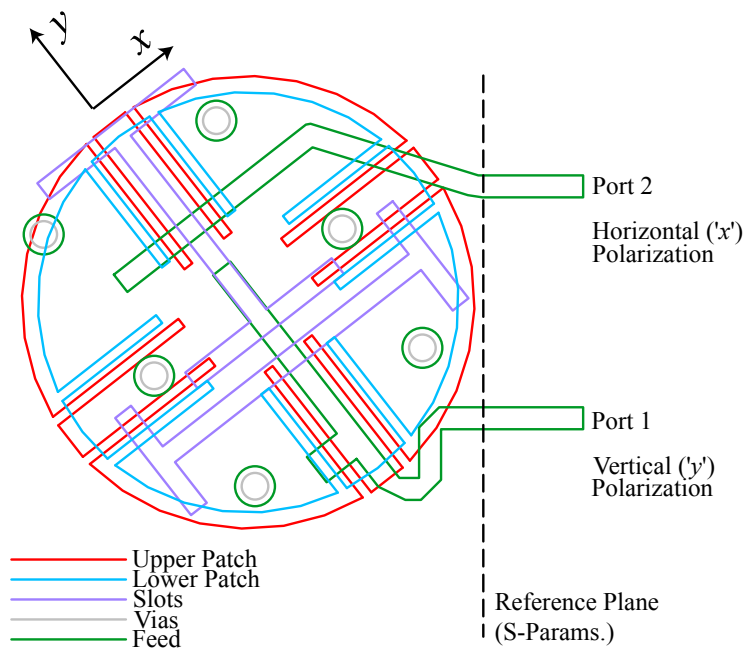
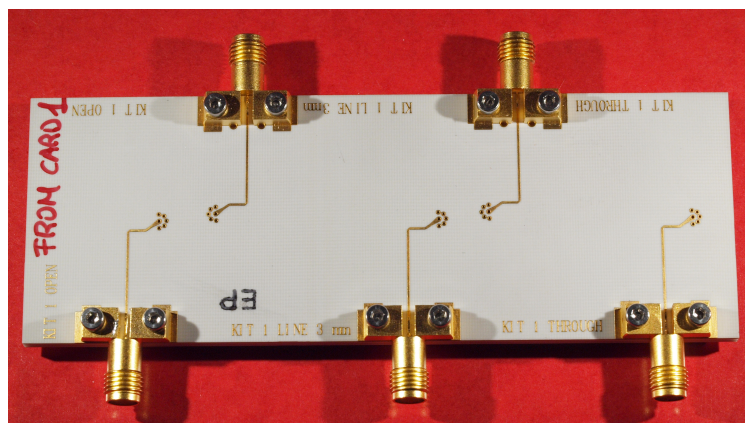
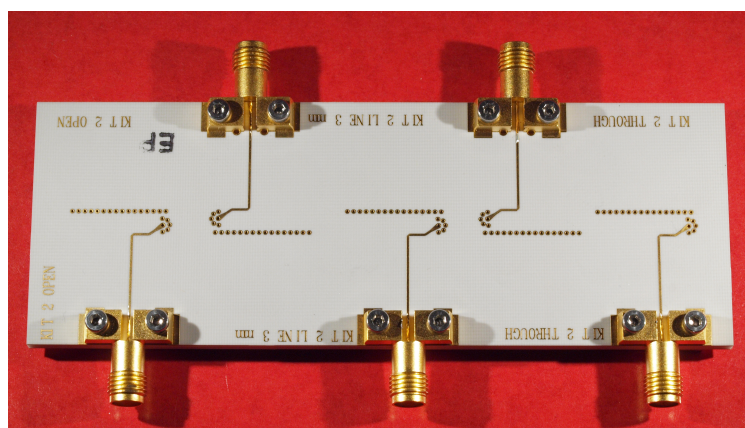


Figure 4.10. Layout outline of the DLPRE prototype. Note the Local Coordinate System, which is aligned with the linear polarization of the element, and the reference plane, that is associated to the *stripline ports* of the RE.

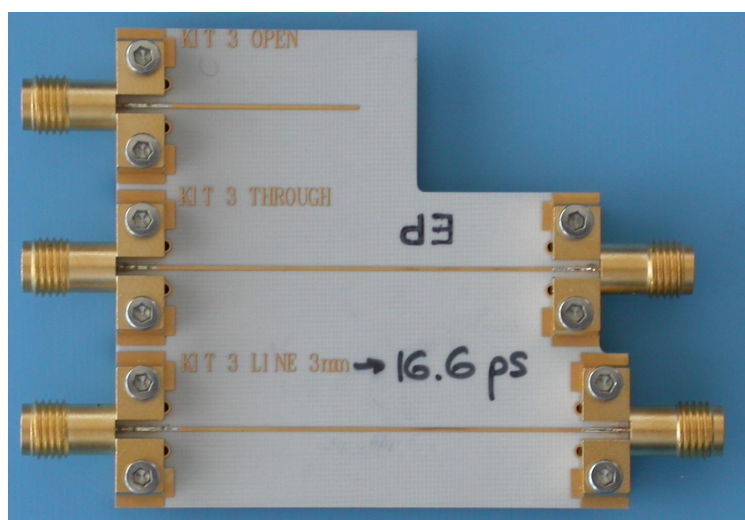
For the measurement of the S-Params. of the DLPRE, the reference plane illustrated in *Fig. 4.10* is set by means of a customized calibration procedure. Beyond the coaxial interface of the instrumentation used for this kind of measurements (a *Vector Network Analyzer -VNA*), this calibration procedure allows the “de-embedding” of all the transitions required to access the stripline ports of the radiating element. In particular, these transitions include the coaxial-to-microstrip ones of the *Connectors* and the microstrip-to-stripline of the *Long Vias*. This calibration procedure relies in the use of dedicated calibration kits (*Cal. Kits*, hereafter) as those shown in *Fig. 4.11*. Each one of these kits consists of three standards that give name to the calibration procedure itself: Thru-Reflect-Line (TRL) Calibration [6–8]. The figure also illustrates the kind of edge-mount coaxial connectors that are used to interface all the PCB samples tested here.



(a) *Cal. Kit #1*: to set the reference planes in the stripline layer.



(b) *Cal. Kit #2*: identical to *Cal. Kit #1*, but with stitching vias alongside the striplines.



(c) *Cal. Kit #3*: to set the reference planes in the microstrip layer.

Figure 4.11. View of the microstrip layer of the different *Cal. Kits* used for the measurement of the S-Params.

With regard to the measurement of the Rad. Params., the reference planes are located in the coaxial connectors of the prototypes. This is not relevant for relative measurements (like the normalized field patterns or the polarization purity), but must be taken into account for absolute measurements (as the gain or the radiation efficiency). Here, the values of these absolute magnitudes in the reference planes of interest, that coincide with those indicated for the S-Params. in *Fig. 4.10*, are deduced by means of an indirect approach. This approach is based on the modeling of a DLPRE whose reference planes match, as much as possible, those of measurements. If, in these conditions, the agreement between measured results and predictions is satisfactory, the *whole* DLPRE model gets thus validated and the predictions made at the reference planes of interest are also assumed to be valid.

Furthermore, all the measurements of Rad. Params. must be consistent with the local coordinate system defined for the radiating element. For the measurement setup used here, this consistency relies on the *manual* alignment of the prototype coordinate system with the polarization reference provided by the probe antenna. Typically, this alignment can be made easier if the edges of the prototype board are parallel to the coordinate system defined for the RE, as it was the case for the proof-of-concept prototype in *Fig. 3.23*.

a) Scattering Parameters

The S-Params. of the DLPRE are displayed in *Fig. 4.12* and *Fig. 4.13*. These figures confirm, beyond the noisy calibration results and the incertitude associated to the manufacturing process, the good performance of the element.² Moreover, there is a reasonable agreement between measurement results and predictions, which validates the theoretical modeling of the radiating element.

The two sets of measurements displayed here are made over the same prototype of the DLPRE, but the Cal. Kits used for these measurements are *slightly* different. In principle, the only difference between these kits lies in the stitching vias alongside the striplines of *Cal. Kit #2*, that are not present in the lines leading to the RE. Rigorously, this difference may call into question the validity of the measurement results obtained after calibrating with *Cal. Kit #2*. In practice, however, these additional measurements can provide some information on the reliability of both stripline Cal. Kits.

In fact, a weakness of PCB Cal. Kits is associated to potential deviations in the processes leading to the assembly of the different standards and the device under test. Such deviations may result in considerable undesired dissimilarities between the standards, which may compromise the reliability of the calibration and the subsequent measurements. These dissimilarities are typically

²Apparently, the only concern is coming from the slight miss-match measured in the upper part of the frequency band. In accordance with the predictions regarding the fabrication tolerances (recall *Fig. 4.4*), this miss-match stresses the convenience of undertaking a further oversizing of the impedance bandwidth of the DLPRE in future design iterations.

accentuated in the interfaces of the PCB samples (the edge mount connectors, in this case), where most of the manipulations (e.g. soldering) take place.

Ideally, the use of two slightly different Cal. Kits should provide slightly different measurement results. This is the case with regard to *Port 1*, as it can be seen in *Fig. 4.13(a)* and *Fig. 4.12(a)*. On the other hand, the two sets of measurements at *Port 2* differ noticeably. The reiteration of the measurements confirms these trends for both ports and suggests that the reliability of the measurements at *Port 1* is better than for the other port. In addition, the improved agreement observed between predictions and measurements at *Port 2* in *Fig. 4.13(b)* suggest that, despite the slight differences between the Cal. Kits, measurements relying on *Cal. Kit #2* might actually be more trustworthy than those using *Cal. Kit #1*.

b) Radiation Parameters

The elevation cuts of the radiation pattern represented in *Fig. 4.14* and *Fig. 4.15* are performed through the main planes indicated by the local coordinate system of the element in *Fig. 4.10*. The main features of this pattern are its high polarization quality (with a maximum crosspolar component very rarely exceeding -15 dB) and the good agreement with predictions.

With regard to the pattern of the proof-of-concept prototype in *Fig. 3.25* and *Fig. 3.26*, it is worth to notice that, here, the amplitude and frequency of the superimposed ripple are diminished considerably. This is attributed to the smaller size of the prototype PCB board and the fact that now the element is much closer to its borders ($\sim \frac{1.7}{2}\lambda_0 \times \frac{1}{2}\lambda_0$ vs. $\frac{3}{2}\lambda_0 \times \frac{3}{2}\lambda_0$). However, this reduced distance to the edges of the board is also believed to contribute to a more intense diffraction in these boundaries and, finally, to the rise in the average level of the crosspolar component observed for the present prototype -this is just an hypothesis. Besides, the rotation of the DLPRE with respect to the edges of the board makes somewhat more difficult the alignment of its local coordinate system to the polarization reference of the probe antenna. These difficulties may result into a degradation of the accuracy of the measurements of the polarization purity. Here, special attention is paid to the alignment of the antennas and the impact of this measurement error is therefore expected to be negligible.

Finally, it is also interesting to note that, as it was remarked for the candidate elements studied in the previous chapter (recall *Section 3.2.1*), the stacking and miniaturization of the patches can help to improve the symmetry of the radiation pattern of the element. This is evidenced here by the *E Plane* elevation cuts of *Port 1* ($\phi = 90^\circ$) in the region $\theta < 0$, where the degradation of such asymmetry with frequency is significantly reduced with respect to the proof-of-concept element (see *Fig. 3.25*).

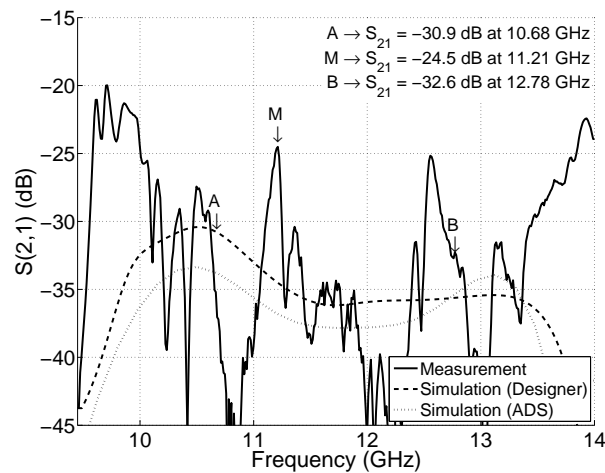
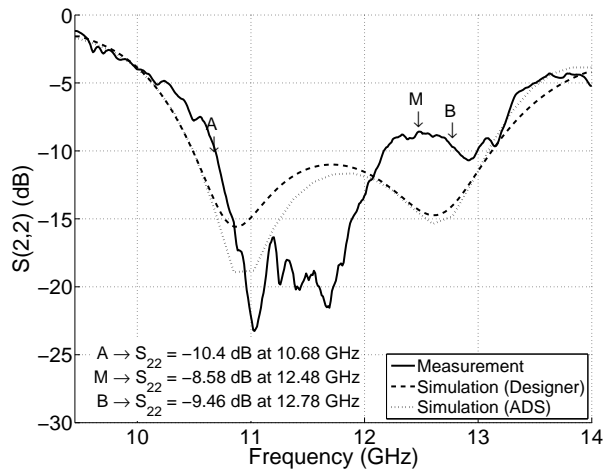
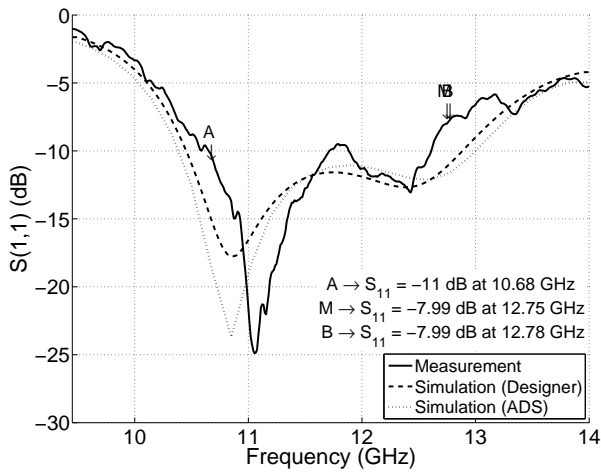
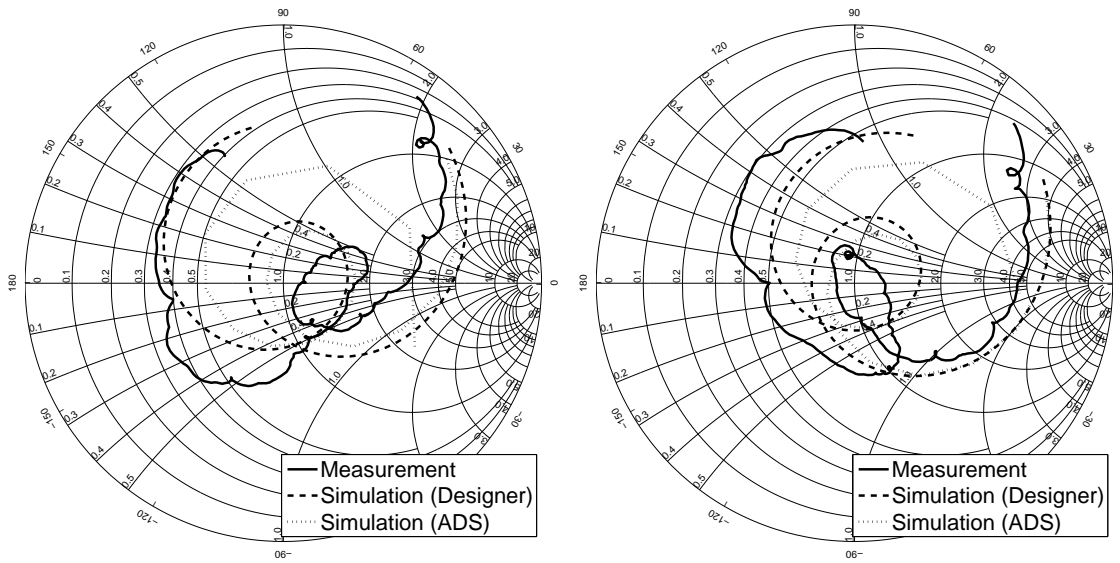


Figure 4.12. Scattering Parameters of the DLPRE. Measurements are done after TRL calibration with *Cal. Kit #1*. From [1].

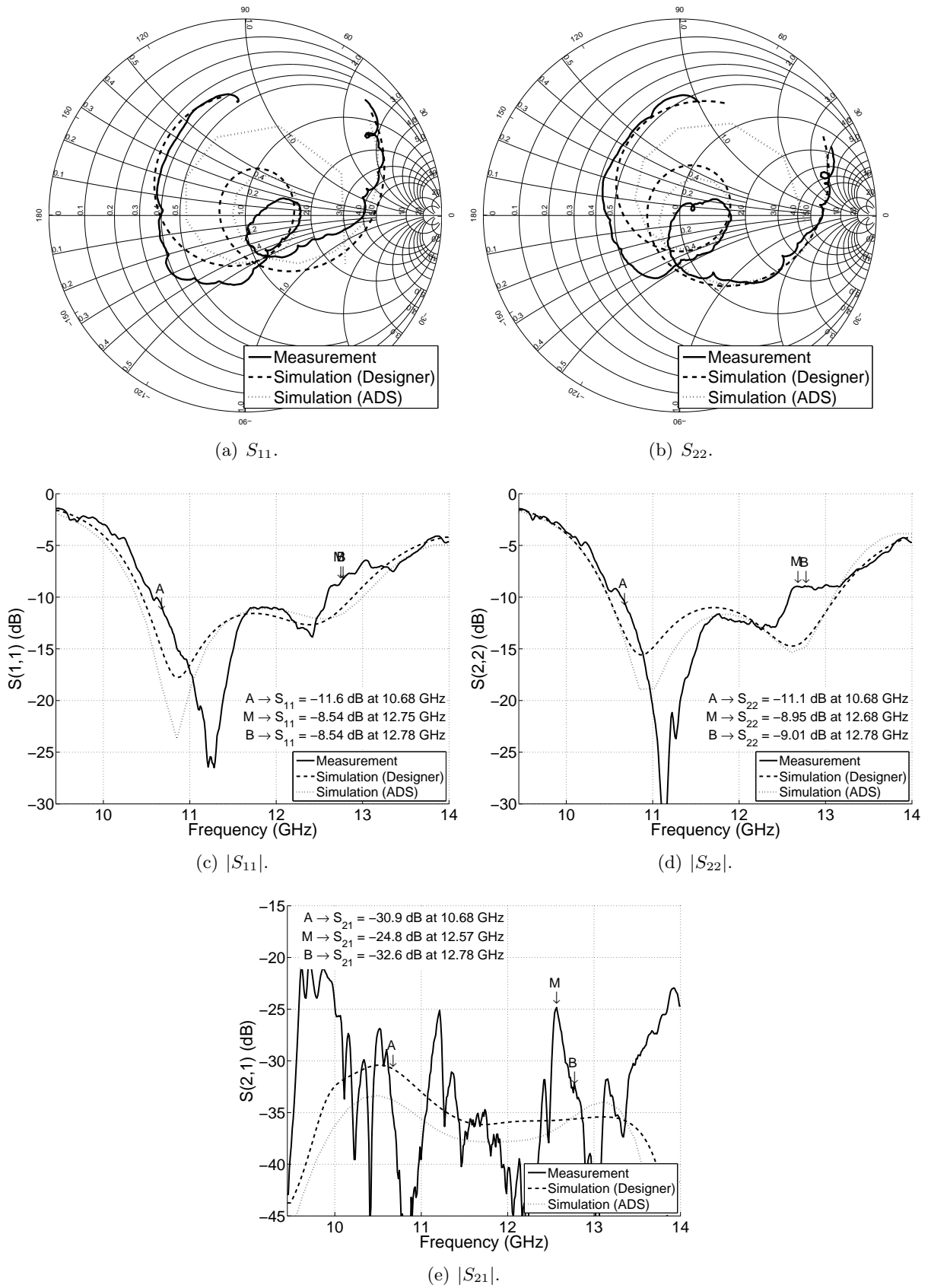


Figure 4.13. Scattering Parameters of the DLPRE. Measurements are done after TRL calibration with *Cal. Kit #2*. From [1].

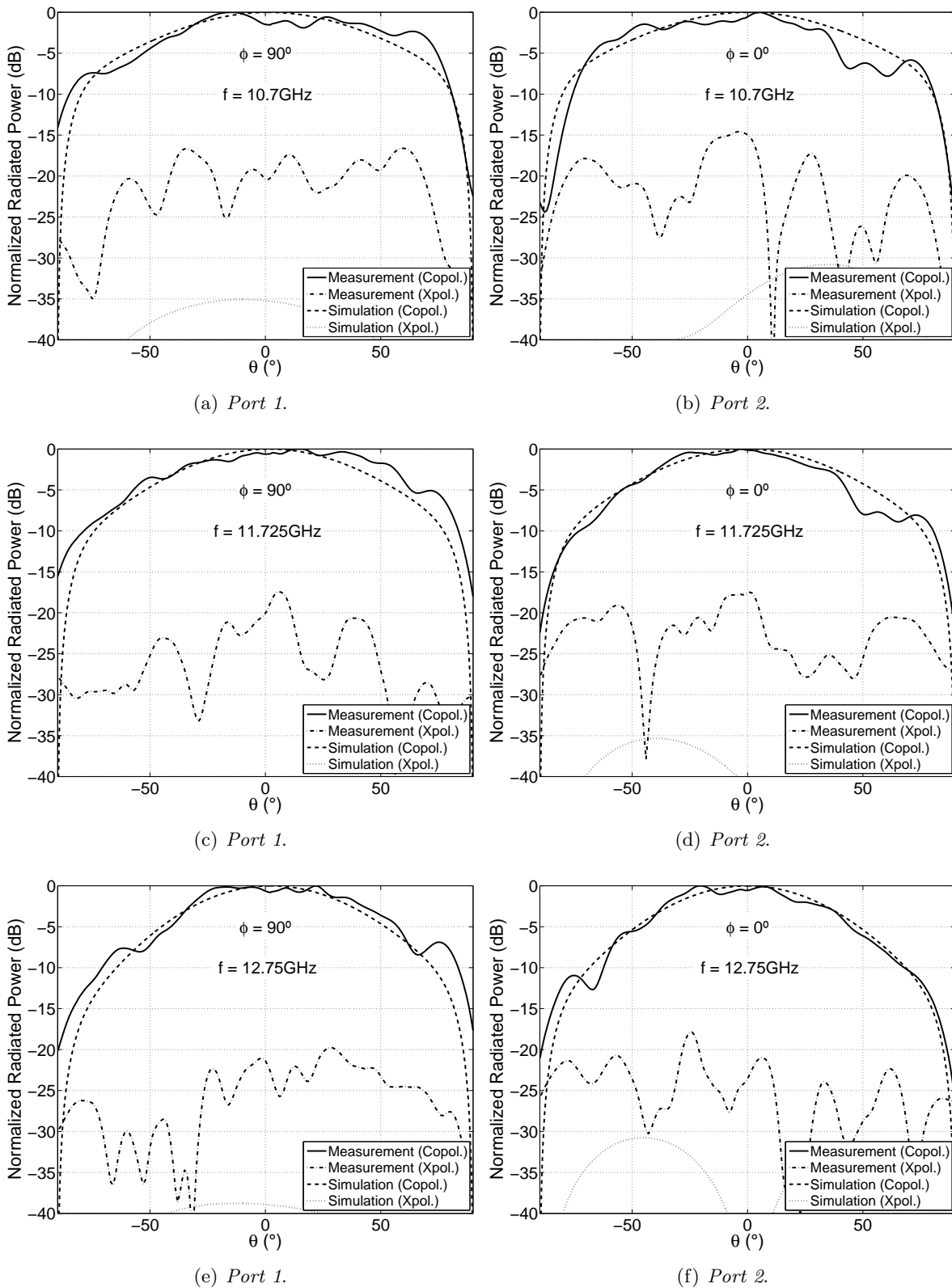


Figure 4.14. Normalized field patterns of the DLPRE. Elevation cuts along the E Plane at different frequencies. *Port 1* (Vertically Polarized Component) vs. *Port 2* (Horizontally Polarized Component). Simulation results assume an infinite ground plane. From [1].

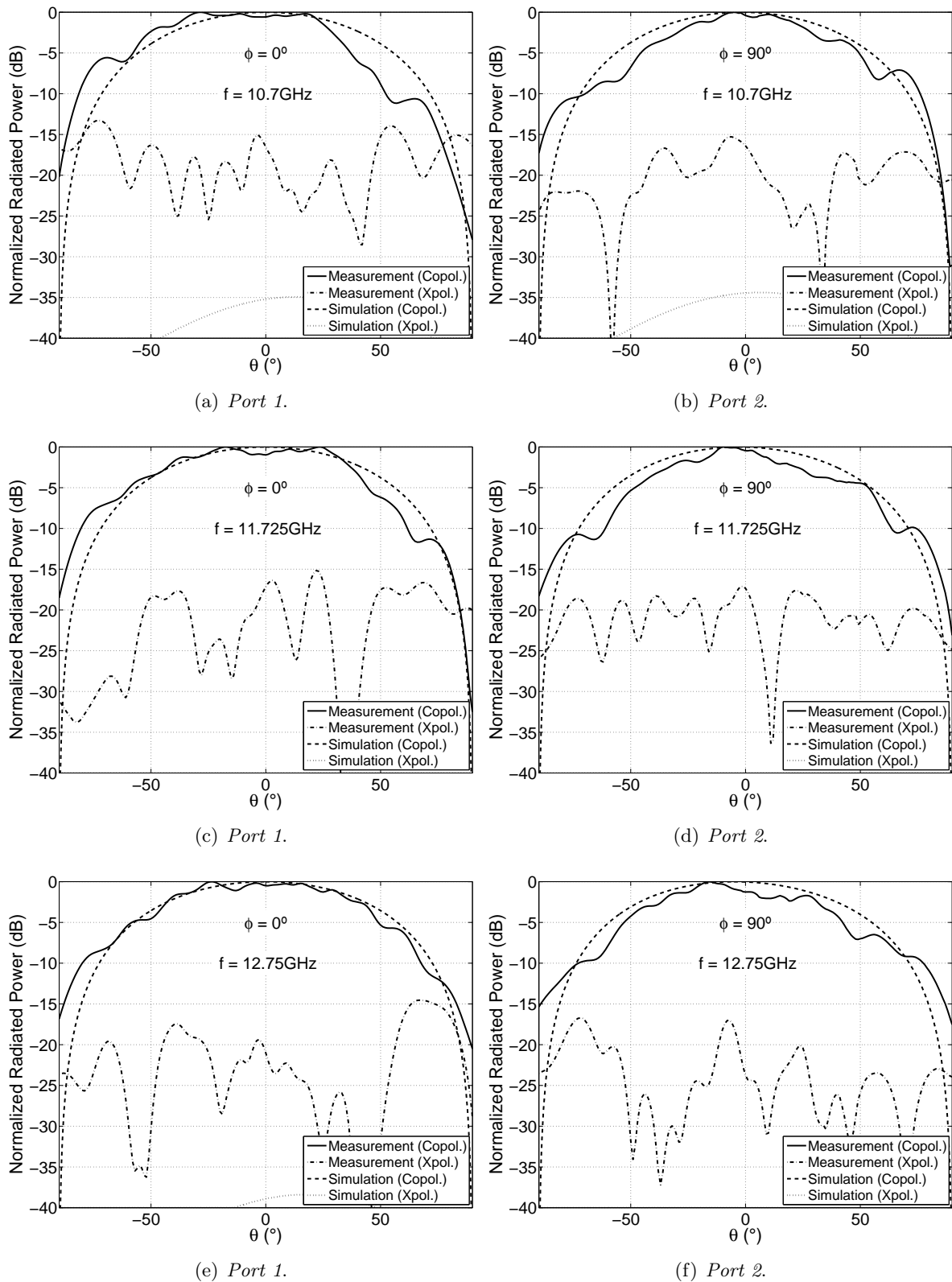


Figure 4.15. Normalized field patterns of the DLPRE. Elevation cuts along the H Plane at different frequencies. *Port 1* (Vertically Polarized Component) vs. *Port 2* (Horizontally Polarized Component). Simulation results assume an infinite ground plane. From [1].

Gain

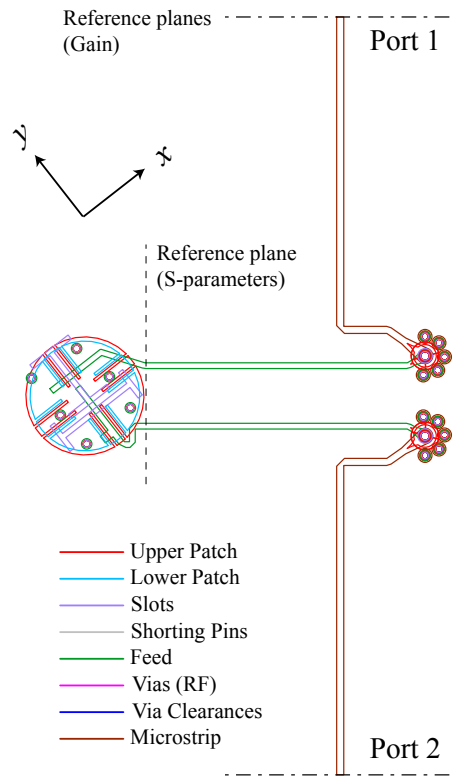
In average, the gain measured for the DLPRE keeps between 5 – 6 dB in the frequency band of interest. *Fig. 4.16* shows a good correspondence, given the uncertainties in the fabrication and testing of the prototypes, between measurement results and predictions for *Port 1*. However, the gain observed for *Port 2* differs considerably from expectations. Several attempts are made to explain this discrepancy, including a refinement of the theoretical model depicted in *Fig. 4.16(a)*, but none is providing a satisfactory answer.

In view of the good agreement between measured results and predictions observed for *Port 1*, the reasonable similarity between the results predicted for the two ports and the satisfying behavior observed in terms of scattering parameters for both ports, the hypothesis of a problem in the measurement of the gain for *Port 2* seems more convincing than that of a faulty prototype. Actually, the yield of the fabrication process is very high (but not 100%, as evidenced in *Fig. 4.17*), the repeatability of the connector mounting is not expected to be so bad and none of these two sources of error are expected to lead to such an important increase of the apparent RE gain.

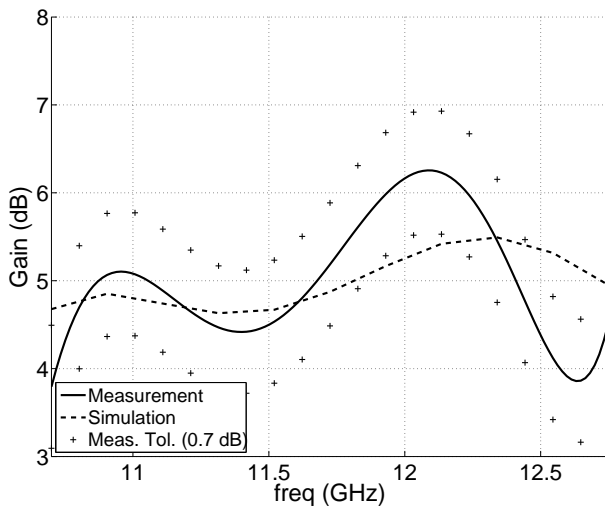
The presumably wrong results obtained for *Port 2* are thus neglected and only the good correspondence between measured and predicted gain levels for *Port 1* is retained. Under these assumptions and according to the theoretical modeling of the element, the *Radiation Efficiency* of the prototype in the reference planes of interest (S-Params. reference plane in *Fig. 4.16(a)*) is expected to be higher than 64% over the whole frequency band and for both ports.

4.3.3 Conclusion

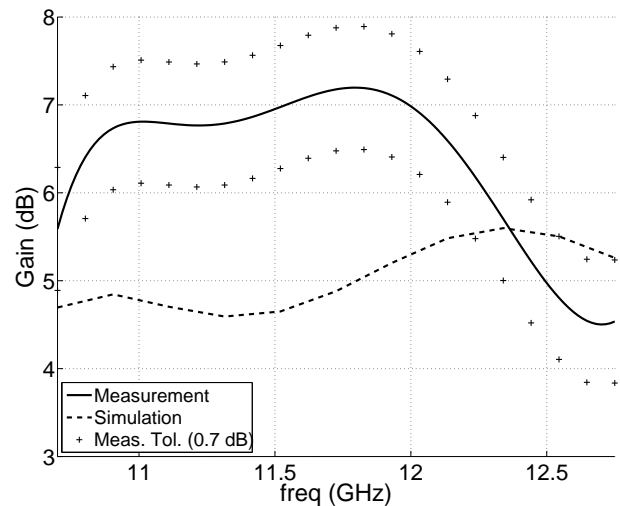
The performance evaluation of the DLPRE is providing very satisfying results. In absolute terms, these results confirm the promising performance of the radiating element. This constitutes an important assessment of the compatibility between the targeted fabrication technology and the RE concept. In relative terms, the overall good agreement observed between measured results and predictions validates the theoretical modeling of the element, which supports a reasonable degree of confidence in the success of subsequent modeling and evaluation steps.



(a) Layout outline of the prototype model (microstrip ports).



(b) Port 1.



(c) Port 2.

Figure 4.16. Realized gain of the DLPRE with illustration of the prototype model and its Local Coordinate System. Simulation results assume an infinite ground plane and do not take into account the connectors of the prototype (2.5D simulation with *Ansoft DesignerTM*). The connectors are edge mount coaxial to microstrip transitions as those visible in *Fig. 4.11*. The location of the reference planes in the simulation model coincides with the edges of the prototype in order to match, as much as possible, the measurement set-up. From [1].

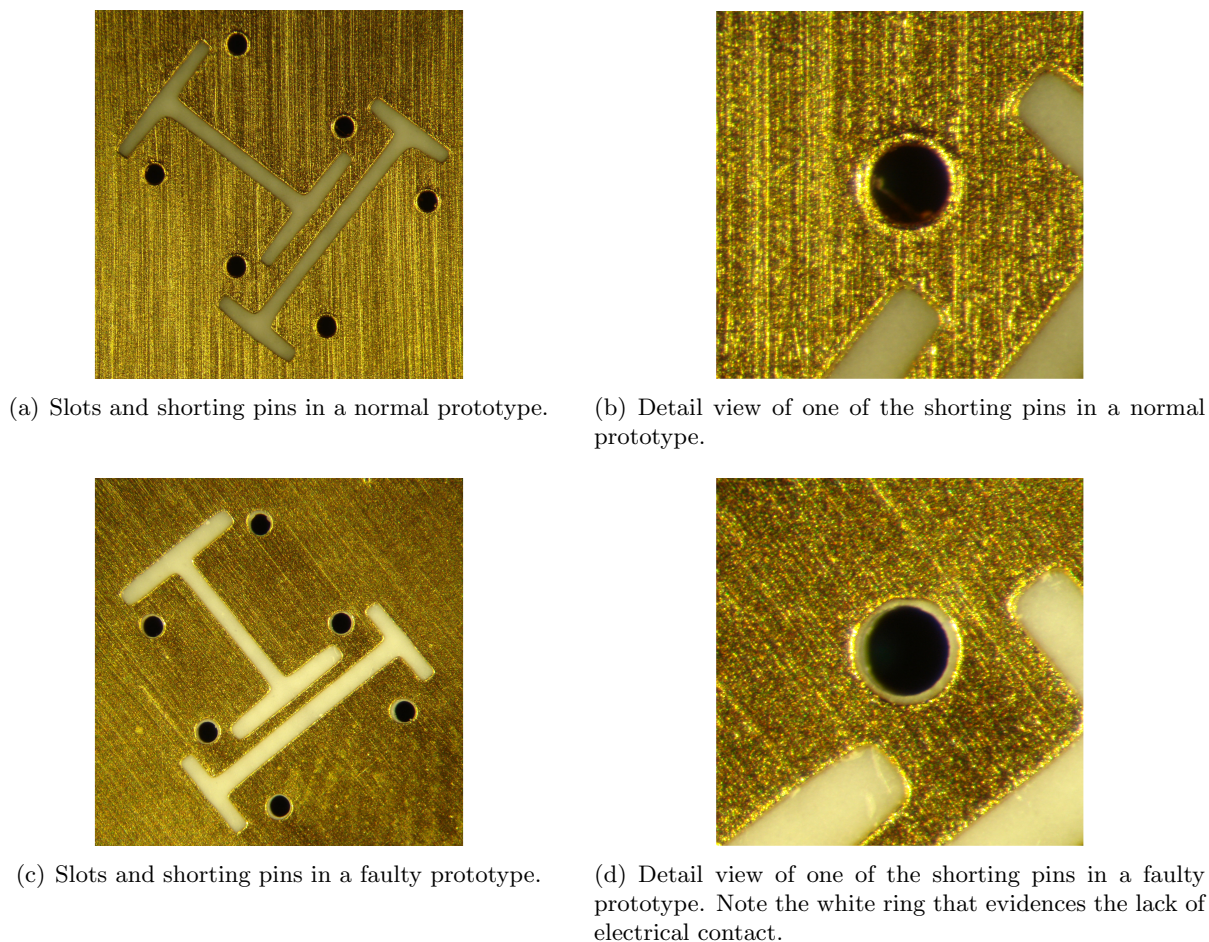
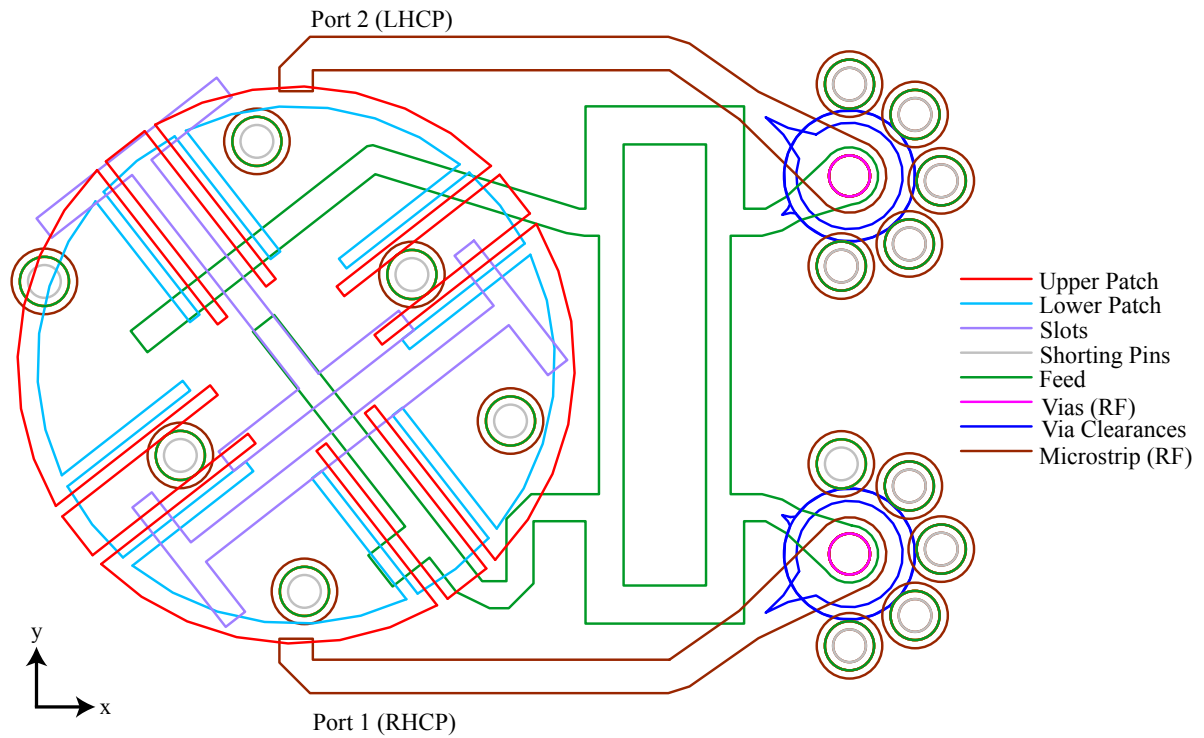


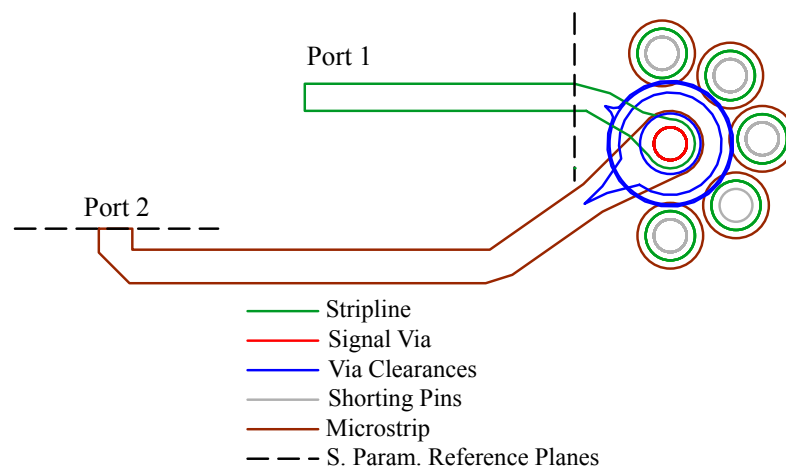
Figure 4.17. Views of the upper ground plane of two different prototypes with fabrication faults highlighted. The couple of images in the bottom evidence a lack of electrical contact between the upper ground plane and the through vias implementing the shorting pins. The impact of this fault on the performance of the affected prototypes (only a few out of several tens) is observed to be dramatic. Photographies courtesy of Mr. J.-F. Zürcher.

4.4 The Long Via

As they were presented in the previous chapter, the couple of twin *Long Vias* depicted in *Fig. 4.18* are a key component of the ERC. These vias are joining the outputs of the dual circularly polarized element, in an upper stripline layer, with the inputs of the MMICs, in the bottom microstrip layer. Therefore, the contribution of these vias to the noise figure of the receiver antenna system (or, equivalently, its G/T) is very important.



(a) Layout outline of the ERC (The Power Combiner is not shown).



(b) Layout outline of the Long Via. The reference planes are matching the interfaces of the Long Via with the ERC.

Figure 4.18. The Long Via within the ERC. From [9].

4.4.1 Nominal Performance

Given the overall thickness of the layout, the length of each Long Via is $\sim 0.1 \lambda_0$, which does not seem to be a considerable length. However, the fact that this via is embedded in the PCB buildup makes it to become electrically longer and its design, consequently, more involved. Moreover, such a via may interact with the ground planes it is passing through. In particular, the clearances in these ground planes and the shorting pins surrounding them play an important role in the EM performance of the Long Via. These constructive parameters, as well as the diameter of the via, are optimized attending, basically, to the impedance matching in the microstrip and stripline terminals of the Long Via and its insertion loss.

The performance of the resulting Long Via is shown in *Fig. 4.19*. This figure compares several predictions for the S-Params. of the Long Via and, though in all cases the operation of the via is very satisfactory, it evidences certain differences between these predictions. This lack of precision is not mitigated despite the multiple refinements applied to the different EM models of the Long Via. The difficulties in the characterization of the Long Via are increased due to the fact that the direct measurement of its performance is not possible, as it happened with the coaxial to stripline transitions studied in the previous chapter. Therefore, the accuracy of the different predictions is to be determined from the measurement of a back-to-back connection of a couple of Long Vias, as will be discussed later.

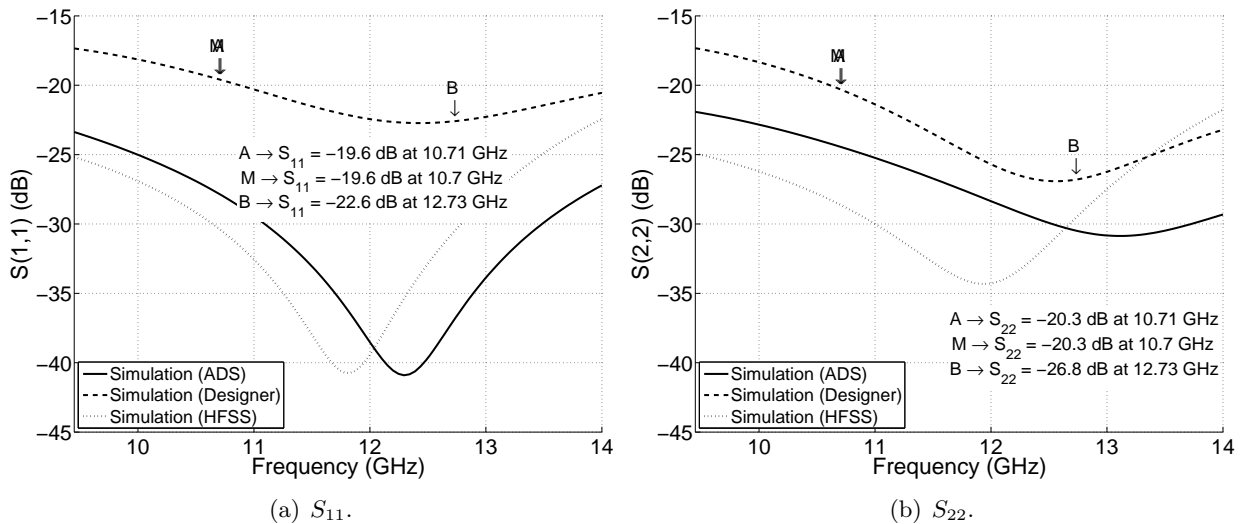


Figure 4.19. Scattering Parameters of the Long Via. The reference planes of the Long Via are as defined in *Fig. 4.18(b)*. From [9].

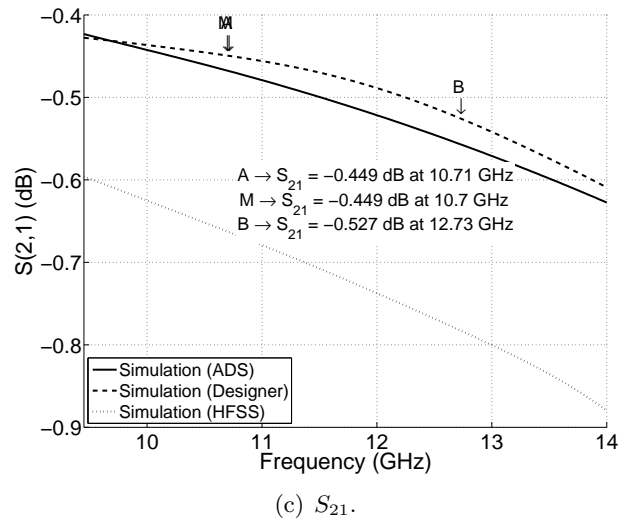


Figure 4.19. Scattering Parameters of the Long Via (contd.).

4.4.2 Fabrication Tolerances

Similarly as it was done for the DLPRE and using the same values listed in *Section 4.3.1*, the effect of the fabrication tolerances on the performance of the Long Via are analyzed next. The structure of the Long Via is illustrated in *Fig. 4.20*

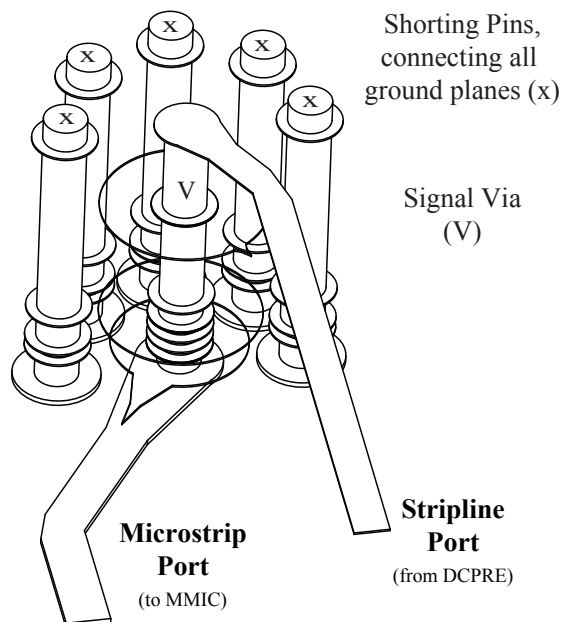


Figure 4.20. Long Via Structure. Note the rings corresponding to the clearances in the ground planes the signal via is passing through and the pads signaling the interfaces between different dielectric layers. Here, the alignment tolerances only concern to the relative positioning of the signal via with regard to the clearances, the pads and the transmission lines.

This study is based on the EM modeling of the Long Via with a 3D ‘Full Wave’ software tool (*Ansoft HFSSTM*), and the results are summarized attending to the impact of the fabrication tolerances on the impedance matching of the Long Via.

The worst value of the Impedance Matching in the frequency band of interest is deteriorated by:

- i) ~ 1.3 dB due to dielectric permittivity tolerances only (*the smallest degradation*),
- ii) ~ 2.4 dB due to alignment tolerances only and
- iii) ~ 8.7 dB due to dielectric thickness tolerances only (*the greatest degradation*).

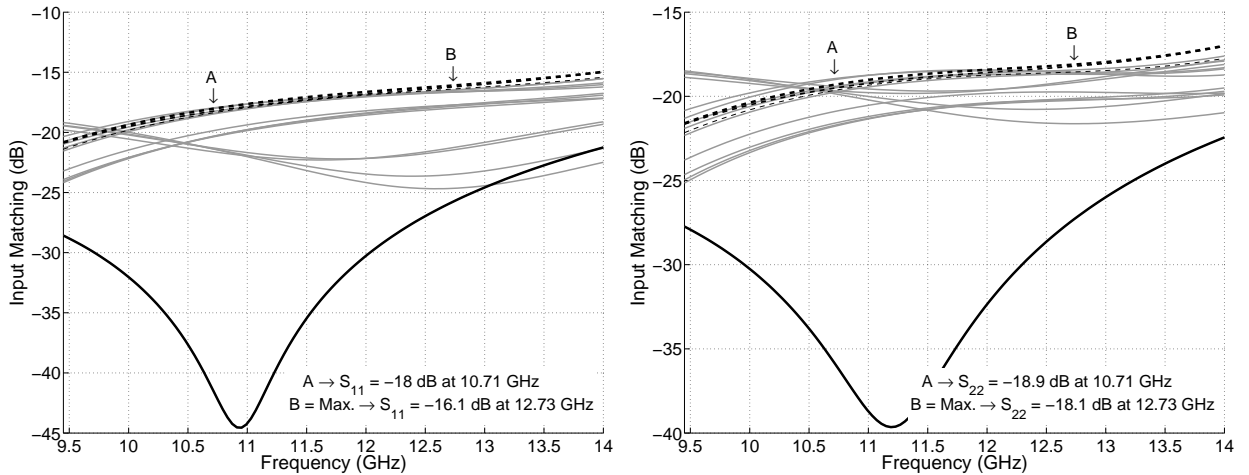
And the combined impact of all these fabrication tolerances on the impedance matching of the Long Via can be, in the worst case, considerable (~ 10 dB). However, this does not seem to prevent that the overall performance of the Long Via remains very satisfying, as evidenced in *Fig. 4.21*.

4.4.3 Measured Performance

The performance of the Long Via is deduced from measurements on a back-to-back configuration. Such a configuration is already present in two of the standards of the stripline Cal. Kit depicted in *Fig. 4.11(a)* (*Cal. Kit #1*). In order to mitigate the effects of the edge connectors in the characterization of the Long Via, these are de-embedded from the measurements by means of a TRL microstrip calibration (using *Cal. Kit #3*). The location of the reference planes after this calibration process is illustrated in *Fig. 4.22*.

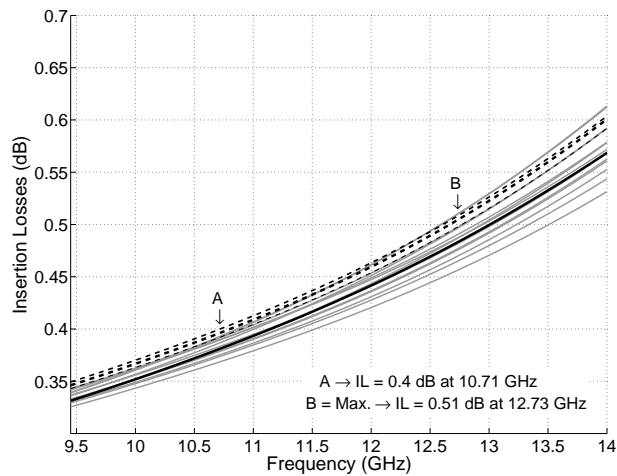
Fig. 4.22 includes a comparison between measurements and predictions for the S-Params. of the back-to-back configuration. This comparison reveals that the most accurate results for the Long Vias are those provided by *Agilent ADS Momentum* (a 2.5D ‘Full Wave’ software tool)³ This agreement validates also the predictions from the different models of the Long Via that are shown in *Fig. 4.19*.

³Surprisingly, the refinement of the Long Via model in *Ansoft HFSSTM* did not improve the poor agreement with measurements observed in *Fig. 4.22(c)*.



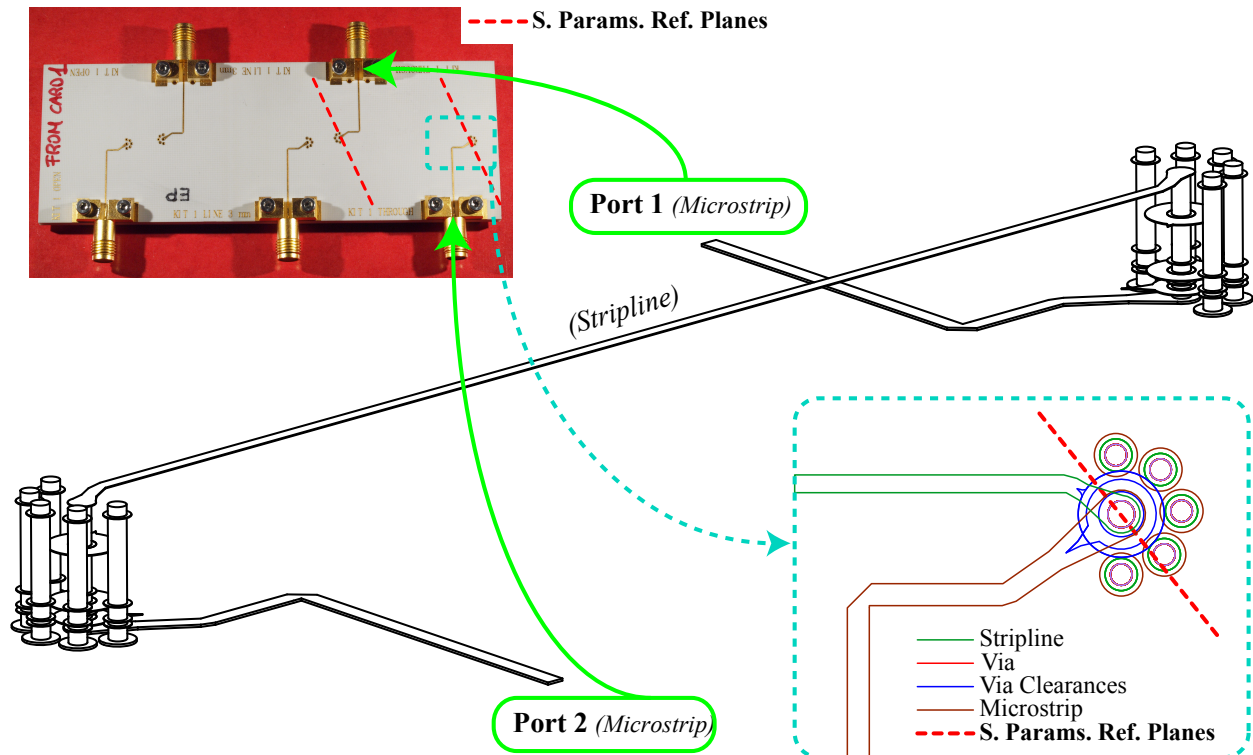
(a) Impedance Matching at Stripline Port.

(b) Impedance Matching at Microstrip Port.

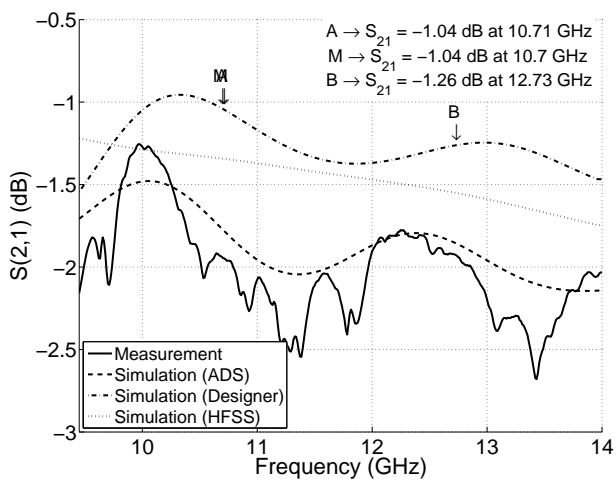


(c) Insertion Loss.

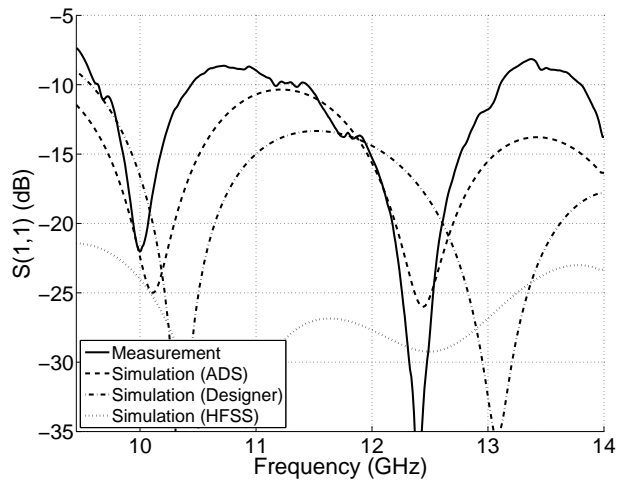
Figure 4.21. Impact of the fabrication tolerances on the performance of the Long Via. The *nominal* curves (in continuous black line), those obtained for different values of the parameters subject to tolerances (in continuous gray line) and the three cases with *worst Impedance Matching* levels (in dashed black line) are displayed superimposed. Here, the alignment between layers and the thicknesses & permittivities of the substrates are considered subject to tolerance. From [10].



(a) The Long Via within *Cal. Kit #1*, with Reference Planes highlighted.



(b) Transmission Coefficients.



(c) Reflection Coefficients.

Figure 4.22. Scattering parameters of *Cal. Kit #1*. The reference planes for measurements and simulations, which are on the microstrip layer for both ports, have been shifted up to the pads of the Long Vias. From [1].

4.4.4 Conclusion

The assessment of the performance of the Long Via presents considerable difficulties, both in terms of theoretical modeling and measurement. These difficulties have been successfully addressed, leading to the design of a Long Via transition whose performance is expected to be very satisfying. The confidence in these promising expectations is supported by the good agreement observed between measurements and predictions for the behavior of the Long Via embedded in a back-to-back configuration.

4.5 The Power Combiner

Located after the first amplification stage, the performance of the Power Combiner is much less critical than that of the Long Vias. Moreover, its connection to the Feeding Network, in an intermediate stripline layer, does not require the use of “long” vertical transitions, which is compatible with an improved electrical performance. In its actual implementation, depicted in *Fig. 4.23*, the overall length of the signal via of the Power Combiner is $\sim 0.03 \lambda_0$ (3 times shorter than for the Long Via).⁴

4.5.1 Nominal Performance

The nominal performance of the Power Combiner is displayed in *Fig. 4.24*. This figure contains a comparison of several predictions for the different performance parameters considered in the design of the combiner. These performance parameters (*Phase and Magnitude Unbalance*, basically) are defined in the legends of the figure. According to the plots, the performance of the combiner is good and the deviation of the different predictions is small, which supports a reasonable confidence in the accuracy of the modeling of the Power Combiner.

An important design constraint for the Power Combiner is related to the shorting pins surrounding it. These pins are associated to the feeding of the Radiating Element and limit, on one side, the routing of the stripline port of the combiner towards the Feeding Network. On the other hand, the presence of these shorting pins contributes to mitigate the power leakage in the feeding of the RE and in the Power Combiner. In the case of the combiner, this contribution is relatively small (up to ~ 0.5 dB [10]) and, in principle, it would be possible to envisage the suppression of some of these shorting pins without a noticeable performance degradation. This suppression would, however, enter in conflict with the performance of the RE, that depends strongly on all these shorting pins.

⁴In terms of performance, instead of the ‘reactive’ Power Combiner proposed here, a ‘lossy’ design, such as the so-called Wilkinson Power Combiner, would be preferred. The implementation of such a combiner with the space & technological constraints proposed here does not seem evident, however.

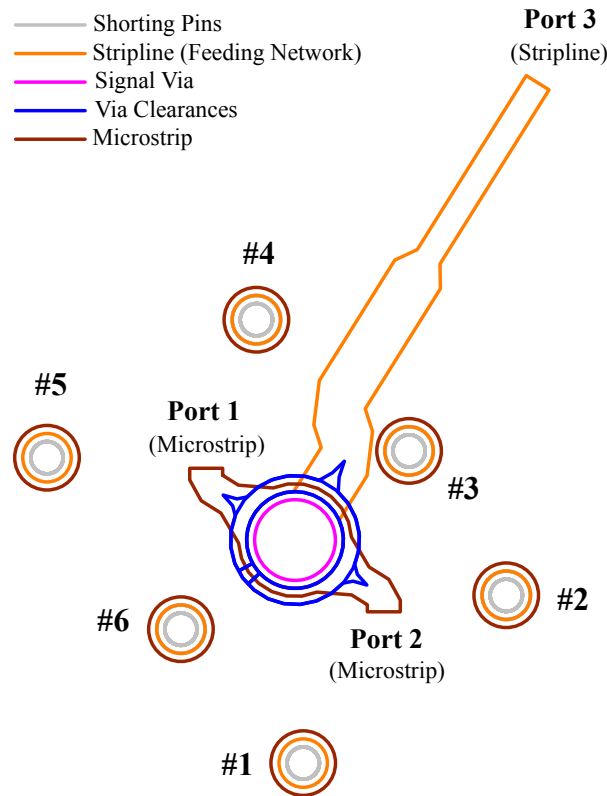


Figure 4.23. Layout outline of the Power Combiner.

A possible trade-off to relax this design conflict is to select the shorting pins whose suppression would have the smallest effect on the performance of the Power Combiner and, instead of just eliminating the pins, implement them as *blind* vias between the *Upper* and *Lower* ground planes of the RE. The price to pay with this approach is that, due to technological constraints, the diameter of these shorting pins would be increased noticeably. This diameter increase would further restrict the placement of such pins and, consequently, the optimization of the Radiation Efficiency of the element (recall *Section 2.4.1*). Moreover, the impact of the modifications of these vias on the remaining performance parameters of the RE (Impedance Matching, Axial Ratio, etc) may require a partial re-design of the element.

The study of several configurations of *blind* & *through* vias reveals that a suitable compromise between routing freedom in the Feeding Network layer, Power Combiner performance and re-design constraints for the RE is given by the “suppression” of a couple of through vias [10]. These vias are the ones labeled as #1 and #4 in *Fig. 4.23*⁵ and the resulting ERC is depicted in *Fig. 4.25*. After some fine tuning, the performance of this *Blind ERC* is made comparable to that of the original cell (*Through ERC* in the same figure) [1]. The additional routing freedom provided by this minor structural refinement becomes decisive when it comes to select the cell that is finally going to be integrated into the foreseen array antenna.

⁵The implementation of these pins as *blind* vias also relaxes considerably the design constraints in the microstrip layer, recall *Fig. 3.44*.

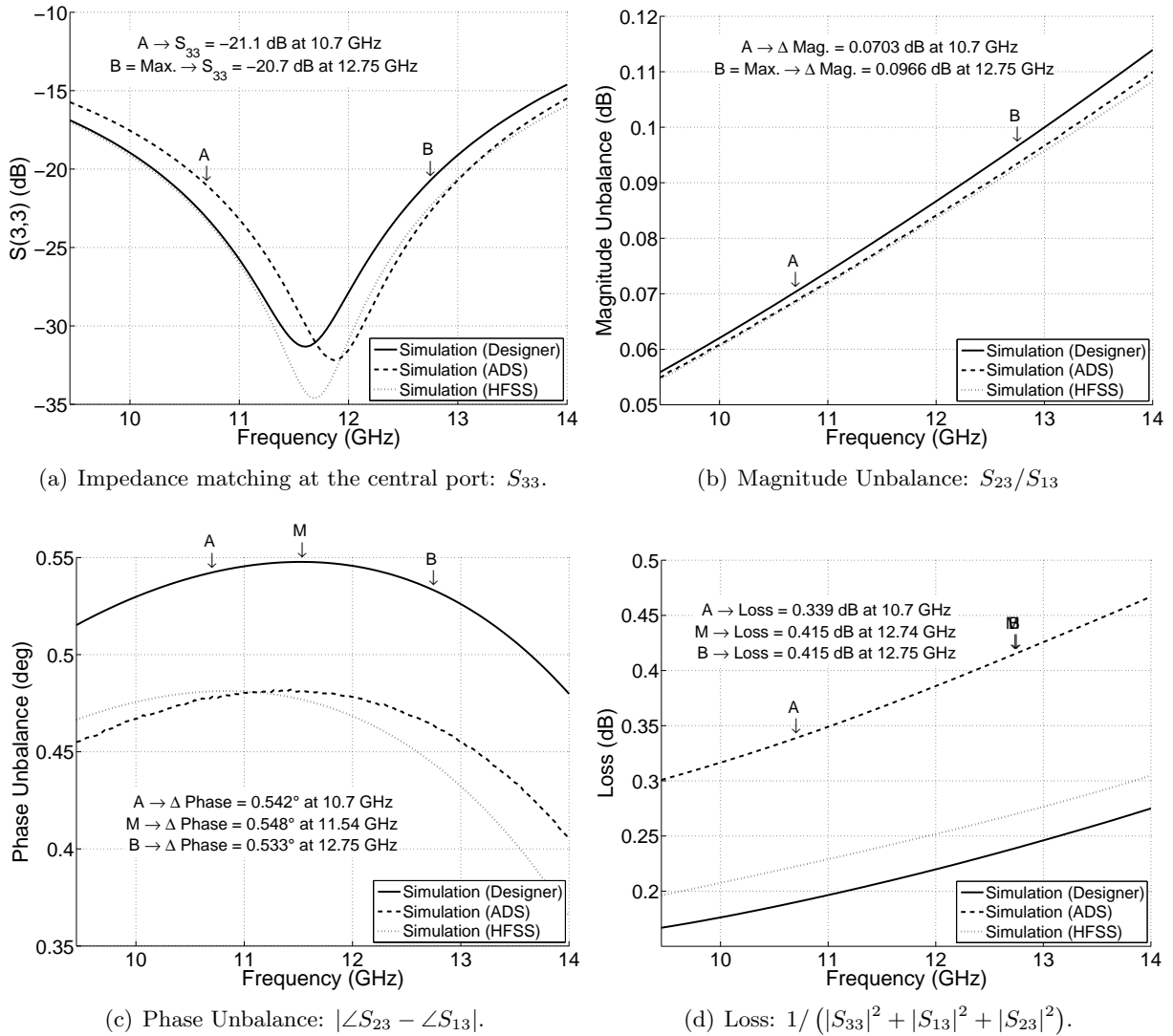
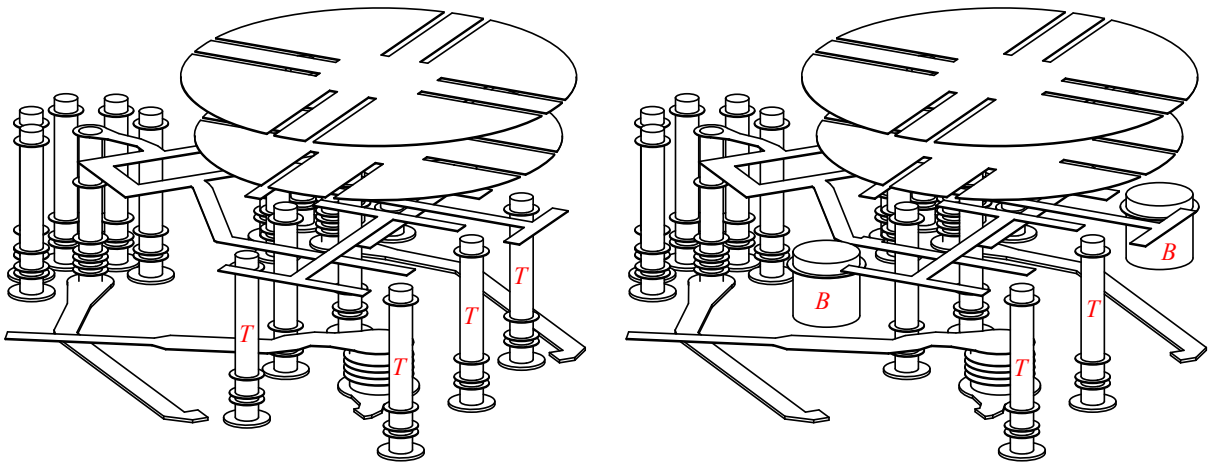


Figure 4.24. Performance of the Power Combiner illustrated in *Fig. 4.23*. From [9].

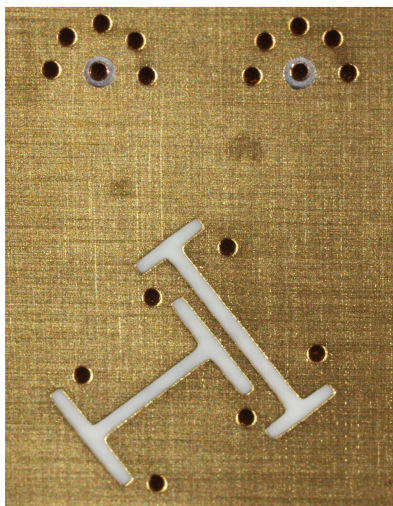
The Power Combiner used in the *Blind ERC*, the so-called *Blind Power Combiner*, can serve to highlight one of the most important performance limitations of the solution proposed here. This limitation is related to the dependence of the combiner Magnitude (and Phase) Unbalance with the angle (Φ) between its central (stripline, output) and lateral (microstrip, input) arms.

The direction of the *microstrip arms* is determined, in principle, by the location of the MMICs outputs (recall *Fig. 3.44*), but a certain margin of variation -see Φ_M in *Fig. 4.26(a)*- is still affordable (up to $\sim 50^\circ$).

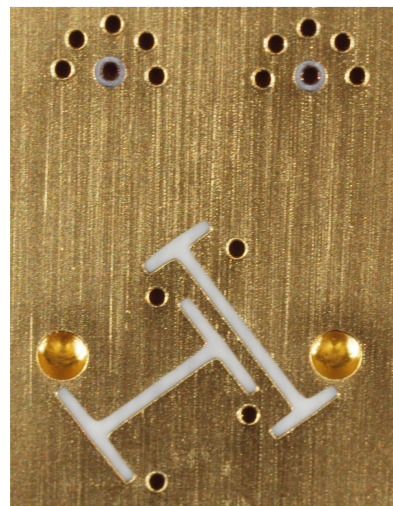
On the other hand, the direction of the *stripline arm* depends strongly on the routing of the Feeding Network, and its variation -see Φ_S in *Fig. 4.26(a)*- is assumed to be arbitrary, within the bounds imposed by the presence of the remaining through vias.



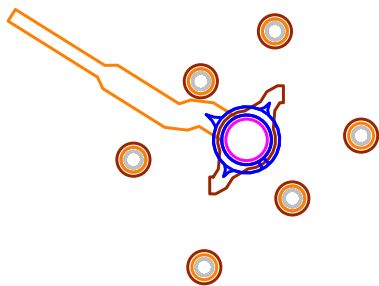
(a) 3-D view of the *Through ERC* (original config.). (b) 3-D view of the *Blind ERC* (improved configuration).



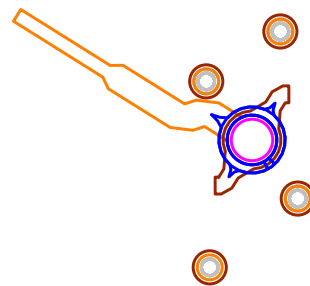
(c) Upper Ground Plane of the *Through ERC*.



(d) Upper Ground Plane of the *Blind ERC*.

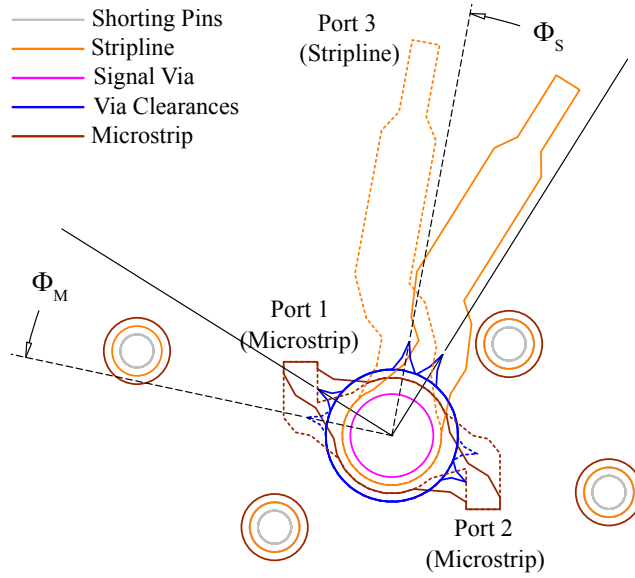


(e) *Through Power Combiner*.

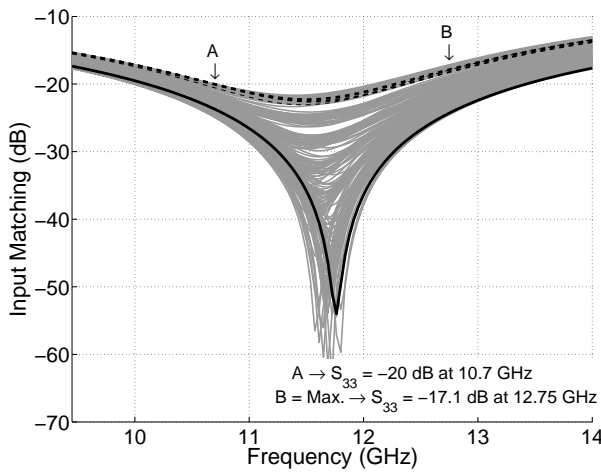


(f) *Blind Power Combiner*.

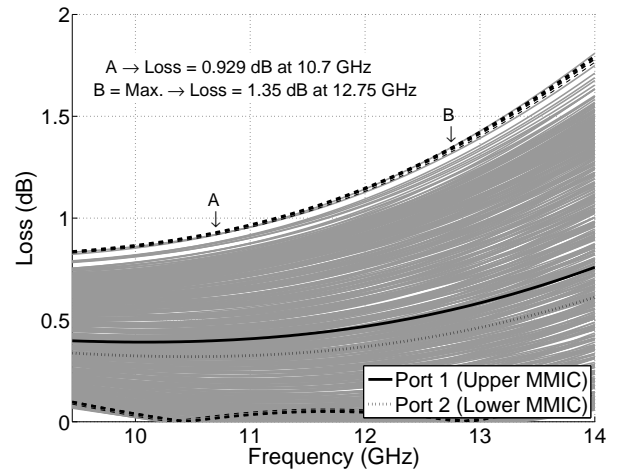
Figure 4.25. Different views of the two of ERC candidates. Note that, in the drawings on the top, *through* vias are labeled with “*T*”, while *blind* vias are with “*B*”. Photographs courtesy of Mr. J.-F. Zürcher.



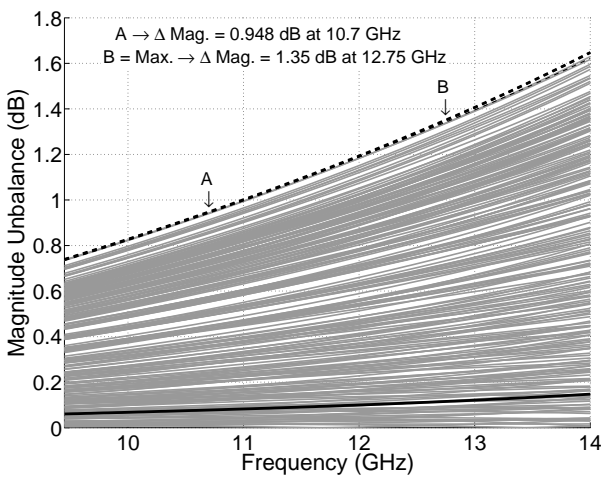
(a) Rotation angles of the arms of the Blind Power Combiner: (Φ_S, Φ_M) .



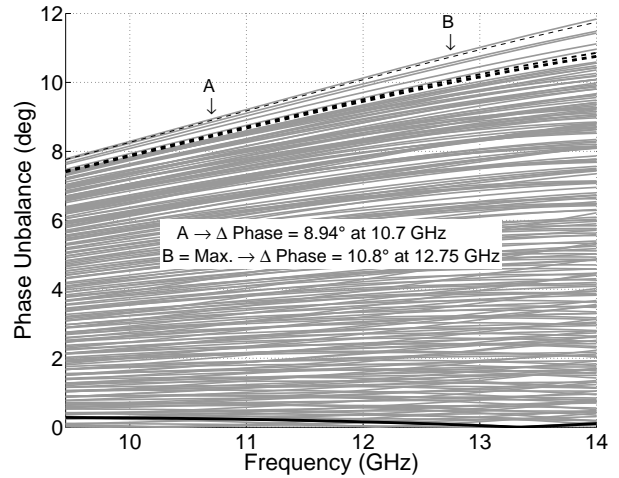
(b) Impedance matching at the central port: S_{33} .



(c) Loss: $|-3dB - S_{i3}|$.



(d) Magnitude Unbalance: S_{i3}/S_{j3} .



(e) Phase Unbalance: $|\angle S_{13} - \angle S_{23}|$.

Figure 4.26. Blind Power Combiner performance for different rotations of its arms. Black continuous line for the *Nominal Case* and dashed line for the cases with worst *Magnitude Unbalance*.

The impact of the angle Φ on the performance of the *Blind Power Combiner* is illustrated in *Fig. 4.26* and *Fig. 4.27*. The last figure tries to highlight that, apart from the Impedance Matching, the degree of freedom available in the microstrip layer (Φ_M) is not enough to compensate for the strong variations in Magnitude and Phase Unbalance (1.35 dB and 11° , respectively) that are associated to the connection of the ERC to the feeding network (Φ_S).

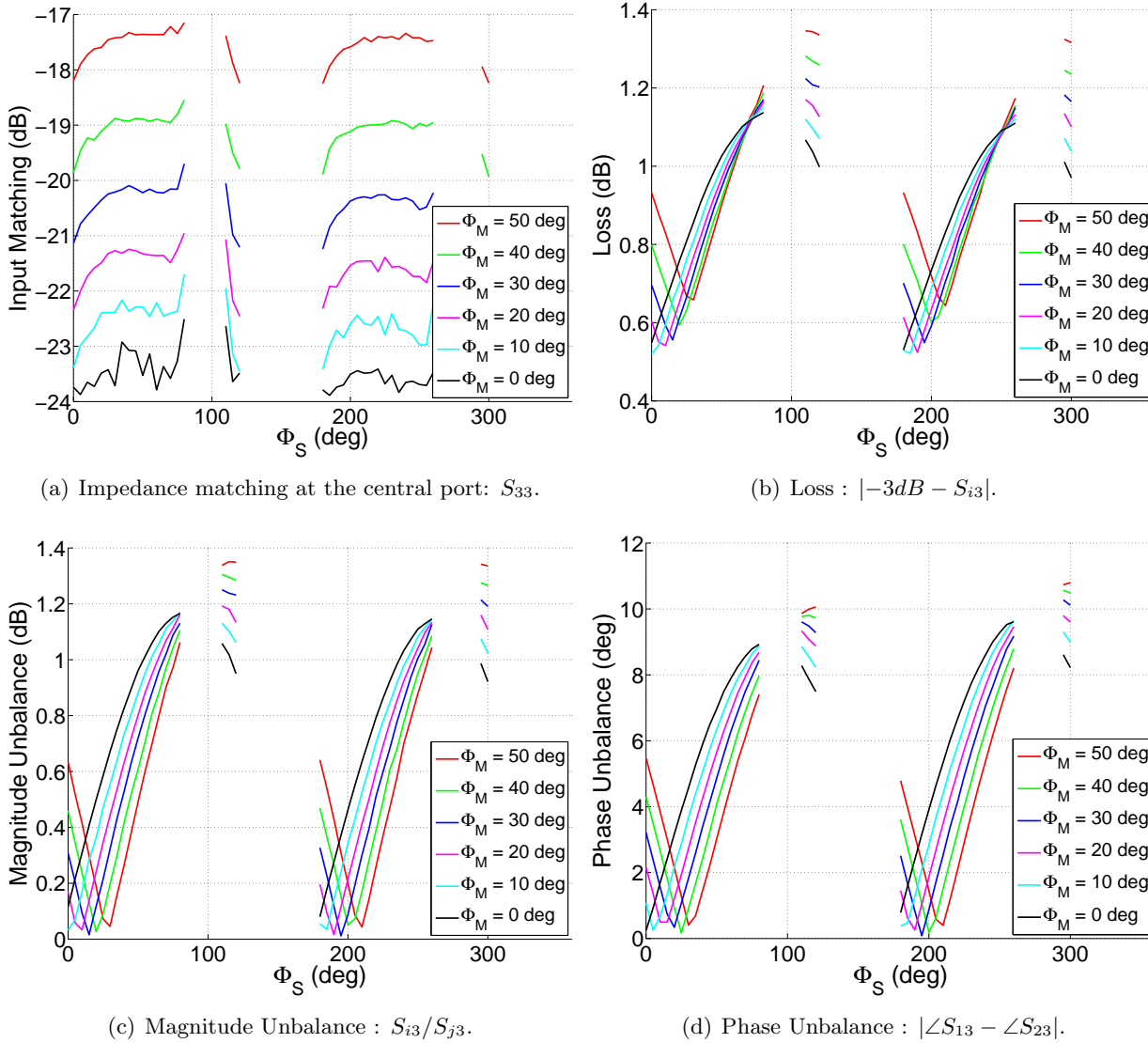


Figure 4.27. Blind Power Combiner performance for different rotations of its arms. The performance curves are made up from the worst levels observed for each performance parameter within the frequency band of interest.

4.5.2 Perturbed Performance

Similarly as it was done for the Long Via and using the same values listed in *Section 4.3.1*, the effect of the fabrication tolerances on the performance of the Power Combiner is analyzed next. The structure of the combiner is illustrated in *Fig. 4.28*.

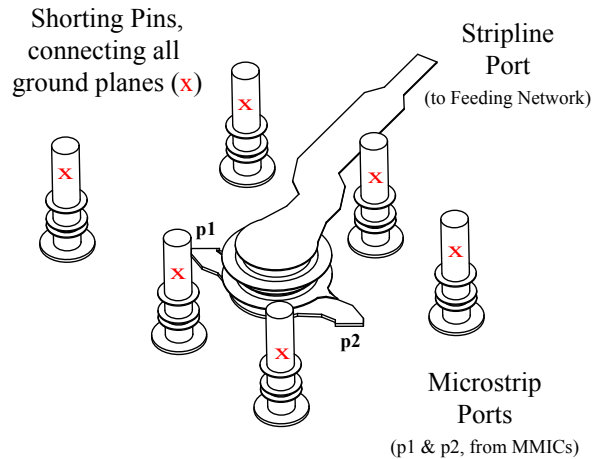


Figure 4.28. Power combiner Structure. Note the rings corresponding to the clearances in the ground planes the signal via is passing through and the pads signaling the interfaces between different dielectric ayers. Here, the alignment tolerances only concern the relative placement of the signal via with regard to the clearances, the pads and the transmission lines.

This study is based on the EM modeling of the Power Combiner with with a 3D ‘Full Wave’ software tool (*Ansoft HFSSTM*), and the results can be summarized as follows:

- the **alignment tolerances** affect, mainly, to the phase unbalance, that can suffer an increase of $\sim 1^\circ$.
- The impact of the **dielectric permittivity tolerances** is negligible.
- And the **dielectric thickness tolerances** have the greatest impact on the impedance matching of the combiner, with a deterioration of up to ~ 5 dB.
- Finally, all these fabrication tolerances are sorted according to their impact on the *Magnitude Unbalance* and those with a higher impact are selected to evaluate their combined effect in the performance of the combiner. The approach followed here is to reduce the computational effort by focusing on a critical performance parameter, similarly as it was done for the DLPRE with regard to the worst levels of Impedance Matching or port coupling. Again, this does not guarantee to attain the worst case scenario, but still provides a representative evaluation of the overall sensitivity of the Power Combiner to the fabrication tolerances.

The combined effect of these tolerances on the performance of the Power Combiner is displayed in *Fig. 4.29*. This figure evidences that the sensitivity of the Power Combiner to the manufacturing tolerances considered here is relatively small. The performance parameters that are more perturbed are again the impedance matching (with a degradation of ~ 4 dB) and the phase unbalance (with an increase of $\sim 1.3^\circ$).

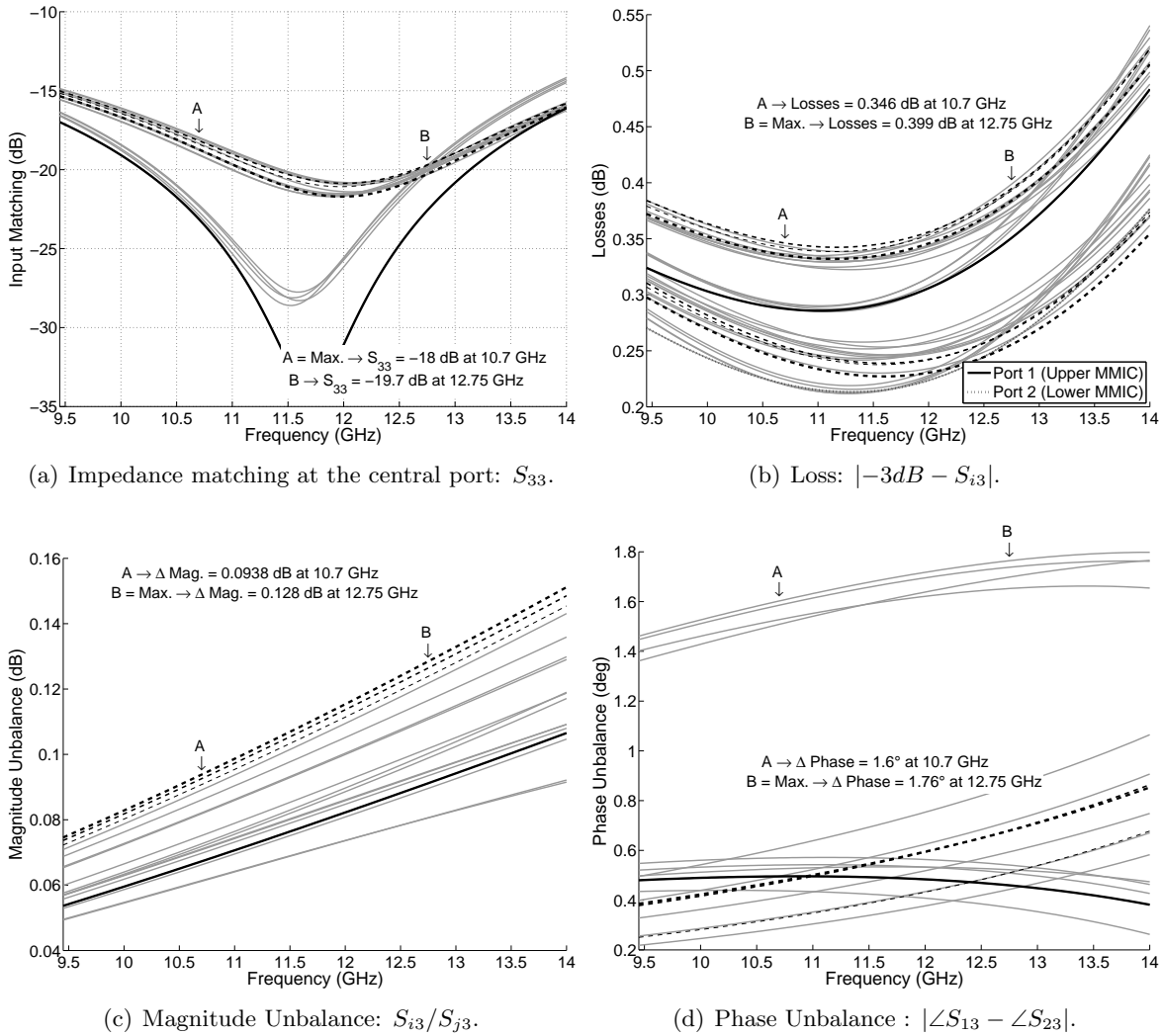


Figure 4.29. Impact of the fabrication tolerances on the performance of the Power Combiner. The *nominal* curves (in continuous black line), those obtained for different values of the parameters subject to tolerances (in continuous gray line) and the three cases with *worst Magnitude Unbalance* levels (in dashed black line) are displayed superimposed. Here, the alignment between layers and the thicknesses & permittivities of the substrates are considered subject to tolerance. From [10].

The reduced impact of the fabrication tolerances on the performance of the Power Combiner is attributable to its small electrical size (especially in the vertical dimension) and its structural simplicity.

4.5.3 Measured Performance

A picture of the prototype used for the evaluation of the Power Combiner performance is shown in *Fig. 4.30(a)*. In the picture, the stripline port of the combiner is not visible. Instead, between this port (*Port 3*, in the figure) and the corresponding edge mount connector, it is possible to appreciate the microstrip pads of the microstrip-to-stripline transition that is intended to access the stripline layer of the combiner.

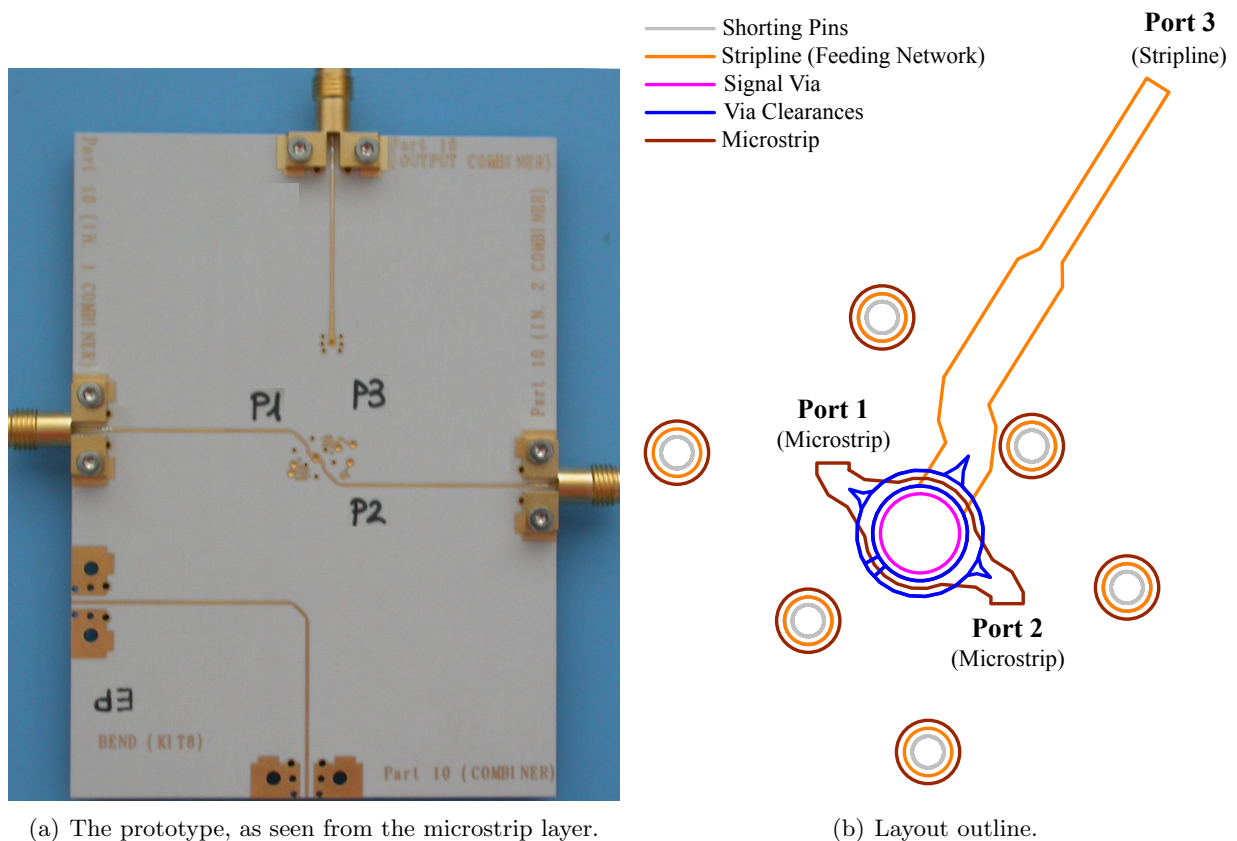


Figure 4.30. Power Combiner prototyping. Note that, in the layout, the port assignment is given, but not the location of the reference planes. These reference planes might be shifted a certain distance along the microstrip or striplines illustrated here, or even, placed in different layers.

A rigorous evaluation of the performance of this 3-port device with the 2-port VNA that is available for the measurements would require an special calibration procedure [11–14]. However, due to time constraints, this rigorous procedure is not applied here. This implies a degradation of the accuracy in the measurement of the S-Params., especially for the off-diagonal parameters (S_{ij} with $i \neq j$).

The procedure used here is limited to a couple of 2-port TRL calibrations. These calibrations are done using *Cal. Kit #3* for measurements at the microstrip ports of the combiner (*Ports 1* and *2* in *Fig. 4.30(a)*), while for *Port 3* a new stripline calibration kit is employed. This new calibration kit is *Cal. Kit #4*, that is depicted in *Fig. 4.31*. *Cal. Kit #4* is a stripline TRL calibration kit that is intended, basically, to de-embed from measurements the joint effects of the connector and the dedicated microstrip-to-stripline transition at *Port 3*.

The measurements at the microstrip ports of the combiner are compared to different predictions in *Fig. 4.32*. These predictions agree relatively well, provided the testing inaccuracies, with measurements. In fact, predictions taking into account the dedicated microstrip to stripline transition (labeled as “T” in the figure) show an incipient ripple (appreciable in the Cartesian plots, mainly)

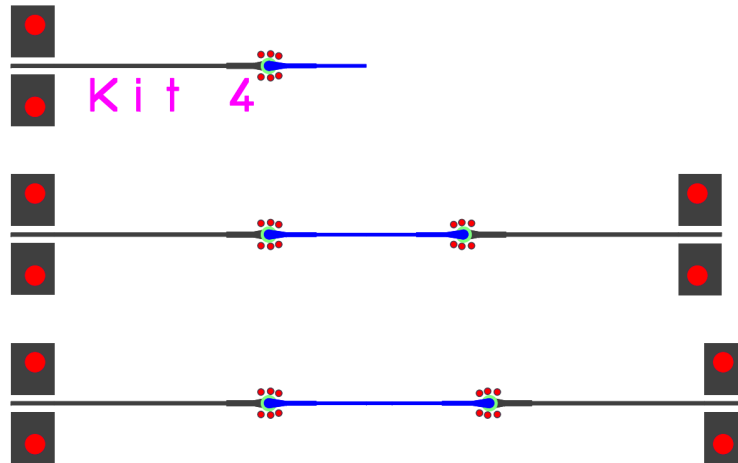


Figure 4.31. Layout of *Cal. Kit #4*: to set the reference plane in the stripline layer of the feeding network. The sections of line in this stripline layer are depicted in blue, while black is reserved for the microstrip layer. Note the pads for the mounting of the edge connectors, and the vias for the microstrip-to-stripline transitions.

that could be attributed to the mismatch-induced errors underlying the simplified measurement procedure used here.

The measurements at the stripline port of the combiner are compared to different predictions in *Fig. 4.33*. Though the agreement between the predictions is limited, the results from *Ansoft DesignerTM* seem more consistent with measurements.

The limited accuracy of the calibration technique used here prevents a more in depth evaluation of the combiner performance (S_{31} , S_{32} , unbalance & loss). However, from the parameters evaluated here it is considered that, in general, there is already a good agreement between predictions and measurement. And from this agreement, it can be expected that the remaining performance parameters of the actual Power Combiner are as satisfying as the predictions above suggest.

4.5.4 Conclusion

The assessment of the performance of the Power Combiner is limited by the simplification that, due to time constraints, is applied to its measurement procedure. This simplification prevents, for example the evaluation of two of the most important performance parameters of this component: the Magnitude and Phase Unbalances. This couple of performance parameters has been found, in fact, to become very critical when it comes to connect the Power Combiner to the Feeding Network.

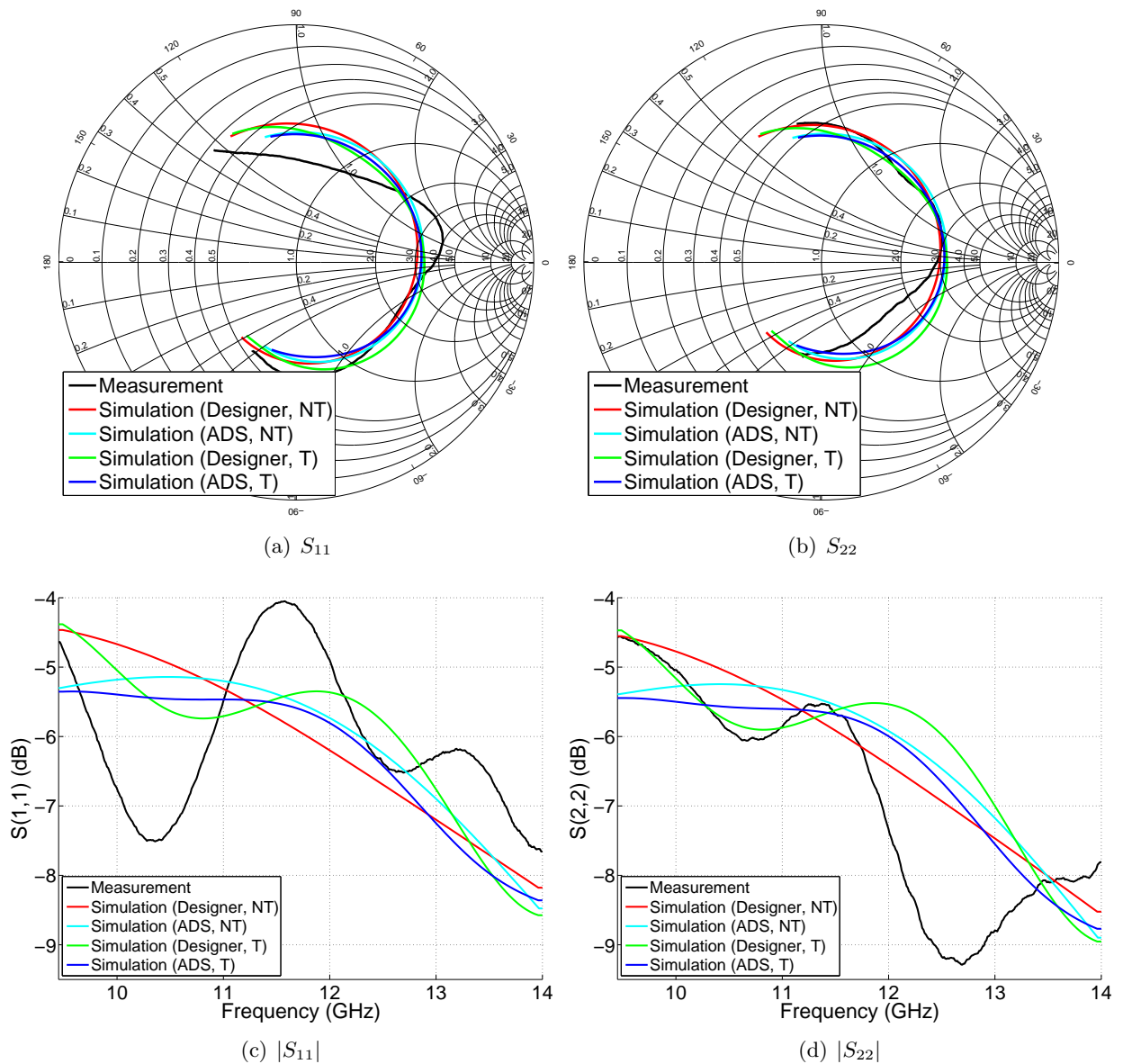


Figure 4.32. Scattering Parameters of the Power Combiner (microstrip ports). The reference planes for measurements are all in the microstrip layer. For this purpose, measurements are done after a 2-port TRL calibration with *Cal. Kit #3*. The reference planes for simulations are in microstrip layer at the for *Ports 1* and *2* (as in measurements), while for *Port 3*, the reference plane is located either in the microstrip layer (i) or in the stripline (ii). Therefore, in the first case, the simulation model includes the dedicated microstrip to stripline transition and the results are labeled as “T”. In the second case such transition is not included and the results are labeled as “NT”. From [1].

There is, however, a reasonable degree of confidence in the fact that the performance of the combiner will match the promising expectations presented here. This confidence is supported by:

- the good agreement observed between different performance predictions,
- the reduced size and the structural simplicity of the Power Combiner, and

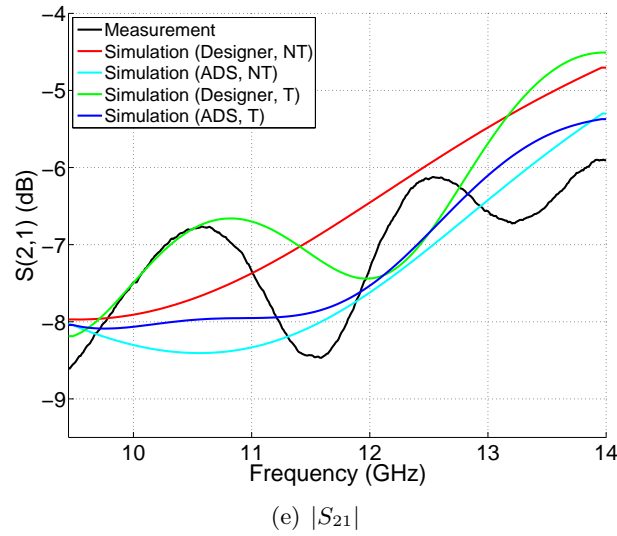


Figure 4.32. Scattering Parameters of the Power Combiner (microstrip ports) (contd.).

- the satisfying correspondence observed between predictions and the measurement results that, provided the simplified calibration procedure, are considered most reliable here.

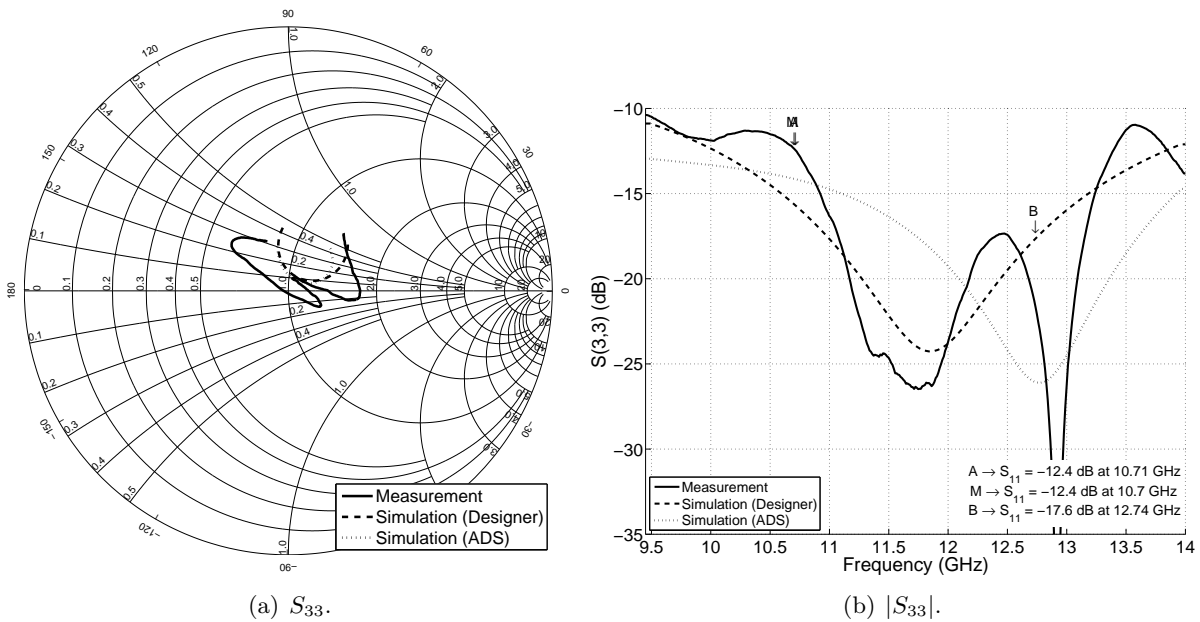


Figure 4.33. Scattering Parameters of the Power Combiner (stripline port). The reference planes for measurements are in the stripline layer of the feeding network. For this purpose, measurements are done after a 2-port TRL calibration with *Cal. Kit #4*. The reference planes for simulations are in microstrip layer at the for *Ports 1* and *2*, while for *Port 3*, the reference plane is located in the stripline layer (like in measurements). Therefore, the simulation model does not include the dedicated microstrip to stripline transition. From [1].

4.6 Circularly Polarized Radiating Element. The Cell

The ERC consists of the Dual Circularly Polarized Radiating Element (DCPRE), the couple of Long Vias, the microstrip lines leading to the MMICs and the Power Combiner. To simplify the measurements, the Power Combiner is tested separately. For the same reason, the measurements of the DCPRE presented here are done with the long vias incorporated. Throughout the present section and just for the sake of convenience, the association of these two blocks of the ERC is referred to as *The Cell*.

The layout of the DCPRE, together with its local coordinate system, is depicted in *Fig. 4.34*. The performance of this element depends strongly on the branch line hybrid, whose structure is illustrated separately in *Fig. 4.35*.

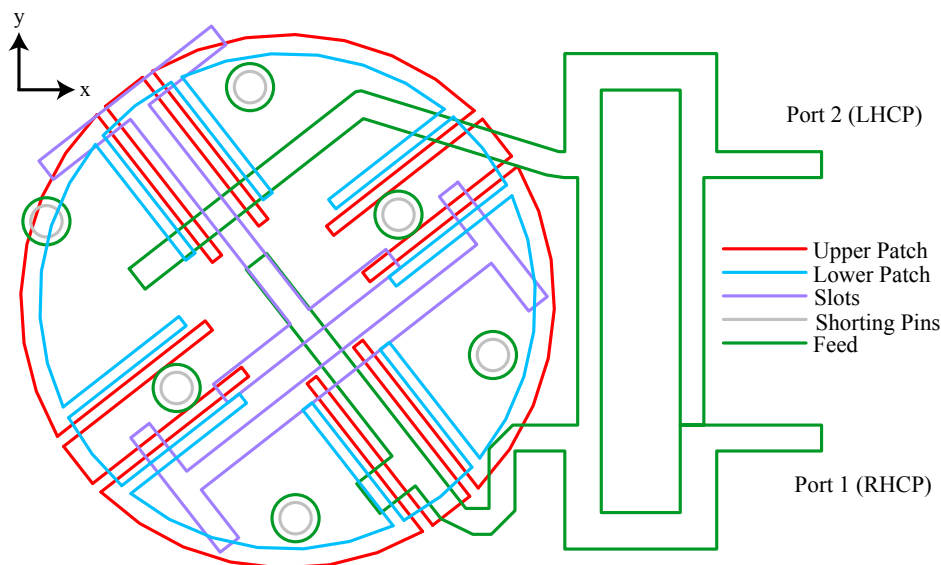


Figure 4.34. Layout outline of the DCPRE. $R(L)HCP$ stands for Right (Left) Hand Circular Polarization. Note that the Local Coordinate System is no longer aligned with the feeding of the linearly polarized element.

This section is devoted to the assessment of the performance and the theoretical modeling of the Cell. The framework for this assessment is given by an evaluation of the impact that the tolerances in the fabrication of the DCPRE may have on its electrical operation. This basic sensitivity study is followed by a comparison between predictions and measurements of the Cell performance.

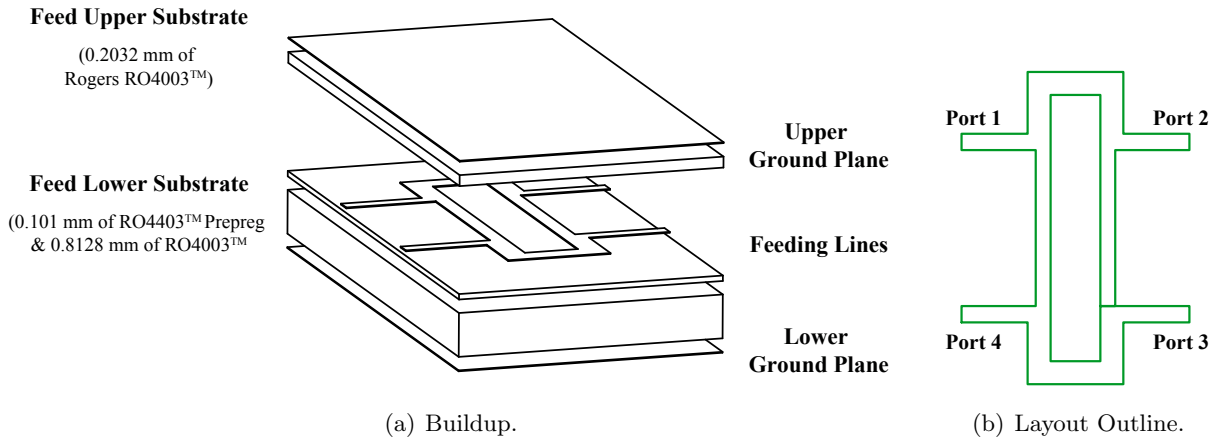


Figure 4.35. Structure of the branch line hybrid.

4.6.1 Fabrication Tolerances

Similarly as it was done for the DLPRE and using the same values listed in *Section 4.3.1*, the effects of the fabrication tolerances on the performance of the circularly polarized element and the branch line hybrid are studied in this section. This study is based on the EM modeling of the element with a 2.5D ‘Full Wave’ software tool (*Ansoft Designer™*).

With regard to the element, the present study focuses only on its Rad. Params. The procedure used here to evaluate the impact of the fabrication tolerances on these parameters is analogous to that described for the linearly polarized element. In this sense, the single particularity is that, in order to optimize the computational effort, some of the information extracted from the sensitivity study of the DLPRE is reused for the present study. In particular, the most critical sets of values for the constitutive parameters of the *circularly* polarized element are determined attending directly to the worst levels of *Impedance Matching* of the *linearly* polarized element.

Just for the sake of illustration, several predictions for the *nominal* S-Params. of the RE are compared in *Fig. 4.36*. This figure evidences that the performance of the element in terms of S-Params. is reasonably good.⁶ Moreover, there is a high level of correlation between all the predictions, which supports a strong confidence on the reliability of the DCPRE modeling.

⁶In principle, the only concern is coming from the relatively high value of S_{21} in the upper part of the frequency band (recall footnote 2 in page 156). Here, it is worth to note that the S_{21} at the ports of the DCPRE represents, basically, the impedance matching of the DLPRE seen through the hybrid coupler. The frequency responses of these two parameters are, in fact, quite similar.

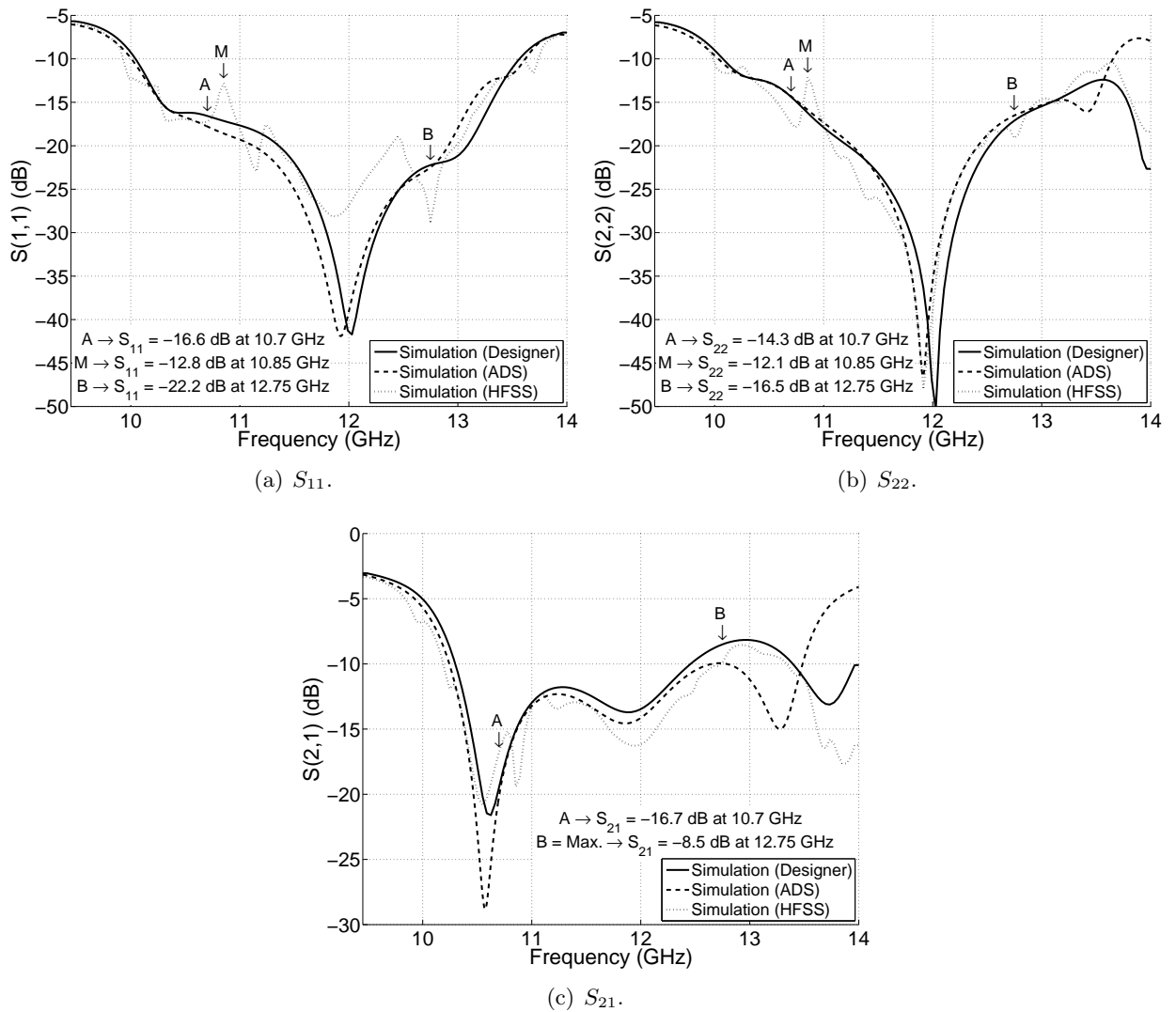


Figure 4.36. Scattering parameters of the DCPRE. The ports of the element are located in the stripline layer, as shown in *Fig. 4.34*. Simulation results assume infinite ground planes, with the exception of those from *Ansoft HFSSTM*, which exhibit a characteristic ripple superimposed. From [9].

a) Scattering Parameters of the Branch-Line Hybrid

As discussed in the previous chapter, the integration of the DCPRE within the area available for the ERC leads to the squeezing of the branch line hybrid in one of its dimensions. Within this size constraint, the performance of the hybrid is optimized to provide a proper balance between the different parameters that are defined and displayed in *Fig. 4.37*. All the performance goals specified for these parameters could not be fully attained, which reveals that, under the actual design constraints, some of these goals may be conflicting.⁷ Despite this conflict, *Fig. 4.37* evidences that the nominal performance of the hybrid is very satisfying.

When it comes to evaluate the impact of the fabrication tolerances on the nominal performance of the hybrid, the procedure used here is the same that was outlined for the linearly polarized element. The structural simplicity of the hybrid permits, however, a more exhaustive (worst case) evaluation of such impact. The results of this evaluation are summarized next:

- the **etching tolerances** affect, mainly, to the Coupled Attenuation, that can suffer an increase of ~ 0.1 dB.
- The **dielectric permittivity tolerances** have repercussions basically on the Central Frequency of the hybrid, with a more significant impact on its Impedance Matching and Isolation. Within the frequency band of interest, these parameters can suffer a deterioration of up to 1 dB.
- And the **dielectric thickness tolerances** have the greatest impact on the performance of the hybrid, with a considerable shift of its central frequency. In particular the coupled attenuation and the Magnitude Unbalance can suffer an increase of ~ 0.1 dB and ~ 0.2 dB, respectively. The impedance matching may be worsened by 1.4 dB and the Phase Unbalance, by 1.6° .
- Finally, the combined impact of all these fabrication tolerances on the hybrid performance is illustrated in *Fig. 4.38*. Under these circumstances, the maximum degradation of the different performance parameters of the branch line can be significant. This worst case degradation is quantified as:
 - i) ~ 2.7 dB for the impedance matching and the isolation,
 - ii) $\sim 3.1^\circ$ for the phase unbalance,
 - iii) ~ 0.3 dB for the magnitude unbalance and
 - iv) ~ 0.1 dB for the coupled attenuation.

⁷The performance goals are ≤ -15 dB for the Impedance Matching and the Isolation, $\leq 0.3^\circ$ for the Phase Unbalance, ≤ 0.2 dB for the Magnitude Unbalance and ≤ 0.2 dB for the Attenuation through the coupled arm of the hybrid.

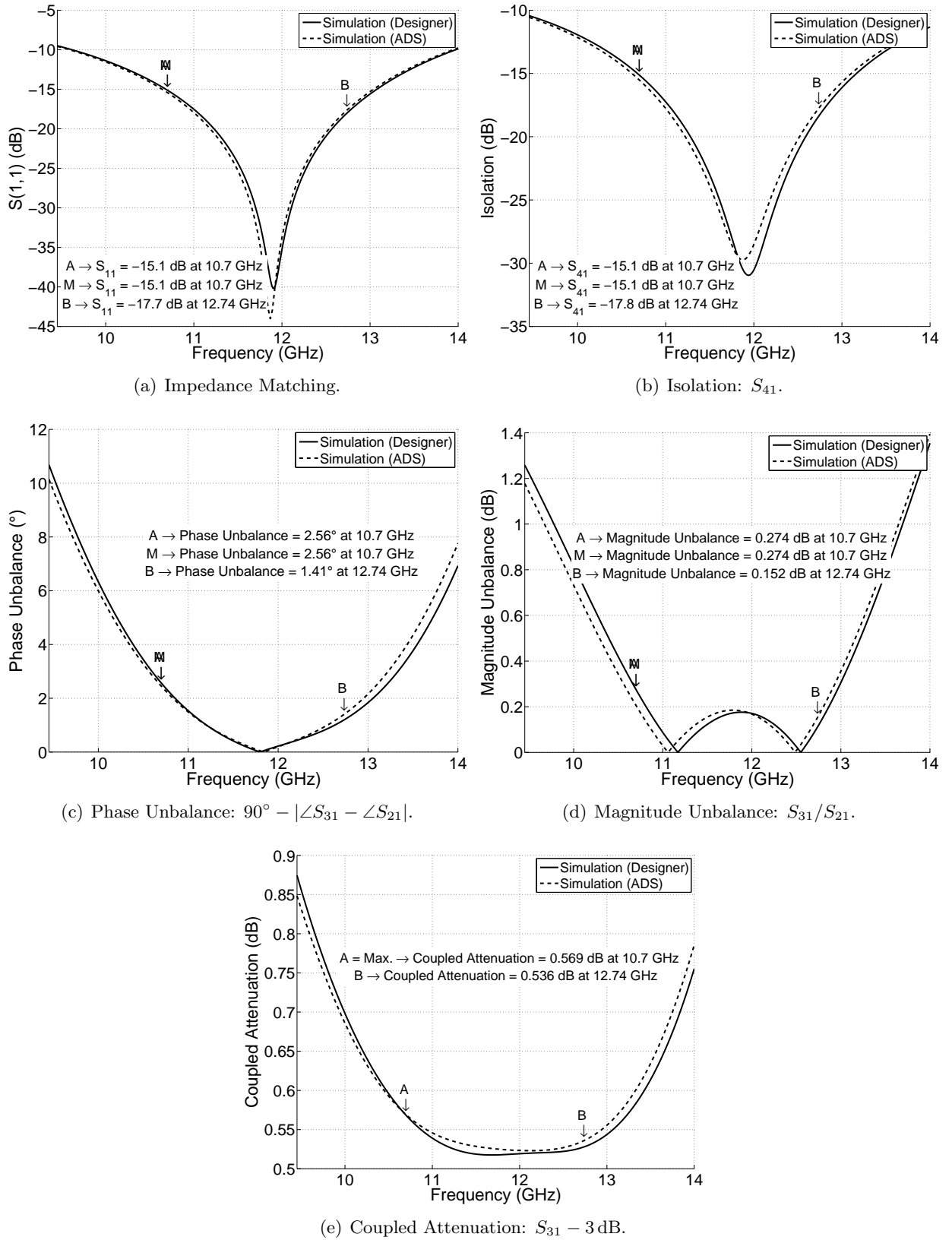


Figure 4.37. Branch line hybrid nominal performance. Simulation results. From [9].

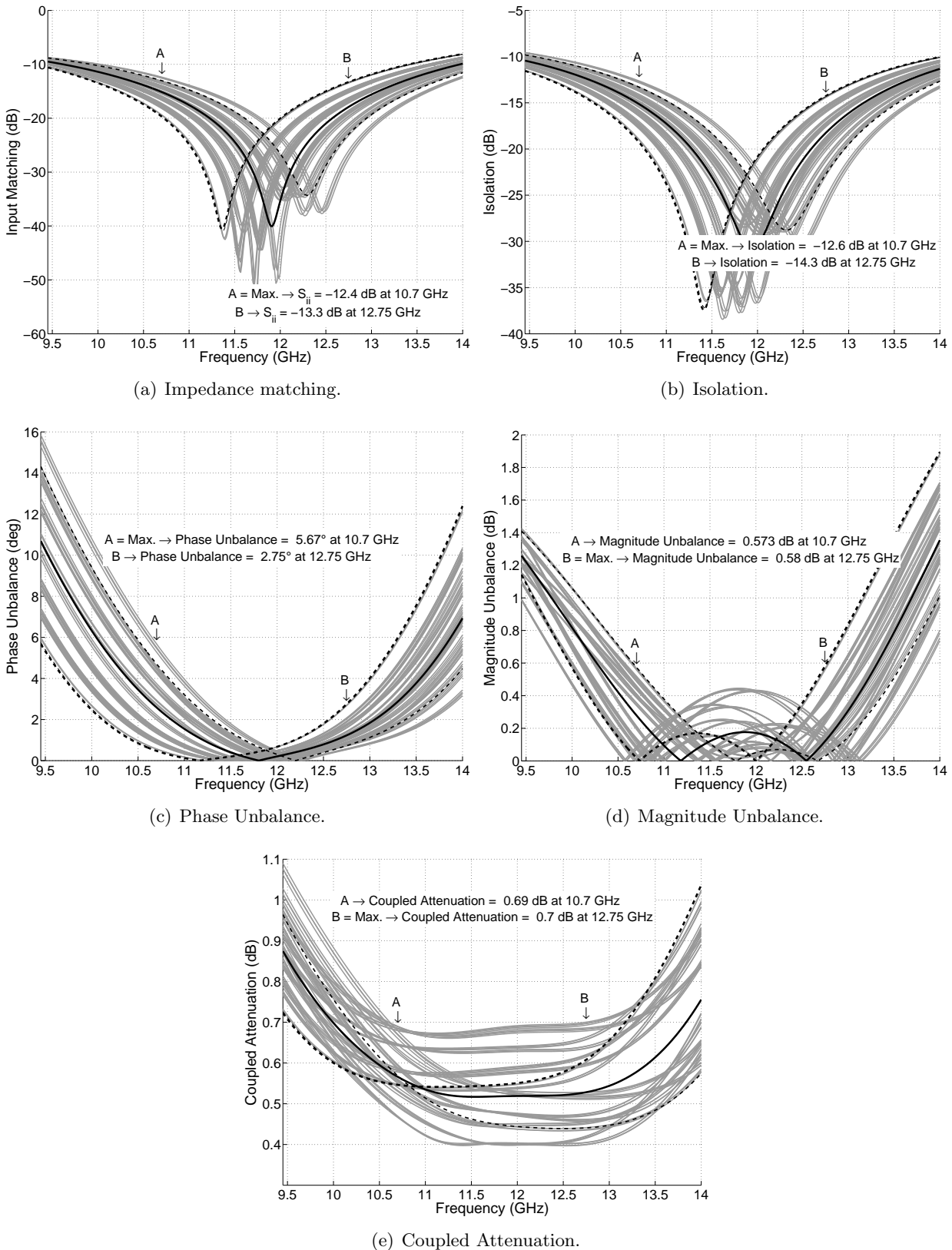


Figure 4.38. Impact of the fabrication tolerances on the performance of the branch line hybrid. The *nominal* curves (in continuous black line), those obtained for different values of the parameters subject to tolerances (in continuous gray line) and the three cases with *worst Magnitude Unbalance* levels (in dashed black line) are displayed superimposed. Here, the etching and the thicknesses & permittivities of the substrates are considered subject to tolerance. From [4].

b) Radiation Parameters of the Circularly Polarized Element

The relative impacts of the fabrication tolerances on the Rad. Params. of the DCPRE are evaluated only within the scan domain and the frequency band of interest. These impacts can be summarized as follows:

- the worst value of *Axial Ratio* (AR) for the *nominal* design is deteriorated by:
 - i) ~ 0.1 dB due to etching tolerances only (*the smallest impact*),
 - ii) ~ 0.7 dB due to dielectric thickness tolerances only,
 - iii) ~ 0.8 dB due to dielectric permittivity tolerances only and
 - iv) ~ 0.9 dB due to alignment tolerances only (*the greatest impact*).

And, as shown in *Fig. 4.39*, the combined impact of all these fabrication tolerances on the AR can be, in the worst case, considerable (~ 2.4 dB). Just for the sake of illustration, several azimuthal cuts of two of the worst AR patterns analyzed here are displayed in *Fig. 4.40* and *Fig. 4.41*.

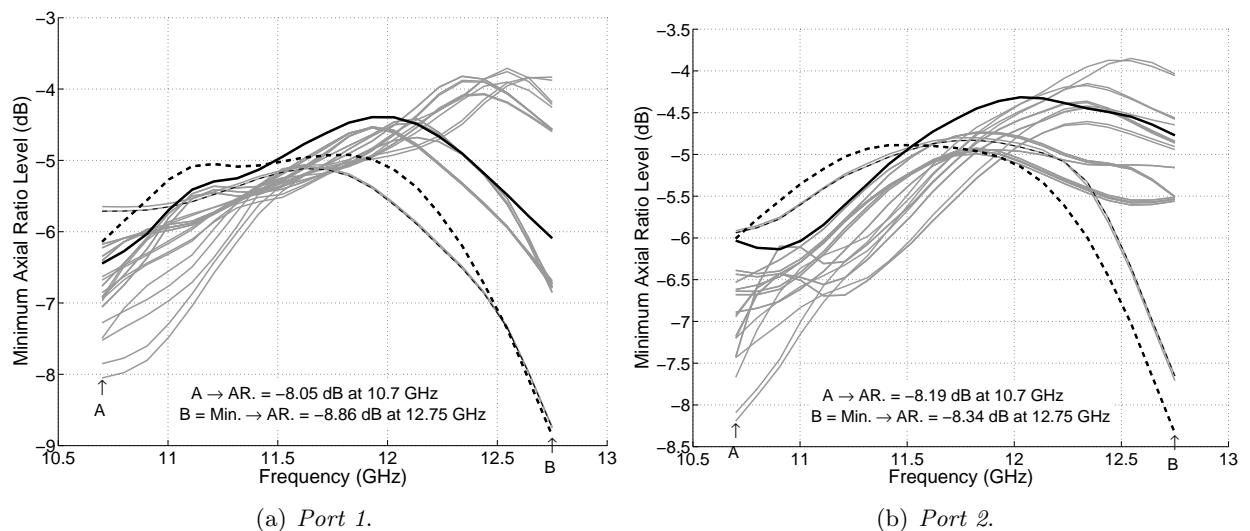


Figure 4.39. Impact of the fabrication tolerances on the Axial Ratio of the DCPRE. Minimum Axial Ratio levels in the scan domain. The *nominal* curves (in continuous black line), those obtained for different values of the parameters subject to tolerances (in continuous gray line) and the three cases with *worst Axial Ratio* levels (in dashed black line) are displayed superimposed. Here, the alignment between layers, the etching and the thicknesses & permittivities of the substrates are considered subject to tolerance. From [4].

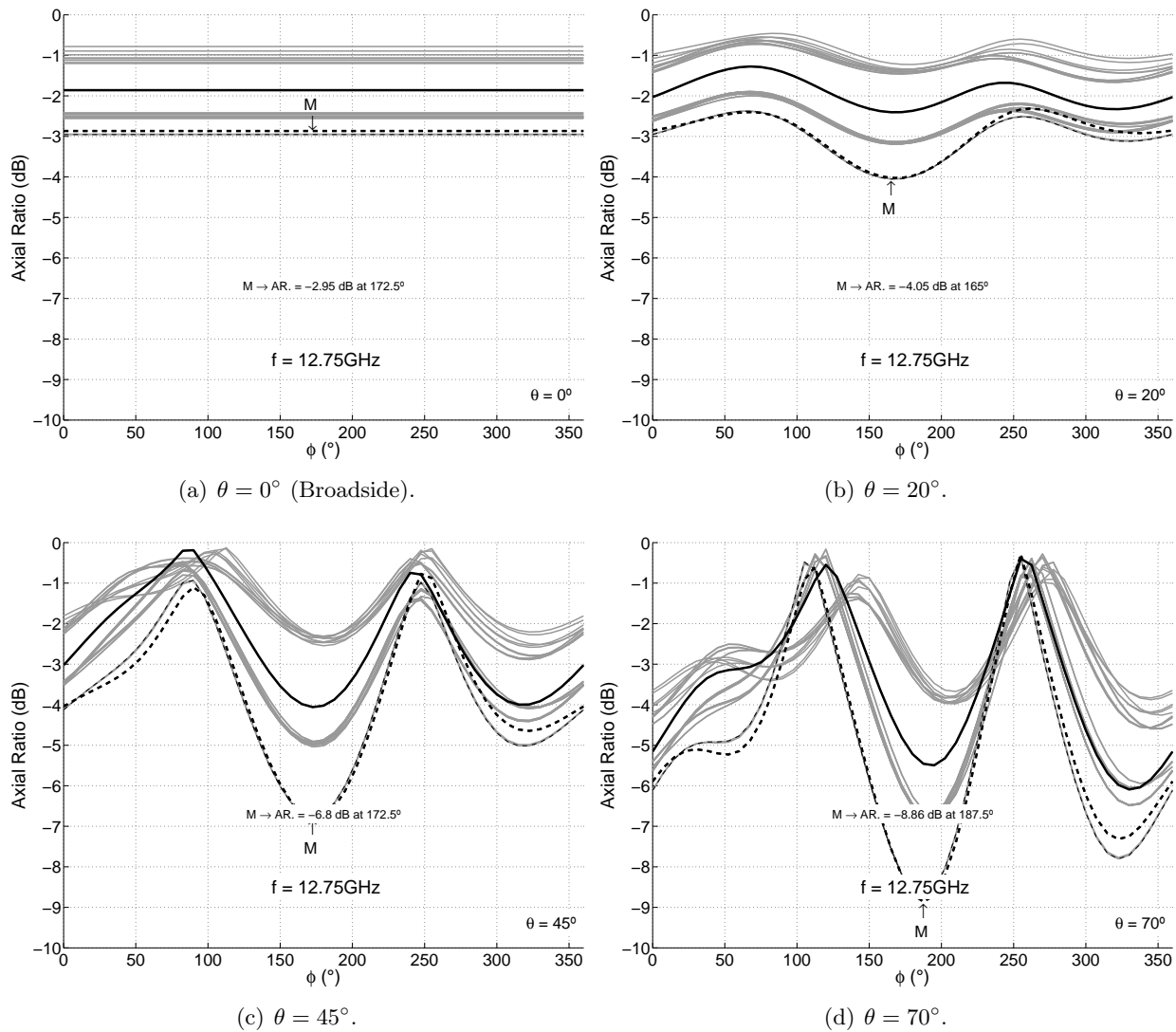


Figure 4.40. Impact of the fabrication tolerances on the Axial Ratio of the DCPRE. Superimposed azimuthal cuts of the Axial Ratio for different elevation angles at $f = 12.75\text{GHz}$ (*Port 1* excited). The *nominal* curves (in continuous black line), those obtained for different values of the parameters subject to tolerances (in continuous gray line) and the three cases with *worst Axial Ratio* levels (in dashed black line) are displayed superimposed. Here, the alignment between layers, the etching and the thicknesses & permittivities of the substrates are considered subject to tolerance. From [4].

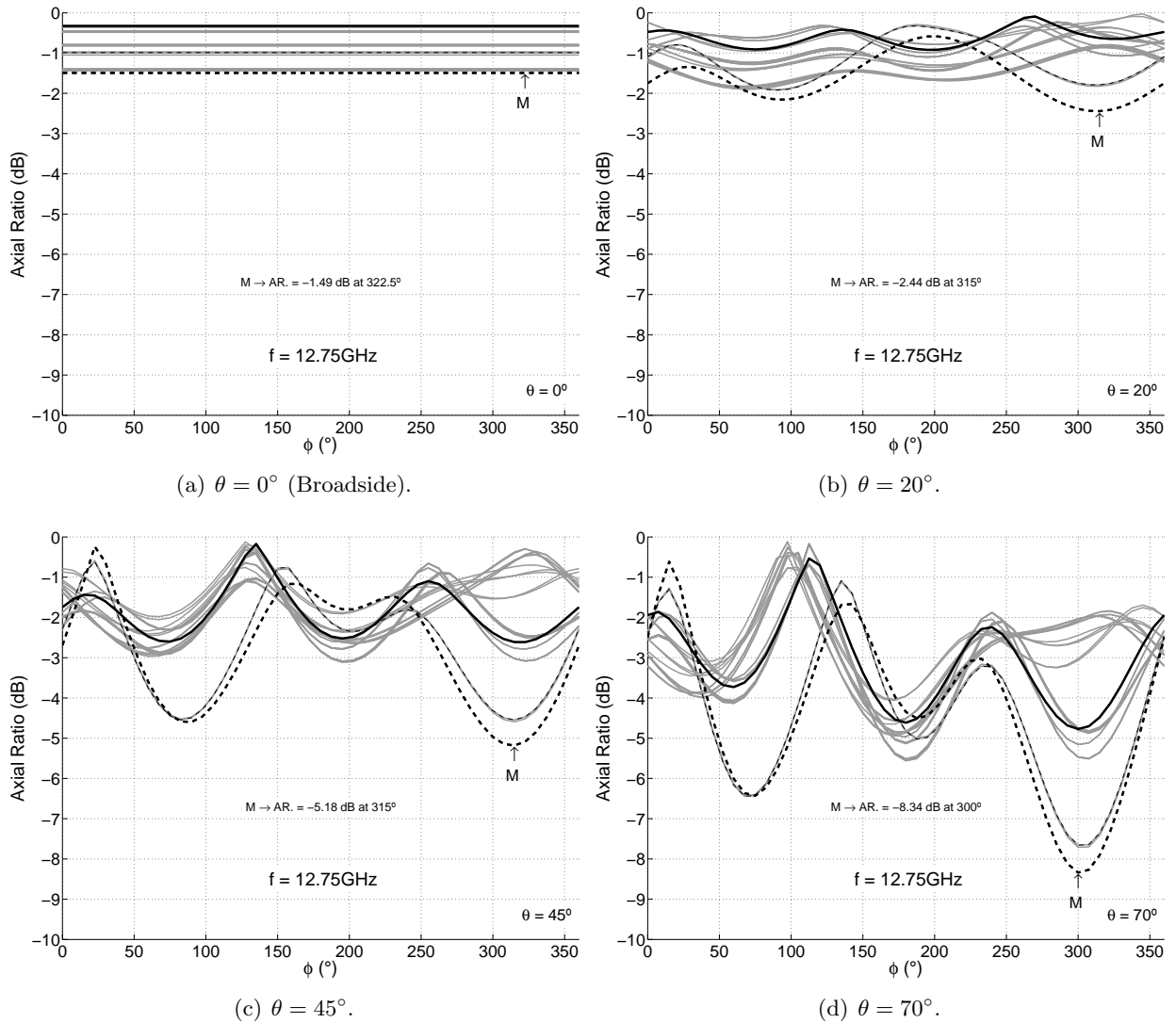


Figure 4.41. Impact of the fabrication tolerances on the Axial Ratio of the DCPRE. Superimposed azimuthal cuts of the Axial Ratio for different elevation angles at $f = 12.75\text{GHz}$ (*Port 2* excited). The *nominal* curves (in continuous black line), those obtained for different values of the parameters subject to tolerances (in continuous gray line) and the three cases with *worst Axial Ratio* levels (in dashed black line) are displayed superimposed. Here, the alignment between layers, the etching and the thicknesses & permittivities of the substrates are considered subject to tolerance. From [4].

- On the other hand, the worst value of *Radiation Efficiency* for the *nominal* design is deteriorated by:

- i) $\sim 0.3\%$ due to alignment tolerances only (*the smallest impact*),
- ii) $\sim 0.5\%$ due to etching tolerances tolerances only,
- iii) $\sim 0.9\%$ due to dielectric thickness tolerances only and
- iv) $\sim 1.1\%$ due to dielectric permittivity only (*the greatest impact*).

And, as shown in *Fig. 4.42*, the combined impact of all these fabrication tolerances on the radiation efficiency of the element ($\sim 2.6\%$) is expected to be quite limited.

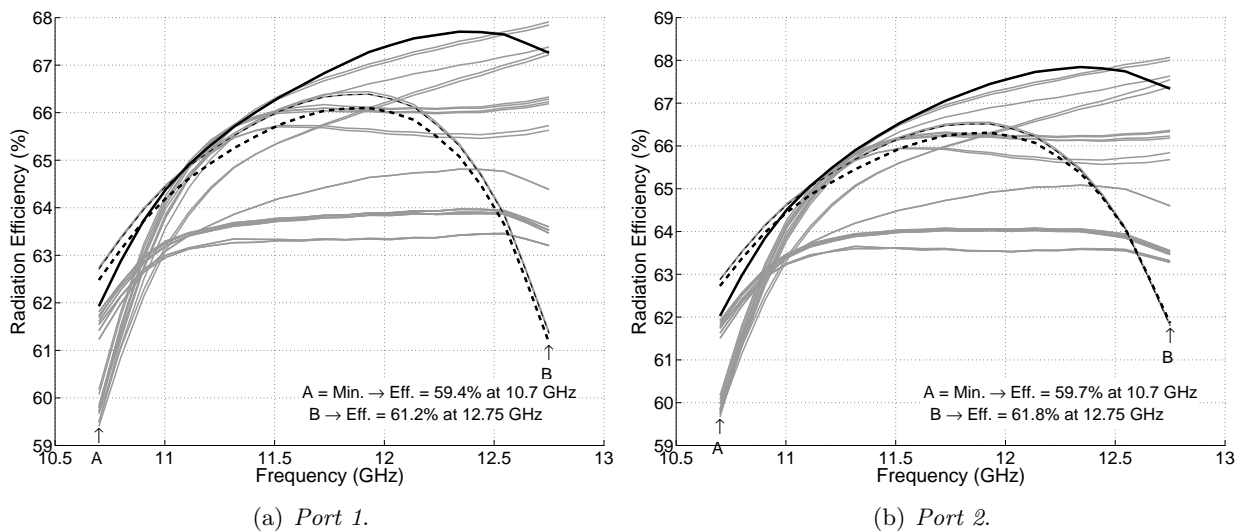


Figure 4.42. Impact of the fabrication tolerances on the Radiation Efficiency of the DCPRE. The *nominal* curves (in continuous black line), those obtained for different values of the parameters subject to tolerances (in continuous gray line) and the three cases with *worst Axial Ratio* levels (in dashed black line) are displayed superimposed. Here, the alignment between layers, the etching and the thicknesses & permittivities of the substrates are considered subject to tolerance. From [4].

4.6.2 Measured Performance

The prototype of the Cell is based on the model depicted in *Fig. 4.43*⁸. As for the linearly polarized element, the figure indicates the location of the reference planes and the local coordinate system used for the evaluation of the Scattering and the Radiation Parameters, respectively.

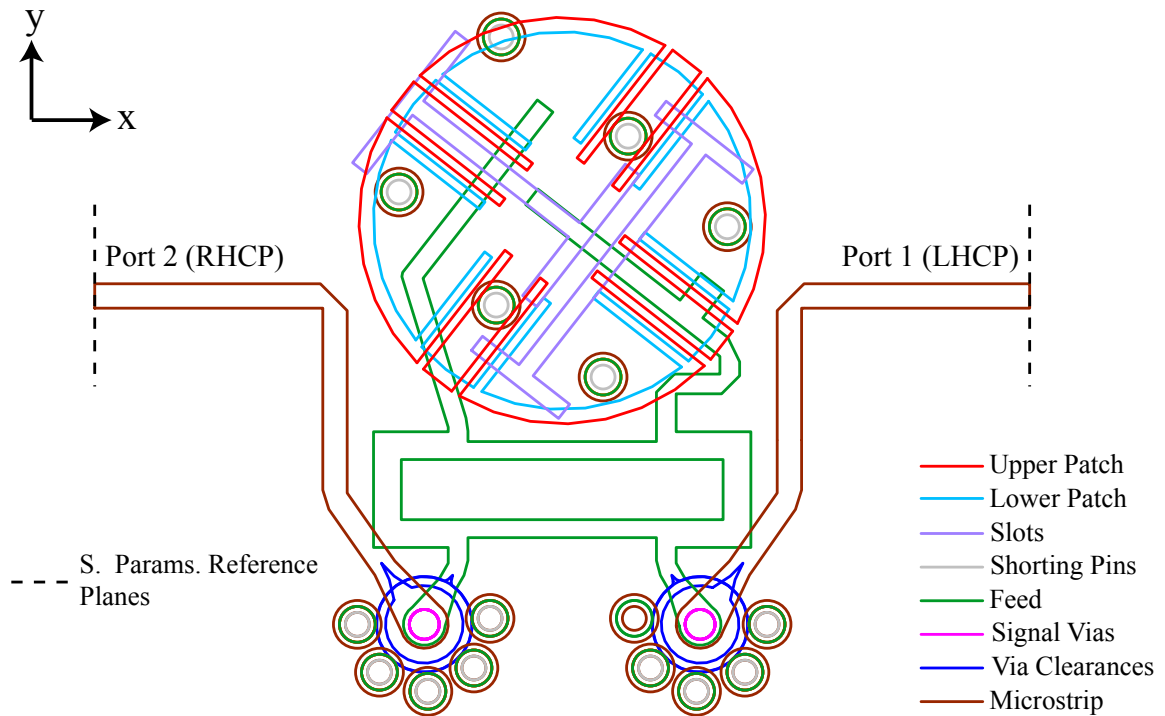
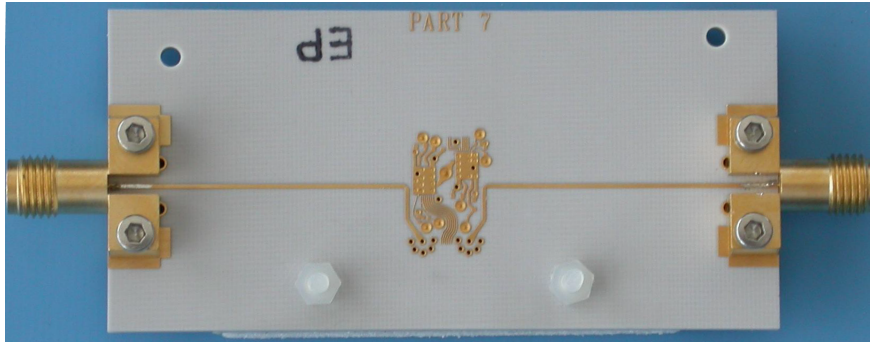


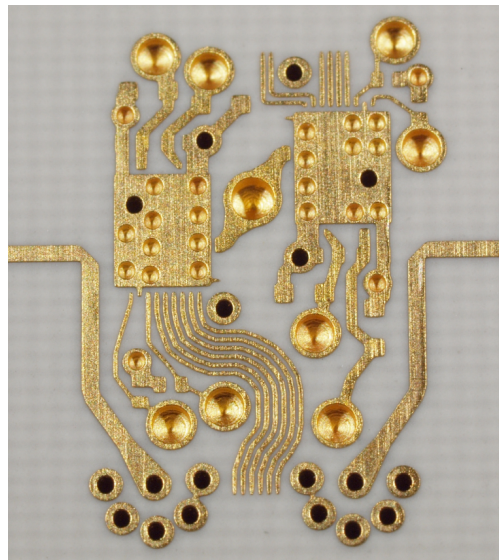
Figure 4.43. Layout outline of *The Cell* prototype (as seen from the upper patch layer: *upper view*). *R(L)HCP* stands for Right (Left) Hand Circular Polarization. Note the Reference Planes and the Local Coordinate System, which is no longer aligned with the feeding of the linearly polarized element, but with the edges of the prototype board. A sample of the prototype board is visible in *Fig. 4.44*.

And *Fig. 4.44* contains pictures of the Cell prototype. This figure features (i) the coaxial connectors mounted in the edges of the prototype PCB board, and (ii) the microstrip layer of the cell prototype. It is worth to notice that, unlike the simulation model, the cell prototype includes the Power Combiner as well as all the pads for the MMICs & its biasing components and some dummy traces of the control network. Though these components do not intervene actively in the evaluation of the prototype, they have been included to allow the identification of possible undesired loading effects.

⁸Note that, for the sake of brevity, the present performance evaluation concerns only the *Through ERC* (recall *Fig. 4.25*). The performance evaluation of the *Blind ERC* is summarized in [1, 10].



(a) Cell prototype board.

(b) Detail view of the Cell. Note the black dots that reveal the location of the *through* vias.**Figure 4.44.** *The Cell* prototype. Rear view, from microstrip layer.

a) Scattering Parameters

The S-Params. of the Cell are displayed in *Fig. 4.45*. In this figure different predictions are compared with measurement results. This comparison reveals that, given the fabrication tolerances involved, there is a reasonable agreement between predictions and measurements. This agreement confirms the promising performance expectations for the cell and provides a validation of its theoretical modeling. Moreover, since the model of the cell does not include the dummy components visible in *Fig. 4.44(b)*, it can also be stated that such components do not have a noticeable loading effect on the operation of the cell.

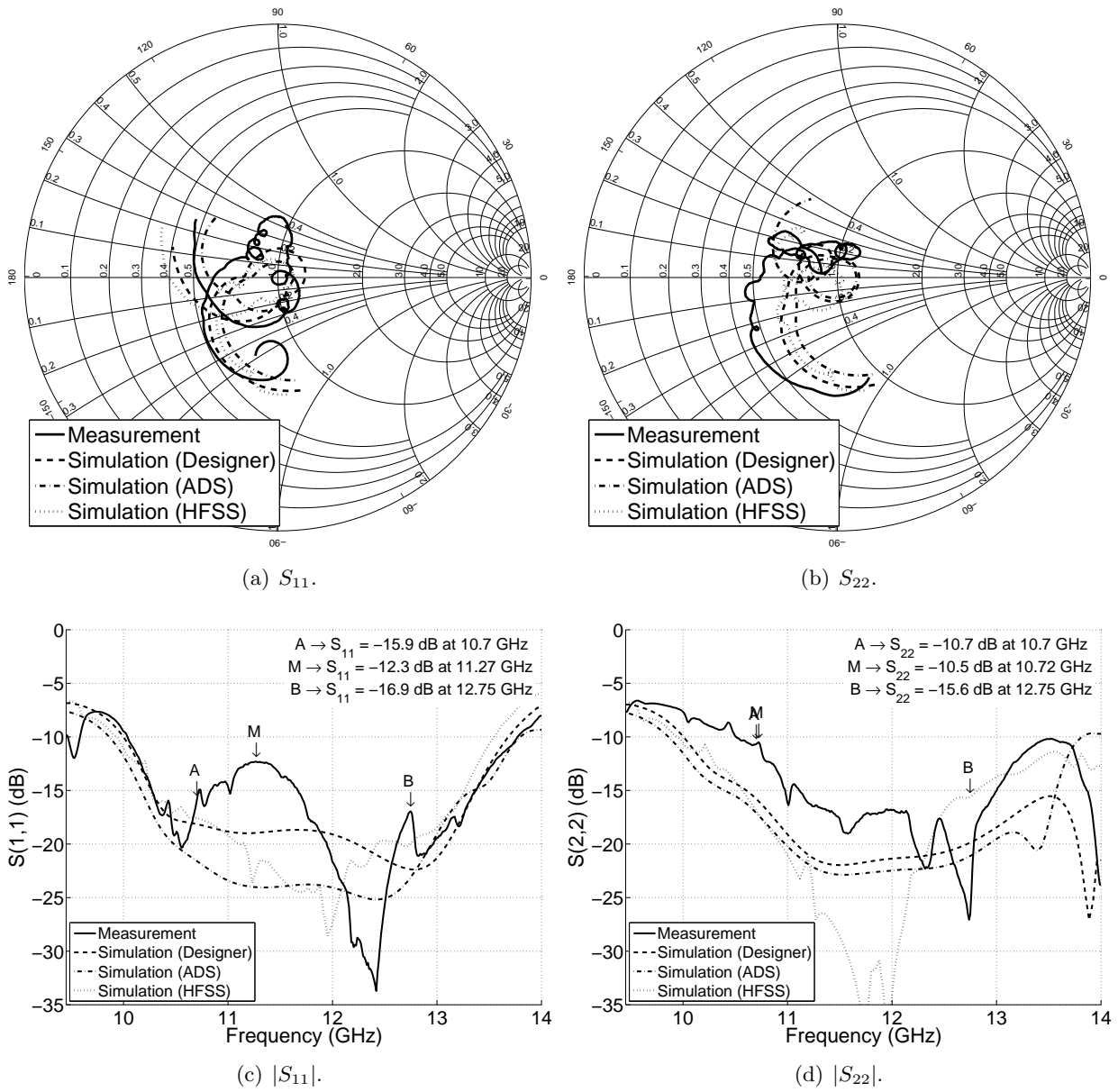


Figure 4.45. Scattering Parameters of the Cell. The reference planes for measurements and simulation coincide in the microstrip layer of the Cell, as depicted in *Fig. 4.43*. Measurements are done after a TRL calibration with *Cal. Kit #3* -recall *Fig. 4.11(c)*. Simulation results assume infinite ground planes, with the exception of those from *Ansoft HFSSTM*, which exhibit a characteristic ripple superimposed. From [9].

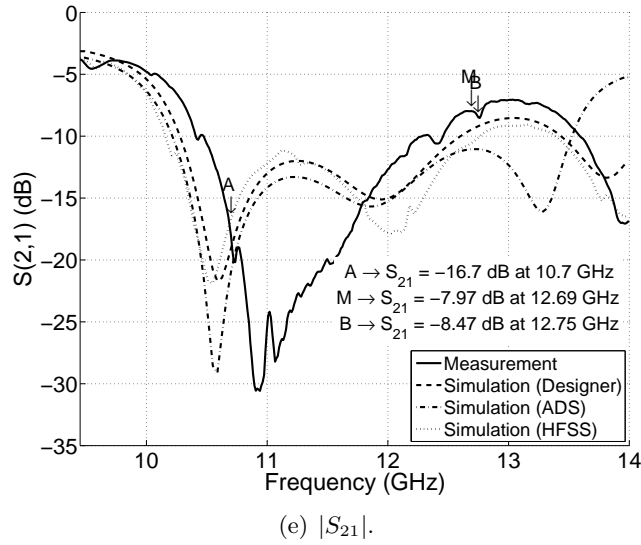


Figure 4.45. Scattering Parameters of the Cell (contd.).

b) Radiation Parameters

The measured radiation patterns of the Cell are shown on the left columns of *Fig. 4.46* to *Fig. 4.49*. These patterns, measured using the *Spinning Dipole* technique, consist of two envelopes whose mutual spacing represents the Axial Ratio of the circularly polarized field radiated by the Cell.⁹ The AR is represented, in Cartesian Coordinates, on the right columns of the aforementioned figures. In these charts, the measured AR is compared with different predictions.

These predictions for the AR correspond to different matching status for the two ports of the Cell. This matching status is, in fact, observed to have a potentially strong impact on the quality of the circular polarization synthesized by the Cell. This impact is attributed to the non-negligible coupling between the ports of the Cell. According to *Fig. 4.36(c)* and *Fig. 4.45(e)*, this coupling is maximum in the upper part of the frequency band.

Such impact, together with the imperfect matching expected at the *coaxial* ports of the Cell prototype and the incertitude associated to the characterization of the stripline terminals of the Long Vias, motivates the analysis of different miss-matching scenarios. These miss-matching scenarios are included in the theoretical modeling of the Cell and labeled in the AR plots as follows:

- *Stripline*: the Long Vias are removed from the Cell model, that becomes equivalent to the DCPRE depicted in *Fig. 4.34*, and it is excited alternatively through each one of its two

⁹The foundations of this measurement technique, also known as the *Polarization-Pattern* method, are described in [15, Ch. 15].

stripline ports. The port of the radiating element that is not excited is passively terminated with a matched load, as usual.

- *Stripline unloaded*: the same as in the previous scenario, with the exception that the unexcited port is not matched, but left in open circuit.
- *Microstrip*: the Cell is excited alternatively through each one of its two *microstrip* ports, which means that the long vias are included, as depicted in *Fig. 4.43*. The port of the Cell that is not excited is passively terminated with a matched load, as usual.
- *Microstrip unloaded*: the same as in the previous scenario, with the exception that the unexcited port is not matched, but left in open circuit.

None of the simplified miss-matching scenarios described above is expected to faithfully capture the real behavior of the Cell AR. Instead, it is expected that, if the *real* miss-matching status of the Cell falls within the bounds defined by these miss-matching scenarios, the predictions associated to such limiting cases should define, all together, several diagnosis regions for the measured AR. In this way, depending on the region to which the measured AR is belonging, it could be possible to make an estimate of which miss-matching scenario is the most representative of the prototype under test.

At this point it must be recalled that the uncertainties in the matching status of the Cell are not the only source of error in the prediction of the AR. As it has been demonstrated in the previous section, the tolerances in the fabrication of the cell (that are also in the origin of the aforementioned matching uncertainties) may have a significant impact on its AR.

Taking all these considerations into account, the fact that the measured AR keeps basically within the curves defined by *Microstrip* and *Microstrip unloaded*, confirms that (i) the Long Via is operating properly and (ii) the inaccuracies in the modeling of the Cell are small, provided the fabrication tolerances. Some exceptions to this overall good agreement between predictions and measurements are coming from the ripple present in the measured AR and the appearance of some sharp dips at low elevation angles. The ripple and the dips are both attributed to diffraction phenomena in the borders of the prototype PCB board. These phenomena are not present in predictions, that assume a board of infinite extent.¹⁰ It is also interesting to note that the most pessimistic predictions from the unloaded scenarios always take place in the upper part of the frequency band, as expected.

Last, but not least, the overall polarization purity of the Cell within the scan domain and the frequency band of interest is considered to be very satisfying. In fact, measurement results show that the AR of the Cell has an average level close to 4 dB and its worst values (excluding the aforementioned dips) rarely exceed 8 – 9 dB.

¹⁰Here, the theoretical modeling of the cell is done using a 2.5D ‘Full Wave’ software tool: *Ansoft Designer™*.

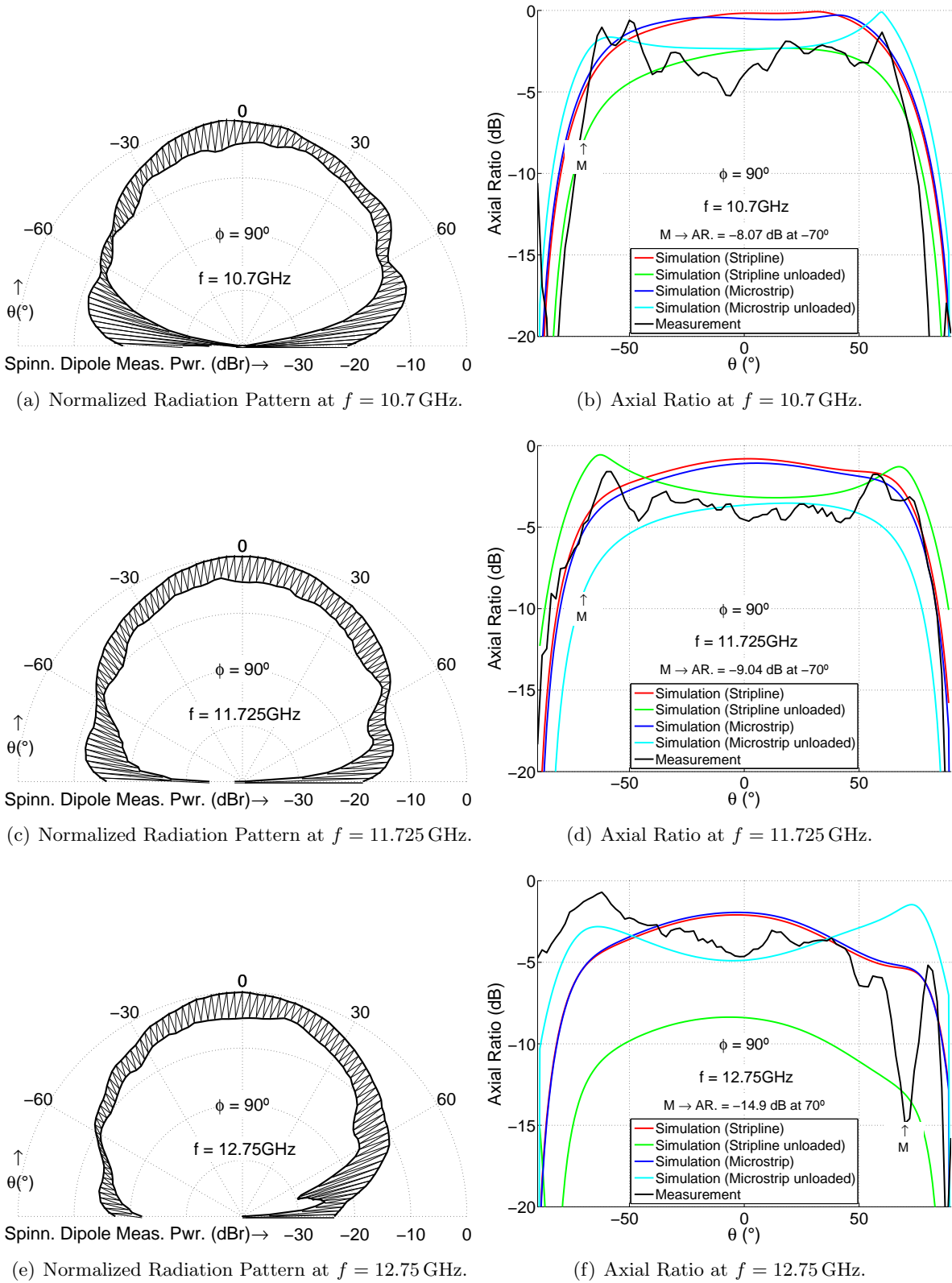


Figure 4.46. Normalized Radiation Pattern and Axial Ratio of the Cell. Superimposed Elevation Cuts along the Vertical Plane ($\phi = 90^\circ$ in Fig. 4.43) at different frequencies. Port 1 is excited. From [1].

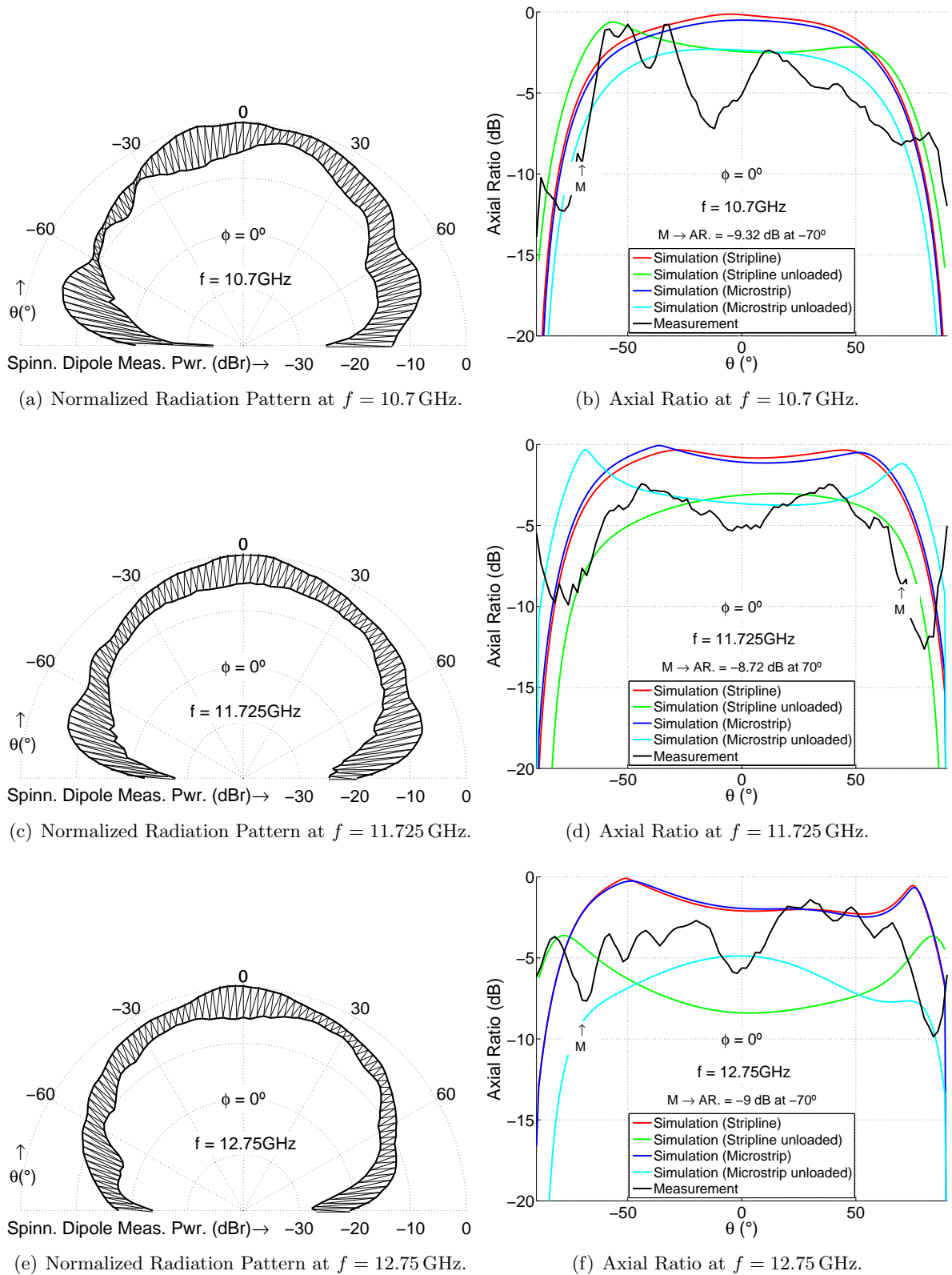
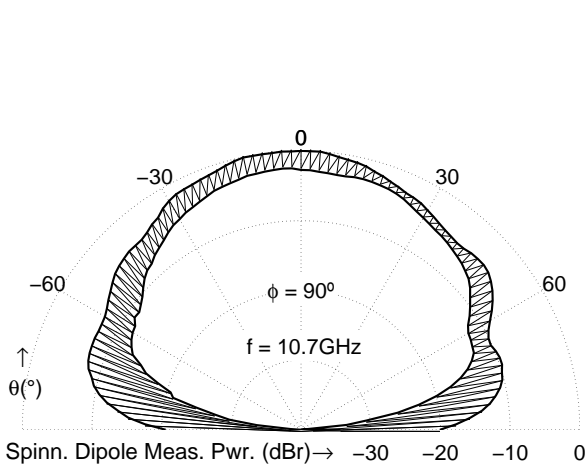
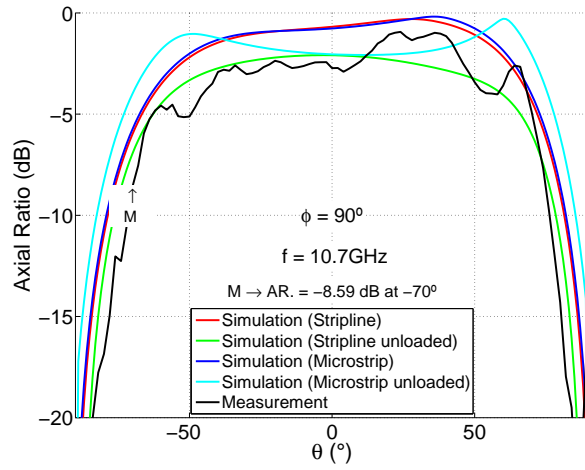


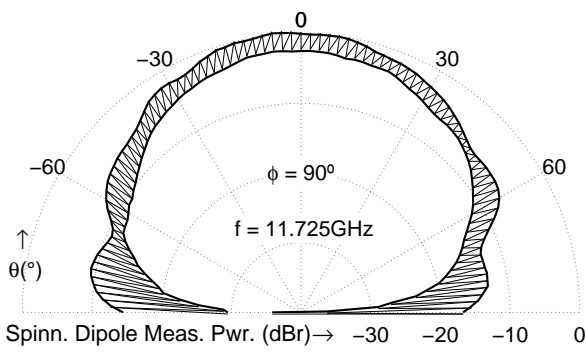
Figure 4.47. Normalized Radiation Pattern and Axial Ratio of the Cell. Superimposed Elevation Cuts along the *Horizontal Plane* ($\phi = 0^\circ$ in Fig. 4.43) at different frequencies. *Port 1* is excited. From [1].



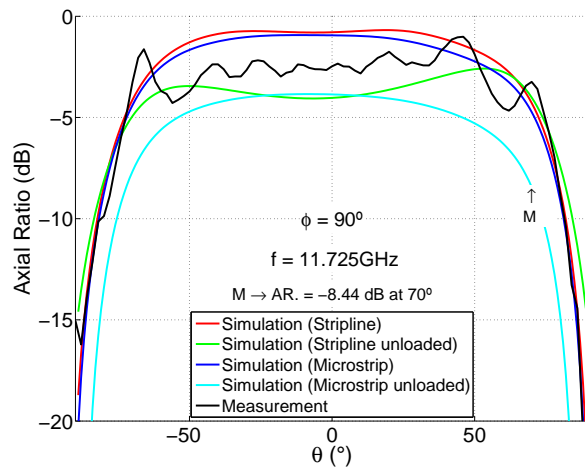
(a) Normalized Radiation Pattern at $f = 10.7$ GHz.



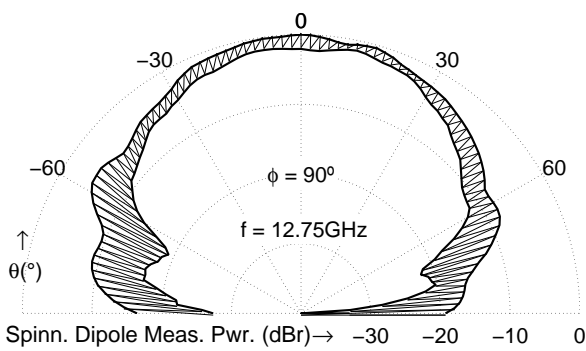
(b) Axial Ratio at $f = 10.7$ GHz.



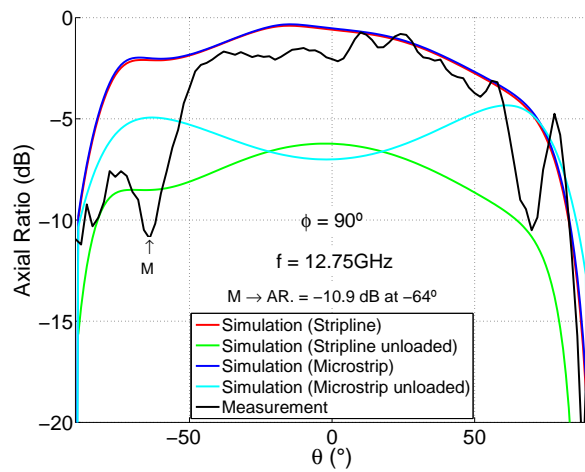
(c) Normalized Radiation Pattern at $f = 11.725$ GHz.



(d) Axial Ratio at $f = 11.725$ GHz.



(e) Normalized Radiation Pattern at $f = 12.75$ GHz.



(f) Axial Ratio at $f = 12.75$ GHz.

Figure 4.48. Normalized Radiation Pattern and Axial Ratio of the Cell. Superimposed Elevation Cuts along the Vertical Plane ($\phi = 90^\circ$ in Fig. 4.43) at different frequencies. Port 2 is excited. From [1].

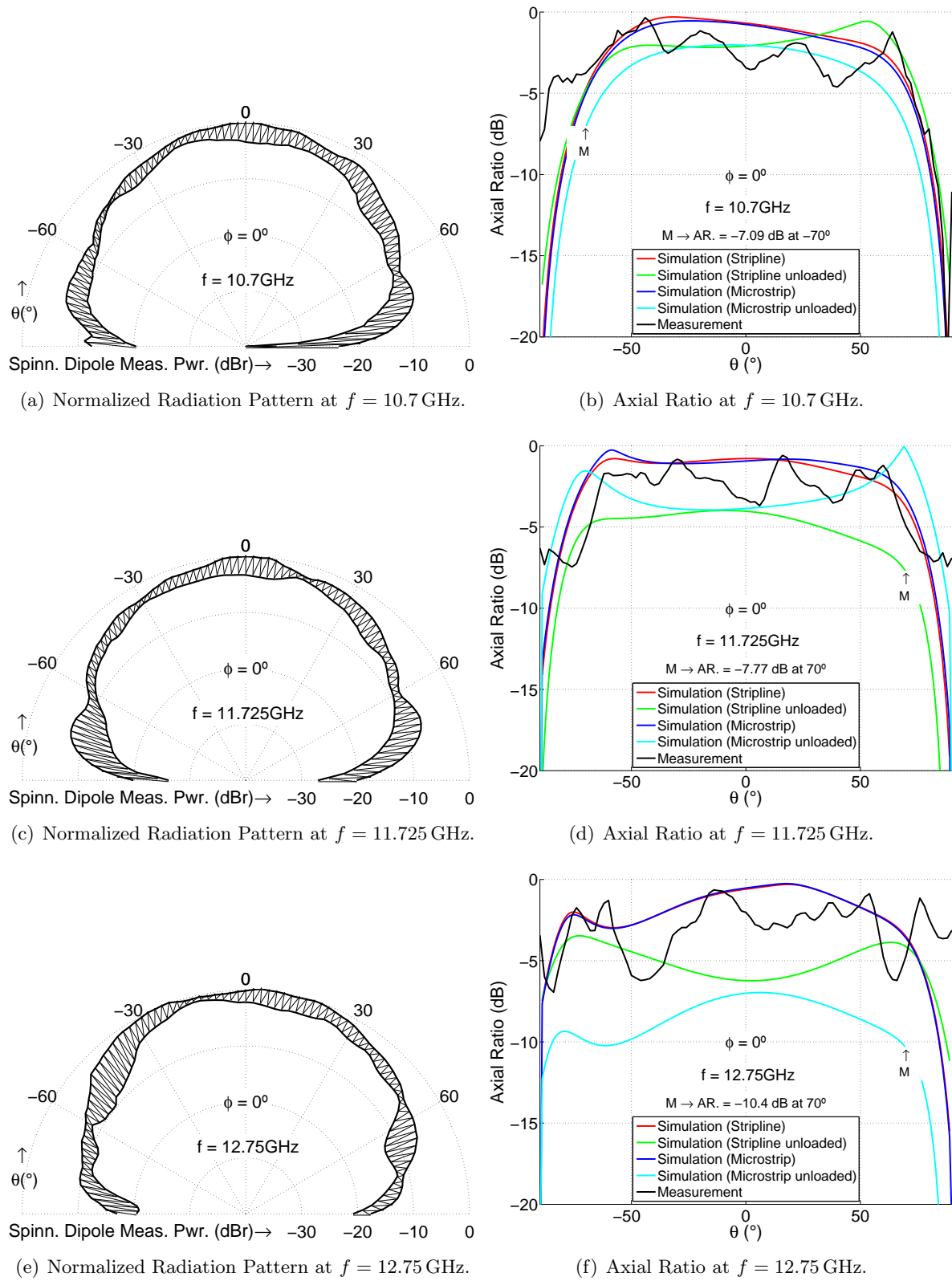


Figure 4.49. Normalized Radiation Pattern and AR of the Cell. Superimposed Elevation Cuts along the *Horizontal Plane* ($\phi = 0^\circ$ in Fig. 4.43) at different frequencies. *Port 2* is excited. From [1].

Gain

In average, the measured Gain for the Cell keeps close to 5 dB in the frequency band of interest. *Fig. 4.50* shows a good agreement, provided the uncertainties in the fabrication and testing of the prototypes, between measurement results and predictions. This agreement validates the theoretical modeling of the Cell and supports the expectation that the Radiation Efficiency of the prototype in the reference planes of interest (S. Params. Reference Planes in *Fig. 4.43*) should exceed 54% all over the frequency band, for both ports.

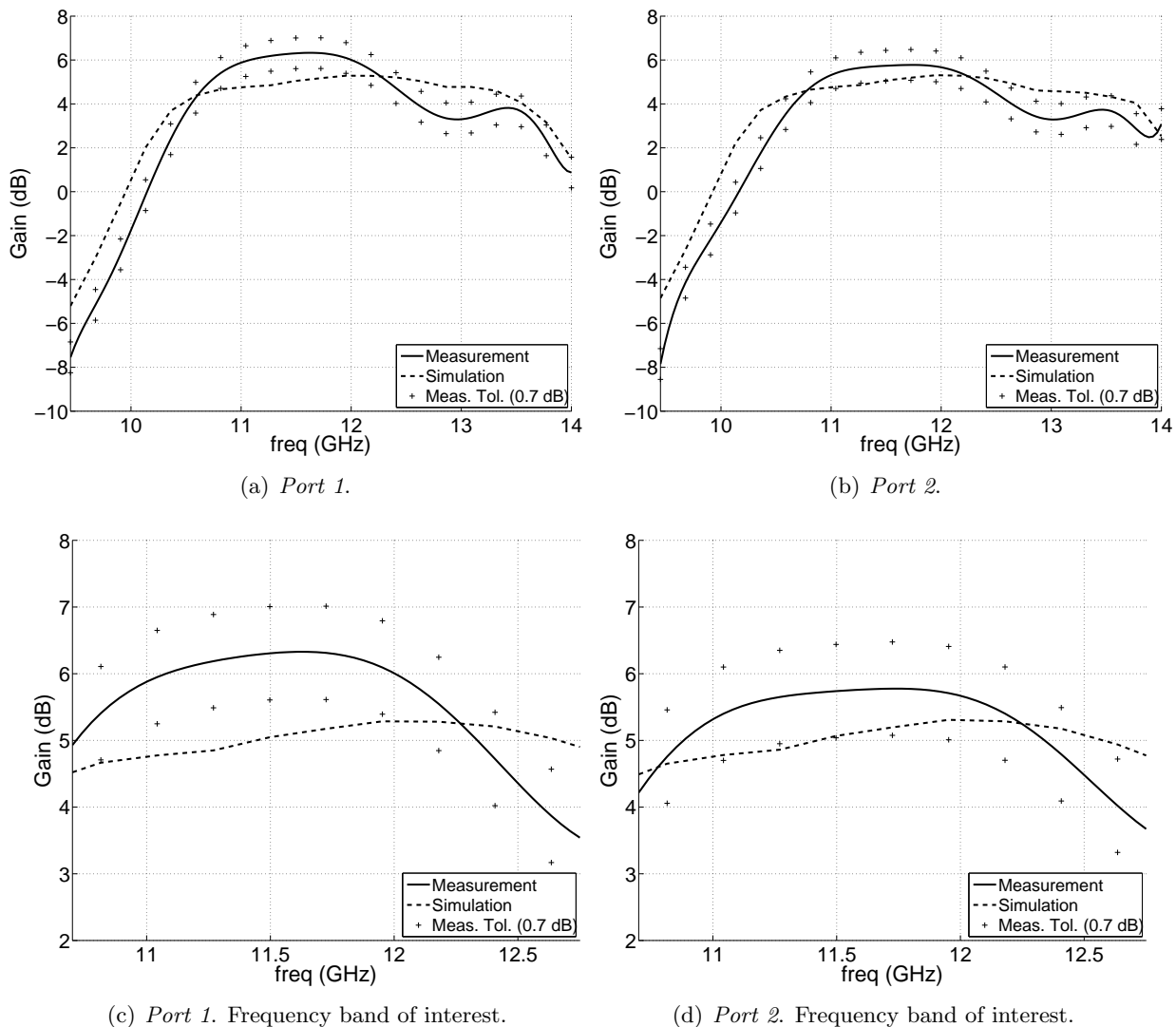


Figure 4.50. Realized gain of the Cell. As for the linearly polarized element -recall *Fig. 4.44(a)*-, simulation results assume an infinite ground plane and do not take into account the connectors of the prototype (2.5-D simulation with *Ansoft DesignerTM*). The connectors are edge mount coaxial to microstrip transitions as those visible in *Fig. 4.44(a)*. The location of the reference planes in the simulation model coincides with the edges of the prototype in order to match, as much as possible, the measurement set-up. From [1].

4.6.3 Conclusion

This section completes the performance evaluation of the ERC with a detailed study of the so-called Cell. *The Cell* contains all the components within the ERC (the DLPRE, the branch line hybrid and the Long Vias), apart from the Power Combiner, whose performance is assessed separately to simplify the prototyping and measurement of the Cell.

The performance of the Cell is evaluated in terms of Scattering Parameters, Radiation Pattern, Axial Ratio and Gain (Radiation Efficiency). This evaluation takes into account the uncertainties associated to the fabrication tolerances and the measurement procedures involved. Though these uncertainties are found to be the most important sources of error in the prediction and characterization of the Cell operation, they do not prevent a successful assessment of its design.

In fact, provided the aforementioned uncertainties, the predictions derived from the theoretical modeling of the Cell keep in an overall good agreement with measurement results. All in all, this agreement

- confirms the promising performance expectations of the Cell,
- validates the modeling of the Cell, and
- proves the compatibility between the targeted fabrication technology and the ERC concept proposed here.

4.7 Conclusion

The previous chapter provided, with the design of the ERC, a first theoretical evaluation of the compliance with the constructive and performance requirements specified in *Table 4.1*. This evaluation was entirely satisfying with regard to the technological and structural requirements, and very promising (though not completely fulfilling) in terms of EM performance.

At this point it must be said that the lack of an absolute fulfillment of the performance requirements at ERC level was not unexpected. The design constraints imposed by the constructive requirements were, in fact, known to be very strong. Actually, the quantification of this performance shortfall constitutes a valuable result by itself, since it provides an *initial estimate* of the maximum EM performance that is achievable at ERC level under the aforementioned design constraints, and supplies a reference for the grading of further design improvements.

Moreover, it must be recalled that some of the performance limitations of the (isolated) ERC are expected to be compensated at array level. In this sense, to determine the range of such

a compensation for the actual "array + ERC" designs, though out of the scope of this thesis, remains a subject of great interest.

The present chapter has completed the compliance assessment of the ERC design. This has been done by means of the evaluation of the ERC performance in multiple real implementations and the contrast of this performance with theoretical predictions.

The evaluation of the performance of the cell provides, within the conditions highlighted above, very satisfying results. Furthermore, the analysis of these results has shown that, beyond the uncertainties associated to the materials and the fabrication processes (that are found to be considerable) and those related to the measurement procedures (generally smaller, but not negligible), the predictions made from the theoretical modeling of the ERC keep in an overall good agreement with the performance observed in the different prototypes.

This good agreement between measurements and predictions validates the theoretical modeling of the ERC and all its components (the Radiating Element, especially). This validation is judged to be extensible to the whole design process described in this memoir, that is largely based on such modeling.

In view of these results, the assessment of the ERC design, of the corresponding performance predictions and, presumably, of the design process itself, can be considered as successful.

References

- [1] R. Torres-Sánchez, “Measurement results of the first NATALIA breadboard,” LEMA (EPFL), Lausanne, Switzerland, Tech. Rep., Jun. 2011, Draft.
- [2] R. Baggen, S. Vaccaro, , D. Llorens, R. Torres-Sánchez, and G. Langgartner, “First prototyping of a compact mobile Ku-band satellite terminal,” in *proc. EuCAP 2010, 4th International Conference on Antennas and Propagation*, Apr. 2010.
- [3] L. Baggen, S. Vaccaro, D. Llorens del Rio, M. Bottcher, S. Weitz, and M. Wleklinski, “Near/farfield measurements of a polarization agile phased array at Ku-band,” in *Antennas and Propagation (EU-CAP), Proceedings of the 5th European Conference on*, april 2011, pp. 1540 –1544.
- [4] R. Torres-Sánchez, “Sensitivity of the NATALIA radiating element to manufacturing tolerances,” LEMA (EPFL), Lausanne, Switzerland, Tech. Rep., May 2009, Draft.
- [5] A. C. Ludwig, “The definition of cross polarization,” *IEEE Trans. Antennas Propag.*, vol. AP-21, pp. 116–119, Jan. 1973.
- [6] “Agilent Technologies Application Note 1287-9. In-fixture measurements using vector network analyzers,” Agilent Technologies, Aug. 2000.
- [7] “Agilent Technologies Product Note 8510-8A. Network analysis applying the 8510 TRL calibration for non-coaxial measurements,” Agilent Technologies, May 2001.
- [8] “Agilent Technologies Application Note 1287-3. Applying error correction to network analyzer measurements,” Agilent Technologies, Mar. 2002.
- [9] R. Torres-Sánchez, “Model Transfer of the NATALIA Elementary Radiating Cell,” LEMA (EPFL), Lausanne, Switzerland, Tech. Rep., Feb. 2011, Draft.
- [10] —, “NATALIA Blind Elementary Radiating Cell & Vias Tolerance Analysis,” LEMA (EPFL), Lausanne, Switzerland, Tech. Rep., Aug. 2009, (v. 2.1).
- [11] J. Tippet and R. Speciale, “A rigorous technique for measuring the scattering matrix of a multiport device with a 2-port network analyzer,” *IEEE Trans. Microw. Theory Tech.*, vol. 30, no. 5, pp. 661 –666, may 1982.
- [12] E. Van Lil, “A rigorous technique for measuring the scattering matrix of a multiport device with a two-port network analyzer (comments),” *IEEE Trans. Microw. Theory Tech.*, vol. 33, no. 3, pp. 286 –287, mar 1985.
- [13] T. Ruttan, B. Grossman, A. Ferrero, V. Teppati, and J. Martens, “Multiport VNA measurement,” *Microwave Magazine, IEEE*, vol. 9, no. 3, pp. 56 –69, june 2008.
- [14] H.-C. Lu and T.-H. Chu, “Multiport scattering matrix measurement using a reduced-port network analyzer,” *IEEE Trans. Microw. Theory Tech.*, vol. 51, no. 5, pp. 1525 – 1533, may 2003.
- [15] J. D. Kraus, Ed., *Antennas*, 1st ed. New York: McGraw-Hill, 1950.

5. Conclusion and Perspectives

*Parfois on regarde les choses
telles qu'elles sont
en se demandant pourquoi.
Parfois on les regarde
telles qu'elles pourraient être
en se disant pourquoi pas.*

Il y a. VANESSA PARADIS

This thesis contains a full overview of the design of an innovative antenna element at Ku-Band for a low-profile phased array antenna. The design of the antenna element is done in the framework of an industrial project that is aiming to address the increasing demand of mobile satellite terminals for consumer applications. The project, called NATALIA (New Automotive Tracking Antenna for Low-cost Innovative Applications), has been funded by the European Space Agency and involves a consortium of several key industrial partners in the sectors of satellite R&D and consumer applications from Germany, Switzerland and Luxembourg, including our laboratory LEMA-EPFL.

A typical scenario of the application targeted by NATALIA is a car external antenna dedicated to the reception of TV signals at 12 GHz. European car makers are willing to offer this service on their high-end models. But the receiving antenna subsystem, to be mounted in the car's roof, must be accommodated within a low profile volume consisting in a cylinder of 20 cm diameter and no more than 2 – 3 cm thick. In addition, this “terminal” (the antenna subsystem including all the RF functions) must have a reasonable power consumption and its cost must be a very small fraction of the car's price (typically 1 – 2%). Even putting aside the non electromagnetic requirements, it is easy to see how formidable is the challenge from the antenna point of view.

Actually, the shortage of cost-effective and compact user terminals constitutes an important market opportunity for antenna concepts able to cope with the severe trade-offs that underlie the implementation of such terminals. This implementation must conciliate multiple conflicting requirements that are basically related to the cost, the size, and the performance of the antenna subsystem.

This industrial framework puts, on one side, strong conditions on the design possibilities of the Radiating Element (RE). But, on the other hand, it has prompted the research for innovative solutions in terms of integration, miniaturization, implementation and measurement of the RE. In particular, the integration of the RE within the antenna buildup has contributed to conciliate the simplicity of a basic PCB process with a set of demanding EM performance requirements, while keeping the whole in the bounds of a low-profile design. This integration also led to the development of a series of dedicated transitions that enabled reliable measurements within the antenna buildup.

It is expected that this work will constitute a valuable practical contribution to the design of “the radiating element”, at the source of all possible array configurations. The main results have been presented and well received in several conferences either as a standalone research or as a collective achievement of the NATALIA project team. This collaboration has resulted in several patents, including one with participation of the author [1–3].

The main short-term perspective of this work is obviously to enable the final commercial implementation of this antenna concept. Indeed, at the moment of finishing this thesis the selected technological strategy for mass production seems very promising and is under way.

But together with this immediate goal, other more scientific perspectives must be mentioned. They should be considered in a more extended time frame, perhaps already looking to the second generation of these satellite terminals for cars.

From the point of view of research associated to the radiating element and its integration into the array, further design iterations should provide a means to go beyond the isolated element design approach followed here. Ideally, the array environment should be effectively incorporated into the design of the element from the very first steps. This may imply an investigation of the interest and, in its case, of the feasibility of incorporating a sequential rotation scheme into the infinite array design approach.

Moreover, such an improved array-element design approach would enable the generalization of the design guidelines summarized in this memoir into an equivalent of the so-called Fragmented Aperture Concept. Actually, for a given aperture size, this generalization could get the best, in terms of performance, out of the available metalization layers. This kind of improvements in the design approach of the radiating element seems unavoidable if the possibilities of a further optimization of the actual array performance or an increase of the array size are to be envisaged.

From a more general point of view, there are other applications that could either benefit from the proposed antenna concept (e.g. radar applications) or promote its evolution to cope with new design challenges. These design challenges could aim towards a further simplification of the array logic (and the final price of the terminal) or to the expansion of its functionality. This evolution might lead whether to low-profile multi-beam and beam-switching array concepts, or to transmit-receive and multi-purpose antenna systems.

References

- [1] M. Bourry, F. Tiezzi, and S. Vaccaro, “Omni-directional antenna for mobile satellite broadcasting applications,” Patent US 20 090 027 294, January 29, 2009.
- [2] D. Llorens, F. Tiezzi, and S. Vaccaro, “Sub-array polarization control using rotated dual polarized radiating elements,” Patent US 20 100 253 585, October 7, 2010.
- [3] F. Tiezzi, S. Vaccaro, D. Llorens, and R. Torres-Sánchez, “Method and apparatus for a compact modular phased array element,” Patent US 20 110 025 574, February 3, 2011.

A. Infinite Array Modeling

A.1 Introduction

As a complement to the infinite array design approach discussed at the end of *Section 1.1.2*, the performance evaluation carried out in *Section 4.3* for the isolated Radiating Element (RE) is extended here to the particular case of the element operating inside an infinite array.

The analysis of the RE within an infinite array can provide a first approximation to the performance of the element embedded in the foreseen array antenna. The medium size of the array, together with the fact that the infinite array modeling is not taking into account the sequential rotation of the elements constitute two important limitations of this approximation, that should be considered as a worst case scenario.

A.2 The Unit Cell

The RE considered here is the *Slitted Element* described in *Section 3.3.1* and keeps the same port assignment proposed in *Fig. 3.36*.¹ The uniformly illuminated infinite array is modeled with *Ansoft HFSSTM* by imposing *Periodic Boundary Conditions* around an *Unit Cell*. These boundaries are grouped in couples of *Master-Slave* boundaries. And the phase shift between the different couples is determined according to the scan direction (θ, ϕ) at which the performance of the RE inside the infinite array is to be evaluated.

The Unit Cell must be able to accommodate the layout of the RE, while fitting the triangular lattice of the array. For the sake of simplicity, the infinite array modeling is applied here to the element with linear polarization and, in order to allow for an eventual contrast with measurements of the embedded element, dedicated miniature right angle coaxial to stripline transitions as that proposed in *Fig. 3.16* are used to access the stripline ports of the RE.²

¹Results for other radiating elements are compiled in [1].

²Predictions and measurements for the performances of the circularly polarized element *embedded* in different locations of the NATALIA array are summarized in [2].

In this case, an hexagonal Unic Cell like that depicted in *Fig. A.1* is used to generate all the results that are presented next. The inclusion of the RE within a rhombic cell, though less evident given the layout of the element, is also found to be possible, as illustrated in *Fig. A.2*. It is worth to note that while the hexagonal cell requires three couples of Master-Slave Periodic Boundaries, the rhombic only requires two.

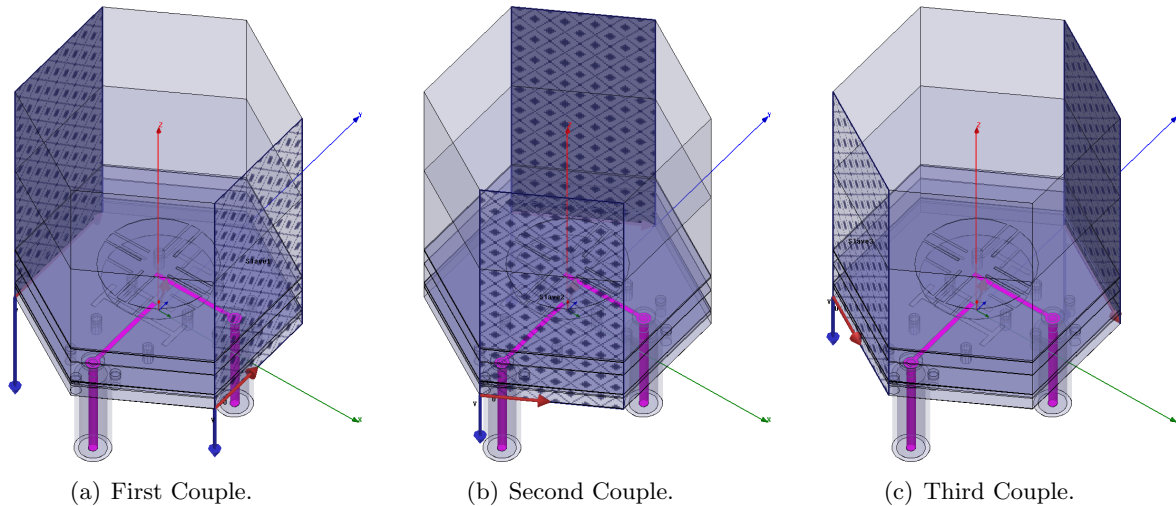


Figure A.1. The Linearly Polarized Radiating Element within an hexagonal Unit Cell. The three couples of Master-Slave Periodic Boundaries and the pair of miniature right angle coaxial to stripline transitions are highlighted.

In order to verify the consistency of the Unit Cell modeling proposed here, the boundaries of the two cells are disposed with respect to the RE as sketched in *Fig. A.2* and the results obtained for several scanning directions using both cell shapes are compared. These results are identical and the impact of the cell shape on the computational cost of the electromagnetic analysis of the cells is found to be small, for the two cases considered here.

The results summarized next concern only the Scattering Parameters of the RE within an infinite array. The dependence of these Scattering Parameters with the array scan direction (θ, ϕ) is displayed using contour plots in polar coordinates. This format of representation can provide, at the expense of rather dense charts, a valuable insight into the embedded operation of the RE (see [3, Fig. 3(a)] and [4]).

A.3 Active reflection coefficients

The contour plots that correspond to the active reflection coefficients at the two ports of the RE, $-S_{11}(\theta, \phi)$ and $S_{22}(\theta, \phi)$, are represented side by side with their *E Planes* aligned to make the comparison of both coefficients easier. This alignment is achieved by means of an azimuthal rotation of the contour curves for S_{22} so that the effect of the transverse disposition of the RE feeding ports gets compensated. Moreover, the vertical color scales are equal for both ports all over the frequency band.

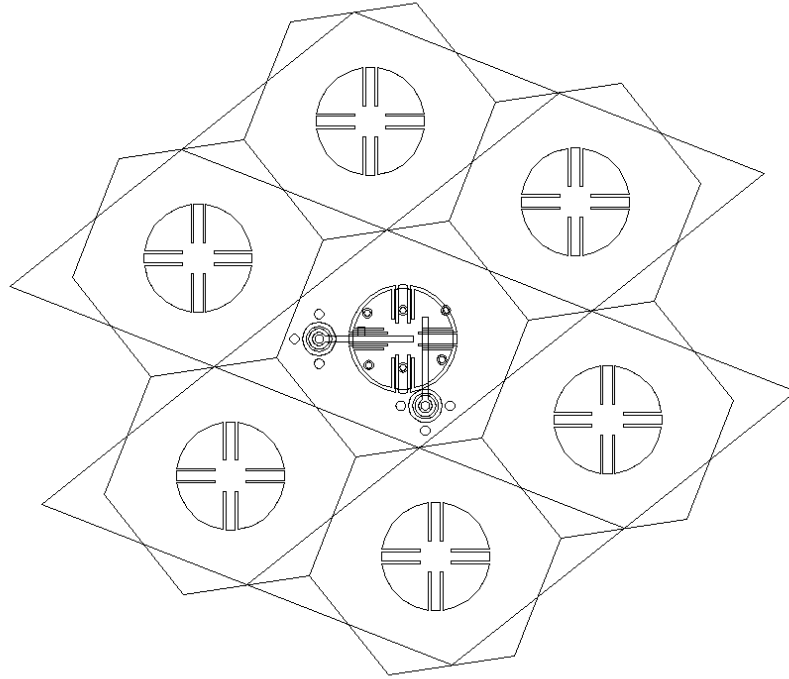
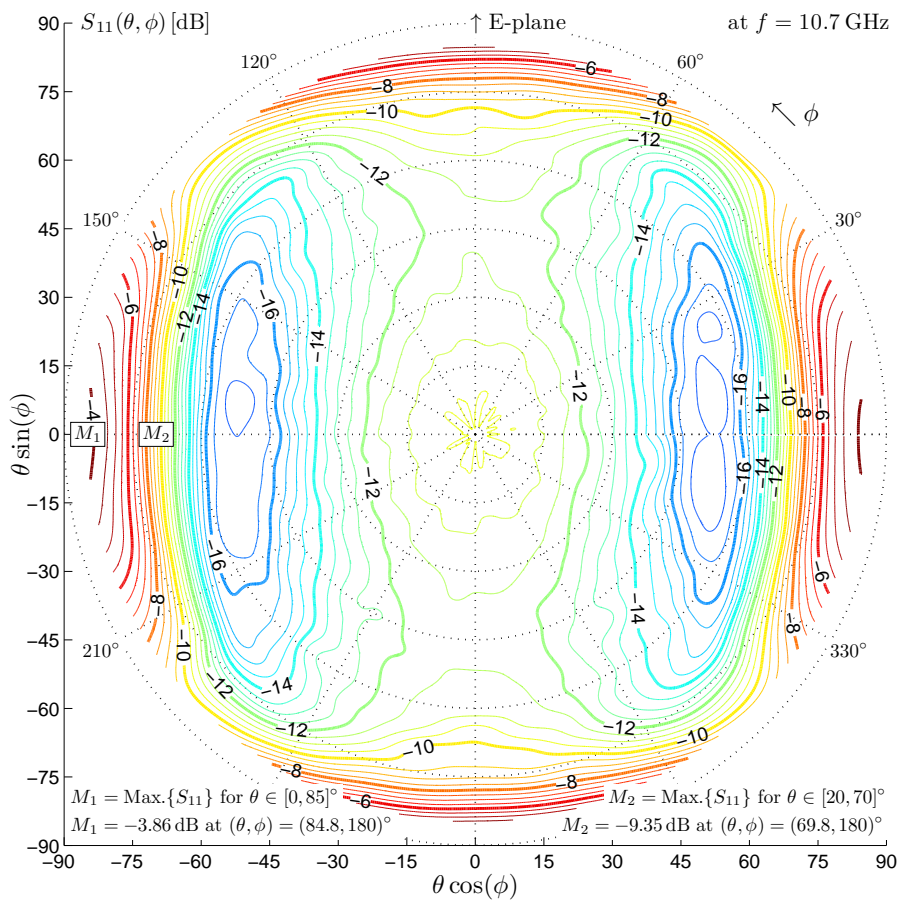


Figure A.2. The Linearly Polarized Radiating Element within two different Unit Cells: rhombic and hexagonal. The ring of patches & cells around the central Unit Cell are drawn here just to highlight that the relative rotations of the two cells with respect to each other and with respect to the element have been chosen so that (i) the layout of the RE fits both cells and (ii) all the replicas of the element will be placed in identical locations regardless of the cell shape.

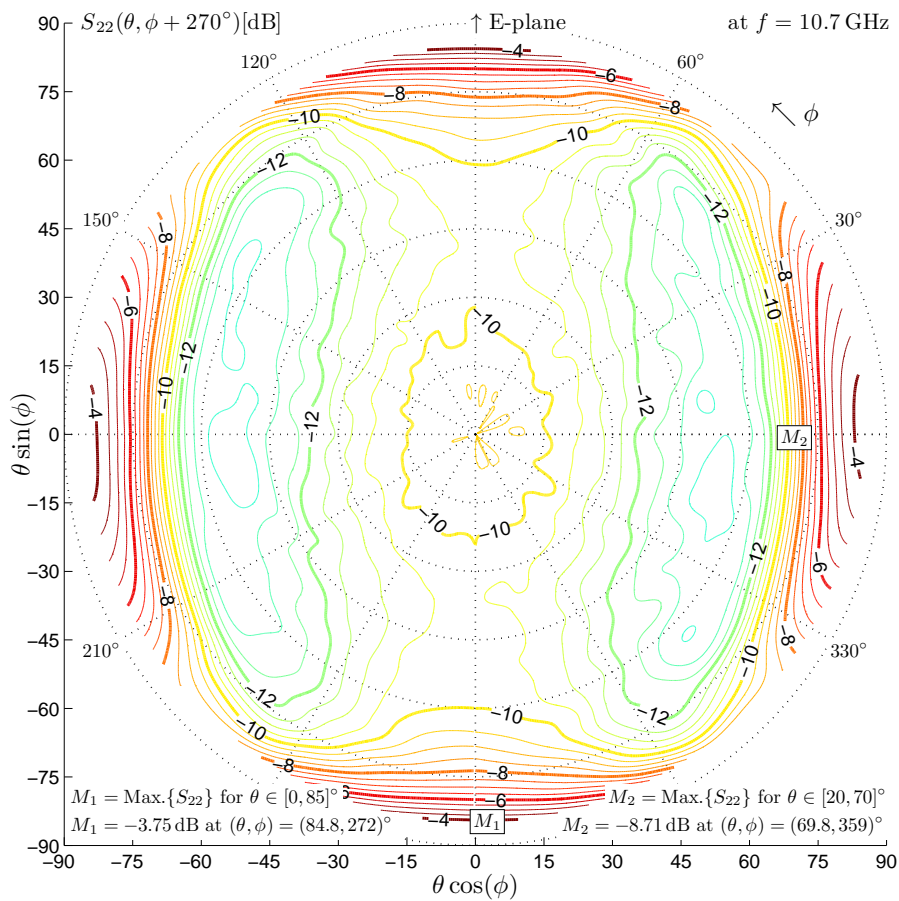
In overall, the active reflection coefficients displayed from *Fig. A.3* to *Fig. A.7* evidence a notable variation of the scanning performance of the embedded element with frequency.

Within the targeted scan domain ($\theta \in [20, 70]^\circ$), this scanning performance suffers of a progressive degradation as the frequency of operation increases, with a sharp worsening in the upper limit of the frequency band, especially for low elevation angles. In fact, $\max \{S_{ii}\}$ evolves from ~ -9 dB at 10.7 GHz up to ~ -2 dB at 12.75 GHz. This particular frequency evolution, provided that the mutual coupling phenomena are typically more intense at lower frequencies, may be related with the emergence of grating lobes, whose impact should be more noticeable at higher frequencies and low elevation angles.

On the other hand, it is also worth to note that the behavior of the active reflection coefficients in the central part of the frequency band at moderate elevation angles ($\theta \lesssim 50^\circ$) is quite good ($\max \{S_{ii}\} \lesssim -10$ dB).



(a) Port 1.



(b) Port 2.

Figure A.3. Active reflection coefficients at 10.7 GHz. The contour plot curves are displayed in steps of 0.5 dB and indexed every 2 dB.

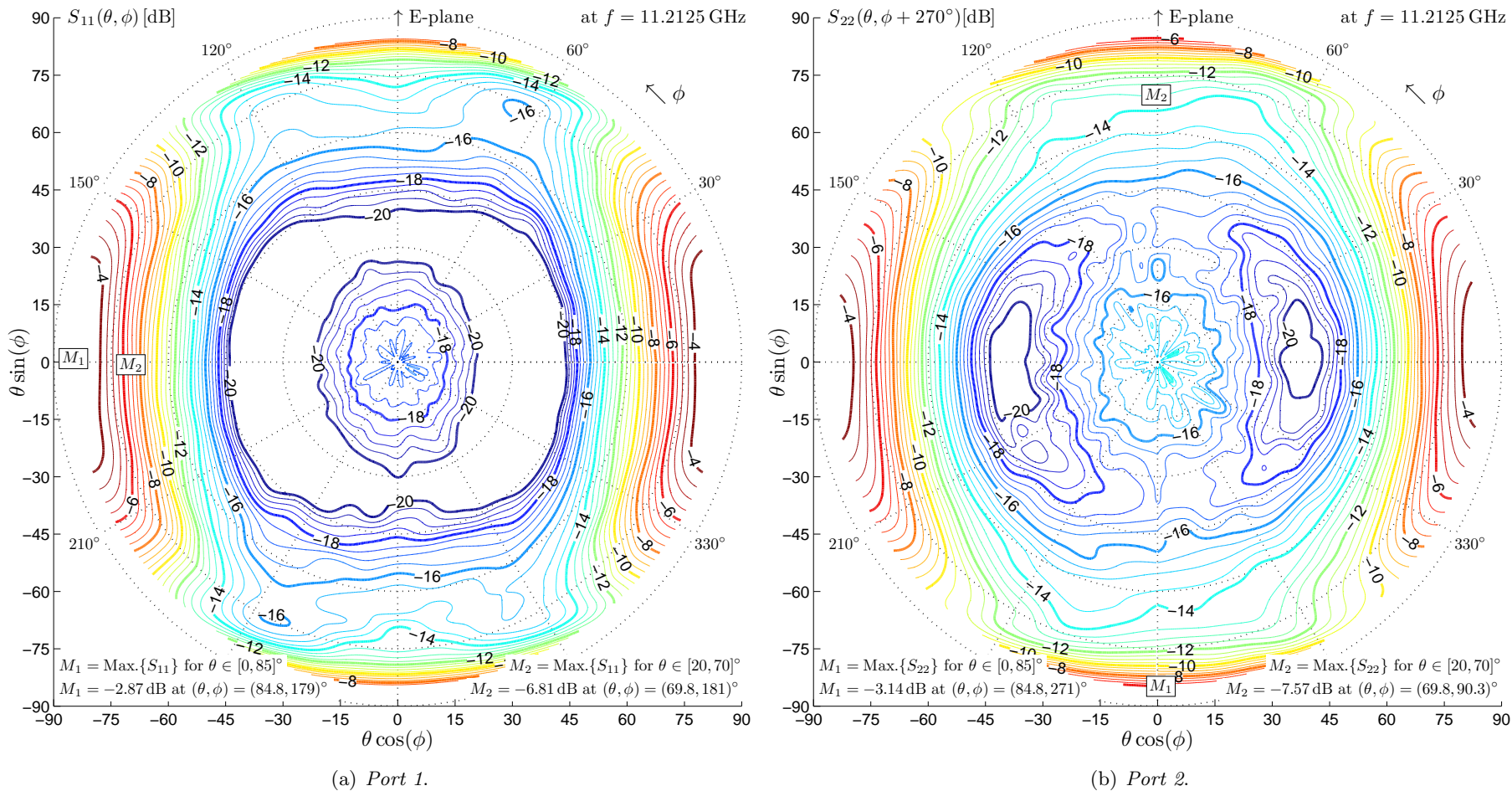
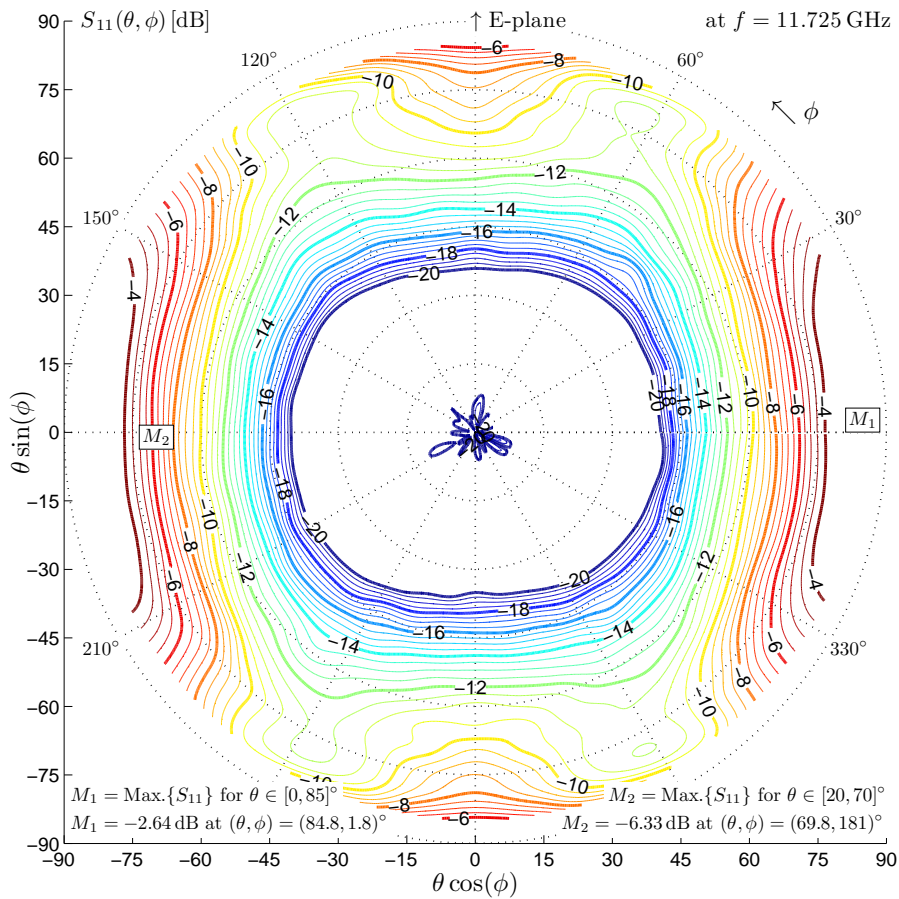
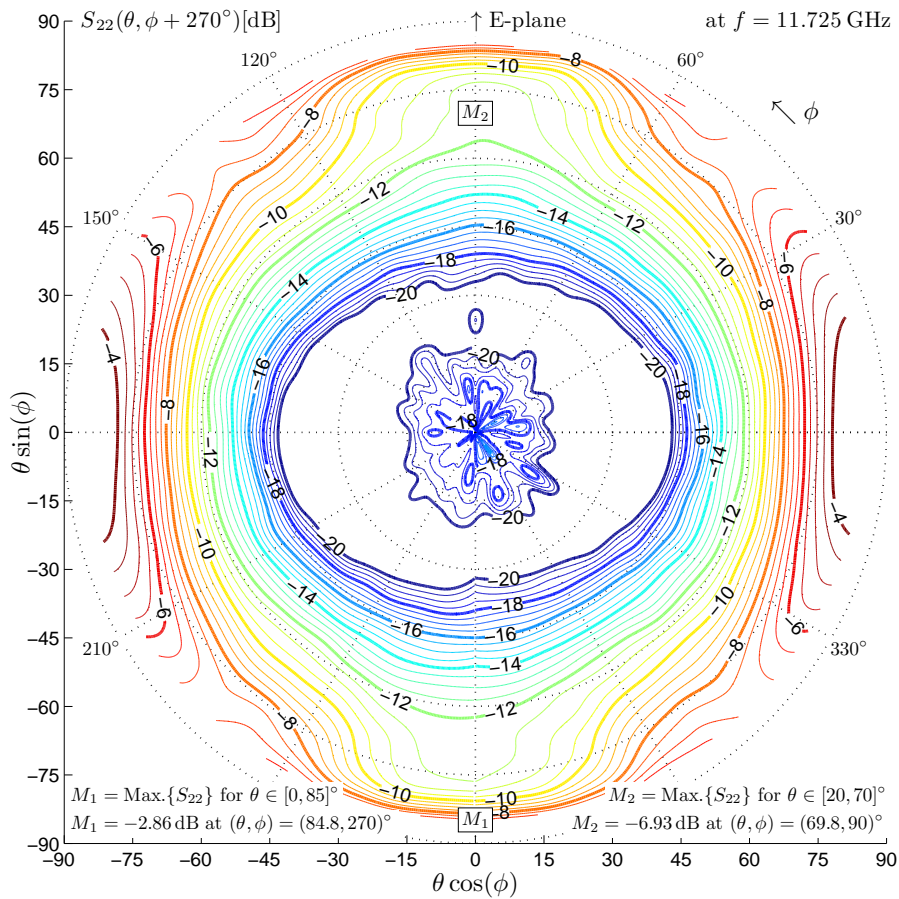


Figure A.4. Active reflection coefficients at 11.2125 GHz. The contour plot curves are displayed in steps of 0.5 dB and indexed every 2 dB.



(a) Port 1.



(b) Port 2.

Figure A.5. Active reflection coefficients at 11.725 GHz. The contour plot curves are displayed in steps of 0.5 dB and indexed every 2 dB.

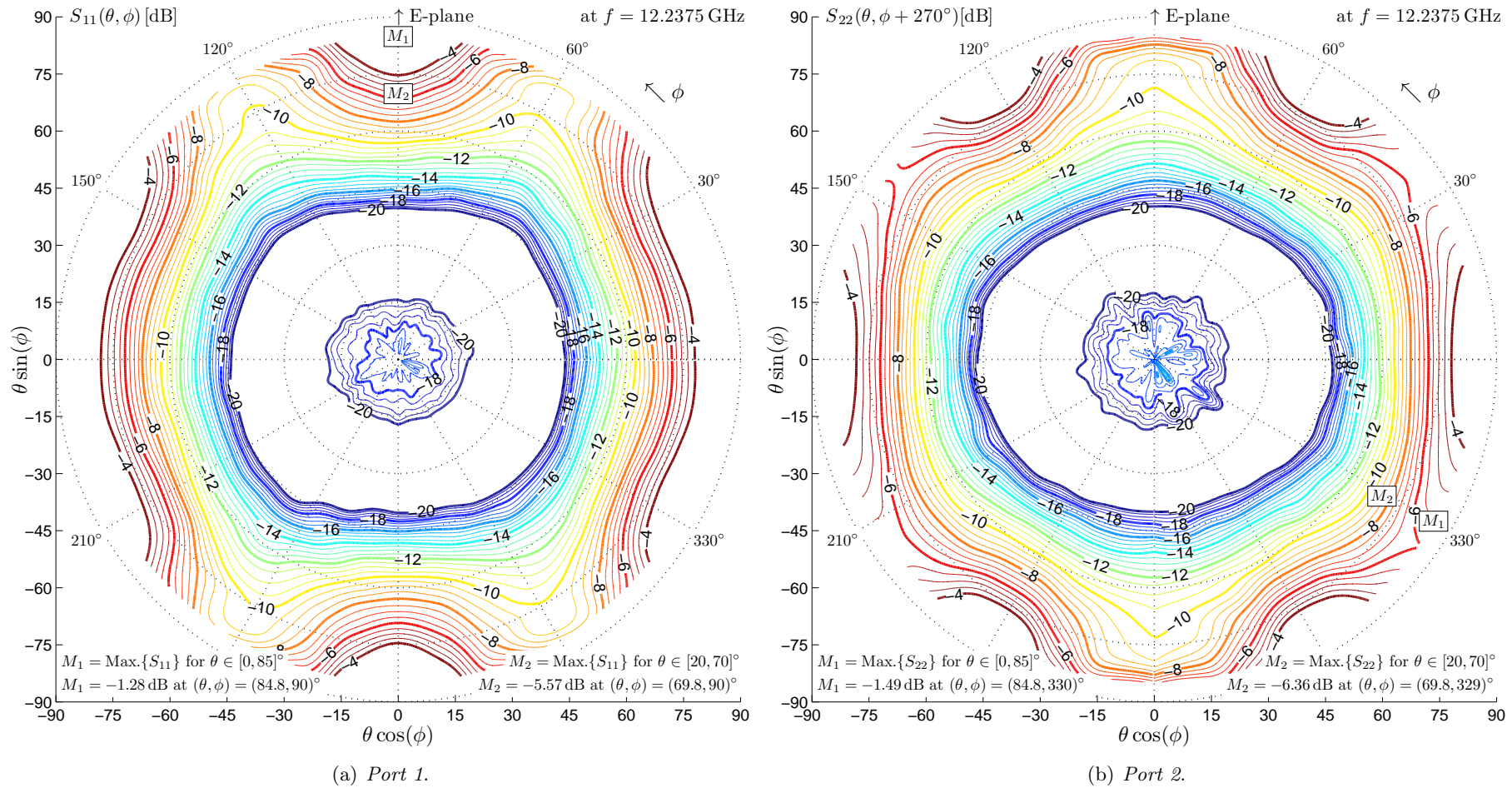
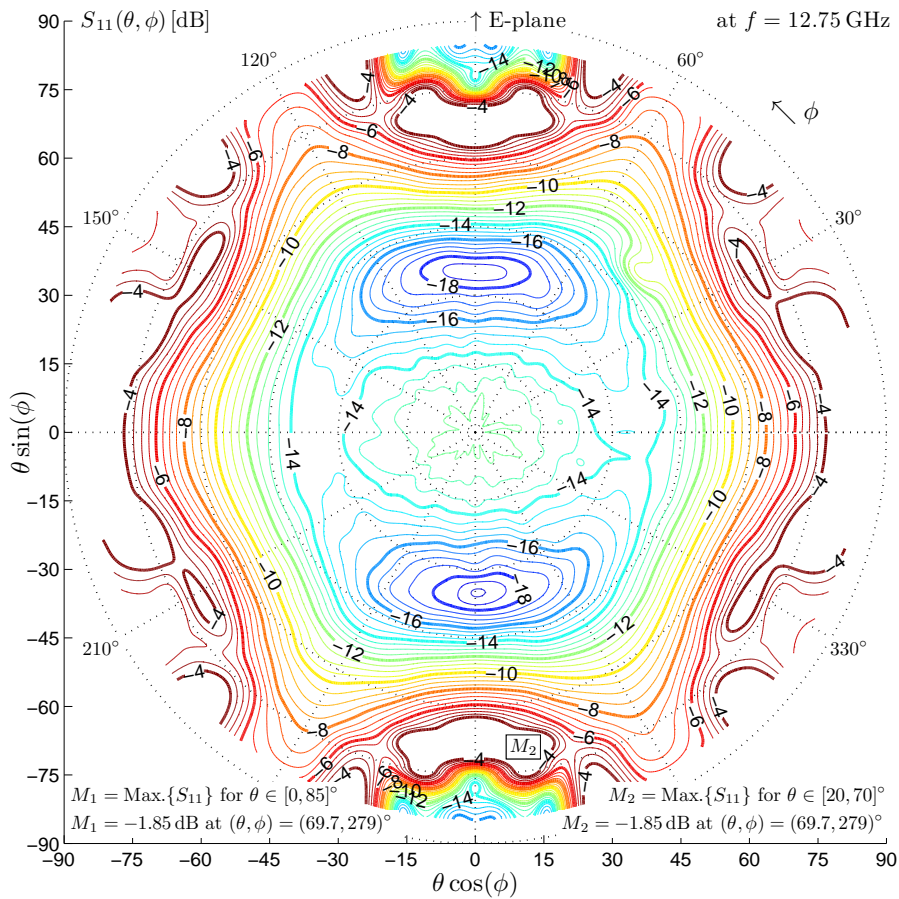
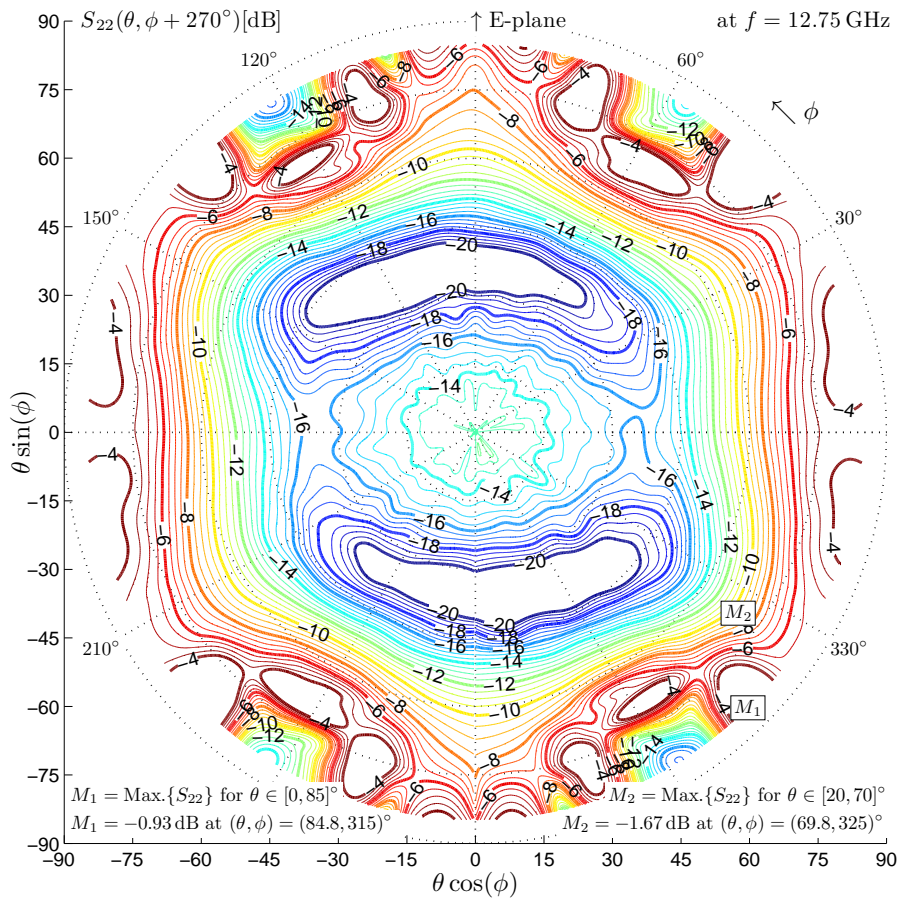


Figure A.6. Active reflection coefficients at 12.2375 GHz. The contour plot curves are displayed in steps of 0.5 dB and indexed every 2 dB.



(a) Port 1.



(b) Port 2.

Figure A.7. Active reflection coefficients at 12.75 GHz. The contour plot curves are displayed in steps of 0.5 dB and indexed every 2 dB.

A.3.1 Active coupling coefficients

Unlike the reflection coefficients, the port coupling of the embedded element shows a moderate worst level ($\max\{S_{ij}\} \lesssim -10$ dB) that remains quite stable with frequency. Beyond this fact, the most remarkable characteristic observed in the contour plots of $S_{21}(\theta, \phi)$ and $S_{12}(\theta, \phi)$ is related with the property of reciprocity.

For the element and the array lattice considered here, the active scattering parameters of the RE, considered here as a two-port component, do not satisfy the property of reciprocity: $S_{21}(\theta, \phi) \neq S_{12}(\theta, \phi)$. This can be appreciated in *Fig. A.8*, where the active coupling coefficients at 12.75 GHz are displayed side by side. Though the differences between S_{21} and S_{12} are relatively small, they are not negligible and are present all over the frequency band, which supports the thesis that they are not just due to modeling inaccuracies.

In fact, this feature has already been observed in other arrays and an effort has been made to highlight the relation of this non-reciprocity with the absence of certain symmetries at both element and array levels [5]. Here, as a quantitative measure of the departure from reciprocity, the reciprocity difference magnitude (\bar{r}_s) is defined as:

$$\bar{r}_s(\theta, \phi) = \frac{1}{2} |S_{12}(\theta, \phi) - S_{21}(\theta, \phi)|. \quad (\text{A.1})$$

The reciprocity difference magnitude at 12.75 GHz is displayed in *Fig. A.9*.³ This figure accentuates the symmetry that was already observable in *Fig. A.8* and encourages the definition of a new magnitude (\bar{r}_{s-r}) to evaluate the departure of the element scattering parameters from a kind of generalized reciprocity:

$$\bar{r}_{s-r}(\theta, \phi) = \frac{1}{2} |S_{12}(\theta, \phi) - S_{21}(\theta, \phi + 180^\circ)|. \quad (\text{A.2})$$

The fact that \bar{r}_{s-r} is observed to remain close to or below the numerical noise of our simulation results ($\lesssim -40$ dB) in the whole scan domain and the frequency band, suggests, therefore, a reformulation of the reciprocity relation.

Intuitively, it could be argued that the phenomena underlying this new formulation $-S_{12}(\theta, \phi) = S_{21}(\theta, \phi + 180^\circ)$ - are related to the vectorial nature of the interactions between the currents that flow through the ports of the radiating element (e.g.: \vec{J}_{12} and \vec{J}_{21}) and the phase progression that the illumination of the host infinite array tends to impose across the element aperture. This phase progression ($\vec{\alpha}$) is obviously a function of the angles (θ, ϕ), that represent the actual scanning direction.

³In the figure, $\bar{r}_s(\theta, \phi)$ [dB] = $20 \log_{10} [\frac{1}{2} |S_{12}(\theta, \phi) - S_{21}(\theta, \phi)|]$.

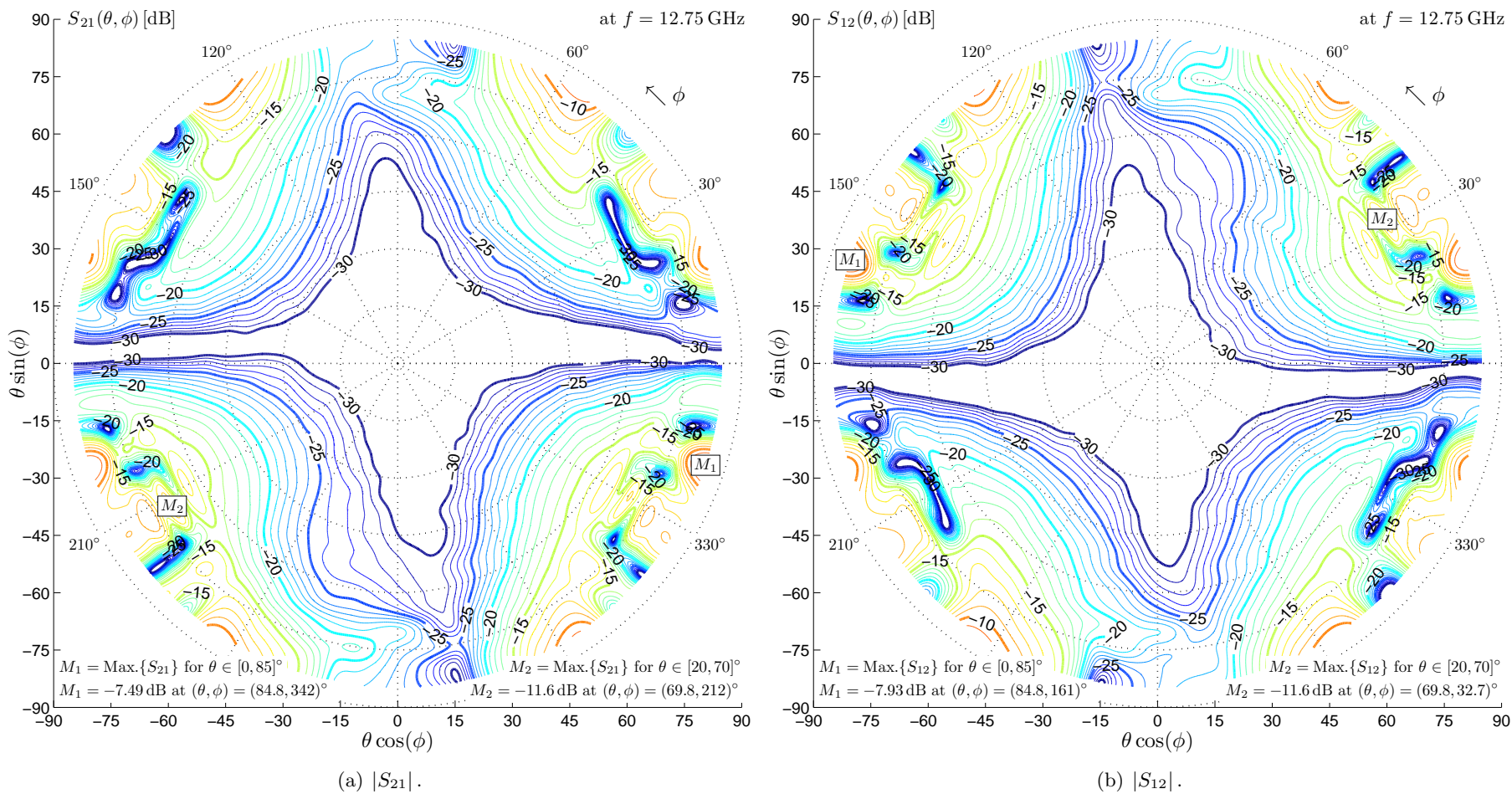


Figure A.8. Active coupling coefficients at 12.75 GHz. The contour plot curves are displayed in steps of 1 dB and indexed every 10 dB.

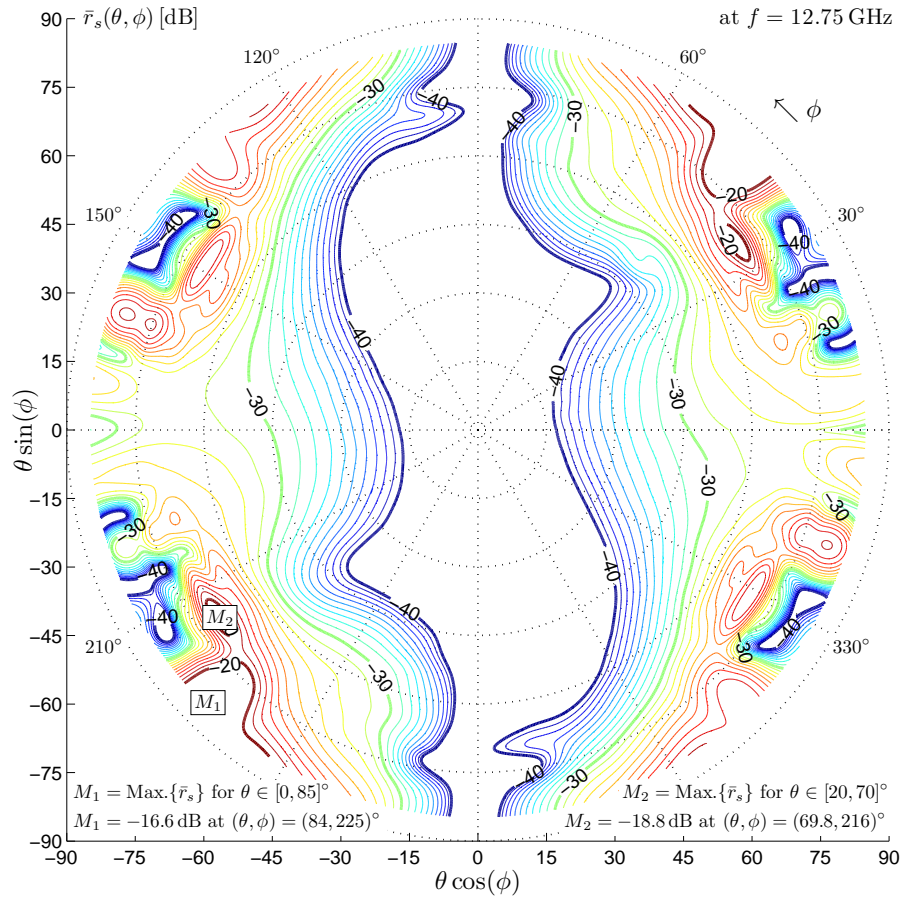


Figure A.9. Reciprocity difference magnitude (\bar{r}_s) at 12.75 GHz. The contour plot curves are displayed in steps of 1 dB and indexed every 10 dB.

Though out of the scope of this work, a rigorous justification of this new formulation of the reciprocity relation is considered to be of great interest and the support from Prof. J. Perruisseau-Carrier (*EPFL*) and Dr. F. Bongard (*JAST Antenna Systems*) in this direction is duly acknowledged here.

References

- [1] R. Torres-Sánchez, “NATALIA radiating element update. Two new candidates,” LEMA (EPFL), Lausanne, Switzerland, Tech. Rep., Dec. 2008, Draft.
- [2] —, “Measurement results of the first NATALIA breadboard,” LEMA (EPFL), Lausanne, Switzerland, Tech. Rep., Jun. 2011, Draft.
- [3] D. M. Pozar and D. H. Schaubert, “Scan blindness in infinite phased arrays of printed dipoles,” *IEEE Trans. Antennas Propag.*, vol. AP-32, pp. 602–610, Jun. 1984.
- [4] A. Ellgardt, “Study of rectangular waveguide elements for planar wide-angle scanning phased array antennas,” in *Antennas and Propagation Society International Symposium, 2005 IEEE*, vol. 1B, 2005, pp. 815–818.
- [5] W. Kahn, “Network reciprocity in modeling and analysis of phased array antennas,” in *Antennas and Propagation Society International Symposium (APSURSI), 2010 IEEE*, July 2010, pp. 1–4.

B. Definition of the Axial Ratio

B.1 Introduction

This appendix is intended to give further information about the definition of an important performance parameter of the Radiating Element. This parameter is the Axial Ratio (AR) and the definition deduced here has been used to generate, among others, the AR plots presented in *Section 3.2.1* and *Section 4.6*.

B.2 Definition

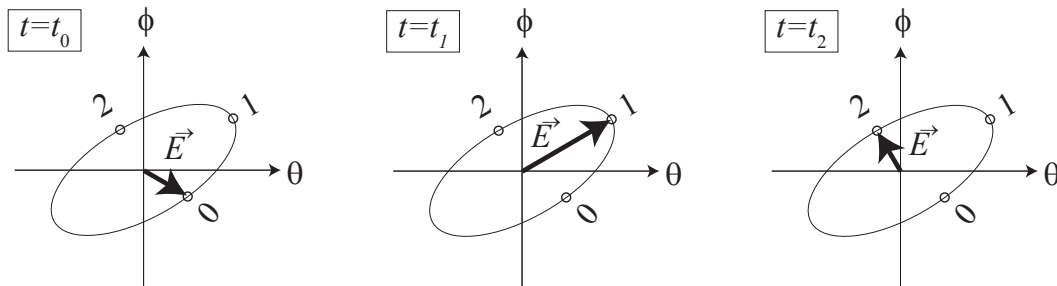
The AR of an electromagnetic (EM) source is defined with respect to the polarization state of the EM wave that the source radiates.

In general, the polarization state of a monochromatic EM plane wave that is propagating in the direction (θ_0, ϕ_0) can be defined using only three parameters. These parameters are related with the closed path described by the instantaneous electric field vector on a plane perpendicular to the direction of propagation. This path is completed by the electric field vector with a periodicity (T) that is determined by the frequency of oscillation of the EM wave (f , with $T = 1/f$) and an angular velocity such that the rate of sweeping out the area within the path is constant [1, Ch. 15].

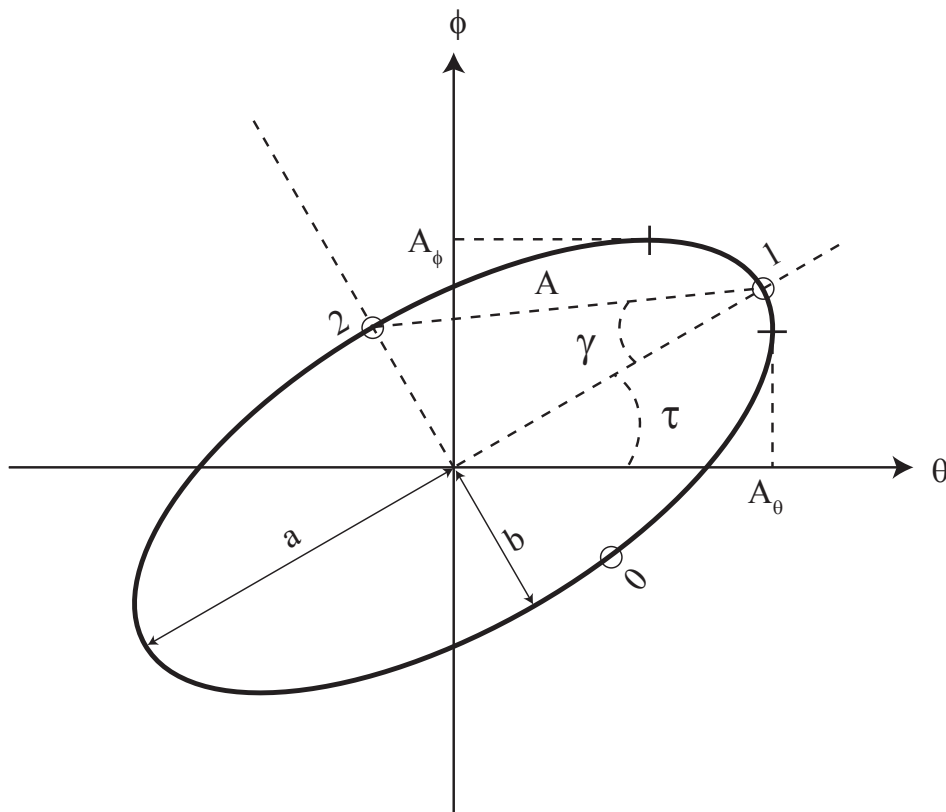
The path described by the electric field vector can be characterized, in general, as an ellipse: the so-called *polarization ellipse*. Therefore, as sketched in *Fig. B.1*, the three parameters that define the polarization state of the radiated field are:

- the **Sense of Rotation** of the electric field: typically referred to as *Left* or *Right-Handed* (LH or RH).
- The inclination of the major axis of the ellipse (τ in *Fig. B.1(b)*, or **Polarization Tilt**) with respect to a certain reference. Such reference is given, in this case, by the spherical unit vectors $(\hat{\theta}, \hat{\phi})$.

- And the aspect ratio between the main axis of the ellipse (b/a), which represents the **Axial Ratio** of the *elliptically* polarized wave and, by extension, of its source (i.e. the radiating element).



(a) Temporal evolution of the electric field vector along the polarization ellipse, with $t_0 < t_1 < t_2$, for example, and $t_2 = t_1 + T/4$ (see detailed geometry below).



(b) Geometry of the ellipse.

Figure B.1. The polarization ellipse.

According to this definition, the extreme values of the AR (0 and 1) correspond, respectively, to the particular cases of perfect linear and circular polarizations, while for any value in between the polarization is elliptical.

For the theoretical evaluation of the AR of an antenna, the radiated electric field can be

always be decomposed into two linearly polarized components.¹ Over the radiation sphere, these components can be chosen so that they coincide with the spherical unit vectors, as depicted in *Fig. B.1(b)*:

$$\vec{E}(\theta, \phi, t) = \hat{\theta} E_{\theta}(\theta, \phi, t) + \hat{\phi} E_{\phi}(\theta, \phi, t) \quad (\text{B.1})$$

In the case of a monochromatic wave oscillating at a frequency f , the two components of the electric field in (B.1) can be written as:

$$E_{\theta}(\theta, \phi) = A_{\theta}(\theta, \phi) \cos[\omega t + \alpha_{\theta}(\theta, \phi, t)] \quad (\text{B.2})$$

$$E_{\phi}(\theta, \phi) = A_{\phi}(\theta, \phi) \cos[\omega t + \alpha_{\phi}(\theta, \phi)], \quad (\text{B.3})$$

where

$$\omega = 2\pi/f,$$

$A_{\theta, \phi}$ represent the amplitudes of the field components and,

$\alpha_{\theta, \phi}$ the phases of such components.

If, for example, the electric field is assumed to rotate as proposed in *Fig. B.1(a)*, the evaluation of its components at the instants t_1 and $t_2 = t_1 + T/4$ provides the following set of expressions:²

$$E_{\theta}(t_1) = A_{\theta} \cos(\omega t_1 + \alpha_{\theta}) = a \cos \tau \quad (\text{B.4})$$

$$E_{\phi}(t_1) = A_{\phi} \cos(\omega t_1 + \alpha_{\phi}) = a \sin \tau \quad (\text{B.5})$$

and

$$E_{\theta}(t_2) = -A_{\theta} \sin(\omega t_1 + \alpha_{\theta}) = -b \sin \tau \quad (\text{B.6})$$

$$E_{\phi}(t_2) = -A_{\phi} \sin(\omega t_1 + \alpha_{\phi}) = b \cos \tau. \quad (\text{B.7})$$

After some manipulations, the previous expressions lead to:³

$$ab = A_{\theta} A_{\phi} |\sin \delta| \quad (\text{B.8})$$

$$A^2 = a^2 + b^2 = A_{\theta}^2 + A_{\phi}^2, \quad (\text{B.9})$$

where

$$\delta = \alpha_{\theta} - \alpha_{\phi}, \text{ and}$$

$|\cdot|$ suppresses from (B.8) the effect of the assumption made above -*Fig. B.1(a)*- with regard to the rotation sense of the electric field.⁴

¹Any elliptically polarized wave can be decomposed into (i) a couple of circularly polarized waves rotating in opposite senses or, alternatively, (ii) two linearly polarized waves [1, Ch. 15].

²For the sake of simplicity, the angular dependences in (B.2) and (B.3) have been suppressed.

³The manipulations are, basically, $(\text{B.4}) \times (\text{B.7}) - (\text{B.5}) \times (\text{B.6})$ and $(\text{B.4})^2 + (\text{B.5})^2 + (\text{B.6})^2 + (\text{B.7})^2$.

Moreover, from *Fig. B.1(b)*, it can be deduced that $\sin 2\gamma = 2ab/A^2$, which, compared to (B.8)÷(B.9), results in:

$$|\sin 2\gamma| = \frac{2 A_\theta A_\phi |\sin \delta|}{A_\theta^2 + A_\phi^2}. \quad (\text{B.10})$$

The right-hand side of (B.10) is known as the *Ellipse Aperture*, also called *Ellipticity* [2, (16)].

Finally, (B.10) can be combined with $\tan \gamma = b/a = \text{AR}$ and the following trigonometric identity⁵

$$\arcsin x = 2 \arctan \left(\frac{x}{1 + \sqrt{1 - x^2}} \right) \quad (\text{B.11})$$

to yield:

$$\text{AR} = \frac{2 A_\theta A_\phi |\sin \delta|}{A_\theta^2 + A_\phi^2 + \sqrt{(A_\theta^2 - A_\phi^2)^2 + 4A_\theta^2 A_\phi^2 \cos^2 \delta}}. \quad (\text{B.12})$$

Just for the sake of completeness, the Polarization Tilt can also be derived from (B.4) to (B.7), as:⁶

$$\tau = \frac{1}{2} \arctan \left(\frac{2 A_\theta A_\phi \cos \delta}{A_\theta^2 - A_\phi^2} \right). \quad (\text{B.13})$$

B.2.1 Discussion

Among the different techniques to measure the polarization characteristics of an antenna, the so-called *Circular-Component Method* is based on the use of two antenna probes with circular polarization and opposite rotation senses [1, Ch. 15]. These probes measure the amplitudes of the two circularly polarized component waves radiated by the antenna under test (E_{RH} and E_{LH}). In these conditions, the AR of the antenna under test is given by:

$$\text{AR} = \left| \frac{E_{\text{RH}} - E_{\text{LH}}}{E_{\text{RH}} + E_{\text{LH}}} \right|. \quad (\text{B.14})$$

When it comes to use (B.14) for the theoretical evaluation of the AR of an antenna, special attention should be paid if the electric field is decomposed into two linearly polarized components, as it was done in the previous section. This comment is motivated by the fact that in the technical notes of many commercial software packages [4, 5], the circularly polarized components appear

⁴The Sense of Rotation of the electric field is given, in fact, by the sign of $\sin \delta$. For the two particular cases in which $b = 0$ or $\sin \delta = 0$, this sense is not defined, since the field is linearly polarized.

⁵This identity can be obtained from the relation between the arcsin and the arctan functions, together with the half angle formulas. See (1.624.2) and (1.317.5) in [3].

⁶It suffices to do (B.4)×(B.5)+(B.6)×(B.7) and (B.4)²+(B.6)²-(B.5)²-(B.7)², to find that $\sin 2\tau = \frac{2 A_\theta A_\phi \cos \delta}{a^2 - b^2}$ and $\cos 2\tau = \frac{A_\theta^2 - A_\phi^2}{a^2 - b^2}$.

related to their linear counterpart as follows:

$$E_{\text{LH}} = \frac{1}{\sqrt{2}} \left| \dot{E}_\theta - j\dot{E}_\phi \right| \quad (\text{B.15})$$

$$E_{\text{RH}} = \frac{1}{\sqrt{2}} \left| \dot{E}_\theta + j\dot{E}_\phi \right| \quad (\text{B.16})$$

where

$$\dot{E}_\theta = A_\theta e^{j\alpha_\theta}, \text{ and}$$

$$\dot{E}_\phi = A_\phi e^{j\alpha_\phi}.$$

These relations can be misleading, since the direct substitution of (B.15) and (B.16) in (B.14) -see [5], for example- does not provide the *correct* expression for the AR, as it is given in (B.12). In fact, such substitution results into an expression for the AR in which the square root term in the denominator of (B.12) is absent.⁷ For the particular case of circularly polarized antennas, the absence of this additive term in the denominator of the AR formula would lead to an overestimation of the quality of their polarization. In particular, the magnitude of this overestimation grows as the AR of the circularly polarized antenna moves away from the ideal case of perfect circular polarization.

⁷The resulting expression coincides, instead, with the *Ellipticity*, as formulated in (B.10).

References

- [1] J. D. Kraus, Ed., *Antennas*, 1st ed. New York: McGraw-Hill, 1950.
- [2] *The Polarimetric SAR Data Processing and Educational Tool. Polarimetry Tutorial. What Is Polarisation?*, ESA, Jun. 2011. [Online]. Available: http://earth.eo.esa.int/polsarpro/Manuals/1_What_Is_Polarization.pdf
- [3] I. S. Gradshteyn and I. M. Ryzhik, *Table of integrals, series, and products*, 7th ed., A. Jeffrey and D. Zwillinger, Eds. New York, NY: Academic Press, 2007.
- [4] *HFSS v. 11.1 Online Help. Technical Notes. Polarization of the Electric Field. Circular Polarization*, Ansoft Corporation, Apr. 2008.
- [5] *Advanced Design System 2008 Documentation. Radiation Patterns and Antenna Characteristics for Momentum*, Agilent Technologies, Jun. 2011. [Online]. Available: http://cp.literature.agilent.com/litweb/pdf/ads2008/mom/ads2008/Radiation_Patterns_and_Antenna_Characteristics_in_Momentum.html#RadiationPatternsandAntennaCharacteristicsinMomentum-Polarization

List of Tables

1.1	Performance and Structural Requirements	5
1.2	Vehicle Dynamics and Environmental Requirements	5
1.3	Elementary Radiating Cell requirements.	16
2.1	Bandwidth and FBR comparison for three exemplary ACMPAs.	52
2.2	Compromise between bandwidth and FBR.	68
2.3	Performance of two Dual Linearly Polarized ACMPAs with symmetric excitation. . .	71
2.4	Bandwidth improvement using the <i>stacked patches</i> technique.	71
3.1	Characteristics of the dielectrics tested for the S3FIP feeding.	87
3.2	Characteristics of the dielectrics materials of <i>Updated Candidate 1</i>	100
3.3	Dielectric characteristics of <i>Slitted Element</i>	126
3.4	Overall performance comparison: <i>Updated Candidate 1</i> vs. <i>Slitted Element</i>	136
4.1	Elementary Radiating Cell Requirements	142
4.2	Dielectric permittivity tolerances for the radiating element	146
4.3	Dielectric layer thickness tolerances for the radiating element	146

List of Figures

1.1	NATALIA typical application scenario.	4
1.2	NATALIA key design parameters	6
1.3	Block diagram with key components of the NATALIA concept	7
1.4	Schematic description of the NATALIA Tracking Unit	8
1.5	NATALIA implementation alternatives and final solution.	9
1.6	NATALIA array lattice with exemplary grouping and sequential rotation	10
1.7	Preliminary NATALIA PCB buildup overview	12
1.8	Integration of the ERC within the NATALIA array lattice	15
2.1	Preliminary NATALIA PCB buildup overview	30
2.2	Microstrip Patch.	33
2.3	Radiating Element Feeding.	34
2.4	SSFIP Buildup.	36
2.5	Sensitivity of the characteristic impedance of a microstrip line	39
2.6	S3FIP Buildup	40
2.7	Effect of the PPWM's in the operation of a S3FIP in different configurations	41
2.8	Sensitivity of the characteristic impedance of a symmetric stripline	43
2.9	Typical patch shapes.	44
2.10	Basic aperture shapes.	46
2.11	Improved aperture shapes.	47
2.12	The feeding line	48
2.13	The Reference Antenna.	49
2.14	Reflection coefficient at the input of the Reference Antenna	50
2.15	ACMPA input impedance for different patch lengths.	54
2.16	Impedance matching of the ACMPA for different patch lengths.	55
2.17	ACMPA input impedance for different patch widths.	55
2.18	ACMPA input impedance for different patch substrate permittivities.	56
2.19	ACMPA input impedance for different patch substrate thicknesses	57

2.20	Effect of the slot length.	58
2.21	Effect of the stub length in a <i>H-shaped</i> slot.	59
2.22	Equivalent circuit of the ACMPA feeding line	60
2.23	ACMPA input impedance for different lengths of the feeding line open stub.	61
2.24	The feeding line as a two-port.	61
2.25	ACMPA input impedance for different widths of the feeding line.	62
2.26	<i>Fork-shaped</i> feeding line.	62
2.27	ACMPA input impedance for different tine separations	63
2.28	ACMPA input impedance for different feeding line substrates	64
2.29	Reference antenna bandwidth improvement process	66
2.29	Reference antenna bandwidth improvement process (contd.)	67
2.30	Two square Dual Linearly Polarized ACMPCAs with different arrangements of the slots	70
2.31	Dual Linearly Polarized ACMPA with multilayer feeding (i)	72
2.32	Dual Linearly Polarized ACMPA with multilayer feeding (ii)	74
2.33	Different architectures of 3 dB-quadrature couplers.	76
2.34	Dual Linearly Polarized S3FIP with asymmetric stripline feeding	77
2.35	Dual Circularly Polarized S3FIP with different the Branch Line Couplers	78
3.1	Dual Linearly Polarized S3FIP with asymmetric stripline feeding and circular patch	88
3.2	Description of the critical performance parameters of the candidate elements	91
3.3	Critical performance parameters summary for Candidate 0	92
3.4	Embedded element patterns of the Linearly Polarized <i>Candidate 0</i>	93
3.5	Axial Ratio of the Circularly Polarized <i>Candidate 0</i>	94
3.6	Critical performance parameters summary for Candidate 1	96
3.7	Critical performance parameters summary for Candidate 2	97
3.8	Critical performance parameters summary for Candidate 3	99
3.9	<i>Updated Candidate 1</i> Structure	100
3.10	Input impedance of the cavity-backed <i>Updated Candidate 1</i>	102
3.11	Structure of the cavity backed elements: <i>Candidate 4</i> and <i>Candidate 5</i>	103
3.12	Impedance matching characteristics of the cavity backed elements	104
3.13	Radiation efficiency of the cavity backed elements.	105
3.14	Field patterns of the linearly polarized cavity backed elements	105
3.15	Axial ratio of the circularly polarized cavity backed elements	105
3.16	Miniature Coaxial-Stripline Transition.	106
3.17	Detail of the slotted ground plane of the S3FIP as fabricated	107
3.18	Glue removal from the Soldering Maneuver Hole using a Flattened Tip Drill.	108

3.19	Prototype of the coaxial to stripline transition in a back-to-back configuration	109
3.20	Scattering Parameters of the coax.-stripline-coax. prototype	110
3.21	Blind mounting of the coaxial to stripline transitions	111
3.22	Scattering Parameters of the coax.-stripline-coax. blind-mounted prototype	112
3.23	Prototype of the linearly polarized Updated Candidate 1	113
3.24	Scattering Parameters of <i>Updated Candidate 1</i> at its coaxial ports	114
3.25	Normalized field patterns of <i>Updated Candidate 1 (E Plane)</i>	115
3.26	Normalized field patterns of <i>Updated Candidate 1 (H Plane)</i>	116
3.27	Realized gain of <i>Updated Candidate 1</i>	117
3.28	Sub-array structure.	118
3.29	Scattering Parameters of the 3 ways power divider	119
3.30	The slotted ground plane of the sub-array as fabricated	120
3.31	Sub-array prototype	120
3.32	Normalized field patterns of the sub-array	121
3.33	Realized gain of the sub-array	122
3.34	Preliminary NATALIA PCB buildup overview	123
3.35	Integration of the ERC with within the NATALIA array lattice	124
3.36	<i>Slitted Element</i> structure.	125
3.37	Layout of <i>Updated Candidate #1</i> compared to that of <i>Slitted Element</i>	126
3.38	Circularly polarized <i>Slitted Element</i>	127
3.39	Comparison of the layouts of different DCPREs	128
3.40	Circularly polarized <i>Slitted Element</i> with Long Vias included (3-D view)	129
3.41	Detailed 3-D view of one of the Long Vias.	129
3.42	Circularly polarized <i>Slitted Element</i> with Long Vias included (layout)	131
3.43	Detailed 3-D view of the Power Combiner.	132
3.44	Layout outline of the ERC microstrip layer with the footprints of the MMICs	132
3.45	Complete layout outline of the ERC	133
3.46	3-D views of the complete ERC	134
3.47	Photograph of the microstrip layer of the ERC	134
3.48	Mutual coupling between the linearly polarized elements.	136
3.49	Integration of the ERC the Antenna PCB Buildup and into the Array Lattice	137
4.1	3-D view of the Elementary Radiating Cell, with dimensions	141
4.2	Photograph of a complete prototypes board	143
4.3	Structure of the linearly polarized element.	145
4.4	Impact of the fabrication tolerances on the reflection coefficients of the DLPRE . . .	148

4.5	Impact of the fabrication tolerances on the port coupling of the DLPRE	149
4.6	Impact of the fabrication tolerances on the Polarization Purity of the DLPRE	150
4.7	Impact of the fabrication tolerances on the Radiation Pattern of the DLPRE (<i>Port 1</i>)	151
4.8	Impact of the fabrication tolerances on the Radiation Pattern of the DLPRE (<i>Port 2</i>)	152
4.9	Impact of the fabrication tolerances on the radiation efficiency of the DLPRE	153
4.10	Layout outline of the DLPRE prototype	154
4.11	View of the microstrip layer of the different <i>Cal. Kits</i>	155
4.12	Scattering Parameters of the DLPRE (<i>Cal. Kit 1</i>)	158
4.13	Scattering Parameters of the DLPRE (<i>Cal. Kit 2</i>)	159
4.14	Normalized field patterns of the DLPRE (<i>E Plane</i>).	160
4.15	Normalized field patterns of the DLPRE (<i>H Plane</i>).	161
4.16	Realized gain of the DLPRE with illustration of the prototype model	163
4.17	Two different prototypes with fabrication faults highlighted.	164
4.18	The Long Via within the ERC	165
4.19	Scattering Parameters of the ERC Long Via	166
4.19	Scattering Parameters of the ERC Long Via	167
4.20	Long Via Structure.	167
4.21	Impact of the fabrication tolerances on the performance of the Long Via	169
4.22	Scattering parameters of <i>Cal. Kit 1</i>	170
4.23	Layout outline of the Power Combiner.	172
4.24	Performance of the Power Combiner	173
4.25	Different views of the two of ERC candidates	174
4.26	Blind Power Combiner performance for different rotations of its arms (i)	175
4.27	Blind Power Combiner performance for different rotations of its arms (ii)	176
4.28	Power combiner Structure	177
4.29	Impact of the fabrication tolerances on the performance of the Power Combiner	178
4.30	Power Combiner prototyping	179
4.31	Layout of <i>Cal. Kit 4</i>	180
4.32	Scattering Parameters of the Power Combiner (microstrip ports)	181
4.32	Scattering Parameters of the Power Combiner (microstrip ports) (contd.).	182
4.33	Scattering Parameters of the Power Combiner (stripline port)	182
4.34	Layout outline of the DCPRE	183
4.35	Structure of the branch line hybrid.	184
4.36	Scattering parameters of the DCPRE	185
4.37	Branch line hybrid nominal performance	187

4.38	Impact of the fabrication tolerances on the performance of the branch line hybrid . . .	188
4.39	Impact of the fabrication tolerances on the Axial Ratio of the DCPRE	189
4.40	Impact of the fabrication tolerances on the Axial Ratio of the DCPRE (<i>Port 1</i>) . . .	190
4.41	Impact of the fabrication tolerances on the Axial Ratio of the DCPRE (<i>Port 2</i>) . . .	191
4.42	Impact of the fabrication tolerances on the Radiation Efficiency of the DCPRE . . .	192
4.43	Layout outline of The Cell prototype	193
4.44	The Cell prototype	194
4.45	Scattering Parameters of the Cell	195
4.45	Scattering Parameters of the Cell (contd.)	196
4.46	Normalized Radiation Pattern and AR of the Cell. <i>Vertical Plane. Port 1</i>	198
4.47	Normalized Radiation Pattern and AR of the Cell. <i>Horizontal Plane. Port 1</i>	199
4.48	Normalized Radiation Pattern and AR of the Cell. <i>Vertical Plane. Port 2</i>	200
4.49	Normalized Radiation Pattern and AR of the Cell. <i>Horizontal Plane. Port 2</i>	201
4.50	Realized gain of the Cell	202
A.1	The Linearly Polarized Radiating Element within an hexagonal Unit Cell	212
A.2	The Linearly Polarized Radiating Element within two different Unit Cells	213
A.3	Active reflection coefficients at 10.7 GHz	214
A.4	Active reflection coefficients at 11.2125 GHz	215
A.5	Active reflection coefficients at 11.725 GHz	216
A.6	Active reflection coefficients at 12.2375 GHz	217
A.7	Active reflection coefficients at 12.75 GHz	218
A.8	Active coupling coefficients at 12.75 GHz	220
A.9	Reciprocity difference magnitude at 12.75 GHz	221
B.1	The polarization ellipse.	224

Curriculum Vitae

Roberto Torres Sánchez was born on July 11, 1979 in Granada, Spain. He received the Ingeniero de Telecomunicación degree from the Escuela Técnica Superior de Ingeniería de Telecomunicación (ETSIT), Universidad de Málaga (UMA), in 2006. In January 2007, he started PhD studies at the Laboratoire d'Electromagnétisme et d'Acoustique (LEMA), Ecole Polytechnique Fédérale de Lausanne (EPFL).

In March 2006, he obtained from UMA his final diploma project with honors for a work entitled “Two beam printed antenna array for satellite reception” in the area of antenna design for space communications. This work received, from the Spanish Colegio Oficial de Ingenieros de Telecomunicación (COIT), the ASTRA Award for the Best Master Thesis Dissertation. In January 2007, he joined LEMA where he is currently Research and Teaching Assistant. He has been active research member in several projects for the European Space Agency (ESA). His main contributions are related with the project:

- “NATALIA” (New Automotive Tracking Antenna for Low cost Innovative Applications). Involved in the conception, implementation and experimental verification of a new generation of high-performance low-profile antenna terminals for mobile satellite communication services. ESA/ESTEC Contract No. 18612/04/NL/US. ESA Project (January 2007-Present).

Among his teaching activities at LEMA he has assisted in the exercises for the course of *Rayonnement et Antennes*, graded exams, been in charge of the *Laboratoires Répartis* and supervised several student projects.

List of Publications

Refereed Journal Papers

1. R. Torres-Sánchez, F. P. Casares-Miranda, E. Márquez-Segura, and P. Otero, “Symmetry, XPD, and port isolation in an ACMPA array with dual linear polarization,” *Microwave Opt. Technol. Lett.*, vol. 49, no. 7, pp. 1722–1727, Jul. 2007.
2. J. Perruisseau-Carrier, F. Bongard, R. Golubovic-Niciforovic, R. Torres-Sánchez, and J. R. Mosig, “Contributions to the modeling and design of reconfigurable reflecting cells embedding discrete control elements,” *Microwave Theory and Techniques, IEEE Transactions on*, vol. 58, no. 6, pp. 1621–1628, June 2010.
3. M. J. Jiménez-Fernández, R. Torres-Sánchez, and P. Otero, “Cavity-backed slot array antenna in substrate-integrated waveguide technology,” *Microwave and Optical Technology Letters*, vol. 53, no. 9, June 2011.

Refereed Conference Papers

1. R. Torres-Sánchez, S. Vaccaro, and J. R. Mosig, “A compact and low cost radiating element for automotive satellite broadcasting reception arrays,” in *30th ESA Antenna Workshop for Earth Observation, Science, Telecommunication and Navigation Space Missions*, ESA/ESTEC, Noordwijk, The Netherlands, May 2008.
2. R. Torres-Sánchez, J. R. Mosig, S. Vaccaro, and D. Llorens, “On the design of a compact and low cost radiating element for satellite broadcasting automotive receiving arrays,” in *33rd Annual Antenna Applications Symposium*, Robert Allerton Park, Monticello, Illinois (USA), Sep. 2009.
3. R. Baggen, S. Vaccaro, , D. Llorens, R. Torres-Sánchez, and G. Langgartner, “First prototyping of a compact mobile Ku-band satellite terminal,” in *proc. EuCAP 2010, 4th International Conference on Antennas and Propagation*, Apr. 2010.

4. S. Vaccaro, D. Llorens, R. Torres-Sánchez, and R. Baggen, “Low cost phased array for mobile Ku-band satellite terminal,” in *proc. EuCAP 2010, 4th International Conference on Antennas and Propagation*, Apr. 2010.
5. R. Manrique, R. Torres-Sánchez, C. Domínguez, F. Tiezzi, and J. R. Mosig, “Design and prototyping of a microstrip transmit-receive array antenna for mobile Ku-band satellite terminals,” in *proc. EuCAP 2010, 4th International Conference on Antennas and Propagation*, Apr. 2010.
6. S. López-Peña, J. Zürcher, R. Torres-Sánchez, A. G. Polimeridis, and J. R. Mosig, “Modeling and manufacturing of a series of identical antennas for a P-band ice sounder,” in *proc. EuCAP 2010, 4th International Conference on Antennas and Propagation*, Apr. 2010.
7. R. Torres-Sánchez, J. R. Mosig, S. Vaccaro, and D. Llorens, “A compact and low cost elementary radiating cell for satellite broadcasting automotive receiving arrays,” in *proc. PIERS 2010, 28th Progress in Electromagnetics Research Symposium*, Cambridge, Massachusetts (USA), Jul. 2010.
8. —, “Design review of a compact and low cost elementary radiating cell for satellite broadcasting automotive receiving arrays,” in *33rd ESA Antenna Workshop*, ESA/ESTEC, Noordwijk, The Netherlands, Oct. 2011.

Patents

1. F. Tiezzi, S. Vaccaro, D. Llorens, and R. Torres-Sánchez, “Method and apparatus for a compact modular phased array element,” Patent US 20 110 025 574, February 3, 2011.

Technical Reports

1. R. Torres-Sánchez, “Preliminary design of the NATALIA radiating element,” LEMA (EPFL), Lausanne, Switzerland, Jun. 2007.
2. R. Torres-Sánchez, “Evaluation of different candidate radiating element for the NATALIA array,” LEMA (EPFL) & JAST Antenna Systems, Lausanne, Switzerland, Sep. 2007, (v. 7).
3. —, “Proof of concept of the NATALIA radiating element,” LEMA (EPFL), Lausanne, Switzerland, Apr. 2008, (v. 4).
4. R. Torres-Sánchez, “NATALIA radiating element update. Two new candidates,” LEMA (EPFL), Lausanne, Switzerland, Dec. 2008, Draft.
5. —, “NATALIA radiating element update. Third new candidate,” LEMA-EPFL, Lausanne, Switzerland, Dec. 2008, Draft.

6. —, “Integration of the NATALIA Radiating Element: Update & Comparison with the previous candidate,” LEMA (EPFL), Lausanne, Switzerland, Feb. 2009, (v. 1.5).
7. —, “Sensitivity of the NATALIA radiating element to manufacturing tolerances,” LEMA (EPFL), Lausanne, Switzerland, May 2009, Draft.
8. —, “NATALIA Blind Elementary Radiating Cell & Vias Tolerance Analysis,” LEMA (EPFL), Lausanne, Switzerland, Aug. 2009, (v. 2.1).
9. —, “State of the art review in switched beam antennas,” LEMA (EPFL), Lausanne, Switzerland, Sep. 2009, (v. 1).
10. J. R. Mosig, F. Tiezzi, and R. Torres-Sánchez, “Design and development of smart array antennas for broadband mobile communications,” LEMA (EPFL) & JAST Antenna Systems, Lausanne, Switzerland, CTI project. Final Report and Implementation Plan, Feb. 2010.
11. R. Torres-Sánchez, “Fragmented Aperture Antennas. A preliminary review,” LEMA (EPFL), Lausanne, Switzerland, Aug. 2010, (v. 1).
12. —, “Model Transfer of the NATALIA Elementary Radiating Cell,” LEMA (EPFL), Lausanne, Switzerland, Feb. 2011, Draft.
13. —, “Measurement Results of the first NATALIA Breadboard,” LEMA (EPFL), Lausanne, Switzerland, Jun. 2011, Draft.

